UNIVERSITÀ DEGLI STUDI DI MILANO
SCUOLA DI DOTTORATO
TERRA, AMBIENTE E BIODIVERSITÀ

Dottorato di Ricerca in Scienze della Terra
Ciclo XXIV

Stability assessment of terraced slopes: field data and numerical modelling

Ph.D. Thesis

Corrado Camera
Matricola R08050

Tutori	**Anno Accademico**	*Coordinatore*
Prof. Tiziana Apuani	**2010-2011**	**Prof. Elisabetta Erba**
Prof. Marco Masetti		

CONTENTS

PART I

INTRODUCTION TO THE STUDIED PROBLEM

1 Chapter 1

GENERAL INTRODUCTION

This work is finalized to the assessment of the stability of terraced slopes. The study therefore includes the understanding of the failure mechanisms of these particular slopes and the quantification of the influence of hydrogeological and mechanical parameters of dry stone walls and backfill soils both at a large and at a detailed scale.

The study was performed in Valtellina. In particular, the slope chosen as study area is the one uphill of the small village of Tresenda, that in 1983 and 2002 was affected by soil slip/debris flow events that caused victims (only in 1983) and severe damages.

The topic is of particular interest because it is demonstrated that, during the periods of intense rainfalls that interested Valtellina in the last 30 years, the areas worst hit by superficial landslide events were those terraced by means of dry-stone walls (Crosta et al., 2003).

Various reasonable hypothesis were suggested by the same and other authors (Azzola and Tuia, 1983; Cancelli and Nova, 1985) about the triggering mechanisms of these events and their principal causes, but nobody has developed a complete, detailed analysis that takes into account both soil and dry-stone walls hydrogeological and resistance characteristics.

The present work wants to plug this gap. After a brief description of the study area in which also a wider overview of the cited historical events is presented (Chapter 2), the attention is turned to the field data acquisition (Chapter 3), on which the following modelling activities are based. Field observations and literature review permit to define a conceptual geotechnical-geomechanical model for which a thin superficial soil horizon, retained by dry-stone walls, lies upon a semi impervious lithic layer. Field and laboratory data allow also to characterize the soil from a physical, hydrogeological and resistance point of view.

At first, a numerical analysis at a very detailed (single terrace) scale is performed, studying the mechanisms of formation of perched groundwater tables at the contact between the soil and the semi impervious layer, taking into account different combinations of bedrock slope and wall height (Chapter 4). The model is calibrated and validated using as input real rainfall events registered at a rain gauge not far from the study area, and comparing the outputs of the model with hydrographs of a piezometric datalogger, specifically installed. The model is later used to define the groundwater pore pressure distributions relative to various rainfall events, in order to study their influence on the stability.

Stability analysis is carried out at the same scale using, also in this case, a numerical model. Performing this kind of analysis great attention is given to the definition of the mechanical properties of dry-stone retaining walls. An original procedure is presented to define their equivalent Mohr-Coulomb cohesion and friction angle values, that are subsequently validated during the calibration phase of the numerical model. In this context, interesting results emerge. In part, they confirm the hypothesis and observations of other authors (Azzola and Tuia, 1983; Cancelli and Nova, 1985, Crosta et al., 2003), regarding the triggering mechanisms of superficial landslides on similar slopes. On the other side, the obtained results show that these mechanisms are not the only possible ones (Chapter 5).

In the following part of the work, the scale changes, passing from a single terrace analysis to an extended area investigation. The approach is similar: In the first instance the analysis is focused on the dynamics of formation of perched groundwater tables and the pattern of redistribution of water within the soil. Their effects on stability are subsequently studied. This part of the work is performed using distributed models that work in a raster environment. In such a context, besides the hydrogeological and resistance parameters of the materials involved, it is necessary to define also maps that describe the geometry of the problem, in particular a digital elevation model for the topography and a soil depth map for the definition of the height of material potentially involved in a superficial landslide. The resolution of these maps must be elevated, in order to take into account the presence of walls. The procedure adopted for their obtaining is presented in Chapter 7 and Chapter 8 respectively.

In the following Chapter 9 and Chapter 10, the raster hydrogeological and stability models are presented and described in detail, together with their results. As previously, the results partly confirm the observation of the authors that have already worked within similar morphological frameworks and in addition they give rise to further hypothesis. Nevertheless, besides these satisfying results, there are also some drawbacks. Advantages and disadvantages of the method applied are therefore carefully analyzed in the final Chapter 11, where also the future plans are described.

2 Chapter 2

STUDY AREA

2.1 Introduction

The study area is located in the central part of Valtellina, an alpine valley in northern Italy. It is a terraced slope on the northern flank of the valley in Teglio municipality, within the Sondrio province, as the whole 3.212 km^2 of Valtellina. Sondrio, which lies in the middle-low part of the valley, is the largest city in the area with about 22.000 inhabitants. Other important centers are Morbegno, in the lower part, Tirano, in the middle-high part, and Bormio in the upper part of the valley.

Valtellina is the basin of the Adda River, that originates in the Cancano Valley, north of Bormio, and flows into the Como Lake near Dubino, 15 km downhill of Morbegno (Fig 2.1).

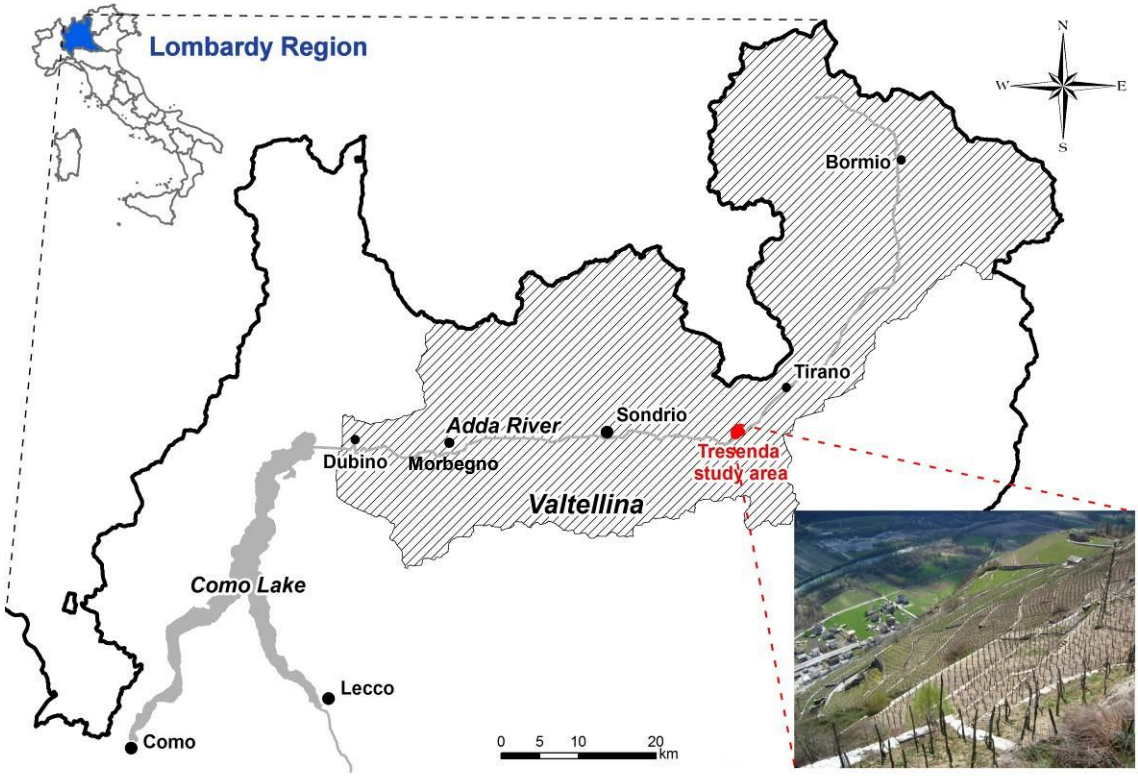

Figure 2.1: geographical setting of Valtellina.

The national road SS 38 and the railway run parallel to the Adda river on the valley floor where most of the commercial and industrial activities of Valtellina are situated. Important economic activities are related to the food farming, wine, touristic, and handcraft sectors. In particular, the wine production is strictly connected to this work, as the study area lies on a slope terraced for vineyard cultivation.

2.2 General geological and geomorphological setting

Valtellina is a typical glacial alpine valley with a wide valley floor and steep flanks whose slope is sometimes interrupted by both natural and anthropogenic morphological terraces. Its trend, which is

W-E from the outlet to its central part where it becomes SW-NE to join to the N-trending upper part, is strictly connected to structural and tectonic factors. The Periadriatic Line, in this area called the Insubric Line or Tonale Fault, which separates the Variscan basement of the Southern Alps from the Alps *strictu sensu* (Austroalpine, Pennidic and Helvetic nappes), runs along the northern flank of Valtellina. This line is approximately 500 m above the valley plain where the Adda flows. The bedrock is predominantly composed of metamorphic (gneiss, micaschist, phillite, and quartzite) and igneous rocks with subordinated sedimentary rocks ("Foglio 19 Tirano" of the Carta Geologica d'Italia 1:100000, 1969).

The study is particularly focused on the slope that lies between the village of Tresenda, which is downhill, and the small Somasassa hamlet, which is uphill, in the municipality of Teglio (0.6 km^2) (Fig 2.1). Tresenda is located in the central part of the valley at the bottom of the northern Rhetic flank.

Tresenda and Somasassa lie south of the Periadritic Line, so they are in the Southern Alps domain. The bedrock, on the Tresenda slope, is made up of micashists (Edolo Schists, "Foglio 19 Tirano" of the Carta Geologica d'Italia 1:100000, 1969), that are interested by folds both at a large and midsized scale. These mid-scale folds are often enlightened by quartz and plagioclase levels and lenses, and interested by drag folds. When outcropping, the rock mass appears irregular, with four principal discontinuity sets. The first one is more or less parallel to the schistosity planes with dip direction towards N, so towards upslope, and high dip. The second set has a dip direction towards S-SE and a mean dip of 45°. The third set presents a similar mean dip while the dip direction is oriented SW. The last family of discontinuities shows a dip direction towards E-NE and a mean dip of 60°. All these discontinuities are joints and except for rare occasions they are closed. The horizontal intercept has a range between 3 and 49 cm with a mean value of 12.5 cm and a standard deviation of 9 cm, while the vertical one has a range between 6 and 37 cm with mean 15.5 cm and standard deviation 8 cm. The Representative Elementary Volume (REV) has been estimated to be 0.14 m^3. Nevertheless, a great part of the study area is covered by soils of morainic, glacio-fluvial, and colluvial origin, often reworked by man's activity for agricultural purposes (Cancelli and Nova, 1985): vineyard cultivation is in fact widespread on the Tresenda terraces.

Apart from soils, whose characterization is treated in the next chapter (Data acquisition), the former presence of a glacier is additionally pointed out by glacial forms and morphological evidences such as morphological terraces, trenches and counterslopes, that also attest a situation of general instability also extending to the portion of the slope uphill of Somasassa. This disequilibrium could be related to a tensional release due to the retreat of the glacier after the last glacial maximum. Although recognized, it is essential to notice that this kind of phenomena has very different deformation times and causes in respect of the rapid soil slips/debris flows events that have interested the Tresenda slope more than once in recent years, and whose dynamics are the real object of this work.

2.3 Historical events

In May 1983, July 1987, November 2000, and November 2002, Valtellina (Fig. 2.1) experienced prolonged periods of intense rainfalls that produced widespread landslides along the whole valley (Cancelli and Nova, 1985; Guzzetti et al, 1992; Crosta et al.; 2003; Aleotti et al., 2004 Blahut et al., 2011). According to Crosta (1990) and Crosta et al. (2003), in 1983 more than 200 superficial landslides affected Valtellina while in 1987 the huge Val Pola landslide (40 millions of m^3), that

caused 12 victims, was the apex of a series of hundreds of mass movements that interested the entire valley from Dubino to Bormio (Fig 2.1). In November 2000, 260 shallow landslides were observed over four days in the lower-middle part only of the valley between Dubino and Tirano. The last large events that occurred in Valtellina and affected the whole valley are those of November 2002, causing the death of two people and huge damages to buildings and infracstructures (Aleotti et al., 2004; Blahut et al., 2011).

In all these occurrences, the most affected areas were the slopes terraced by means of dry-stone walls on the northern flank of the valley between Sondrio and Tirano (Cancelli and Nova, 1985; Crosta et al., 2003). In particular, according to Cancelli and Nova (1985), most of the events were triggered on terraced areas with slope angles between 30° and 40°.

It is therefore clear that in Valtellina stability analysis on terraced slopes is a key issue to assess and improve people and infrastructure safety. Crosta et al. (2003) identify some possible causes of failure in the lack of maintenance of dry retaining walls, in a stratigraphical setting where failures are more prone to form along the contact between layers bearing different mechanical characteristics, and in various hydrological and hydrogeological properties that affect the preferential way of drainage, both superficial and at the contact between the soil and the semi-impermeable layer.

In particular, between the 22nd and 23rd of May 1983, Tresenda and the neighbouring village of Valgella were affected by three soil slip/debris flow events that caused 14 victims in Tresenda and 4 in Valgella (Fig 2.2). Furthermore, many other people were injured, some buildings and infrastructures were completely or partially destroyed and others damaged (Cancelli and Nova, 1985). On the 26th of November 2002 a similar event onstructed the provincial road that connects the bottom of the valley to the villages on its right flank and caused little damages to some buildings. Azzola and Tuia (1983) directly observed the second of the three events in 1983 and gave a complete description of it. The triggering was caused by the failure of a dry retaining wall and the mass movement began as a slow mud flow that increased in volume by incorporating the backfill of other terraces downhill of the initiation zone. These terraces failed under the overload caused by the flow itself. According to Cancelli and Nova (1985) these events are usually shorter than 50 m in length, signifying that the material involved is often not enough to increase its volume and evolve into a debris flow. On the other hand it is easy to imagine how even a slight increasing in the slope angle a few meters downhill of the initiation zone could build up the speed of the collapsed mass, sustaining its movement and favouring its morphing into a potential destructive debris flow.

Figure 2.2: the event of May 1983 in Tresenda (photo by geologist Maurizio Azzola).

3 Chapter 3

DATA ACQUISITION

Most of the work to acquire the data for following elaboration was done in summer 2009. Different goals were pursued. First of all field surveys were performed to define the geological and geomorphological features of the area and to focus on the definition of the terraces characteristics (geometrical parameters and land-use, soil thickness and bedrock geometry). The subsequent field work was devoted to geotechnical and hydrogeological investigations by means of geotechnical *in situ* tests and sample collection for soil laboratory tests. Finally, instruments were installed to hydrogeologically monitor the slope.

During summer 2009 a laser scanner acquisition of the slope was also performed, in order to obtain a high resolution DEM for the subsequent modelling analysis. This acquisition did not return positive results, so the high resolution DEM was obtained by aerial photographs interpretation combined with a GPS survey carried out in early spring 2011.

A second field campaign was carried out in spring 2011, to investigate soil thickness with geophysical methods. This study was performed on a little portion of the study area and it was addressed to acquire detailed data to validate the soil depth map obtained from geostatistical analysis of direct punctual measures on a limited number of measure points.

3.1 Terracement characteristics, land-use, soil thickness and bedrock geometry

The quantitative geomorphological survey, performed at a 1:5000 scale, was applied to depict the typology of the terracements in the studied area, draft the land-use map, and infer the soil thickness.

The slope is terraced mainly by dry retaining walls, and it grows vineyards receiving a southern exposure. The wall geometry varies; the height can range from 70 cm up to 5 m, but 90% of the walls are between 1.40 and 2.50 m in height. Strip length and width depend on the characteristics of the slope. In the western part of the study area, the slope presents many outcrops, some subvertical rock-walls and, in general, a more irregular geometry that results in walls with small lengths (up to ≈15-20 m) and widths (up to ≈6-7 m). The eastward slope is gentler, especially in its middle and lower parts, as shown by the geometry of the walls, which can reach a length of 100 m and a width of 15-20 m. The covering soils are often thin, as the walls are founded on small outcrops or on shallow bedrock. Their thickness is regulated by the height of the walls and the stepped geometry of the slope. Runoff water drainage is enhanced by an artificial network of channels, called *valgelli*. Cemented roads built after the events of 1983 are used to facilitate access to the vineyards and to cut off the hydrogeological continuity of the slope. The local geological context and the past occurrence of landslides make this sector of the valley highly representative of many other sectors in the area.

A land-use map of the slope was drawn (Fig. 3.1), the soil depth was measured and instruments for slope monitoring were installed (Fig. 3.2). Some soil samples were collected for laboratory tests, and some *in situ* tests were performed.

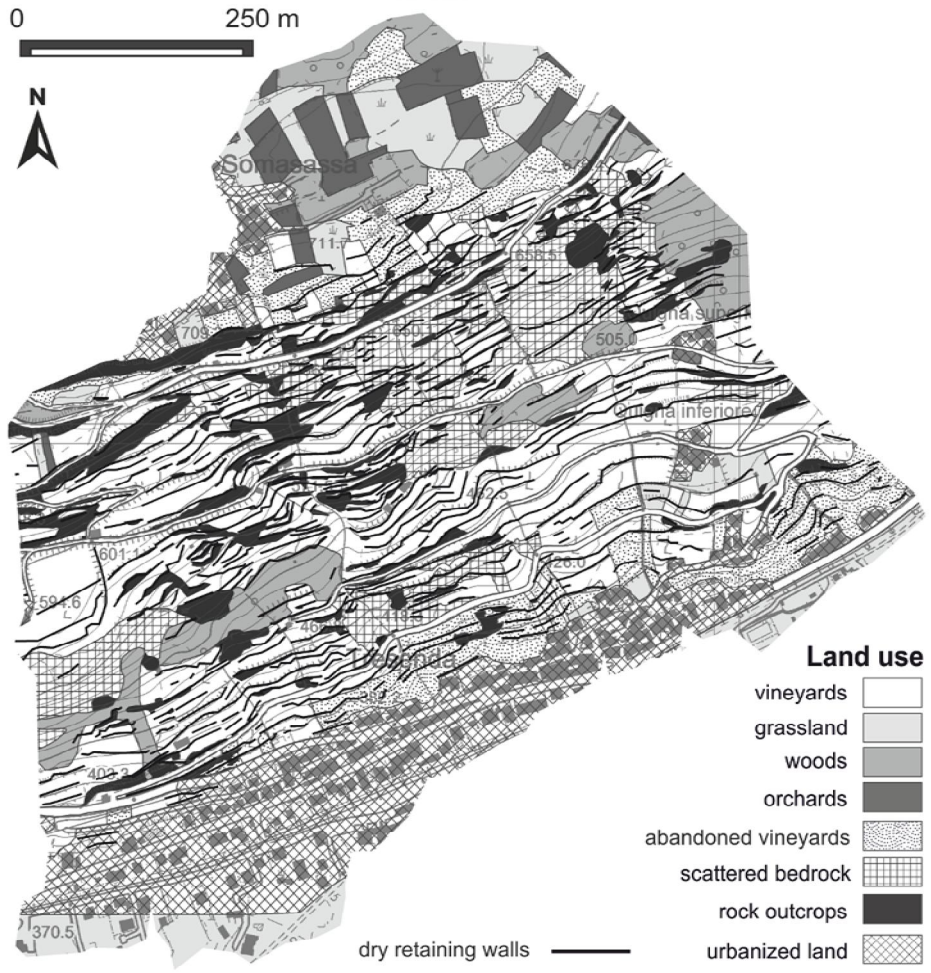

Figure 3.1: land use map

At first thirteen land-use classes were recognized, subsequently reduced and merged into five, seven or eight depending on the needed use of the map. Fig. 1 shows the eight class map, which displays with sufficient detail the variations of land use in the study area without becoming overmuch rich and heavy-reading. The prevalent class is vineyards; another large area is occupied by lands where the cultivation of grapevines was abandoned, and another class is characterized by scattered bedrock outcrops.

The soil thickness spatial distribution was derived by interpolating direct measurements taken along the slope (a more detailed description can be found in chapter 8). There are several rock outcrops on the western part of the slope, and a dry retaining wall is located on almost every outcrop. Here, the height of the wall equals the soil thickness. In the eastern part, vineyards are more continuous, and there are only small rock outcrops. In spite of that, the walls there are founded directly on the bedrock; on this evidence it was assumed that the bedrock was close to the surface even when it was not in an outcrop, and the wall height was considered to be an acceptable measurement of soil thickness. Some direct measurements of soil thickness were also taken during the drilling done for installing the instruments. During the survey, soil thickness was found to have great spatial variability; for example, in the western part of the slope, the values could change from 2 m to 80 cm within a distance of 10 m. During the fieldwork, 682 points were measured.

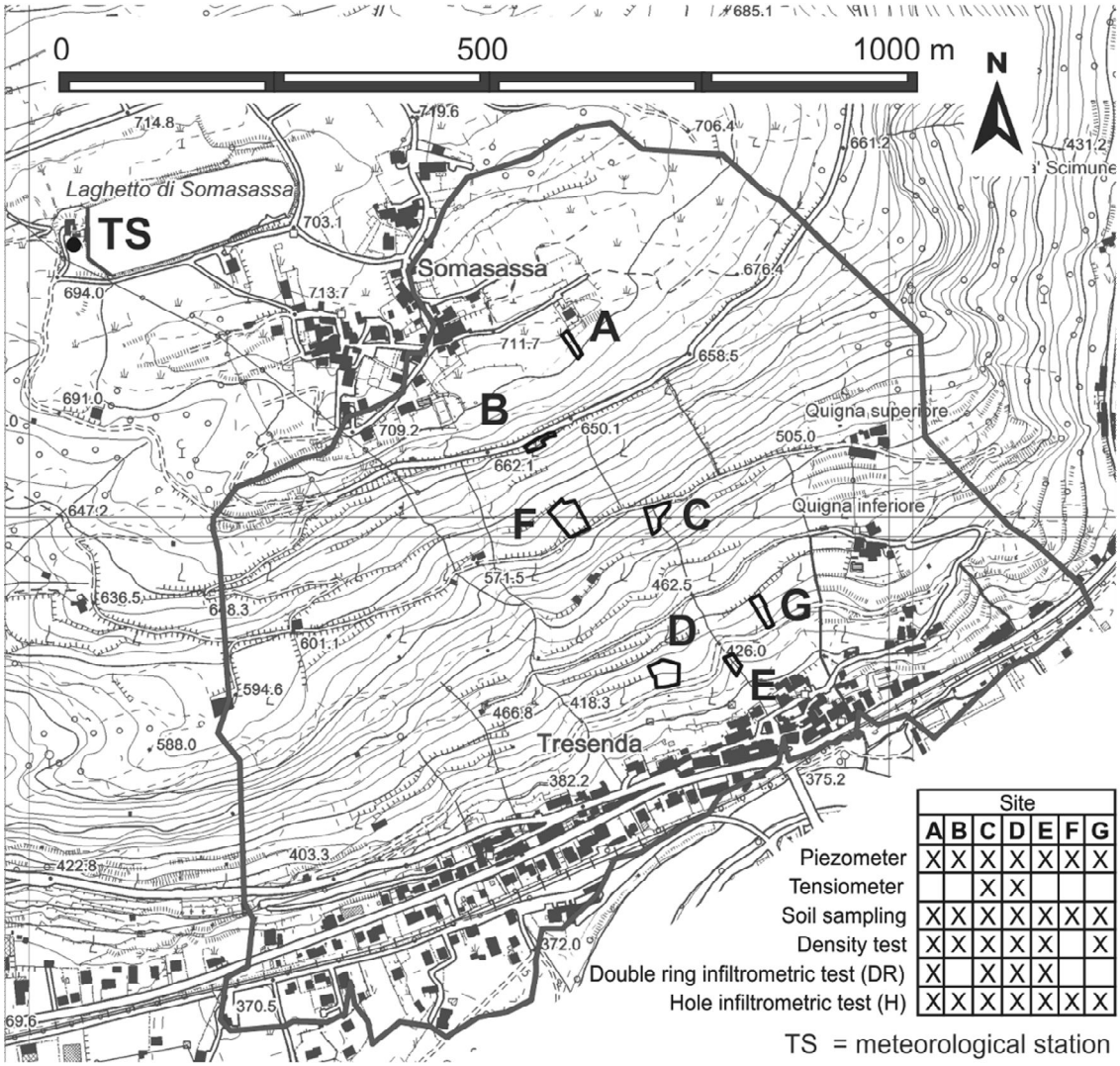

Figure 3.2: test sites within the study area

3.2 Geotechnical and hydrogeological features

Three different types of test were performed in the field: double ring infiltrometric tests (DR), hole infiltrometric tests (H) and soil density measurements using the sand cone method (ASTM D1556, 2007). 20 samples were collected for laboratory geotechnical investigations between July 2009 and February 2010. The location and typology of the *in situ* tests and the monitoring system are detailed in Fig. 2. The test sites were chosen considering their position on the slope, the land use that characterized them and above all the permissions obtained from the owners through the co-operation with the local Comunità Montana and Municipality.

The soil hydraulic conductivity (k_s) from *in situ* tests ranged between 1.1 x 10^{-4} and 5.4 x 10^{-6} m/s as detailed in Table 1. The hole infiltrometric tests were interpreted as variable head Lefranc tests using a known approximation of the static groundwater level (Cestari, 2005). All of these tests were performed with a time interval of two seconds between measurements. The interpretations of the double ring infiltrometric tests are presented in Annex I, those of the hole infiltrometric tests in Annex II.

Table 3.1: Some soil properties measured in place along the hillslope.

Soil property	Site						
	A	B	C	D	E	F	G
Hydr conduct, $k_{(DR)}$ (m/s)	$2.05 \cdot 10^{-6}$	-	$2.87 \cdot 10^{-5}$	$3.35 \cdot 10^{-5}$	$3.78 \cdot 10^{-5}$	-	-
Hydr conduct, $k_{(H)}$ (m/s)	$2.44 \cdot 10^{-5}$	$6.56 \cdot 10^{-5}$	$5.37 \cdot 10^{-6}$	$1.75 \cdot 10^{-5}$	$1.33 \cdot 10^{-5}$	$1.03 \cdot 10^{-5}$	$1.10 \cdot 10^{-4}$

DR = double ring infiltrometer test
H = hole infiltrometer test

Laboratory permeability and direct shear tests were performed, besides the classical identification analysis. The investigated backfill soils had a natural bulk density (γ_0) of 13.5-15.8 kN/m^3, a calculated dry density of γ_d = 12.8 – 15.7 kN/m^3, a computed porosity of n = 40 - 52 %, and a specific gravity of the solid soil particles of G_s=2.42 – 2.69 g/cm^3. At the time of the sampling, the natural moisture content was W = 1.2 - 14.4%, and the saturation was Sr = 10 - 38%. Grain-size analyses were performed on 20 samples. According to the Unified Soil Classification System (U.S.C.S.) adopted by the *American Society for Testing and Materials* (ASTM D2487, 2010), the investigated backfill soils are SM (silty sand with gravel) or GM (silty gravel with sand) with a coefficient of uniformity (CU) between 20 and 157, which means that they are well-graded soils. The only exception was Site G, which showed a greater abundance of gravel and an almost total absence of fine elements (GW – well graded gravel with sand), and a grain size distribution that affected the soil's hydrogeological behaviour (for details see Table 3.3). All the granulometric curves can be seen in Annex III.

Constant (ASTM D2434-68, 2006) and falling head permeability tests were performed on 6 samples. The laboratory permeability tests gave a range of hydraulic conductivity between 2.1 10^{-6} and 1.4 10^{-5} m/s, which, considering the scale effect, is comparable with the values of k_s obtained on the field (minimum, maximum and mean values in Tab 3.2, graphs and results of every test in Annex IV).

Direct shear tests (ASTM D3080, 2004) were performed on 3 x 3 samples (normal load 50 – 100 – 200 kPa) both with and without the organic content and in peak and residual conditions. Minimum, maximum and mean values for cohesion and friction angle are reported in Tab 3.2, for the curves and the graphs of every test see Annex V.

Table 3.2: Summary of backfill soils hydrogeological and geotechnical principal properties from laboratory analysis: saturated hydraulic conductivity (k_s) from constant head (CH) and falling head (FH) permeability tests; peak (p) and residual (r) values of cohesion (c) and friction angle (ϕ).

Parameter	Min	Mean	Max
$k_{s(FH)}$ [m/s]	3.2×10^{-6}	5.3×10^{-6}	1.5×10^{-5}
$k_{s(CH)}$ [m/s]	2.1×10^{-6}	4.7×10^{-6}	9.9×10^{-6}
c_p [kPa]	3.5	11.0	18.5
ϕ_p [°]	27.5	34.0	36.5
c_r [kPa]	0.0	9.5	17.5
ϕ_r [°]	26.0	32.5	38.5

Table 3.3: summary of the identification tests, sample by sample, where ID = sample name; P_o= natural weight; P_d = dry weight; Gr. Aero = granulometric analysis; LL PL SL = liquid, plastic and shrinkage Atterberg limits; Wn = natural water content; O.C. = organic content; γ_0 and γ_d = natural, and dry bulk density respectively; Gs = specific gravity of the soil solid particles; n = porosity, Sr = saturation degree. N.D. = not determinable; * incorrect measurements.

ID	Identification Tests – Soil Properties													
	P_0 (g)	P_d (g)	Gr. (USCS)	Aero	LL	PL	SL	W_n (%)	O.C. (%)	γ_0 (g/cm³)	γ_d (g/cm³)	G_s (g/cm³)	n (%)	Sr (-)
SiteA_a	1166,2	1087.8	SM (silty sand with gravel)		///	///	///	7.2	///	1.03*	0.96*	///	///	///
SiteC_a	2005.4	1954.6	GM (silty gravel with sand)		///	///	///	2.6	///	1.61	1.57	///	40	0.10
SiteD_a	2040.5	1965.9	SM (silty sand with gravel)		///	///	///	3.8	///	1.38	1.33	///	50	0.10
SiteE_a	2077.5	1853.5	SM (silty sand with gravel)		///	///	///	12.1	///	1.55	1.38	///	46	0.36
SiteA_o	2349.1	2322.9	GM (silty gravel with sand)		///	///	///	1.1	///	///	///	///	///	///
SiteB_o	2421.1	2393.3	GSM (silty gravel and sand)		///	///	///	1.2	///	///	///	///	///	///
SiteC_o	2872.7	2853.4	SM (silty sand with gravel)		///	///	///	0.7	///	///	///	///	///	///
SiteD_o	3397.0	3324.9	SM (silty sand with gravel)		///	///	///	2.2	///	///	///	///	///	///
SiteE_o	3164.6	3096.6	GM (silty gravel with sand)		///	///	///	2.2	///	///	///	///	///	///
SiteF_o	2538.5	2509.5	GM (silty gravel with sand)		///	///	///	1.2	///	///	///	///	///	///
SiteG_o	2990.8	2982.6	GW – GM (well graded gravel with silt and sand)		///	///	///	0.3	4.7	///	///	///	///	///
Orchard	2531.2	2396.5	SM (silty sand with gravel)		///	///	///	5.6	3.58	///	///	///	///	///
Wood	2874.4	2681.2	GM (silty gravel with sand)		///	///	///	7.2	3.27	///	///	///	///	///
Grass	1935.3	1757.5	SM (silty sand with gravel)		///	///	///	10.1	///	///	///	///	///	///
SiteA_d	5825.6	5343.6	SM (silty sand with gravel)		N.D.	N.D.	N.D.	9.0	4.61	///	///	2.635	///	///
SiteC_d	6935.2	6179.1	GM (silty gravel with sand)		N.D.	N.D.	N.D.	12.2	4.96	///	///	2.637	///	///
SiteE_d	7442.2	6508.1	GM (silty gravel with sand)		N.D.	N.D.	N.D.	14.4	7.32	///	///	2.554	///	///
Site A_f	4062.4	3683.0	SM (silty sand with gravel)		N.D.	N.D.	N.D.	10.3	3.80	1.41	1.28	2.694	52	0.25
Site B_f	3484.7	3193.7	GM (silty gravel with sand)		N.D.	N.D.	N.D.	9.1	6.23	1.46	1.34	2.524	47	0.26
Site G_f	3246.6	2912.4	GW (well graded gravel with sand)		N.D.	N.D.	N.D.	11.5	3.04	1.56	1.40	2.423	42	0.38

3.3 Hydrogeological monitoring

Seven piezometers, two of which using a datalogger for continuous acquisition, and two manual tensiometers were installed along the slope (Fig. 3.2).

They were installed in the second half of July 2009, and the acquisition began on the 11th of August at Sites A and G. The sites were chosen because of their position; one is on the upper part of the slope, and the other is located on the lower part. In the following months, one of the data-loggers was first moved from Site G to Site E and then to Site C because temporary perched water tables were never measured at the first two sites. Acquisition was stopped after exactly two years, on the 11th of August 2011.

All piezometers reached a depth of 90 cm, except for those at Site A (95 cm) and Site G (140 cm). The lower filtering part of each piezometer tube (40-45 cm) was covered with a non-woven textile. The hole was filled with sand until it reached the height of the textile, and then it was filled with soil. In the last 10 cm, bentonite was used to seal the bore. The tensiometer installed at Site C had a length of 60 cm, and the one at Site D was 90 cm. Both contained sand around a porous cup, soil along their body and bentonite in the last 5-10 cm to seal the hole.

PART II

ANALYSIS AT SINGLE TERRACES SCALE

4 Chapter 4

RAINFALL DATA ANALYSIS AND HYDROGEOLOGICAL 2D MODELING

Terraced slopes are very common in hilly and mountainous areas and serve two primary functions: to create conditions for agricultural development in otherwise inaccessible areas and to stabilise slopes by breaking up their high gradients, thereby protecting anthropogenic structures from landslides. These two functions are strictly related to one another because slope stability must be guaranteed to allow for the development of sustainable agricultural activity, which relies on the presence of an appropriate amount of land surface over a given time span.

However, in modifying the morphology of the slope, such structures also cause a momentous change in the hillslope hydrology by decreasing the surface water runoff, thus favouring infiltration and the development of groundwater flows. Although this decrease in runoff is generally beneficial to agriculture, an increase in the amount of water in the soil should be carefully monitored to avoid the occurrence of local instabilities in the terraced systems.

As a final consequence of the infiltration process, the formation of perched groundwater tables (PGTs) can be considered as one of the most influential factors controlling slope stability in different environments, such as river terraces (Xu et al. 2011), alluvial deposits in river valleys (Zhang and Liu 2010) and human terraced system (Crosta et al. 2003). The terraces are typically formed by backfill soil, which is composed of loose deposits with medium to high hydraulic conductivity lying on compacted soil or bedrock with generally low hydraulic conductivity. In this geological context, the formation of PGTs immediately above the low hydraulic conductivity formation is favoured, and it is strongly influenced by the hydraulic conductivity ratio between the high and low permeability layers (Huat et al. 2006). The development of PGTs is extremely important in controlling superficial slope stability; in spite of their transient nature, they can develop pore-water pressures sufficient to trigger local slope instabilities (Li et al. 2005; Dahal et al. 2009a). This occurrence is critical because it often develops along the contact area between layers with different mechanical characteristics, where failure surfaces are more likely to evolve. In terraced slopes, this condition can be very dangerous because once a single terrace becomes unstable, it can easily involve other terraces in its downhill movement, eventually forming a potentially destructive debris flow (Azzola and Tuia 1983).

Monitoring and understanding the dynamics of the formation of PGTs is vital in order to manage the stability of these environments, in consideration of their potential danger to existing and future anthropogenic structures and their liability to remove arable soil, with highly detrimental consequences to the economies of mountain municipalities.

4.1 Rainfall data

During the two years of perched ground water levels acquisition, rainfall data were collected at the rain gauge of Teglio Somasassa (TS) (Fig. 3.2), and Valgella Pisciotta (VP), which are the property of the *Fondazione Fojanini* that kindly allowed the use of their data. The TS meteorological station was situated immediately outside the upper part of the study area at an elevation of 695 m a.s.l., and the VP station was no more than 2 km west of it at 420 m a.s.l.. Data from VP were used only when the TS data were not reliable due to some failure in the acquisition system as declared by the

representative of the station. In the rare cases when data from both these automatic stations were not available, rainfalls registered at Sondrio – via Paribelli (290 m a.s.l.) by ARPA (Regional Agency for Environmental Protection) were used. This rain gauge is located 15 km west of the study area.

The historical data (1980-2002) were also furnished by *Fondazione Fojanini*. They were registered by a mechanical pluviograph at Castelvetro (≈ 610 m a.s.l, 3 km west of the study area) and so first of all they needed to be digitized. The pluviograph was removed every winter from middle October to middle March, so the elaborated data mainly refer to the spring-summer period.

4.1.1 Statistical analysis

23 years of hourly rainfall from Castelvetro pluviograph (1980-2002) and 4 years of data from the Teglio-Somasassa automatic station (2007-2010) were used to calculate the Rainfall Intensity Duration Frequency Curves (RIDFC – Fig. 4.1) (Camera et al., 2011; Quan Luna et al., 2010; Quan Luna et al., under review) with the Gumbel Extreme Value Type I distribution (Gumbel, 2004).

The automatic station of Teglio Somasassa is the natural substitute of the Castelvetro pluviograph. In the four years between 2002 and 2007 no rainfall data, that could be consistent with those of these stations, are available in the proximity of the study area.

The rainfall events and the registered groundwater levels from the 11th of August 2009 to the 11th of August 2011 were combined and analyzed together in order to find some relations between these phenomena. At first 133 events were recognized, 62 in the first year and 71 in the second. An event is defined as a precipitation of at least two hours that ends at the last hour with rain followed by at least 12 dry hours. Among these 133 events only 24 (15 in the first year of acquisition) caused the formation of a recorded saturated horizon at the contact between the backfill soil of the terrace and the bedrock on site A, while on site C only 5 perched groundwater tables were recorded. Therefore, the following elaborations were performed on data coming from the piezometer of site A only.

For every rainfall event its duration, cumulated rainfall, and mean intensity were calculated. Other parameters were recognized, such as maximum hourly intensity, time of maximum hourly intensity from the beginning of the event, and the presence or not of a saturated horizon with its maximum level. In particular regarding duration, cumulated rainfall and mean intensity, the precipitation events were categorized in 8 classes, based on the Sturges formula (Sturges, 1929 wikipedia); the number of rainfall events with groundwater table formation and without it were then determined for every class (Fig 4.2).

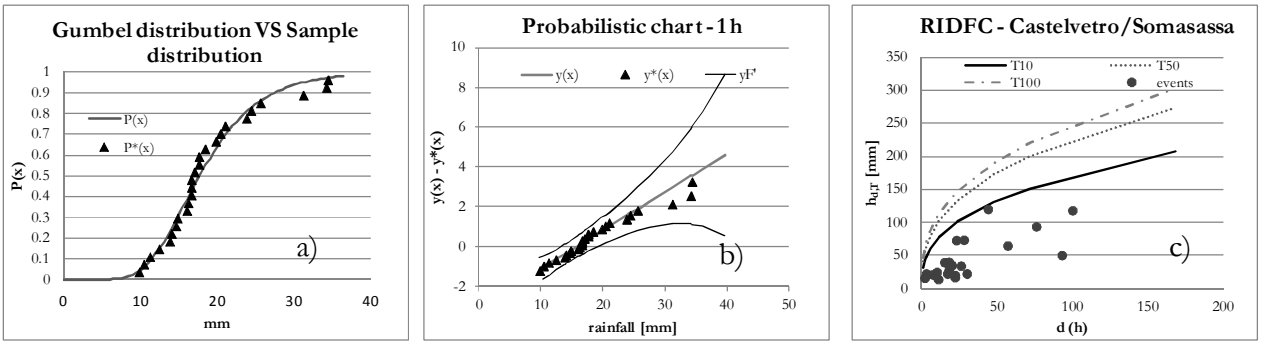

Figure 4.1: a) comparing the Gumbel distribution P(x) with the sample distribution of the data related to 1 hour lasting extreme events; b) probability chart with the reduced variables of Gumbel distribution y(x) and samples y*(x) of events of 1 hour with the 95% confidence band; c) rainfall intensity duration frequency curves for the study area. Frequency is expressed in terms of return period in years (T). In this image the events registered between August 2009 and August 2011 that caused the formation of a perched groundwater table are also reported, in order to give an idea of their return period.

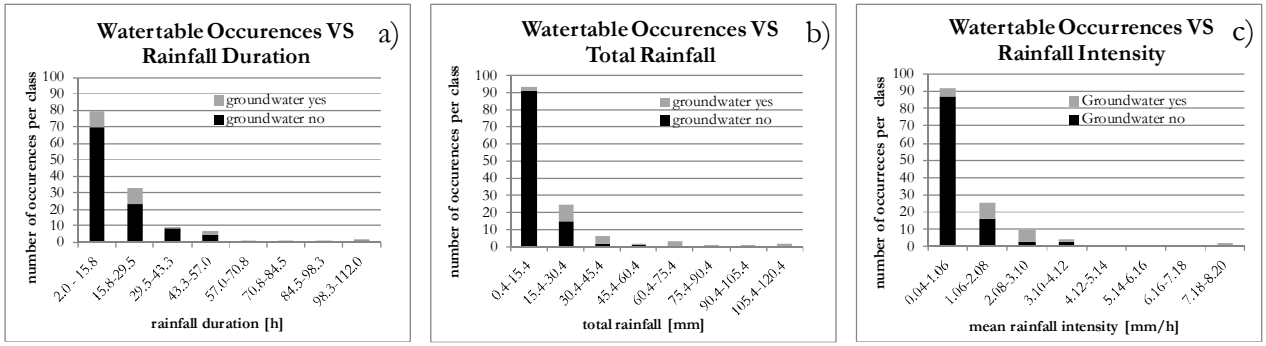

Figure 4.2: histograms of the number of occurrences of water table for every class of a) rainfall duration; b) total rainfall; c) mean rainfall intensity with respect to the entire number of rainfalls for each class.

Duration, total rainfall and intensity were also analysed to determine an empirical threshold, above which they could be considered to be major predisposing factors for the formation of a perched groundwater table. Empirical thresholds calculated from a relation between the intensity and the duration of a rainfall event are very common if applied to the occurrence of landslide events (Campbell 1975; Caine 1980; Wieczorek 1987; Cancelli and Nova 1985; Govi et al. 1985; Ceriani et al. 1992; Larsen and Simon 1993; Ceriani et. 1994; Crozier 1999; Crosta and Frattini 2001; Bacchini and Zannoni 2003; Aleotti 2004; Guzzetti et al. 2004; Zezere et al. 2005; Guzzetti et al. 2007; Dahal and Hasegawa 2008; Guzzetti et al. 2008). The principle of the curves drawn in Fig 4.3 is the same, but in this instance it is applied to the occurrence of a temporary perched groundwater table. The rainfall threshold, which is expressed by the equation in Fig 4.3, was chosen considering the duration and the mean intensity of rainfall events, which generated perched groundwater tables (triangles) and tables in which no saturation was recorded (circles). The threshold was drawn looking at the first year of acquisition events (Fig. 4.3a - Camera et al., 2011) and then verified using the second year set of data. This second set of data confirms the effectiveness of the threshold even if it seems a little conservative.

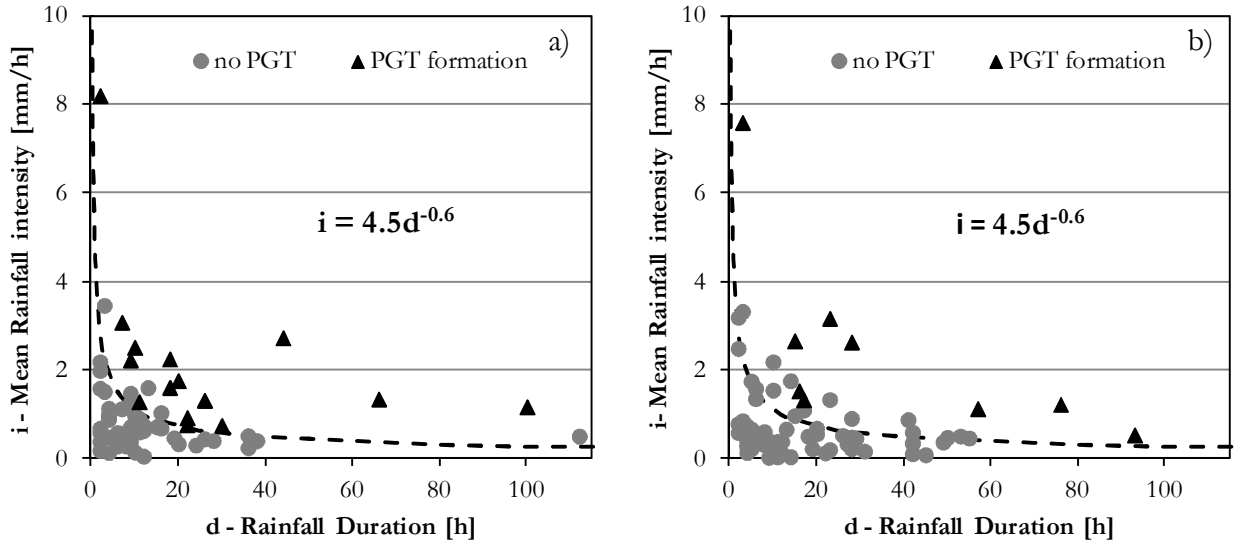

Figure 4.3: a) rainfall intensity – duration threshold for the formation of perched groundwater table drawn on the basis of rainfall events registered from August 2009 to August 2010; b) verification of the threshold with the rainfall data registered between August 2010 and August 2011.

Particular attention was later devoted to the 24 events that generated a perched groundwater table. Two of them stand out as they are characterized by the presence of snow. They occurred both in

December, the first one in 2009 and the second in 2010. The one in 2009 is a long lasting precipitation with numerous relative peaks of groundwater table levels. Looking at the temperatures registered by a sensor of the piezometer, it seems possible to relate these peaks to temperature variations, as shown in Fig. 4.4a, and not only to precipitations (Fig. 4.4b), that nevertheless are the predisposing factor. A groundwater table indeed formed a few hours after the temperature reached a level constantly over 0 °C.

The same happened also in the same period of the following year. In this case it is possible to observe two different events, with a relative short duration (16 and 28 hours respectively) and a medium-low total cumulated rainfall (24.6 and 6.6 mm). During the first event temperature was always below zero, so that precipitation was in the form of snowfall. Snow accumulated on the ground surface and when the temperature reached values higher than 0 °C, it began to melt and infiltrate. It is in fact only after the end of the first event that melting could begin (Fig. 4.5a) and so the perched water table that formed in this situation can be attributed to the sum of the two events (Fig 4.5b), though in particular to the first one, responsible for the accumulation of quite a considerable snow cover.

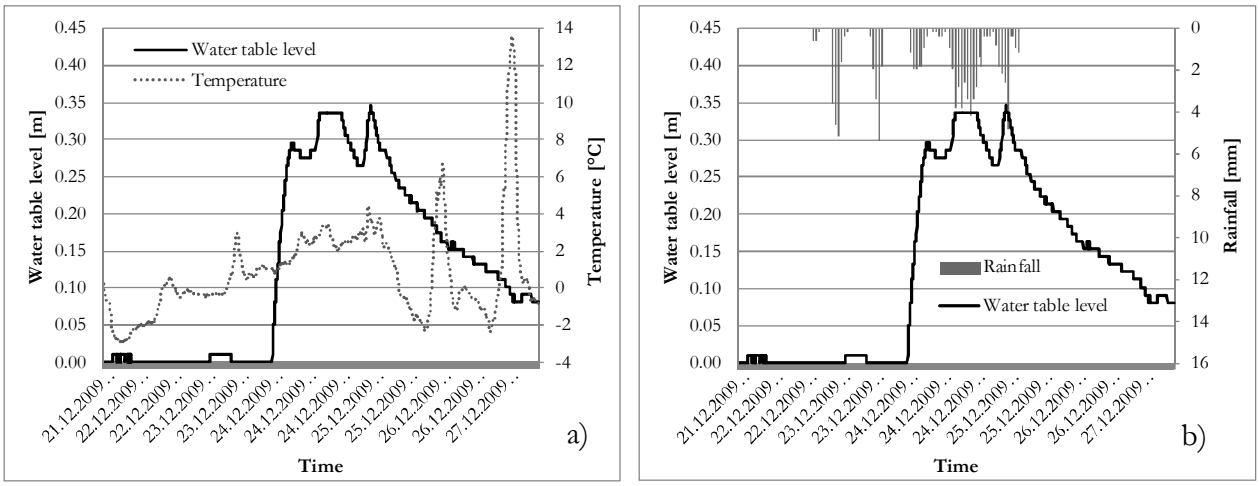

Figure 4.4: a) Relationships between temperature and water table level. First saturated horizon forms only after more than a day from the beginning of the precipitation event but after a few hours with temperature constantly over 0 °C.

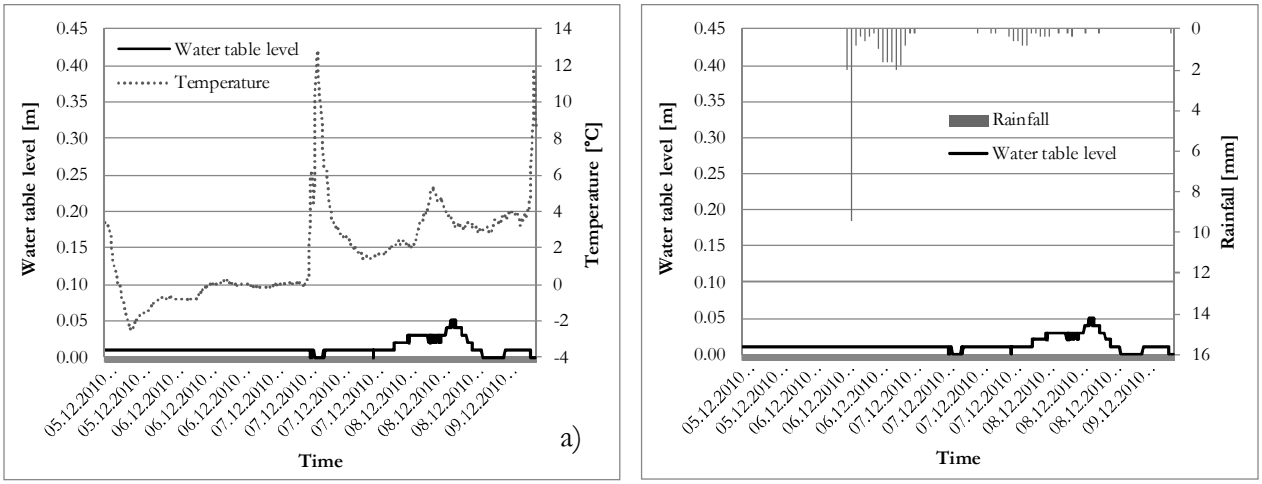

Figure 4.5: a) Water table and temperature with respect to time; b) water table and precipitations with respect to time. Temperature increases after the finish of the first precipitation event, melting begins and a water table forms during the second event, characterized by temperature over 0 °C.

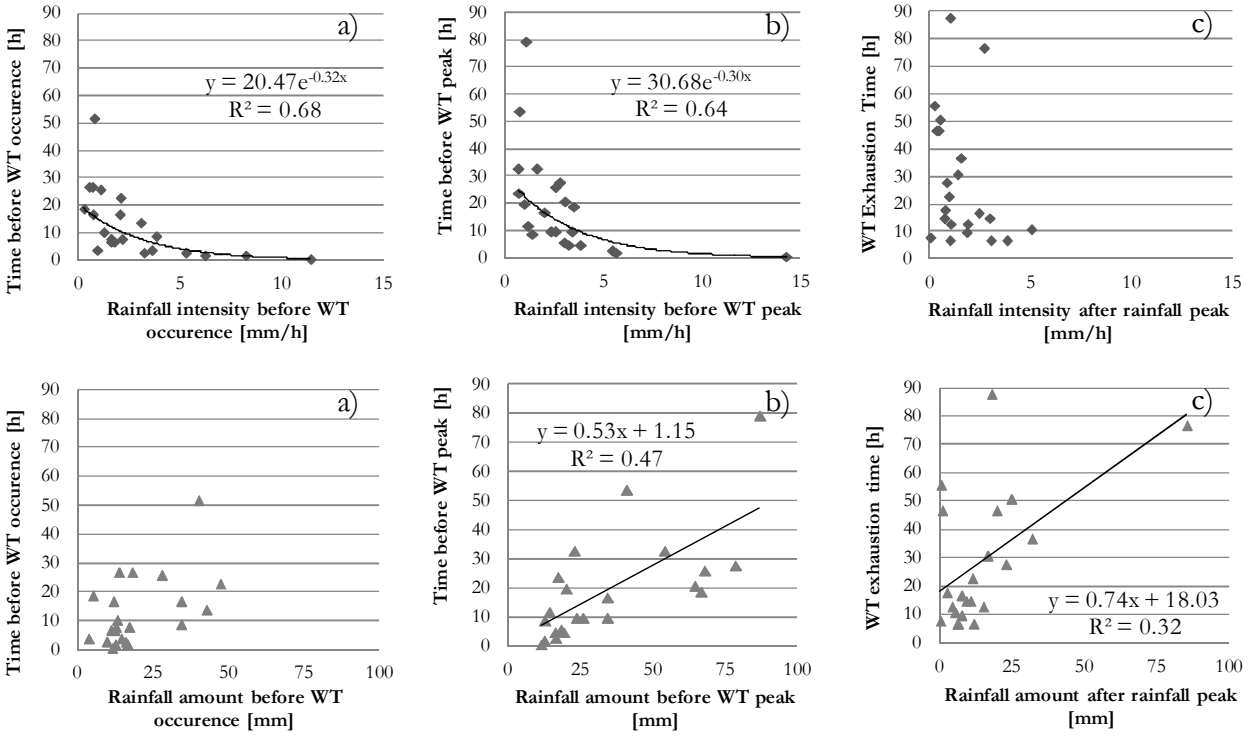

Figure 4.6: a) rainfall intensity and time of formation of the first groundwater table; b) rainfall intensity and time of groundwater table peak; c) rainfall intensity after the rainfall peak and the exhaustion time of the groundwater table; d) amount of rainfall and time of formation of the first groundwater table; e) amount of rainfall and time of groundwater table peak; f) amount of rain fallen after the rainfall peak and exhaustion time of the groundwater table.

Regarding the other 22 events that formed a perched groundwater table, a great number of different factors were recognized in addition to those already cited that were analyzed for all the events. In particular these 22 events were characterized, besides the previous defined factors, by the peak of groundwater level both in height and time from the beginning of the rainfall event and the lag distance in time from the maximum hourly intensity; the time of formation (always from the beginning of the event) of the first saturated horizon was determined and the total rain and the intensity up to that moment calculated. The same was done for the groundwater exhaustion time that was calculated from the end of rainfall, from the peak of rainfall intensity and from the peak of groundwater level. An estimate was done (Fig 4.1c) of their return period, considering duration and total rainfall and the Rainfall Intensity Duration Frequency Curves (RIDFC) and relationships between the characteristics of the events were established. In particular it was noticed that the formation of the groundwater table (WT) is mainly controlled by the rainfall intensity(Fig 4.6a and 4.6d); in the determination of WT peak, intensity has still a primary role even if a certain low correlation can be recognized also with the rainfall amount (Fig 4.6b and 4.6e); the exhaustion time, on the contrary, shows very little correlation with the amount of rain fallen after the rainfall peak and almost no correlation with intensity (Fig 4.6c and 4.6f).

4.1.2 Historical analysis of rainfall data

The acquired data were also used for analyzing the evolution of the main rainfall properties in the last 30 years. The considered parameters are, on a yearly basis: the number of rainfall events, distinguishing those above the threshold previously presented (Fig 4.7a); the total cumulated rainfall and the mean quantity of rainfall for each event (Fig 4.7b); the total rainfall hours and the mean event duration (Fig 4.7c); the event mean total intensity and mean maximum intensity (Fig 4.7d).

The drawn trend lines are moving averages with period three in all the graphs. This type of interpolation allows both to flatten single years peaks in the short period, and to clearly identify the parameter trend in a mid-long period.

The total number of rainfall events (Fig 4.7a) constantly increases during the Eighties and reaches its peak around 1990. From there, between relative maxima and minima, it seems to have a slow decreasing trend that is still going on. The number of events above threshold, as the total number of rainfalls, increases during the Eighties with a peak around 1985. Then, after a relative minimum, it remains almost constant till the mid Nineties, where there is the absolute peak. The peak is followed by a period of continuous slow decrease that has probably seen its finish in recent years. Nowadays, the trend is constant or slowly increasing.

The total cumulated rainfalls (Fig 4.7b) show an increasing trend during the Eighties, with a peak in the second half of the decade. The peak is followed by a relative minimum and maximum, respectively during the early and mid Nineties. After this second maximum the trend decreases constantly, even if it seems that an inversion is now taking place. The mean cumulated rainfall for a single event shows a trend that is completely comparable to that of total cumulated rainfalls.

Both the trends of the total number of rainfall hours and the mean duration of a single event are comparable with the trend of the cumulated rainfall, but some minor differences have to be highlighted. The mid Eighties peaks in Fig 4.7c are relative maxima while the mid Nineties ones are absolute, at variance with the maxima positions observed in Fig 4.7b. After these peaks there is a long period of slow decrease, and a recent trend inversion is well visible.

The total mean intensity (Fig 4.7d) shows a slightly increasing trend in the first half of the Eighties, with a little peak around 1985-1987. Then the trend decreases, and from the beginning of the Nineties till now it appears almost constant. Somewhat different is the trend of the maximum mean intensity, which represents the mean of the hourly rainfall peaks registered during every event of the same year. The trend presents a relative little peak in the first half of the Eighties and the absolute peak in the second half of the same decade. Then a sudden decrease can be observed, followed by a gradual increase that lasts until the end of Nineties, when the trend seems to become approximately constant.

Considering the strong relationship existing between rainfall events and the possibility for them to act as predisposing and/or triggering factors for the onset of mass movements, this analysis is useful to recognize that in the past there were probably two periods in which rainfalls could have caused problems related to hillslope stability: during the mid-Eighties and the mid-Nineties. In particular, in the first period various landslides occurred: in Tresenda in 1983, but also the great Val Pola landslide in Alta Valtellina and the flood of the medium-low valley of 1987 must be remembered. During the Nineties, instead, events of a similar magnitude did not occur.

It is also interesting to note that the only parameters at their maximum in the middle Eighties are the ones related to intensity. Duration and cumulated rainfall are at mid-high levels in these years, but not at their maximum. Therefore, since mid Nineties values are somewhat lower, it seems that intensity parameters are crucial for turning a rainfall event into a landslide triggering factor.

Regarding the present days, i.e. the beginning of the new millennium and its first 5-8 years, the analyzed trends are all showing a slow decrease or remain levelled around constant values, lower than those that characterized the mid Eighties, and also a decreasing of slope instability processes can be outlined. In the last 3-5 years, with the exception of 2009, which was a very dry year, some

values have been inverting their trend. Anyway this inversion, at the moment, does not appear to be significant.

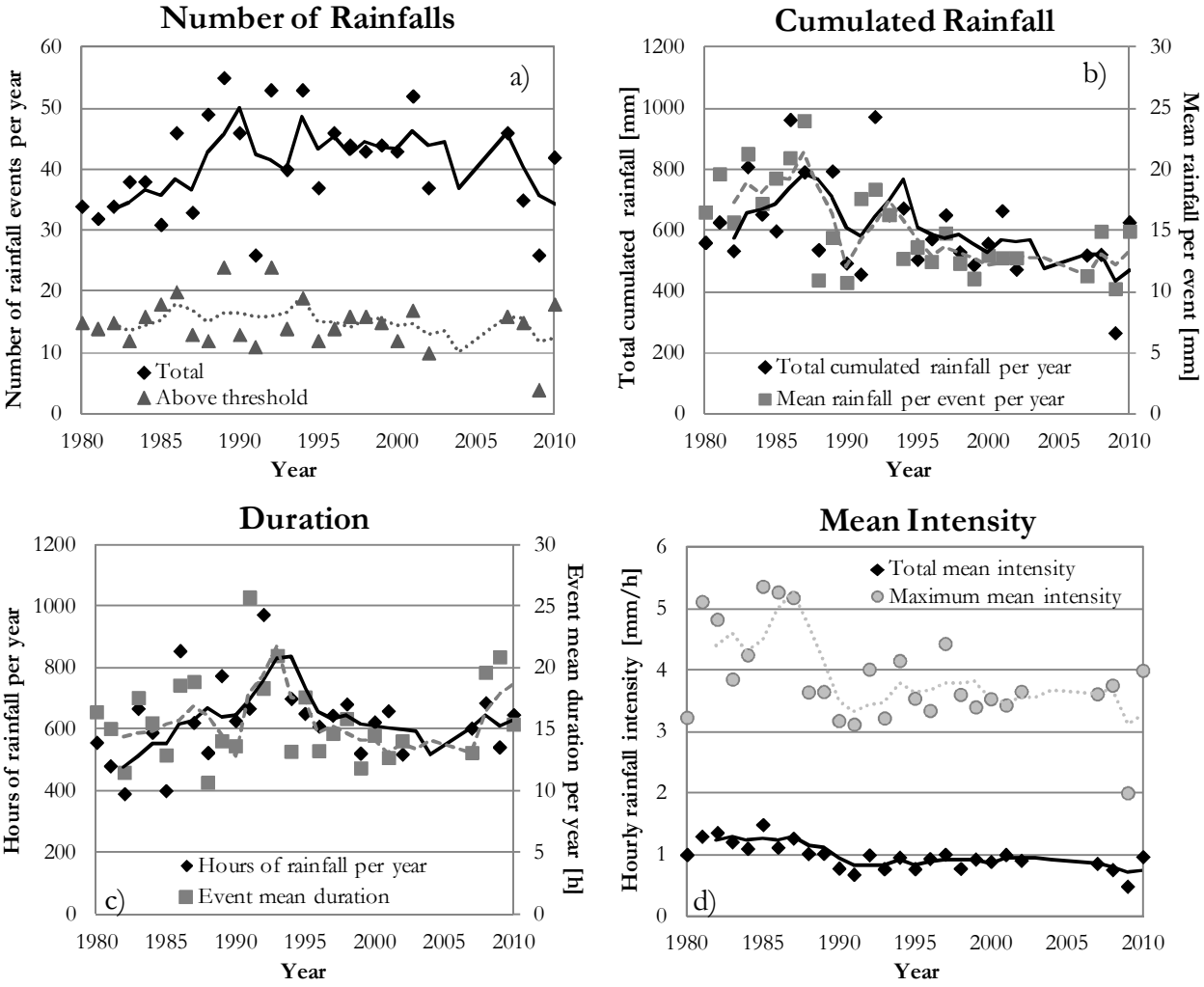

Figure 4.7: a) number of total rainfall in a year and number of rainfall events above the threshold per year; b) total cumulated rainfall during a year and mean cumulated rainfall during a single event; c) total number of rainfall hours during a year and mean duration of a single event; d) Total mean intensity of a single event and maximum mean intensity calculated from the hourly rainfall peaks of each event.

4.2 Hydrogeological 2D Modelling

Numerical modelling of the infiltration process, considering both unsaturated and saturated conditions, has proven to be the most effective tool to relate landslide to rainfall events (Trandafir et al. 2008; Tsai et al. 2008; Dahal et al. 2009b; Rahardjo et al. 2010). In this study the numerical modelling was performed using SEEP/W, which is a finite element numerical modelling code (GEO-SLOPE International Ltd. 2002). SEEP/W enables the modelling of groundwater flows both in saturated and unsaturated zones and allows for the study of steady and transient states.

The aim of the modelling was to reproduce the temporary PGT that forms as a consequence of certain rainfall events. The work progressed by adding different complexities step-by-step. At first, simplified geometry considering a single terrace only was used. The geometry consisted of a dry stone retaining wall founded on bedrock with a wedge of soil at its back. Different combinations of wall height and bedrock slope angle, representing the actual combinations measured in the field, were then investigated. (Fig 4.8) To achieve realistic values of moisture content in soils, a dummy

water table in the bedrock was used, and a low intensity rainfall value was applied to the top boundary to perform an initial transient state analysis. This procedure enabled the creation of initial conditions of pore water pressures in agreement with those measured by the tensiometers. During calibration and validation, a second transient phase characterised by actual rainfall was performed. To prevent an anomalous rise of the water table in the bedrock, the flow boundary condition, reviewed for head, was set at the bottom of the model. A boundary condition of the same type was also applied to the downstream face of the retaining wall to allow for drainage. Once the model was calibrated and validated, it was used to determine, in terms of duration and return period, the events that can cause saturation behind the walls and thus lead to conditions of possible instability.

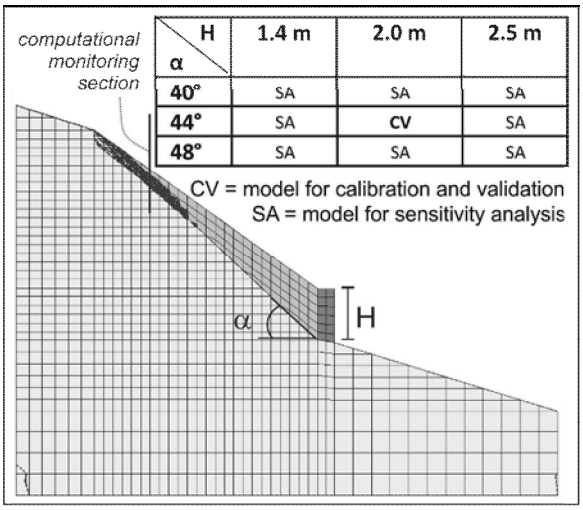

Figure 4.8: geometry of the model for calibration, validation and sensitivity analysis. It is shown that the saturated horizon never reached the area of soil immediately behind the wall. This result is in agreement with the recorded data at Sites E and G, where the piezometers were installed near the wall in the front part of the terrace where perched groundwater was not observed.

4.2.1 Calibration and validation

The rainfall events of the 22nd October 2009 and the 17th February 2010 and the corresponding groundwater tables recorded at Site A were used to calibrate and validate the model. Aside from the boundary conditions, the software requires the definition of some hydraulic and hydrogeological parameters for the three materials (soil, wall and bedrock) involved in the model. These parameters include the Soil Water Retention Curve (SWRC), saturated hydraulic conductivity (k_s), and the ratio between vertical (k_v) and horizontal (k_x) hydraulic conductivity ($k_r = k_v/k_x$). The SWRC was calculated using the results of grain size analyses with the Gupta & Larson (1979) equation, whereas the hydraulic conductivity functions were determined by SWRC and k_s, which were obtained through field and laboratory data using the Green & Corey method (1971). k_s was then adjusted in the calibration phase (1×10^{-5} m/s). Considering that changes in soil moisture conditions in the bedrock and the wall had a very small impact on groundwater circulation, their SWRCs were considered to be flat, i.e., constituted by a constant value of soil water content. The k_s of the wall was initially set to an order and a half of magnitude greater than that of the soil (5×10^{-4} m/s), assuming a hydraulically efficient wall with a good draining capability. The k_s of the bedrock was set to 1×10^{-8} m/s, three orders of magnitude less than that of the soil, representing its role as a barrier to infiltration. k_r was initially considered as equal to 1 for all three materials.

The goal was to reproduce the groundwater hydrograph registered by the continuous datalogger. The parameters at the experimental site were a wall height of 2 m and a bedrock slope angle of 44° (Fig 4.8) During the calibration, a good agreement in terms of height between the recorded and the calculated value was reached. The timing of the peak was good, but a problem arose regarding the descendant limb of the calculated groundwater hydrograph, as it declined faster than the measured one (Fig 4.9a). Once the model was calibrated, it was then validated using a second rainfall event as

an input. The results were acceptable, and they were even more precise than those of the calibration, especially in terms of the maximum pressure head. They reproduced with a good approximation the recorded data (Fig 4.9b). The problem associated with the fast exhaustion time of the perched groundwater table persisted in this phase.

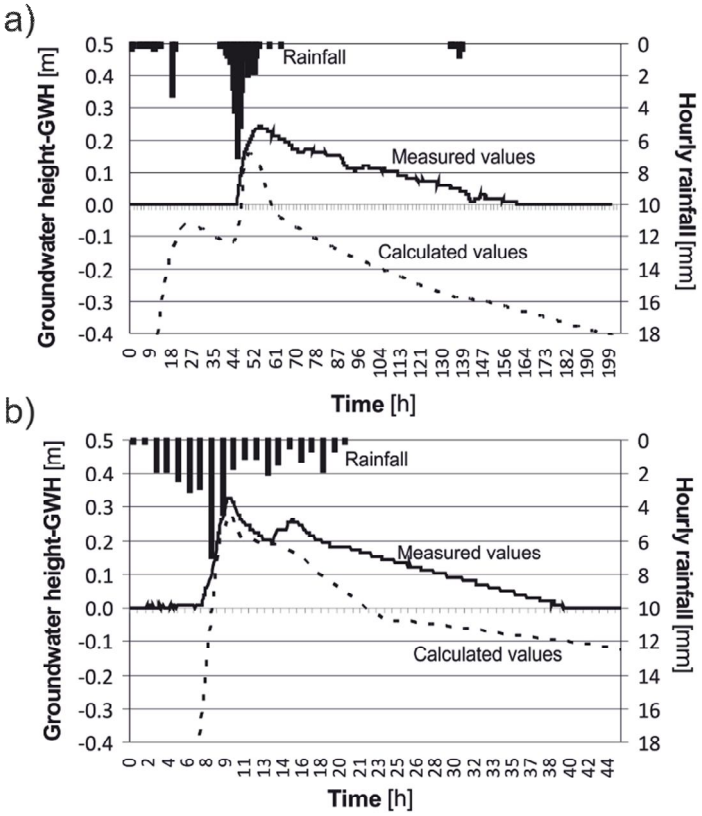

Figure 4.9: Comparison between the groundwater levels recorded in the field and those calculated by the model at the specified node; a) during the calibration phase; b) during the validation phase.

The results of the simulations were also useful to represent and describe the process of perched water table development in these contexts, in which a progressive increase in soil thickness from the top of the slope to the wall plays a key role. When rainfall intensity is sufficiently high, a water table begins to form in the high part of the slope where the low hydraulic conductivity bedrock is close to the topographic surface. As soon as the water table forms, the groundwater flows downhill along the soil-bedrock interface, where it can also be fed by infiltration in the lower part of the slope. The possibility that a significant water table reaches the back of the wall mainly depends on the combination of soil hydraulic characteristics and geometry and rainfall intensity and duration.

If the nearly formed water table in the upper part of the slope is adequately fed for a sufficient time in its movement downhill, then it spreads throughout the soil without forming a saturated zone in the lower part of the slope. This is why the data-logger that was positioned in the lower part of the slope recorded evidence of a water table only during one of the rainfall events.

4.2.2 Sensitivity Analysis

Next, the study looked at the reaction of the model to changes in the geometry of the problem (the height of wall and bedrock slope angle – Tab 4.1) and in the hydrogeological properties of the soil (k_s and k_r).

Table 4.1: Input data and results of the sensitivity analysis performed on wall height (H) and bedrock slope (a) for the rainfall events used for calibration and validation.

		17 February 2010			22 October 2009	
H	1.4 m	2.0 m	2.5 m	1.4 m	2.0 m	2.5 m
α						
40°	0.19	0.21	0.22	0.22	0.27	0.31
44°	0.16	0.18	0.21	0.24	0.28	0.31
48°	0.10	0.16	0.17	0.17	0.25	0.22

An increase in wall height often causes a higher level of groundwater table, whereas an increasing slope angle of bedrock in most cases produces the opposite effect; it leads to lower groundwater maximum levels. These trends can be simply explained because a greater height corresponds to a larger quantity of soil in which the water can be stored, whereas a higher slope angle can cause an increase in the mobility of the water and lessen its ability to accumulate. Moreover, it has been demonstrated that an increase in the slope steepness causes a decrease in infiltration (Huat et al., 2006). The analyses conducted on k_s and k_r variations led to the results summarised in Fig 4.10a,b,c. The influence of their variation, both on the maximum height and the maximum length reached by the saturated horizon, was examined. An increase in k is expected to produce a decrease of water table maximum height because of the greater velocity of groundwater flow in the saturated zone; in fact, this behaviour is shown in all three graphs in Fig 4.10. On the contrary, the response of the maximum length is less straightforward and should be analysed considering that infiltration flow is controlled by vertical hydraulic conductivity, whereas groundwater flow is controlled by both vertical and horizontal hydraulic conductivity and occurs along an 'imposed' path, i.e. with an angle of about 45° corresponding to the bedrock dip angle. When k_x is higher than k_v the flow along the 'imposed' path is too high with respect to the infiltration rate, and a saturated zone can develop only where the soil has low thickness. The length of this zone increases as the k_r value increases from zero to the isotropic condition k_r=1. A further increase of k_r does not modify the modulus of the k vector along the 'imposed' path where groundwater flow occurs. Thus, the maximum length of the saturated zone remains unchanged. (Fig 4.10b,c).

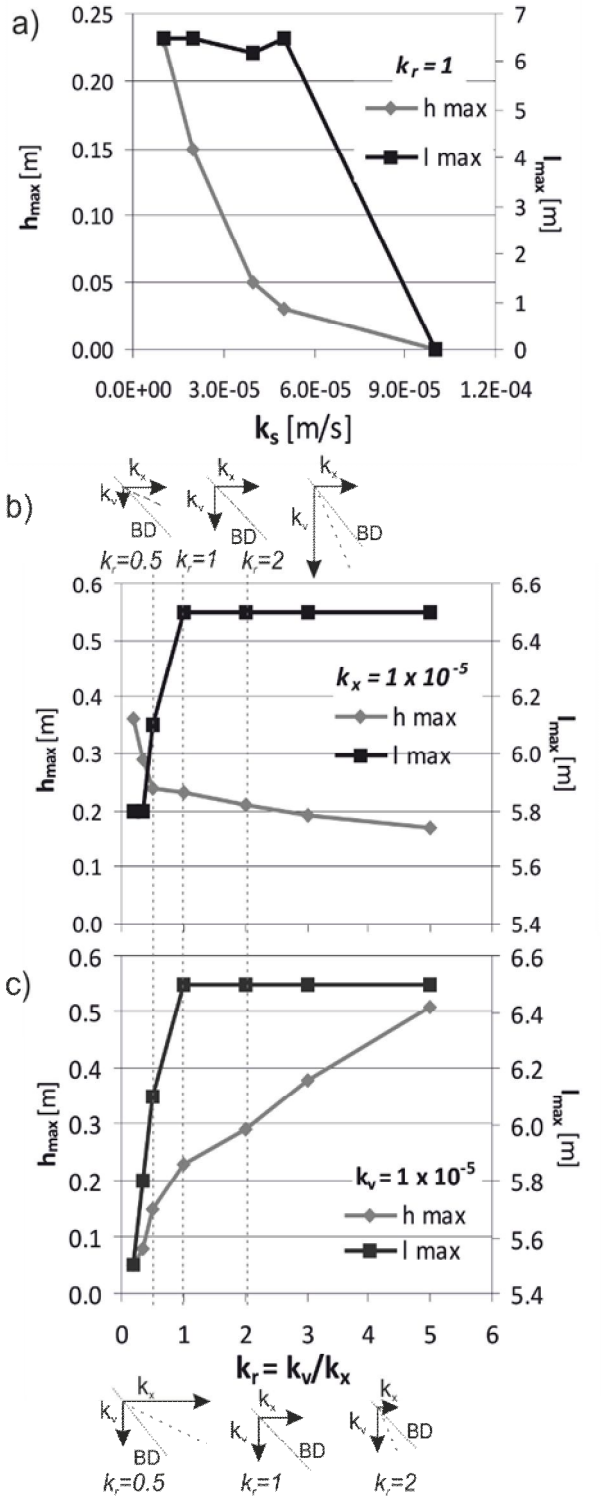

Figure 4.10: Results of sensitivity analysis: a) on isotropic *k*s; b) on *k*r with *k*x constant, where a higher value of *k*r corresponds to an increasing *k*; c) on *k*r with *k*v constant, where a lower value of *k*r corresponds to an increasing *k*x.

4.2.3 Extended section

Once the model had been calibrated and validated using the single-terrace case, it was applied to an extended section of the slope (Fig 4.11).

Considering the rainfall used for the calibration model, the result was applied to an extended section including five terraces characterised by differing geometries of the stone wall-backfill system.

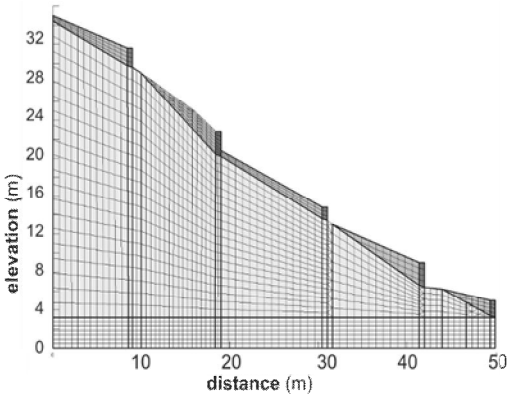

Figure 4.11: the extended section.

The same two rainfall events used for the calibration and validation phases were used in the numerical simulation. The results in Fig. 4.12a,b depict the influence of terrace geometry on the development of a perched groundwater table within each terrace. The graphs reproduce the values of pore pressure head with time ('hydrographs') in the terraces where a positive pore pressure head was reached, considering for each of these terraces a low-depth point uphill and a deeper point in the middle (downhill). These graphs showed some interesting features.

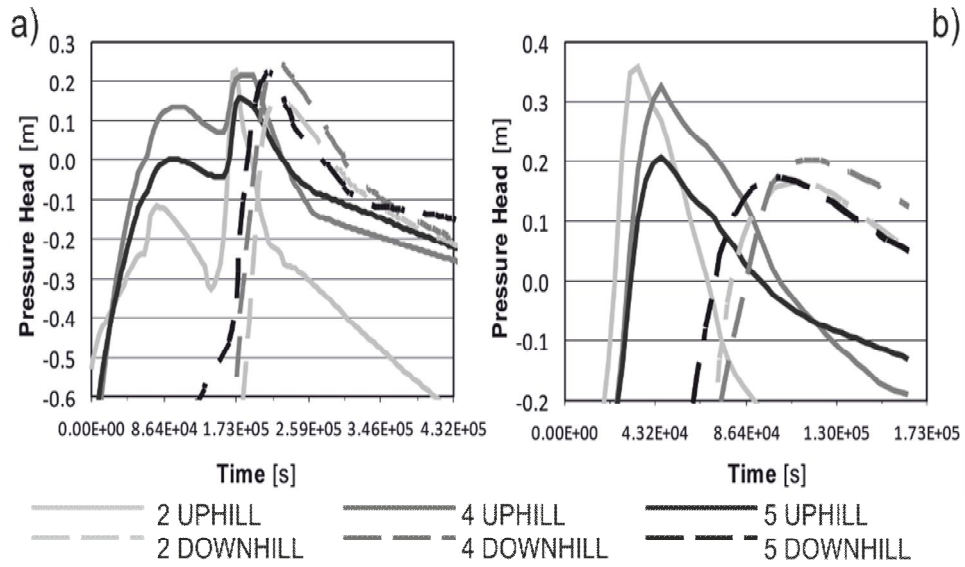

Figure 4.12: Comparison between recorded and calculated groundwater levels at different nodes for the extended section. Two nodes for Terrace 2, Terrace 4 and Terrace 5. In Terrace 1 and Terrace 3 no saturated levels were observed; a) calibration phase; b) validation phase.

During the same rainfall event, a perched groundwater table developed in only a few terraces, which indicates that the combination of soil thickness and bedrock dip angle did not cause the groundwater velocity to be too high with respect to the arrival time of the infiltration water.

The form of the calculated hydrographs was very different according to the position of the observation node; the shallow points (uphill) clearly showed a more rapid response than the deep ones (downhill) and followed the relative peak of the hyetograph more strictly (Fig 4.12a). The form of the hydrographs can greatly influence the position where the maximum pore pressure head forms. Short and single peak rainfall events more easily produced a maximum in the uphill zones, whereas longer double-peak events tended to generate the highest pressure values in the downhill sectors as shown by Fig 4.12b and 4.12a, respectively. The numerical simulation shows the complexity of the process of perched groundwater table formation in these contexts and that many variables act in concert to influence the process.

4.2.4 Model Application

The model was then used as a predictive tool for different rainfalls that were calculated using statistical methods on the basis of fixed return periods (10, 50, and 100 years) and durations (3 and 7 days). The aim was to determine when it is possible to observe the formation of a saturated horizon that could push on the wall and trigger its possible failure. The database used for this calculation comprises 26 years of hourly recorded rainfall registered by an old pluviograph in Castelvetro (1980-2002) and its substitute, the new automatic station in Somasassa (2007-2009). The result is represented by the frequency curves (total rainfall – duration) shown in Fig 4.1c.

Rainfall intensity was considered to be constant when applied to the model. A water table was present at the back of the wall, but due to its draining action, there was no hydrostatic pressure on the wall. The case of an aged, poorly maintained wall was analysed next; in this case, k_s was set to a value lower than that of the soil, assuming that the pores between the stones were filled with a low permeability material. When decreasing the k_s of the wall from 5 10^{-4} to 1 10^{-6} m/s, the amount of rainfall of a week coupled with a return time of 10 years was sufficient to cause a small saturated volume in the backfill of the wall. A groundwater table appeared behind the wall when the return period was increased to 50 years. Fig 4.13a,b show the results obtained with a return period of 50 years and a rainfall duration of three days. In Fig 4.13a, where k_s was higher than that of the soil, the wall was able to drain water from the perched water table that was present at the contact area between the soil and the bedrock. However, when k_s was decreased to 1 x 10^{-6} m/s, the wall acted as a barrier to water (Fig 4.13b). An overpressured area formed in the lower part of the wall, which favours bulging at the toe as described by Azzola and Tuia (1983).

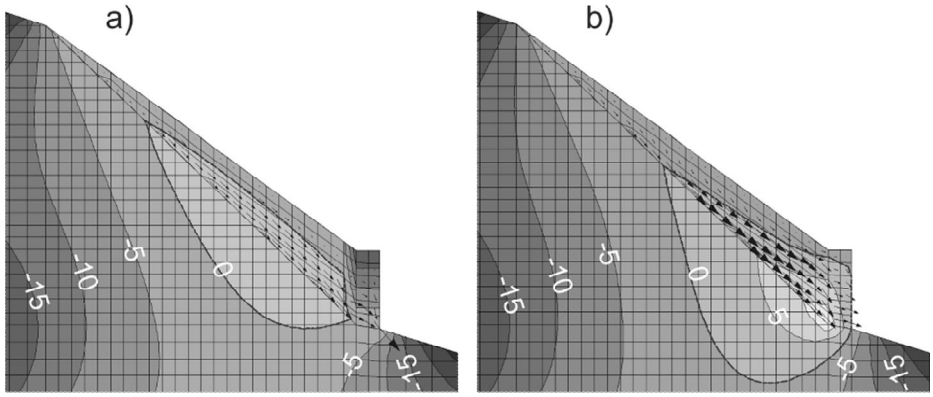

Figure 4.13: a) Pore-water pressure contours [kPa] calculated for rainfall with a return period of 50 years and a duration of 3 days with a) *k*s of the wall = 5 x 10^{-4} m/s; and b) *k*s of the wall = 1 x 10^{-6} m/s. The bold lines border the saturated zones.

4.2.5 Summary of the results

The main goal of this work was to examine the hillslope hydrology of a terraced area. This study focused on rainfall events, infiltration, groundwater movement, and the relationship among all these factors, which were simplified using a numerical model. To completely understand the behaviour of water in this context, it is essential to have access to a large database with measurements of rainfalls, hydrological and hydrogeological soil characteristics, soil moisture and temporary perched groundwater tables. For this reason, all the results presented are based on the data acquired during a whole year (August 2009–August 2010).

An analysis of the connection between rainfall and the response of groundwater towards forming a perched water table indicates that water table formation in this context is related above all to the intensity of the rainfall event, whereas the exhaustion time is more dependent on the amount of rain

fallen in the final part of the event. Once these relationships were obtained, it was possible to define an intensity duration threshold for the onset of a perched groundwater table.

Numerical modelling was then used to determine how a perched groundwater table is formed. The study attempted to reproduce the groundwater hydrographs during different actual rainfall events beginning with the recorded pressure head values from a datalogger installed in the field. The model, once calibrated, returned a good output in terms of both time and height of the maximum level reached by the groundwater table. The model was also validated, and a sensitivity analysis was performed showing the effect of the variation of isotropic and anisotropic hydraulic conductivity. The sensitivity analysis has also helped to clarify the infiltration process in the studied context, exploiting one of the main characteristics of a demonstrably reliable model, which is the ability to show something that is difficult to demonstrate in the field. After its reliability was ensured, the model was used to predict specific measurements of rainfall (duration and return period) to determine when significant pore pressure in the backfill of the wall can be expected. Considering that the hydraulic conductivity of the wall was greater than that of soil, for any combination of duration and return period, the wall was able to successfully drain the water from its backfill; therefore, no overpressure occurred. When the hydraulic conductivity of the wall was lowered to an order of magnitude inferior to that of the soil, large high positive pore-water pressures zones developed in the backfill of the wall for rainfall events with return periods of 50 years and even lower. Therefore, the model is able to not only reproduce a real event but also to correctly represent the differing behaviour between well and poorly maintained walls.

5 Chapter 5

2D STABILITY ANALYSIS

Slope stability analysis is a key issue in the Alpine environment, where landslides often represent an important risk factor for anthropogenic structure. Valtellina (Northern Italy) is an extended area within the Italian Alps, where many landslides occurred historically due to a great variety of predisposing factors.

Indeed, it is demonstrated that in Valtellina terraced slopes are more prone than woodland areas to trigger superficial mass movements (Crosta et al., 2003). These movements often originate from soil slips or shallow landslides, after a Coulomb-type failure, and then evolve into flows, due to the increase of pore pressure, or for dilatancy processes(Fleming et al., 1989; Iverson et al., 1997; Johnson and Rahn, 1970) that, in the case of Tresenda, are caused by a sudden change of slope steepness (Azzola and Tuia, 1983).

The study of factors that lead to instability in a terraced slope should focus on the role played by the dry stone walls. Several authors have studied the failure mechanisms of these structures by means of numerical modelling, considering different geometrical characteristics (Harkness et al., 2000; Powrie et al., 2002; Zhang et al., 2004; Walker et al., 2007), or through analytical models at different scales (Villemus et al., 2007), or combining the two approaches (Lourenço et al., 2005). On the other hand, one of the most widespread techniques to study the triggering of landslides, at various scales, consists in coupling a hydrological model to a stability one (Angeli et al., 1998; Crosta and Frattini, 2003; Delmonaco et al., 2003; van Beek and van Asch, 2004; Biavati et al., 2006; Tofani et al., 2006; Meisina and Scarabelli, 2007; Talebi et al., 2008; Simoni et al., 2008; Kuriakose et al., 2009; Cho, 2009).

In the present work, a similar approach at a very detailed scale (one terrace) was applied, using the output of the already presented unsaturated-saturated and groundwater flow numerical model in the stability analysis, in which the mechanical and hydrogeological characteristics of the dry stone retaining wall are taken into account.

The principal aim of this part of the work was in fact to analyse and determine which are the main causes that lead the terrace to generate superficial landslides. Once the stability model was calibrated, the effects of factors such as extreme rainfall events calculated on a statistical base, together with variations of initial hydrogeological conditions, state of maintenance of walls, and different pattern of distribution of rainfalls were analysed.

5.1 Mechanical characterization of dry-stone walls

The mechanical characterization of dry retaining walls is therefore a key issue for the stability analysis of slopes in Valtellina, where vineyard terraces have already been involved in rapid mass movements. The study presents the solution adopted to approach the problem by numerical modelling, focusing on the difficulties in the geomechanical and hydrogeological parameterization of dry walls.

Physical and hydrogeological parameters were used to model the infiltration process and the formation of perched groundwater tables (see section 4.2 *Hydrogeological 2D Modelling*), that was then used as input in the stability model. Mechanical properties of the materials were defined as follows. For the backfill soils, the laboratory tests provided all the needed data; for bedrock, geomechanical

surveys were performed to assign proper value of Geological Strength Index (GSI) to the rock mass (Hoek et al., 1998; Marinos et al., 2005); finally the bedrock deformation modulus and the equivalent Mohr-Coulomb strength parameters (cohesion and friction angle) were determined by the Hoek and Brown criterion (Hoek et al., 2002).

Figure 5.1: a typical dry stone wall of the study area, founded on bedrock and 1.50 m height.

Regarding the walls, a similar procedure was originally followed based on the consideration that the wall is not built up as a continuum material but can be roughly considered as a fractured rock mass. In fact, a dry stone retaining wall (Fig 5.1) can appear as a very jointed rock mass: stones represent the intact rock while spaces among them are discontinuities. Nature, size and geometry of blocks, together with the characteristics of the contact surfaces, were described, and a value of Geological Strength Index (GSI) was assigned.

Spacing, aperture, and stone interlocking depend on the construction technique of the wall, mainly geometry and dimension of blocks. Usually two main discontinuities sets can be recognized, one almost horizontal and the second vertical. In the past small stones with an elongated form were preferably used, resulting in an irregular pattern with a spacing of few centimeters, both vertically and horizontally. Nowadays, almost squared stones are used, with side dimension of 10-20 cm or more in few cases, which produce a more regular pattern but a wider spacing. Joints can be filled or not with fine material and in some cases also weeds can be seen. During or immediately after wet periods, discontinuities can be interested, mainly at their base, by water flow.

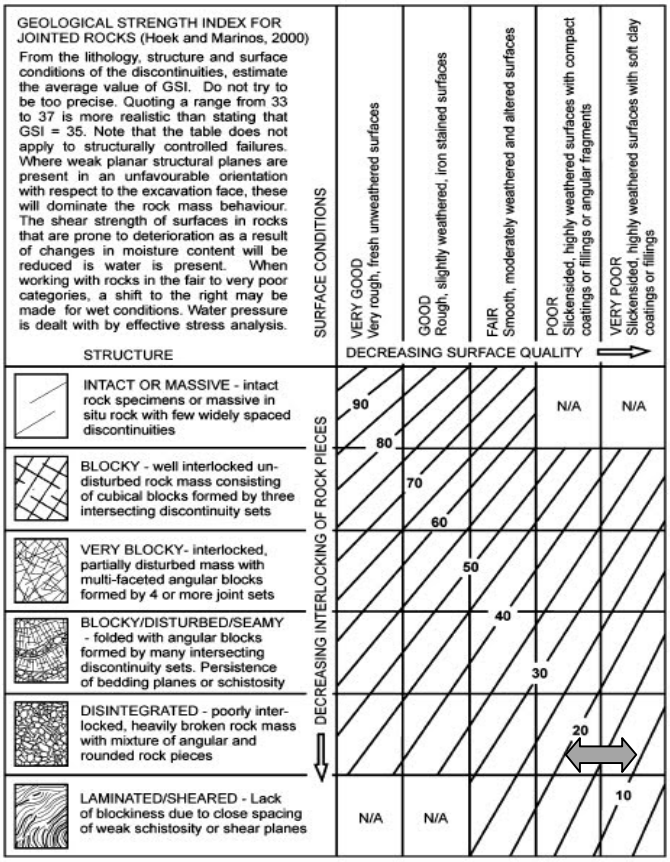

Figure 5.2: geological strength index (GSI) table (from Hoek and Marinos, 2000), with enlightened the range of value assigned to the dry-stone walls.

In particular, considering the GSI table of Fig 5.2, the wall can be considered as a disintegrated rock mass with a quality of the discontinuity surfaces between poor and very poor. The corresponding GSI value is therefore ranged between 10 and 20. Considering that the single blocks consist mainly of schists, a uniaxial compressive strength (σ_{ci}) between 20 (for very weathered rocks) and 50 MPa (Hoek et al., 1998) was applied in the calculus of the elastic modulus of the wall (E_m) using the following formula:

$$E_m(GPa) = 10^{\frac{GSI-10}{40}} \cdot \sqrt{\frac{\sigma_{ci}}{100}} \text{ (Hoek et al., 1998).} \qquad \text{(eq. 5.1)}$$

Once the material constant m_i (13) and the disturbance factor D (0) are also defined, it is possible to calculate, according to Hoek et al. 2002, the following parameters:

$$m_b = m_i \cdot \exp\left(\frac{GSI-100}{28-14\cdot D}\right) \qquad \text{(eq. 5.2)}$$

$$s = \exp\left(\frac{GSI-100}{9-3\cdot D}\right) \qquad \text{(eq. 5.3)}$$

$$a = \frac{1}{2} + \frac{1}{6}\cdot\left(e^{-GSI/15} - e^{-20/3}\right) \qquad \text{(eq. 5.4)}$$

where m_b is a reduced value of the material constant m_i , and s e a are constants for the rock mass. They permit to define the state of stress through the following equation:

$$\sigma_1' = \sigma_3' + \sigma_{ci}\cdot\left(m_b\cdot\frac{\sigma_1'}{\sigma_{ci}} + s\right)^a, \qquad \text{(eq. 5.5)}$$

and to arrive to the equivalent Mohr-Coulomb resistance values of cohesion (c) and friction angle (ϕ) applying the following empirical formulas:

$$\phi' = \sin^{-1}\left[\frac{6am_b(s+m_b\sigma'_{3n})^{a-1}}{2(1+a)(2+a)+6am_b(s+m_b\sigma'_{3n})^{a-1}}\right] \qquad \text{(eq. 5.6)}$$

$$c' = \frac{\sigma_{ci}\left[(1+2a)s+(1-a)m_b\sigma'_{3n}\right](s+m_b\sigma'_{3n})^{a-1}}{(1+a)(2+a)\sqrt{1+\left(6am_b(s+m_b\sigma'_{3n})^{a-1}\right)/\left((1+a)(2+a)\right)}} \qquad \text{(eq. 5.7)}$$

where:

$$\sigma_{3n} = \sigma'_{3\max}/\sigma_{ci}\,. \qquad \text{(eq. 5.8)}$$

For problems concerning slope stability, the value of σ'_{3max} used in the previous equations can be obtained from a previous definition of the uniaxial compressive strength of the rock mass (σ'_{cm}):

$$\sigma'_{cm} = \sigma_{ci}\cdot\frac{(m_b+4s-a(m_b-8s))(m_b/4+s)^{a-1}}{2(1+a)(2+a)} \qquad \text{(eq. 5.9)}$$

$$\frac{\sigma'_{3\max}}{\sigma'_{cm}} = 0.72\left(\frac{\sigma'_{cm}}{\gamma H}\right)^{-0.91} \qquad \text{(eq. 5.10)}$$

where H is the slope height. Considering the slope geometry and the height of the dry-stone wall, in the present study H was put at 5 m.

The resulting ranges of variation of equivalent cohesion and friction angle are:

$30 < c < 74$ kPa

$45 < \phi < 57°$.

Later, these mechanical parameters have been calibrated during the modeling phase (Tab 5.1).

Table 5.1: Parameters used during simulation for soil and bedrock. Those of the walls are both initial ($Wall_{ini}$) and after calibration ($Wall_{cal}$). γ: bulk density; E: elastic modulus; ν: Poisson's ratio; c: cohesion; ϕ: friction angle; phi_b, matric suction friction angle; dil: dilation angle; k_s: saturated hydraulic conductivity; n: porosity. The two values of k_s indicated for walls state a different condition of maintenance of these structures. The higher value represents a well-maintained state that permits the wall to drain.

	γ [kN/m³]	E [kPa]	ν [-]	c [kPa]	ϕ [°]	dil [°]	phi_b [°]	k_s [m/s]	n [-]
Soil	16	2.0 x 10^4	0.30	10	30	1	15	1 x 10^{-5}	0.50
Bedrock	26	1.8 x 10^6	0.35	345	40	2	20	1 x 10^{-8}	0.07
$Wall_{ini}$	24	4.2 x 10^5	0.32	25	45	1	22	5 x 10^{-4} or 1 x 10^{-6}	0.25
$Wall_{cal}$		2.5 x 10^5		120	55		30		

5.2 Finite elements stress-strain modelling

The geometry of the model is equal to that used for the ground water movement modelling. It is simple and it represents a single terrace, with the dry stone wall, backfill and bedrock (Fig 5.3). The wall is founded directly on an outcrop of the bedrock; this is common in the eastern part of the study area and rare in the western part, where the slope is more gentle and only few evidences of walls founded on outcropping bedrock were observed. The particular combination assumed was a slope angle equal to 44° and a mean wall height of 2 m. The slope angle is similar to the average terrain gradient of 42° for terraced slopes indicated by Crosta et al. (2003); considering a horizontal width of 8 m, the surface angle results in approximately 35°, a rather extreme value compared to the mean terraces gradient of 15° – 25° suggested by Crosta et al. (2003). For groundwater modelling and stability analysis, the finite elements codes SEEP/W and SIGMA/W were respectively used (GEO-SLOPE International Ltd. 2002). The great advantage in using two codes of the same package as SIGMA/W and SEEP/W is represented by the simplicity with which it is possible to use the output of one as input for the other. In the previous part of the work (Chapter 4 - Camera et al., 2011), the mechanism of formation of perched water tables was analysed. This chapter essays to determine their effects on stability.

SEEP/W provides a series of saved timesteps, with their own pore water pressure distribution resulting from defined material properties, boundary conditions and recharge characteristics. The recorded output can be used in sequence in SIGMA/W. For every different saved distribution of pore pressure, SIGMA/W calculates its relative state of stress that consequently controls the strain behaviour.

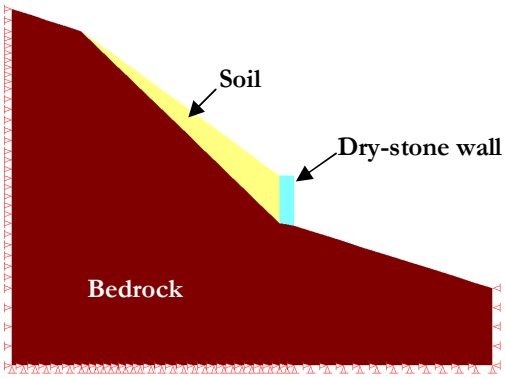

Figure 5.3: Geometry of the model, equal to that of hydrogeological modelling section, and boundary conditions.

For the stress-strain analysis, horizontal and vertical displacements were forbidden at the base of the model and the side boundaries were fixed in horizontal direction. Before applying pore pressure configurations, the initial state of stress was reproduced at the dry state by simulating the construction of the wall and its backfill in three different phases. The different hydrogeological inputs were then applied and the model response was analysed in terms of effective stress and pore water pressure distribution, displacement and shear stress increments.

5.2.1 Model preliminary results

The wall parameters reproducing stability and instability as observed in reality resulted in a cohesion of 120 kPa, a friction angle of 55°, an Elastic Modulus of 2.5 x 10^5 kPa and a Poisson's ratio of 0.32. In addition, SIGMA/W considered also the evolution of the matric potential in the unsaturated zone, as calculated by SEEP/W, through the phi_b parameter, that is a sort of apparent cohesion. The failure criterion used is in fact the Fredlund-Rahardjo (Fredlund and Rahardjo, 1993), which is a modified Mohr-Coulomb.

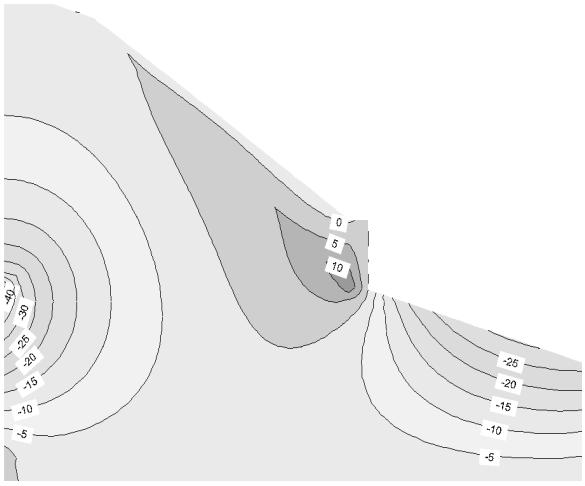

Figure 5.4: pore water pressure (kPa) distribution at collapse. Rainfall input data coherent with the May 1983 event.

The pore water pressure distribution at collapse, obtained simulating the May 1983 event (Fig 5.4), is coherent with the description of Azzola and Tuia (1983), who observed saturated backfill soils during the triggering of the second superficial landslide. However, the simulated mechanism of failure seems to be different, or at least more detailed. The same authors reported about a bulging at the toe and a consequent collapse that involved the entire height of the wall. Instead, in the step preceding the collapse, the model shows a tendency to the toppling of the whole structure, that at the moment of failure evolves in a sort of flexure in the lower/middle part of the wall (Fig 5.5a,b). As expected, the positive shear strains are concentrated at the base of the wall (Fig 5.5c), but probably for numerical reasons the model balances them with an uphill displacement of the middle-low part of the wall rather than with a homogeneous downhill movement. Such a numerical solution could be affected by the different rigidity between the wall and the bedrock to which it is bound.

The model was then used with rainfall events of duration and constant intensity defined by statistical methods. The database is composed of 27 years of hourly data for the two periods 1980-2002 and 2007-2010. In particular, return periods of 10, 50 and 100 years were used, each of them with total

durations of events of 72 hours (Fig 5.6). For every combination of duration and return period, it was decided to vary the initial conditions and the state of maintenance of the wall. Initial conditions were therefore considered dry, applying the pore pressure distribution being used in the previous steps of the research, or very wet, adding the recorded rainfall of the 15 days that preceded the May 1983 event, before the project precipitation. Regarding maintenance, two cases are simulated: in the first, the hydraulic conductivity of the wall was put higher than that of the backfill soil, thus maintaining its draining function; then a lower hydraulic conductivity was assumed in order to represent the behaviour of a badly maintained wall clogged with fines (Tab 5.1). Results are summarized in Tab 5.2. Results strengthen the findings obtained during calibration as to the importance of the initial hydraulic conditions; in fact, the collapse is reached only if the 15 days of rainfall before the event of 1983 are used to determine the initial soil moisture of the triggering event. Furthermore, they emphasize some details that did not emerge during the previous calibration phase. In particular, the collapse is reached only for very high return periods (100 years) and in both conditions of well and badly maintained walls. With a well maintained wall, the rainfall event of 1983 with its 15 days of previous rainfall does not cause any instability.

This fact highlights that failures occurring during very extreme events can proceed not only through water overpressure directly acting on the wall, but also from the previous failure of the backfill soil, as shown by the XY shear strain increment at the moment of collapse in the simulation number 10 (Tab 5.2) in Fig 5.7b. In addition, the simulation 8 (Tab 5.2) results in stability, despite its showing a return period higher than that of the second trigger of May 1983 (Fig 5.6) used for calibration and well reproduced by the model. An explanation of this result could be that also the rainfall pattern is likely to affect stability.

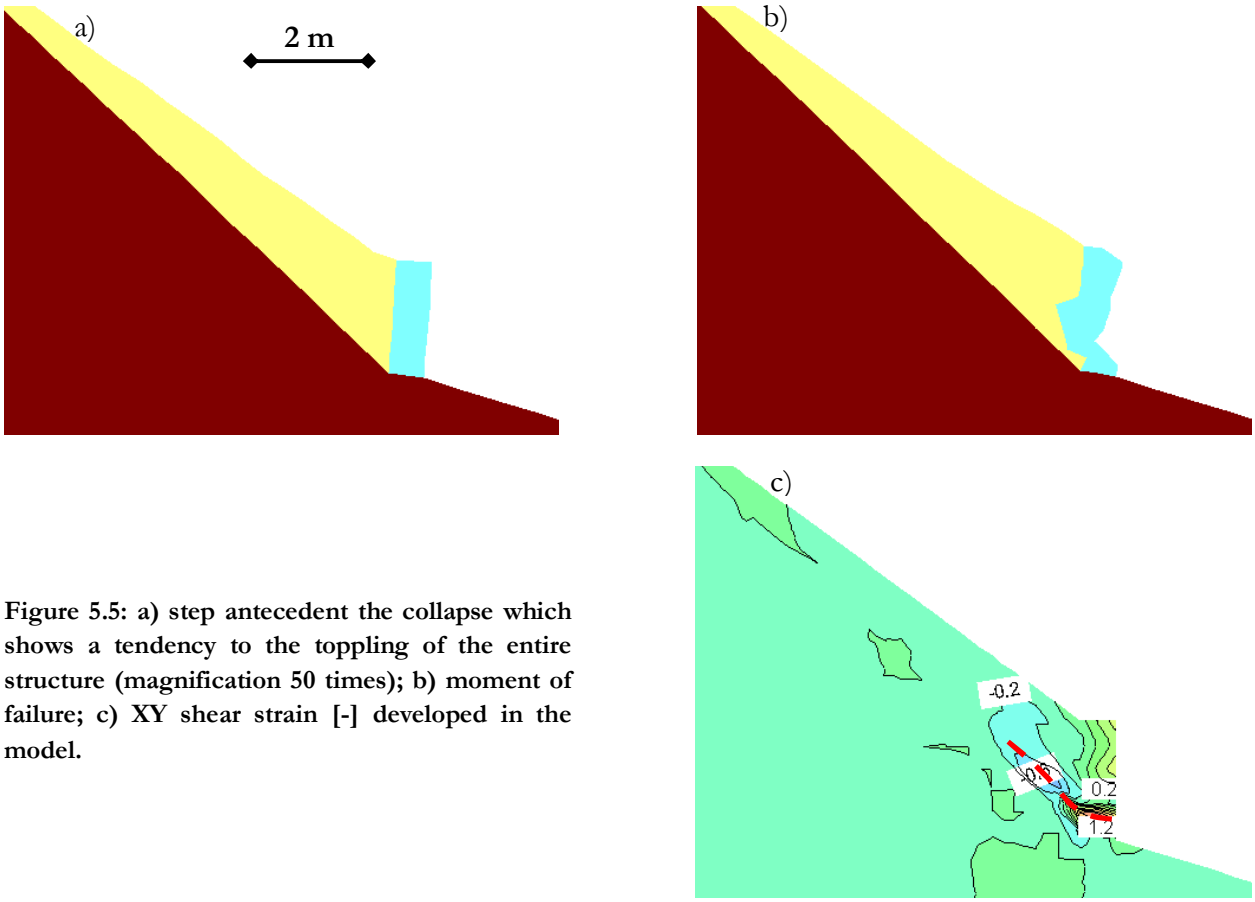

Figure 5.5: a) step antecedent the collapse which shows a tendency to the toppling of the entire structure (magnification 50 times); b) moment of failure; c) XY shear strain [-] developed in the model.

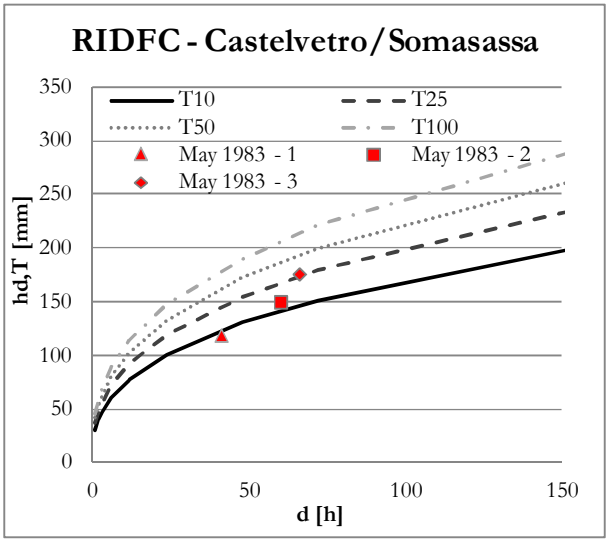

Figure 5.6: duration-total rainfall frequency curves, calculated with statistical method. The three points show the characteristic of the rainfall event of May 1983 at the moment of the triggering of the three occurred landslides.

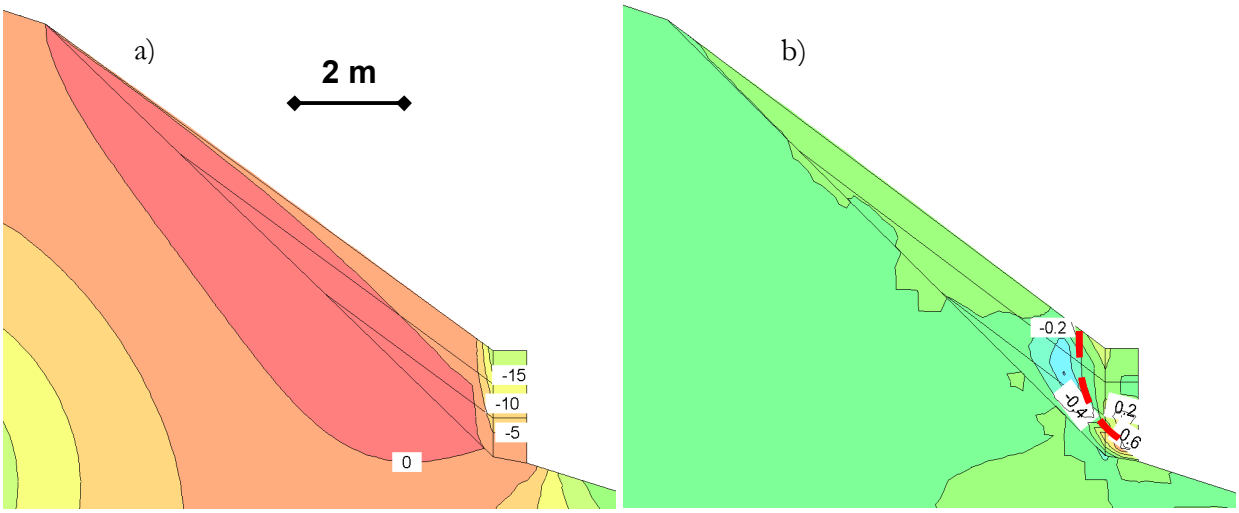

Figure 5.7: results of the simulation 10. a) pore water pressure distribution at collapse and b) XY-shear strain that enlighten the possible surface of failure.

Table 5.2: summary of the results of the SIGMA/W, finite elements analysis performed with statistical project rainfall events and constant intensity.

ID	Return period	draining function	Initial condition	Result
1	10 years	yes	Dry	Stable
2	10 years	yes	15 days previous 22th May 1983 event	Stable
3	10 years	not	Dry	Stable
4	10 years	not	15 days previous 22th May 1983 event	Stable
5	50 years	yes	Dry	Stable
6	50 years	yes	15 days previous 22th May 1983 event	Stable
7	50 years	not	Dry	Stable
8	50 years	not	15 days previous 22th May 1983 event	Stable
9	100 years	yes	Dry	Stable
10	100 years	yes	15 days previous 22th May 1983 event	Unstable
11	100 years	not	Dry	Stable
12	100 years	not	15 days previous 22th May 1983 event	Unstable

5.3 Finite differences stress-strain modelling

In order to better reproduce the actual mechanism of the dry stone wall failure, a finite difference numerical analysis through the FLAC 6.0 code (Fast Lagrangian Analysis of Continua - Itasca Consulting Group Inc, 2008) was performed. General results of the two different codes were also compared to see if they were consistent with each other, thus increasing their degree of reliability.

The same geometry was reconstructed and the grid was also reproduced as similar as possible to the one of SEEP/W and SIGMA/W. The main difference lies in the fact that with FLAC the wall is separated from soil and bedrock by means of interfaces, in order to react to forces and pressures in an independent way, without being bonded to the rest of the system. Another difference is related to the failure criterion, as the FLAC simulation does not consider the contribution of apparent cohesion (phi_b) of the unsaturated soils; the soil is either saturated or completely unsaturated, not having the possibility of using the FLAC two phase flow package.

Mechanical and hydrogeological properties were assigned to the materials, applying the calibrated values gleaned from the previous modelling phases and an initialization of the state of stress was obtained cycling the model in dry conditions, till an elastic equilibrium was reached. As the infiltration and groundwater movement process was well described by SEEP/W (Chapter 4 and Camera et al., 2011), it was decided to reproduce the groundwater table geometry applying a constant infiltration on the terrain surface, cycling subsequently the model only for groundwater flow purposes, till arriving to the pore water pressure distribution obtained by the groundwater numerical modelling.

The most critical water table levels for the three events of 1981, 1983, and 2009, as calculated by SEEP/W, were reproduced both for a draining and a not-draining wall. Concerning the mechanical analysis, the physical parameters of the wall calibrated with SIGMA/W appeared to be too high, above all in terms of cohesion, the system being always stable. Instability is observed for the 1983 event with a not-draining wall, lowering the wall cohesion value from 120 kPa to 15 kPa. This lower value seems also more reliable if compared to the GSI and Hoek-Brown method applied to define the parameters of the wall, which gave a range for cohesion between 30 and 74 kPa. Changing only this value, the results obtained with SIGMA/W can be replicated by FLAC, with the exception of the events 8 and 10 (Tab 5.2) that in this case resulted in collapse and in stability respectively. Additionally, the FLAC simulation appears to better reproduce the mechanism of failure (Fig 5.8).

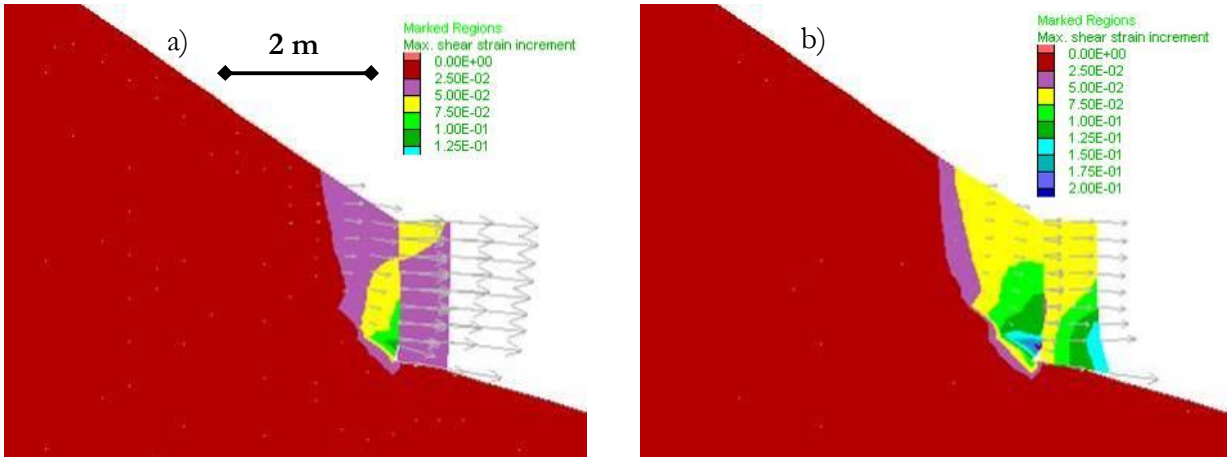

Figure 5.8: results obtained from FLAC showing the shear strain increments and the displacement vectors. (a) At the beginning the displacement is greater in the upper part of the wall as in toppling but later (b) the collapse occurs from bulging at the toe and sliding of the base of the wall.

With FLAC 6.0 it is possible to observe an initial toppling (Fig 5.8a) that later evolves in bulging and sliding at the base of the wall (Fig 5.8b) until collapse occurs. It is also possible to see how the failure surface resembles the one that forms in SIGMA/W for a draining wall (Fig 5.7b), although the model in Fig 5.8 represents a condition of bad maintenance of the retaining structure. This difference in behaviour is controlled by the presence and mechanical properties of the contact interface between the wall and bedrock.

5.4 Summary of the results

Defining and understanding the conditions and the processes that could lead to collapse in a terraced slope are the main objectives of this part of the work. Numerical modelling, supported by an intense geotechnical and hydrogeological monitoring plan, appeared to be a good methodology to approach such analysis. In particular, the comparison of the results obtained with two different codes allowed to calibrate the mechanical parameters of the dry retaining walls and to analyse in detail the import and the effects on slope stability of different factors such as initial moisture content conditions, return periods of the rainfall events, maintenance characteristics of walls and rainfall patterns.

The processes were studied at a very detailed scale, reproducing the model of a single terrace with a dry wall and its backfill, laying on a semi-impermeable bedrock. In particular, it was possible to calibrate the mechanical parameters of the walls by back analysis, coupling a groundwater numerical model with a stability one. The two codes show only a difference in the values of wall cohesion, giving a discrete proof of their reliability. Nevertheless, this difference in the cohesion value, that is in the range of an order of magnitude, is not fully explained and cannot be completely ignored.

The code that shows the lower cohesion value is FLAC, although the wall is not bonded to the soil nor to the bedrock, and no contribution from the unsaturated soil is given to stability. The higher freedom of movement, as well as the lack of the apparent cohesion contribution due to the matric suction friction angle (phi_b) may suggest that the cohesion required in this instance to maintain stability should be greater than for a structure anchored to the bedrock. The impression is that a certain influence on the results could be due to the interaction between the saturated horizon and the unsaturated soil, with reference to the SIGMA/W model. During the calibration phase, some results, obtained with low values of wall cohesion (30-40-90 kPa), show instability before the saturated horizon has been reached in the proximity of the wall. Probably, in the contact area between the saturated and the unsaturated soil, a sort of weakness zone forms, maybe due to the difference in the rheological behaviour of the two means.

Moreover, from a first analysis, it seems that the probable onset of a failure is most to be expected when the passage from a saturated soil to medium-high values of matric suction gets shorter. This could be an explanation of the higher value of cohesion, required by SIGMA/W with respect to FLAC 6.0, to maintain stability. Then, looking at Fig 5.7 and Fig 5.9, it is possible to see that the failure surface has a geometry very similar to that shown by the contact between the saturated or almost saturated and the unsaturated soil. An hypothesis, not demonstrated till now, is that also the slope of this contact surface could have a role in determining a failure.

Once calibrated, the SIGMA/W model was used to analyze the influence of initial backfill moisture content conditions and different drainage capacities of dry wall, using as input rainfalls with a duration of 72 hours (similar to those that in the past years led to instability) and constant intensities, calculated on the basis of different return periods.

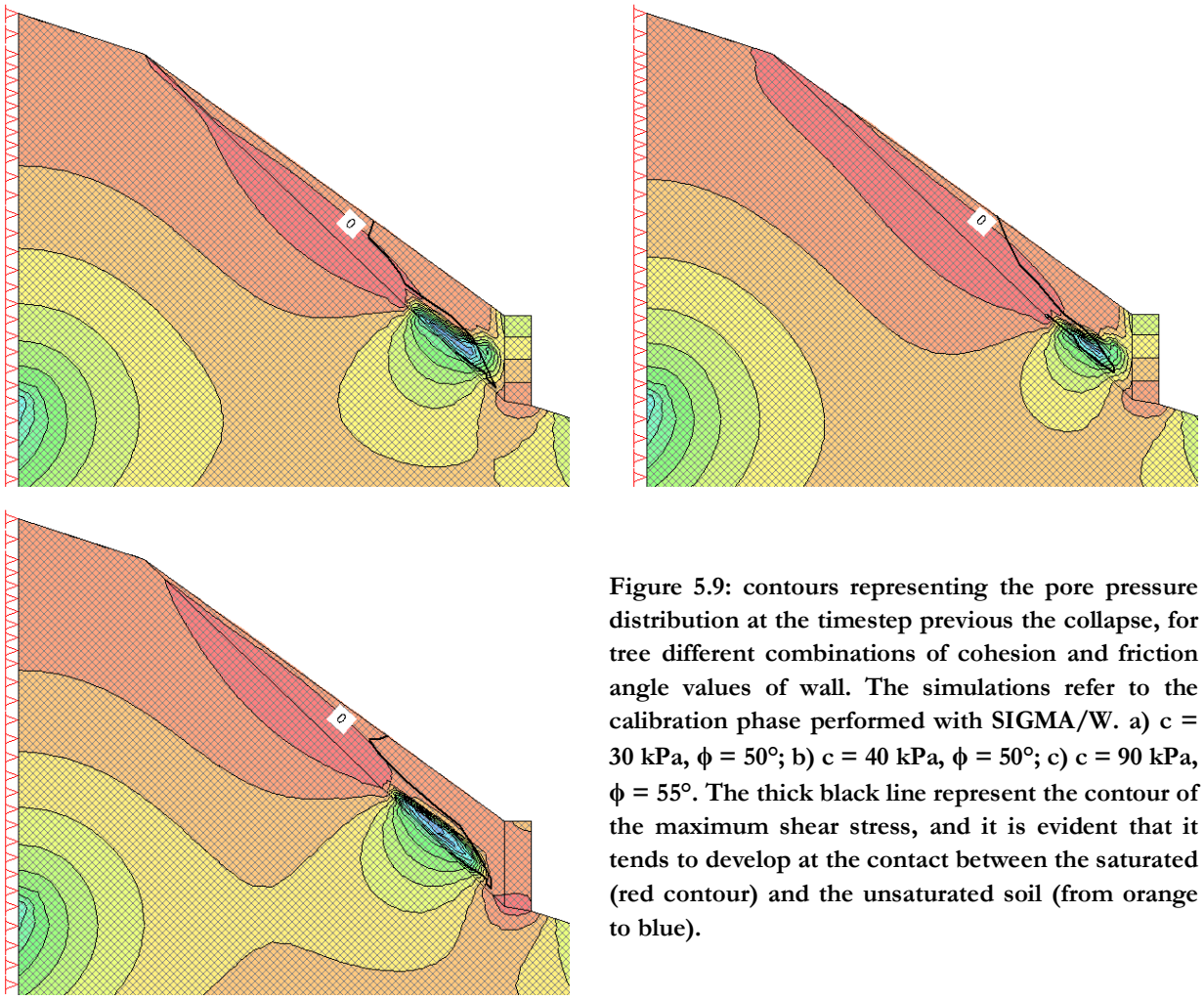

Figure 5.9: contours representing the pore pressure distribution at the timestep previous the collapse, for tree different combinations of cohesion and friction angle values of wall. The simulations refer to the calibration phase performed with SIGMA/W. a) c = 30 kPa, ϕ = 50°; b) c = 40 kPa, ϕ = 50°; c) c = 90 kPa, ϕ = 55°. The thick black line represent the contour of the maximum shear stress, and it is evident that it tends to develop at the contact between the saturated (red contour) and the unsaturated soil (from orange to blue).

The only drawback of this model is that it does not completely reproduce the dynamic of failure as observed on the field. However it confirms the great influence of previous rainfall on stability, and for very high return periods it suggests that the wall drainage capacity influences the failure mechanism. Finally, the comparison between simulations performed with measured rainfalls and those calculated on a statistical base with constant intensity, both characterized by similar or higher return periods, shows a different disposition to instability, suggesting a possible influence of different rainfall patterns in the development of failures.

The subsequent analysis, carried out with FLAC 6.0, confirms almost all the results obtained with SIGMA/W even if it demonstrates that the most important role in the triggering of the landslides is played by the overpressure that is created behind the wall. This factor, related to a condition of the wall that does not permit an effective drainage, seems to be crucial for rainfall events both with low and very high return periods. The possibility that a landslide is triggered lies in the groundwater level just behind the wall. FLAC 6.0 can better reproduce the mechanism of failure than SIGMA/W, appearing therefore the most appropriate tool to describe the phenomena. On the other hand it is worth mentioning that the coupled analysis performed with SEEP/W and SIGMA/W describes the processes with greater detail. They in fact consider also the evolution of matric suction in the unsaturated zone. From the SIGMA/W analysis it seems that the triggering is also controlled by the combination of different factors: the wall conditions above all, but also the rainfall pattern distribution, the evolution of the water table and the behaviour at the saturated-unsaturated soil interface.

PART III

ANALYSIS AT THE SLOPE SCALE

6 Chapter 6

INTRODUCTION TO THE SLOPE SCALE ANALYSIS

Having understood the processes that can lead to the formation of a perched groundwater table behind a dry-stone retaining wall and their relationships with stability, the work focuses on the definition of the zones of the Tresenda slope more prone to the triggering of superficial landslides.

In order to perform this survey it was decided to use a coupled hydrological-stability model developed in a raster GIS environment with an implemented programming language for environmental dynamic analysis (for further details and extended references on PcRaster see http://pcraster.geo.uu.nl/support/publications/applications-of-pcraster/). The coupled models, physically based, are STARWARS (STorage and Redistribution of Water on Agricultural and Revegeted Slopes) and PROBSTAB (PROBability of STABility), both developed by van Beek (2002) and already used in various studies (van Beek and van Asch, 2004; Malet et al., 2005; Kuriakose et al. 2009a).

STARWARS was developed for the study of the effects of different land uses on stability in a Mediterranean environment. It allows to link the specific land use to hydrological variables using simple tables. The first processes that are considered are those related to the calculus of the net precipitation that can reach the topographical surface, considering the interception and the evapotranspiration that could occur from canopy storage. Then, the precipitation that reaches the earth surface can infiltrate or remain available as surface detention, on the basis of a defined infiltration capacity. The soil lies above a semi impervious formation and is divided into three different layers, to eventually consider changes of hydraulic properties dependent on depth, typical of most of the soils. In unsaturated conditions water moves through these layers only for vertical percolation driven by gravity, not considering the fluxes due to the gradient generated by the matric potential, that are considered negligible with respect to the vertical gravitational ones (van Beek, 2002). The unsaturated level hydraulic behaviour is controlled by the Soil Water Retention Curve (SWRC) and the unsaturated hydraulic conductivity, which determine the entity of the unsaturated fluxes. At the contact with the bedrock the drainage is reduced and a perched groundwater table may form. Saturated lateral fluxes depend on the water table gradient. Water that remains available as surface detention is routed along the slope through a linear drain direction map but without considering in detail the physics of the process.

PROBSTAB uses as input the output of STARWARS in terms of water levels and volumetric water content. It is based on the infinite slope concept (Nash, 1987) and therefore not applicable to the case study presented. In fact, the aim is to recognize the areas prone to the triggering of superficial landslides on a terraced slope, where the single terrace must be considered a single entity. The mean length of terraces is around 10 m, not much greater than a typical soil depth of 2 m, and therefore it cannot be approximated to an infinite slope. The problem is even more evident if it is considered that PROBSTAB neglects the interactions between cells and the stability only depends on single cell properties. The solutions adopted are illustrated in the section dedicated to the stability analysis of the entire area.

Apart from STARWARS and PROBSTAB, the use of coupled models with a physical base for the study of the influence of pore water pressure distribution in soils on landslide triggering is widespread in literature. It is in fact possible to cite different models, SINMAP (Stability Index

Mapping - Pack et al., 1998), SHALSTAB (Dietrich and Montgomery, 1998), SHETRAN (Ewen et al., 2000), TRIGRS (Transient Rainfall Infiltration and Grid based Regional Slope Stability - Baum et al., 2002), and GEOtop-FS (Simoni et al., 2008), and different works where the methodology is applied (Angeli et al., 1998; Crosta and Frattini, 2003; Delmonaco et al., 2003; Biavati et al., 2006;; Tofani et al., 2006; Meisina and Scarabelli, 2007; Talebi et al., 2008; Cho, 2009).

With respect to these previous studies, the slope of Tresenda has a peculiar characteristic represented by the presence of the dry-stone walls. The study area has a limited extension (about 0.6 m^2), but in order to consider the hydrogeological and geotechnical influence of walls, a great detail is necessary in the resolution of the raster maps of input. In particular, besides the maps related to the environmental, hydrogeological and geotechnical characteristics of soils, the model must strictly rely on a digital elevation map (DEM) and a soil depth map. Considering that the walls often have a thickness between 0.60 and 1 m, a single pixel dimension of 1 m x 1 m is required for the raster maps. The procedures adopted for the definition of these essential, high resolution maps and their qualities and flaws are described in the following chapters.

7 Chapter 7

THE HIGH RESOLUTION DIGITAL ELEVATION MODEL (DEM) DEFINITION

The process that has led to the construction of the final high resolution DEM has been long and beset by problems. As already said, the necessity was to correctly identify the dry stone walls on the topographical model surface.

The first idea was to perform a laser scanner acquisition of the slope during the summer 2009 field survey. In order to perform such an analysis an expert from the University of Vienna was invited to organize and supervise the acquisition.

7.1 Laser scanner analysis

At first, considering the instrument specifications, it was chosen a primary position for the scan, close enough to the slope to permit to the signal to reach the target and to get an adequate density of the points cloud. At the same time, it was also necessary that the instrument could cover the greatest part of the slope (Fig 7.1) from that position, in order to reduce the number of subsequent integrative acquisitions from different points on the valley floor or on the slope itself.

The processing of the points cloud acquired was later performed by Rainer Bell, a researcher at the University of Vienna, with the collaboration of specialists from the Vienna University of Technology.

The different scans performed were merged together on the basis of objects visible in the data as walls, houses, and roads. The final georeferencing of the complete scan was done using a digital orthophoto (Rainer Bell, personal communication).

Great problems in the processing of the data were related to the presence of vegetation and in its removal. At the Vienna University of Technology a filtering process was performed using a specific software for laser scanner data processing with a routine that is able to automatically roughly separate the points into vegetation/highest surface data and ground/terrain data.

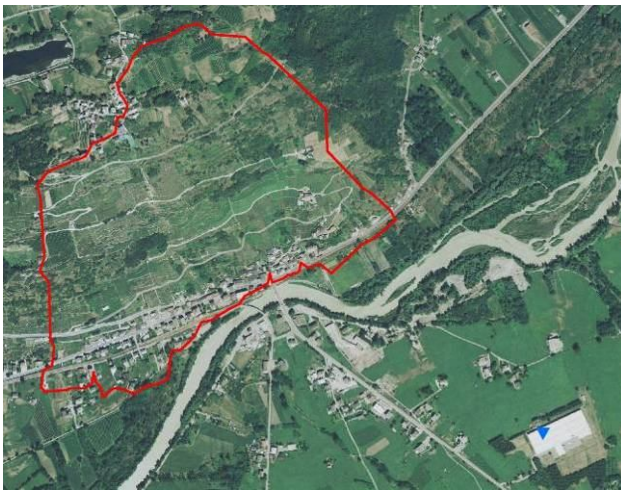

a)

b)

Figure 7.1: a) primary scan position (the blue triangle in the lower right corner) with respect to the study area seen from an aerial photograph; b) laser scanner during acquisition (photo by dr. Rainer Bell).

This automatic procedure led to the creation of gaps in the 0.5 x 0.5 m cell high resolution Digital Terrain Model (DTM) obtained from the edited points (Fig 7.2). Besides the gaps, there are also other areas where the DTM was reclassified to 0.5 m resolution from a more dispersed points cloud, always for the removal of vegetation. In order to fill the gaps, the merging of the acquired data with others from different sources was taken into account.

A Digital Surface Model (DSM) of Regione Lombardia with a 2 m resolution became available between 2009 and 2010. The cell resolution of this model is good but, being a surface model, vegetation and houses were not removed. Moreover, the elevation is expressed in integer and not floating values, causing a loss of resolution in the z-direction. In fact, comparing a little portion of the 0.5 m DTM with the same area on the 2 m DSM it is possible to see how certain features (e.g. walls) are visible in the first case but not in the second (Fig 7.3). The conclusion was that these 2 m data were not sufficiently accurate to perrfect the DTM in project. Regione Lombardia DSM is nevertheless the results of an airborne laser scanning activity. A last attempt was therefore done asking the company that had performed the scan if it was possible to buy the raw data relative to the area of interest. The answer was that they did not sell raw data but could produce and sell us the DTM of the Tresenda slope. The price requested was too high.

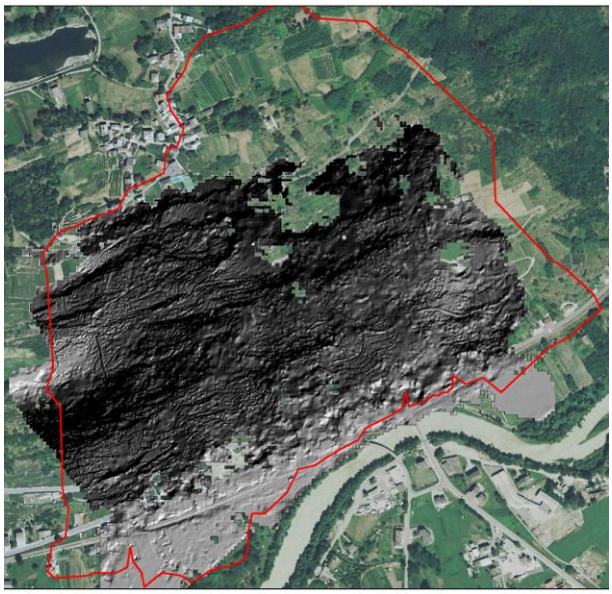

Figure 7.2: the hillshade of the DTM obtained from the terrestrial laser scanner acquisition. Gaps and lack of resolution in some areas are due to the filtering of vegetation. Where vegetation is scarse it is possible to notice the great detail of the model with the walls well visible.

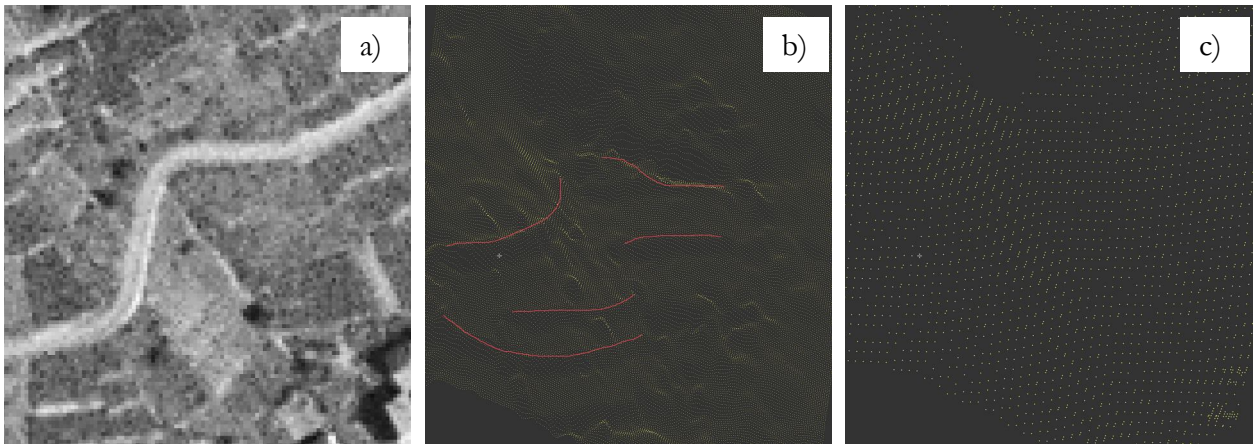

Figure 7.0.3: a) digital orthophoto of a section of study area; b) corresponding 3D view of terrestrial laser scanner with breaklines enlightened that correspond to walls or roads; c) same 3D view of the 2 m DSM of Regione Lombardia. No breaklines are evident. (Images by dr. Rainer Bell).

7.2 GPS and photogrammetric methods

Once understood that there was not the possibility to acquire very detailed laser scanner data to complete the DTM, other methods were taken into account. It was decided to verify the possibility of covering the gaps with kinematic DGPS (Differential Global Positioning System) surveys. The help and the expert supervision of Fabio Villa, a consultant/researcher of the University of Milano-Bicocca, were fundamental for this purpose. A first survey of only one day was programmed in December 2010 to gauge the effectiveness of the method, and the comparability between this kind of data and those acquired via the laser scanner. For the post-processing of the kinematic survey, a receiver was positioned over a survey marker, a point whose coordinates are known, of the IGM (Italian Military Geographical Institute) net for the entire duration of the work (Fig 7.4).

The results of this first survey were not encouraging for two reasons. First of all walking on the terraces carrying the pole that sustains the render receiver takes a lot of time, as even in winter the terraces are full of weed and bushes, if not cultivated and maintained, and so it is necessary to pay great attention while moving. In the vineyards it is no better, in fact the ground is clean but the rows of vines hinder walking straight and so an up and down path between the plants must be followed. The second and more stringent problem was related to the georeferencing of the survey. As said, the GPS surveys was based on the IGM net while the terrestrial laser scanner was georeferenced using the Regione Lombardia orthophoto of the 2004 flight. Comparing GPS points and the DEM obtained from the laser scanner acquisition, it is possible to see how the points are often some meters above the DEM (Fig 7.5), leading to the failure of this work procedure too.

Figure 7.4: a) the position of the IGM marker (the red circle in the center bottom) with respect to the study area seen from a digital orthophoto; b) the reference for the identification of the marker and c) the view of the Tresenda slope from the point.

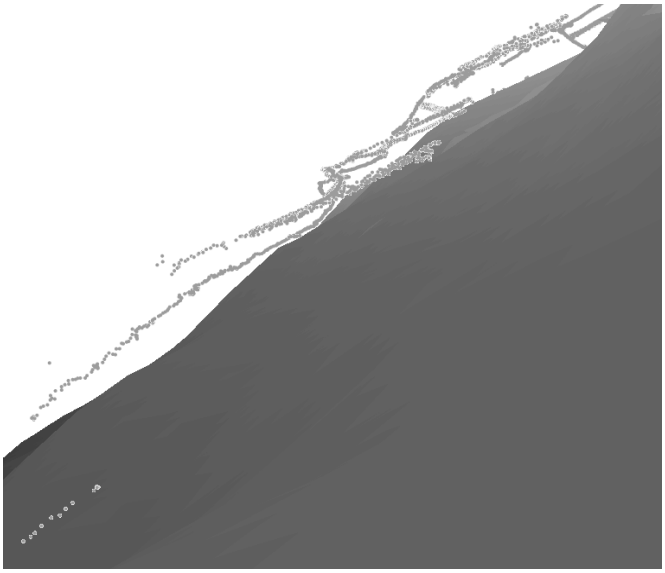

Figure 7.5: the points acquired with the GPS technique lie some meters above the DEM acquired from the laser scanner survey.

At last, it was decided to abandon the laser scanner data and try to obtain a 1 m resolution DEM from photogrammetry. Two adjoining photos were sufficient to cover the study area. In particular the aerial photos relative to the 2004 flight were used, as they were the most recent available.

The initial georeferencing of the photos in a three axis coordinate system (longitude, latitude and elevation) is essential in order to obtain a good final model. Ten points, easy to locate on site, were at first recognized on the photos. Besides the simplicity of site identification, some of these points had to be located on the edges of the photos, in order to guarantee the georeferencing of the entire area, and others in the proximity of the study area, to minimize possible errors in that sector.

Another GPS survey was organized towards the end of February 2011 to acquire with precision the x, y, and z coordinates of these points. In this case a stationary differential GPS survey was performed. The same IGM marker used in the first survey and shown in Fig. 7.4 was utilized also in this case. In each unknown point the position was registered for about 10 minutes but three of ten points were impossible to reach because located on secondary mountain roads covered by snow fallen in the previous days. Anyway, this seven points were sufficient to georeference with a good accuracy the photos for the subsequent analysis.

The result of the photogrammetric interpretation was a points cloud with more or less a million points bearing a resolution of a point every meter. RFD evolution, the software used for this analysis, returned as output the points cloud divided in four different classes on the basis of an internal algorithm that classifies the points on the basis of the difference in elevation with respect to its neighbors and the computational method used. The points are classified as good, sufficient, insufficient or interpolated. The last ones are those whose height is not directly extracted from the photo but interpolated on the base of the neighbouring values, so there was no guarantee of accuracy. The insufficient and interpolated points were immediately rejected and the subsequent work was done only on the other two categories. As for the laser scanner acquisition the post-processing is concerned, above all, with recognizing and removing points related to vegetation. A first manual cleaning of the data was done by visualizing the points cloud in a CAD 3D environment (Fig. 7.6), which allows to see the points that are clearly above or below the topographical surface but does not permit a detailed cleaning of the data.

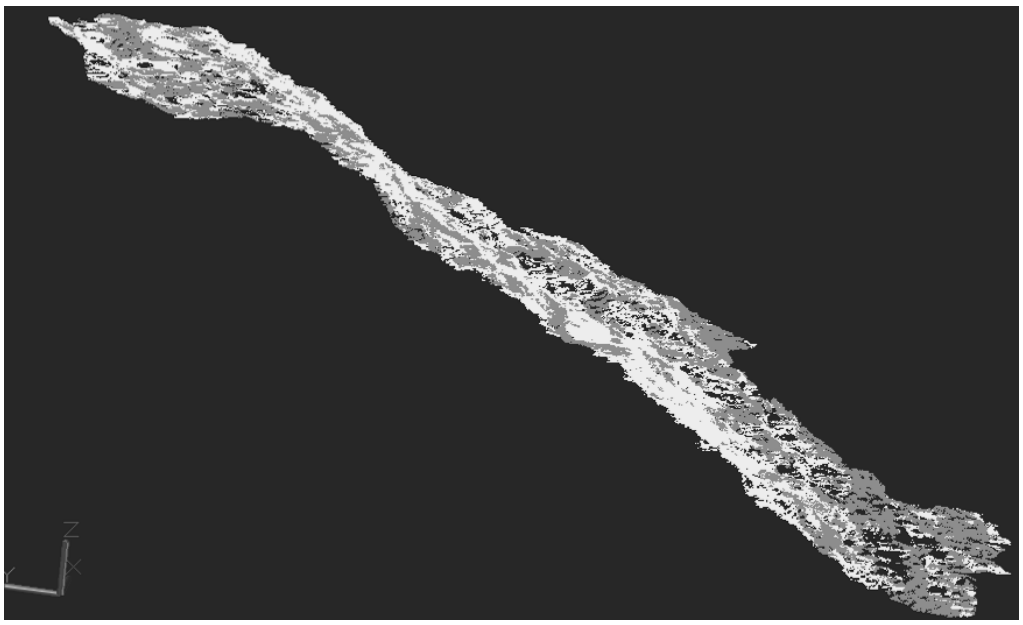

Figure 7.6: 3D view of the points cloud. In dark grey the good points, in light grey the sufficient ones.

The points cloud was therefore later imported into a GIS environment. Besides the points obtained with the photogrammetric analysis, the contour lines of the Regional Topographical Map at a 1:10.000 scale and the Comunità Montana Valtellina di Tirano topographical database DB2000 (2003) at a 1:2.000 scale were available. The 1:10.000 contour lines cover all the Regional surface, while the DB2000 (2003) covers only the urban areas in the territory of the Comunità Montana of Tirano. Hence, in order to obtain the final DEM, it was decided to use only the 1:2.000 contour lines of the DB2000 where available, that is on the valley floor where the village of Tresenda lies and in the other zones on the slope where houses are present. The photogrammetric derived points relative to these areas were not considered in the following work steps.

Where only the 1:10.000 contour lines were available, a DEM with a 2 x 2 m resolution was derived on their basis. Clearly, this DEM does not have a real resolution of 2 m as it comes from 1:10.000 contour lines, but it is useful to determine the preciseness of the single photogrammetric points by calculating the difference between the DEM elevation and the points elevation. The 2 m DEM resolution was chosen because, even if interpolated, it allows depicting a generally quite detailed geometry of the topographical surface. Points were divided into 7 classes based on their difference in elevation to the 2 m DEM:

- Class 1 with a difference between -1 m and +1 m
- Class 2 between +1 m and +5 m;
- Class -2 between -1 m and -5 m;
- Class 3 between +5 m and +10 m;
- Class -3 between -5 m and -10 m;
- Class 4 with a difference greater than +10 m;
- Class -4 with a difference greater than -10 m.

The points of Class 4 and Class -4 were rejected because their difference with the DEM was superior to the resolution of the input data, used for the creation of the DEM itself, and so considered wrong.

The remaining points were further divided from the remaining five classes into nine new ones to get smaller groups to be analyzed, each time controlling also their position with respect to the digital orthophoto:

- Class 1 with a difference between -1 m and +1 m
- Class 2 between +1 m and +3 m;
- Class -2 between -1 m and -3 m;
- Class 3 between +3 m and +6 m;
- Class -3 between -3 m and -6 m;
- Class 4 between +6 m and +8 m;
- Class -4 between -6 m and -8 m;
- Class 5 between +8 m and +10 m;
- Class -5 between -8 m and -10 m.

The points of Class 5, according to the digital orthophoto, lay above all on areas with vegetation and so almost all the points were rejected. The points of Class -5 were similarly rejected because from the orthophoto no evidences of hollows or flat areas were recognized. A procedure equivalent to that followed for Class 5 was used for the analysis of the points in Class 4. All the points that fell on densely vegetated areas were erased as well as those laying on flat areas where only little differences in height should be possible. Among Class -4, all the isolated points were cut as well as those not correlated to any morphological evidence shown by the contour lines or the orthophoto. The points of the other classes were all maintained if not located clearly on dense vegetation. All the remaining points were then used for a first interpolation. The systems used were an Inverse Distance Weight (IDW) interpolation and a Natural Neighbor (NN) interpolation. As it is possible to see from Fig 7.7, the IDW interpolation caused a lot of peaks while the NN ones produced a better result. It was decided to continue the work using the NN interpolation for extracting 2 m contour lines. They appeared very irregular so it was decided to manually edit them looking at the already existing 1:10.000 contour lines, at the digital orthophoto, at the position of the dry-stone walls that had been previously identified and digitalized from the orthophoto, and considering also the contour lines of the DB2000 of the urban areas to which the new elevation contour lines had to be joined. The hillshade of the final resulting DEM is shown in Fig 7.8.

From the hillshade it is evident that the DEM is more precise and clean in the areas where it was possible to count on the DB2000 contour lines and it is known that this model can be improved. This model is the result of a post processing work on photogrammetric data, that required to tackle the difficulties due to the particular morphology of the study area, and was performed above all by the employment of common sense with the only aid of classical CAD and GIS. In the end, even with the lack of more detailed and accurate data due to the failure of various techniques, the resulting map was assessed to be an acceptable input for the scale of the subsequent analyses.

Figure 7.7: a) a 3D view of the IDW interpolation with the remaining points after the filtering. It is possible to notice the high number of peaks in the area that make the surface very irregular. b) The NN interpolation appears more smooth than the IDW one even if it is possible to see some bumps on the surface.

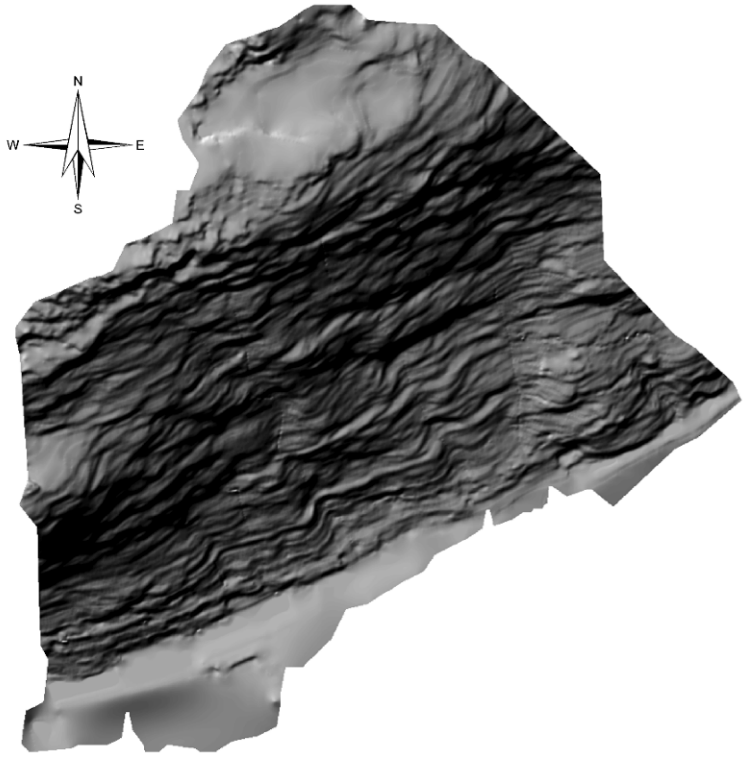

Figure 7.8: the hillshade of the final 1 m resolution DEM. In the south-east area it is possible to detect the enhanced cleanliness of the surface due to the presence of the DB2000 contour lines as input data.

8 Chapter 8

THE SOIL DEPTH MAP DEFINITION

The estimation of the soil depth is of fundamental importance in order to investigate the superficial dynamics of an area interested by landslide phenomena (Kuriakose et al., 2009a; Kuriakose et al., 2009b). Different methods were tested in order to find the best procedure to estimate a soil depth map that could take into account the particular morphology of the study area, characterized by the presence of numerous terraces. The systems applied were in particular a morphological-topographical approach, which uses a deterministic method of interpolation, and geostatistical techniques. The procedures were at first tested using, as topographical base, a DEM with a 5 m resolution, given by the Comunità Montana of Tirano. This is due to the fact that the work for the evaluation of the best method for an estimation of the soil depth began before the finalization of the high resolution (1 m) DEM.

8.1 A morphological-geometrical method

The morphological-topographical analysis aimed at defining the soil depth through the difference between the known elevation of the topographical surface and the bedrock elevation. Hence, in this case, the unknown parameter to be estimated is the bedrock geometry. 26 profiles longitudinal to the slope, and 28 transversal profiles were drawn on the study area (Fig 8.1).

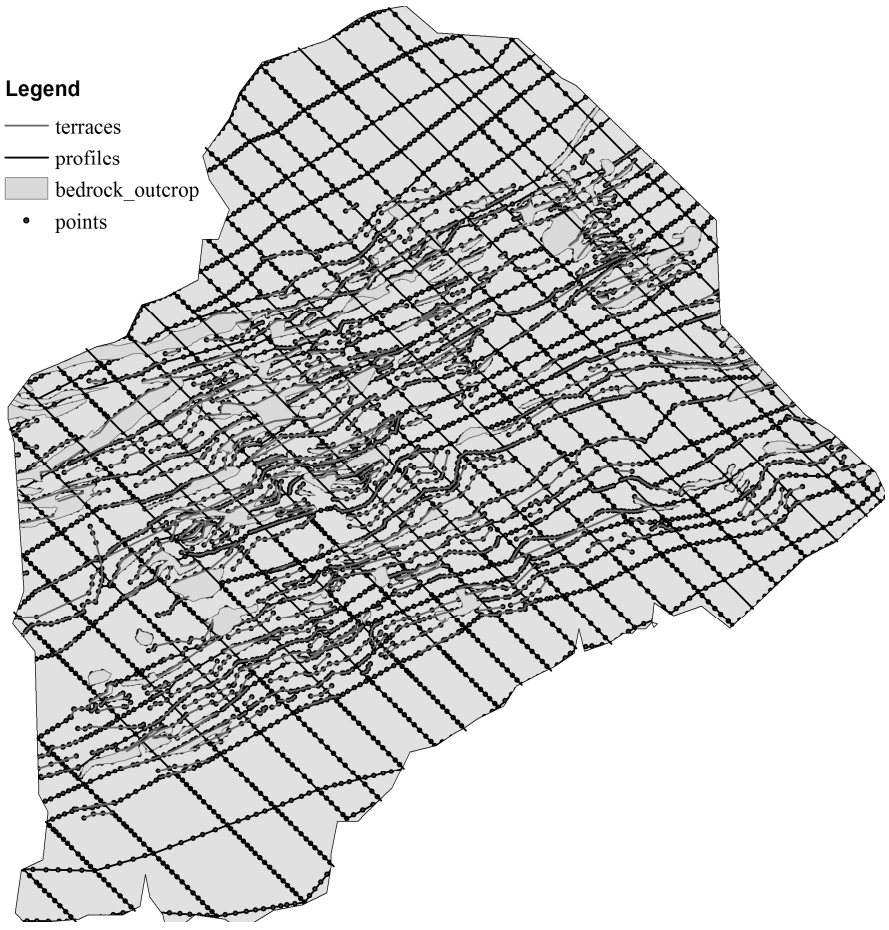

Figure 8.1: the 26 longitudinal and the 28 transversal profiles. Along each profile it is possible to recognize different points. Every point has an elevation attribute obtained as described in the text.

Other points were recognized in correspondence to bedrock outcrops and bases of terraces.

All these points were later used to infer the bedrock geometry.

Along each profile, every outcrop of the bedrock and base of wall, mapped during the field work of summer 2009, was marked with a point. The elevation value of the DEM cell where each point falls was assigned to the points themselves. Polylines-Z, which are polylines with an added attribute of

elevation at every point, were drawn from these points, thus obtaining broken lines similar to the black line in the cross-sectional view of Fig 8.2. Along the polylines-Z, points with an attribute of elevation were added to increase the number of points for the final bedrock interpolation. In order to calculate the elevation value of the added points, the following equation, written with respect to the point D and its nearest vertexes B and C (Fig 8.2), was used:

$$D_{el} = \left(B_{el} - C_{el}\right) \cdot \frac{\overline{CD}}{\overline{CB}} \qquad \text{(eq. 8.1)}$$

where B_{el}, C_{el} and D_{el} are the elevation values at the contiguous B, C, and D points of Fig 8.2, while CD and CB are the lengths of the respective segments.

Other points were added to those along the profiles in correspondence to the bedrock outcrops and the bases of the terraces. All these points were used to estimate the bedrock surface elevation and geometry (Fig 8.1).The interpolation was done with the Inverse Distance Weight (IDW) and the Natural Neighbor algorithms of ArcGIS, but the result was quite unsatisfying with both the methods. As usual, the IDW method returns a result where the desired surface is full of peaks and hollows. The surface calculated with the NN method is smoother than that obtained from IDW, but it still shows problems. In fact, the soil depth maps calculated for difference from the DEM using both the two bedrock elevation maps shows a lot of cells with negative values.

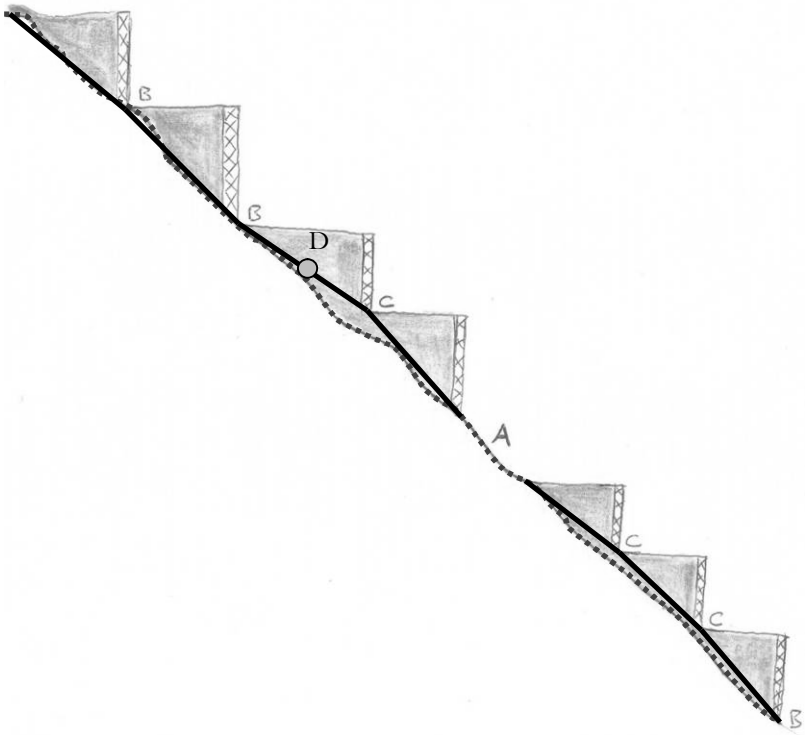

Figure 8.2: a simple schematic 2D longitudinal section of a terraced slope, with different relationships between the walls and the bedrock. In correspondence to the letter A the bedrock crops out. In correspondence to the letter B the wall is founded directly on the bedrock, while in correspondence to C the wall is founded in the soil and the bedrock is a little deeper. The dark grey dashed line represents the real geometry of bedrock while the black line defines the supposed one, considering all the walls founded on bedrock. The point D is added later for interpolation between the two known points B and C.

The problem persisted even fixing the lower limit to zero as too many cells have zero values. At first, it was believed that the unsatisfying result could depend on the resolution of the initial raster map (i.e. the 5 m resolution DEM), that did not permit to reach the needed precision in the positioning of the points for the assignment of the correspondent values of elevation. This hypothesis fell when the same procedure was applied with the 1 m resolution DEM as initial map. In Fig 8.3 it is possible to see both the maps obtained from the NN interpolation of the bedrock surface elevation using the 5 m and the 1m resolution DEM, respectively.

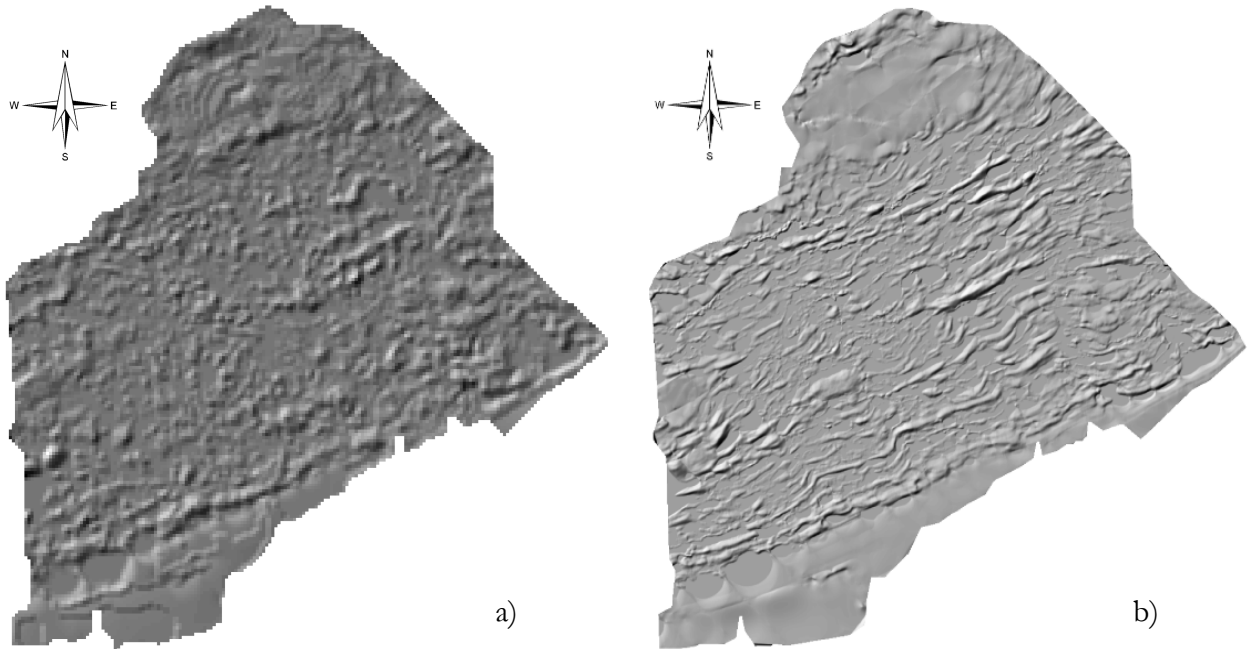

Figure 8.3: a) the hillshade of the soil depth map with resolution 5 m evaluated with the morphological-topographical method and b) the same map estimated from the 1 m resolution DEM.

8.2 Geostatistical methods

The failure of the morphological-geometrical method led to try alternative ways. It was therefore decided to follow the procedure proposed by Kuriakose et al. (2009b), with the help of Kuriakose himself. In their paper, they used geostatistical methods (Matheron, 1963), joining environmental co-predictors to the variable of interest, in order to find the better interpolation technique for their study area, i.e. the Aruvikkal catchment (9.5 km^2) in the Western Ghats of Kerala, India. They compared different methods, both mathematical/geometrical such as linear multiple regression using terrain attribute and environmental maps (Moore et al.,1993; Odeh et al., 1994; Gessler et al., 1995; Odeh et al., 2005; McKenzie and Ryan, 1999; McBratney etal., 2000), and geostatistical approaches such as ordinary kriging (Krige, 1951), regression kriging with environmental maps (Odeh et al., 1994, Odeh et al., 1995; Goovaerts, 1999a) and stochastic simulations from regression kriging. Regression kriging considering all the variables resulted to be the best predictor for their study area. Moreover, the application of the following stochastic simulations permits to introduce also a random component in the resulting map that can supplement the inability of kriging to explain and reproduce the short-range variability represented by the variogram nugget effect.

In the last decades many authors have tried to link the information included in highly detailed environmental maps with data of a soil variable of interest. A complete historical evolution of the methods is contained in Goovaerts (1999b) and in Hengl et al. (2004).

The environmental variables considered in this work are altitude, land use, slope, aspect, curvature, wetness index, and distance from streams (Fig 8.4). The aim is to verify if the proposed method can help to assess soil depth also in a very different, highly human-modified location as it is a terraced slope in Valtellina. For the Tresenda study area a land use map with 5 classes was used and *valgelli* (the local artificial channels) were considered as streams. The 5 land use classes are: 1) grass lawns , bushes and woods; 2) cultivated lands; 3) urban areas and roads; 4) prevalent rocks; 5) *valgelli*.

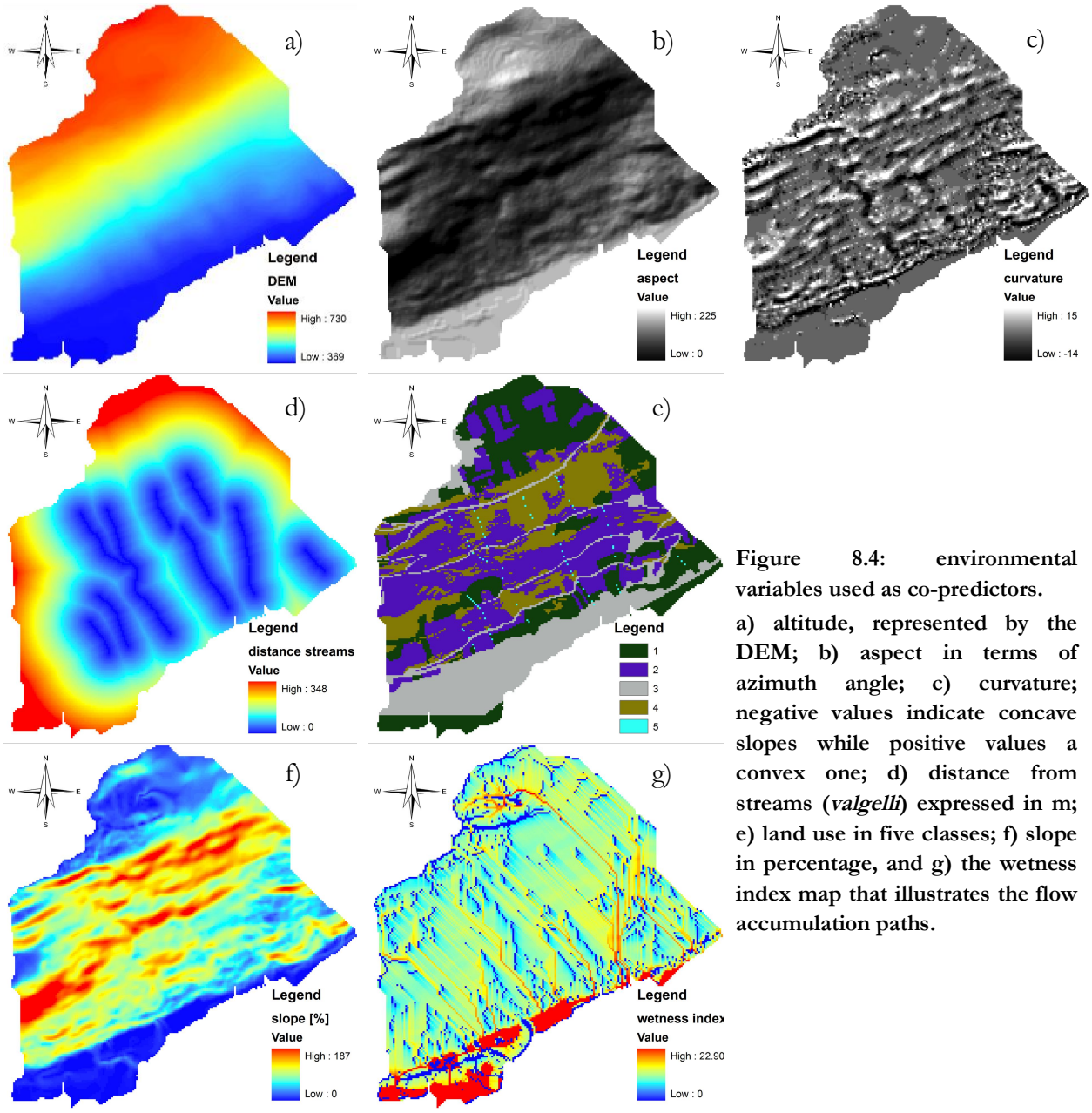

Figure 8.4: environmental variables used as co-predictors. a) altitude, represented by the DEM; b) aspect in terms of azimuth angle; c) curvature; negative values indicate concave slopes while positive values a convex one; d) distance from streams (*valgelli*) expressed in m; e) land use in five classes; f) slope in percentage, and g) the wetness index map that illustrates the flow accumulation paths.

During the fieldwork 682 points were measured (see Chapter 3 about data acquisition). These points, as already described, are wall heights. Evidences of rock outcrops were later added to them, resulting in the distribution of the data set shown in Fig 8.5a. Although only one or few points of zero soil depth were considered for every outcrop in relation with its extension, these measures were too many and could have deeply influenced the estimates obtained by the applied methods. In fact, on the one hand they would have generated a bimodal distribution of the input data, which is difficult to manage and, on the other, an underestimation of the values in the final result would have been probable. Furthermore, considering that all the outcrops in the area are mapped and known, it was reckoned unnecessary to include them in the estimates. In the end, it was decided to work only with the soil depth measures greater than zero, to estimate their trend and then force the result to zero in the zones of outcropping bedrock.

The data set, deprived of its zero values, was integrated with reasonable soil depth values in the uphill and downhill flat zones, where it was not possible to carry out direct measures for the absence of terraces, in order to have sufficient data all over the study area. The distribution of these data

seems to be approximately comparable to a lognormal (Fig 8.5b). The ideal distribution for multiple linear regression and kriging is a normal one (Draper and Smith, 1998), therefore it was decided to transform the distribution of the data into a Standard Gaussian with mean 0 and standard deviation 1 (Fig 8.5c).

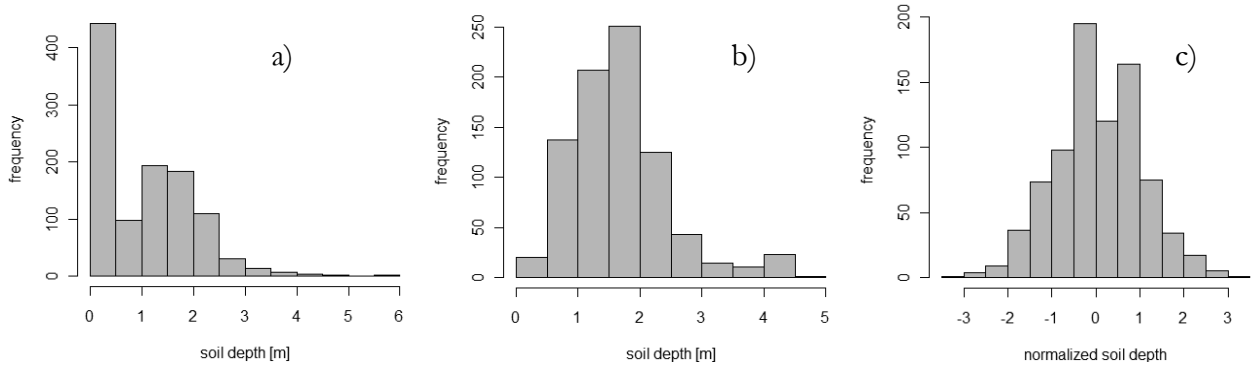

Figure 8.5: frequency histograms representing a) the data set with zero values included; b) without zero values and integrated with reasonable data in the flat zones, and c) normalized to a Standard Gaussian.

The normalized data set, made up of 832 samples, was divided into two casual subsets, the first including 632 values (76% of total data), and 200 values (24%) the second. Points of the larger subset were used as training values for the estimation phase, the others as test for validation (Tab 8.1). The two subsets, being casual, are expected to have more or less the same distribution of the undivided data set; looking at Fig 8.6 it possible to see that this obtains better for the bigger training subset.

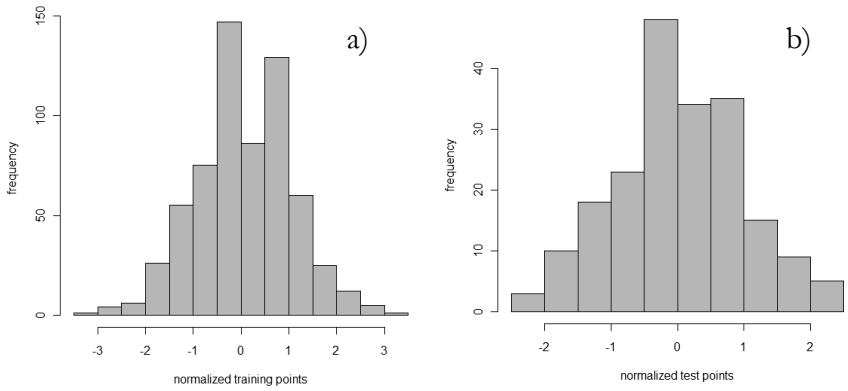

Figure 8.6: frequency histograms of normalized training (a) and test (b) points. Both of them show a distribution similar to that of the entire data distribution reported in Fig 6.13c, but this similarity is more evident for the training subset, made up of more values than the test subset.

All the estimates were done using the normalized values, while some indexes of the fit between the results of the estimated models and the test points were calculated for both normalized and back transformed, resulting soil depth maps (Tab 8.2 and Tab 8.3).

At first, estimates with linear multiple regressions were done, using all the secondary environmental predictors in a first case, and only some of them in a second instance. The choice of the predictors to use in the second model was based on Akaike's information criterion (AIC - Akaike, 1974). It is an automatic procedure where, starting from a certain number of predictors, they are removed one by one till the lower value of AIC is reached. The AIC index is significant in that, the lower its value is, the less information in describing reality is lost. The resulting model should be, among those analysed, the most parsimonious one that is able to better describe the variable of interest (Tab 8.2). This criterion is a tool that permits to compare different models when the physical relationships between different predictors and the searched variable are not known (Venables and Ripley, 2002). In addition to the linear multiple regression, regression kriging was also used. Regression kriging is a variation of universal kriging (Matheron, 1969). The difference is that universal kriging searches a

trend only in the coordinates, while regression kriging identifies a trend (or drift) also considering external variables and then it sums this contribution with the fit of the residuals (Odeh et al., 1994, Odeh et al., 1995; Goovaerts, 1999a). Finally, an estimation of soil depth with ordinary kriging was also performed. The model variogram parameters of the various kriging methods, as well as some statistics related to the results, are summarized in Tab 8.3.

For all the proposed models the validation is presented with respect to both normalized and original test data. Considering that the estimates were done on normalized data, the validation with respect to the normalized test values should represent the soundness of the performed estimates, while the validation with respect to the original measured test data, carried out after the back transformation of the results, represents the quality of the maps after the introduction of the error related to the transformation itself.

The normalized training points were used for the prediction with ordinary kriging, while the fit was searched among the residuals of the correspondent linear multiple regression when regression kriging was used. The residuals of both the regressions with all the predictors and that done with the stepwise procedure are not normally distributed, as it is possible to see in Fig 8.7. In this case it was necessary to normalize the residuals, do the estimates with kriging, back transform the kriging results, sum it to the linear regression components already calculated, and back transform these results with respect to the original distribution of the data set.

Table 8.1: summary of training and test points, both original (O) and normalized (N).

	Min	1st Quartile	Median	Mean	3rd Quartile	Max
Training (O)	0.100	1.200	1.650	1.736	2.100	4.600
Test (O)	0.300	1.200	1.600	1.708	2.000	4.600
Training (N)	-3.035550	-0.630739	0.009028	0.062642	0.769196	3.035550
Test (N)	-2.446980	-0.630739	-0.004514	0.014466	0.638099	2.341480

Table 8.2: summary of the linear multiple regression (LMR) models. For the significance: 0 < * < 0.001; 0.001 < ** < 0.01; 0.01 < * < 0.05; 0.05 < # < 0.1; 0.1 < $ < 1. (VN) Validation between original normalized results and normalized test data; (VB) validation between back transformed results and original test data.**

	LMR all predictors		Step wise LMR	
Predictors	**Intercept**	**Coefficients**	**Intercept**	**Coefficients**
Altitude		-0.0027245***		-0.0027270***
Aspect		0.0002362 $		NA
Curvature		0.0337847 $		0.0336070 $
Distance from streams		0.0021960**		0.0021573**
Slope		0.0005279 $		NA
Wetness Index	0.8708228**	0.0431148**	0.9400086***	0.0426622**
Land Use class1		NA		NA
Land Use class2		0.0486935 $		0.0546026 $
Land Use class3		0.3676525*		0.3606577*
Land Use class4		0.1683132 $		0.1846573 $
Land Use class5		0.9328147*		0.9382718*
AIC	-101.33		-105.21	
R^2 (VN)	0.0077		0.0066	
RMSE (VN)	1.1650		1.1720	
NRMSE (VN)	0.2432		0.2447	
R^2 (VB)	0.0303		0.0305	
RMSE (VB)	0.8473		0.8465	
NRMSE (VB)	0.2072		0.2070	

Table 8.3: summary of the different kriging methods used to infer a soil depth map for the study area. The variogram model parameters refer to the normalized training set for the block ordinary kriging and to the residuals, resulting after the linear regressions, for the two cases of regression kriging. (VN) Validation between original normalized results and normalized test data; (VB) validation between back transformed results and original test data.

	Block Ordinary Kriging	Regression Kriging all	Regression Kriging step wise
Variogram Model	Spherical	Spherical	Spherical
Nugget	0.64	0.64	0.64
Partial Sill	0.32	0.30	0.30
Range	386	75	75
R^2 (VN)	0.2863	0.0726	0.0698
RMSE (VN)	0.8098	1.0910	1.0980
NRMSE (VN)	0.1691	0.2279	0.2294
R^2 (VB)	0.3852	0.1225	0.1209
RMSE (VB)	0.6160	0.7949	0.7970
NRMSE (VB)	0.1507	0.1944	0.1949

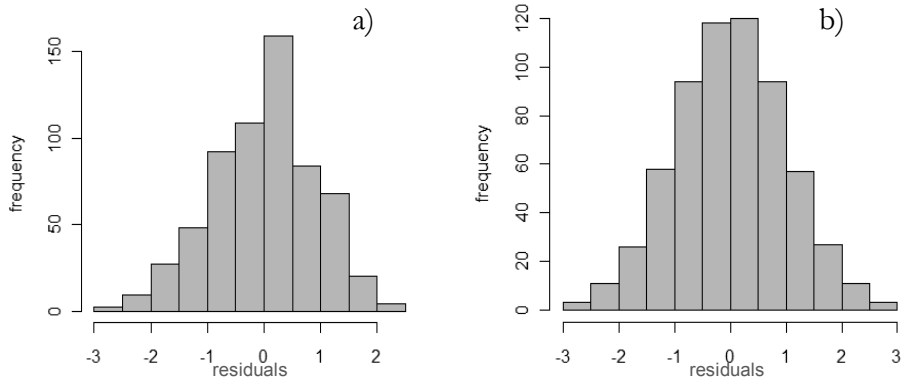

Figure 8.7: frequency histograms of a) the residuals after linear regression with all the predictors and normalized training data; b) the residuals in (a) normalized.

Analyzing the results of linear multiple regression methods (LMR), it is possible to notice that the model with all the predictors and that obtained after the stepwise procedure, based on the AIC, are very similar. In both cases, the results seem to best fit the original test data set than the normalized one, although the regression was based on this latter. It is possible that errors that surely had been introduced with the transformation and back transformation procedure resulted in a random increase of prediction capacity with respect to the original data. Two secondary variables are rejected in the most parsimonious model (slope and aspect) but the result remains very similar to that obtained with all the predictors, in terms of adjusted coefficient of determination (R^2), Root Mean Squared Error (RMSE) and Normalized Root Mean Squared Error (NRMSE). This is true not only for the check carried out comparing the original results and the normalized set of test points, but also for the comparison between the back transform results and the original test data. Both the results are not satisfying considering the very low adjusted R^2, which means that the models are not able to explain the variance of input data, and the high values of RMSE and NRMSE. In particular the latter indicates a mean error around the 25% within the interval of estimation.

Considering the results of regression kriging (RK), the two different estimates performed are still very similar, both looking at the numerical summary and at the maps(Fig 8.8). The comments made for the linear regressions results remain valid also for the regression kriging. In fact, the results better approximate the original data than the normalized one. Moreover, they cannot be considered satisfying as the variance explained by the models, although four times higher than that of linear multiple regressions, is only 12%, and the mean error is around 20%.

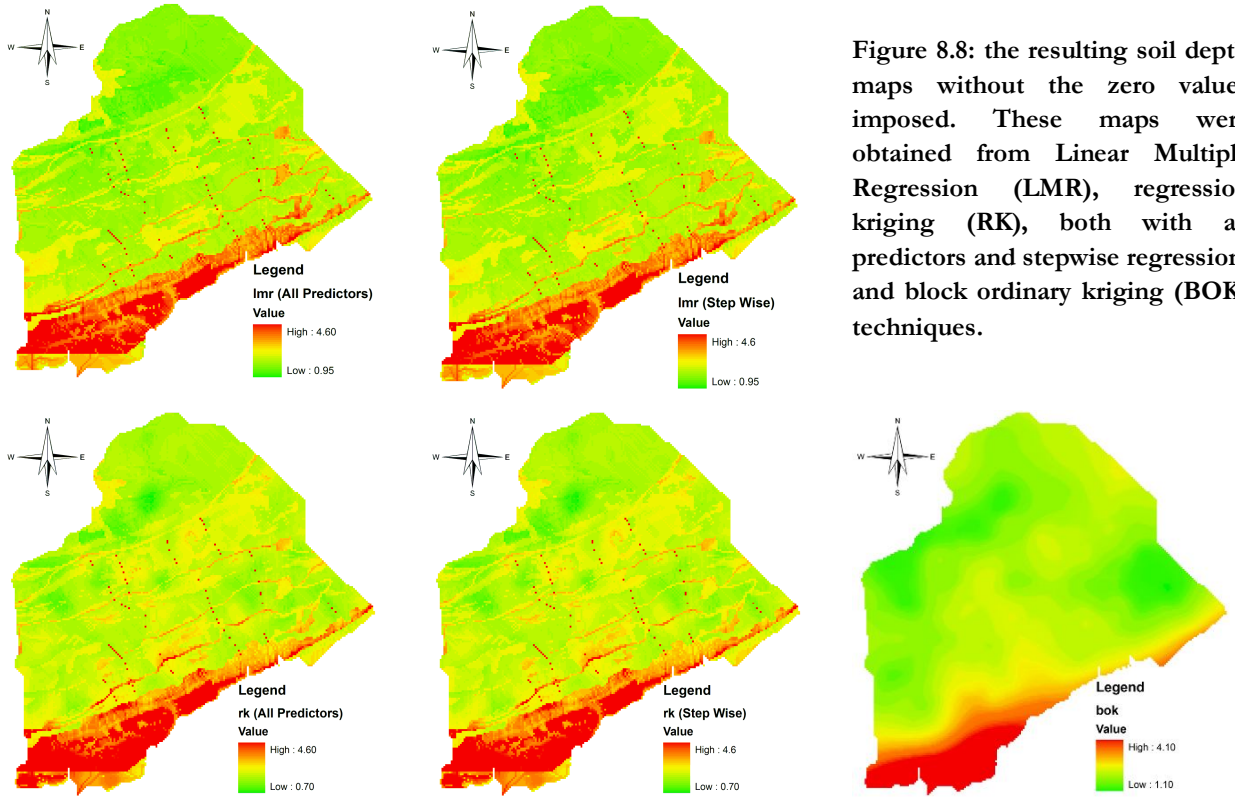

Figure 8.8: the resulting soil depth maps without the zero values imposed. These maps were obtained from Linear Multiple Regression (LMR), regression kriging (RK), both with all predictors and stepwise regression, and block ordinary kriging (BOK) techniques.

On the contrary, the results obtained with block ordinary kriging (BOK) are quite different. This diversity is immediately evident looking at Fig 8.8. The BOK map appears more continuous and regular, even if it is possible to see a general trend in it analogous to the RK maps. In addition, the summary of validation is more encouraging. Adjusted R^2 is 0.29 with the normalized test data and 0.38 with the original measured values. NRMSE decreases from 17% (normalized test data) to 15% (original test data), confirming that the results better reproduce the original data than the normalized ones. Results are quite good but considering the high variability expected in the soil-depth, and the superficial terraced morphology that should be connected with the bedrock geometry, it was decided to do a last attempt using as predictor a soil depth class map (Fig 8.9) drawn on the base of the field measures. The intention was to use this map as a reinforcement of the field measures in order to force the result to be more similar to the observed/expected geometry. The same procedure used to obtain the previous maps was therefore followed, starting from a linear multiple regression with normalized training data, where a correlation coefficient was assigned to each soil depth class. The residuals were calculated after the regression and it was observed that they were normally distributed (Fig 8.10a), so it was not necessary to transform them. Ordinary kriging was performed on these residuals and the result was added to the regression contribution. Once the two terms had been added one to the other a back transformation was carried out, in order to obtain the final result and to compare it with the original field-measured test points. Considering the fact that the linear regression had been performed on classes, its result and that of regression kriging tend to align all the values around the mean of each class. It means that contiguous points, which are in the same class in the predictor map, have (more or less) the same value, while contiguous points originally in different classes have very different values. This is clearly an influence of the regression, and also of the variogram of the residuals, for kriging (Fig 8.10b). In fact, the model is almost a pure nugget effect variogram, meaning that it is almost unable to explain and predict the variance of the residuals, which seems casual. In this situations kriging is not the appropriate technique.

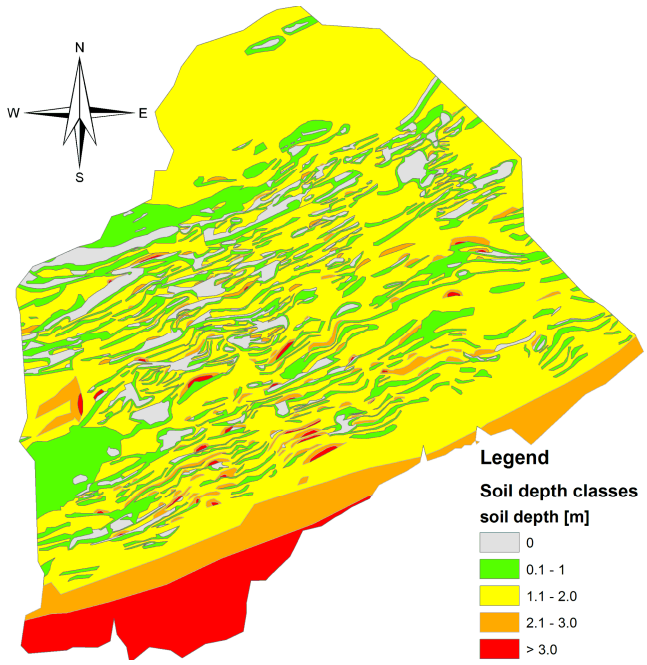

Figure 8.9: soil depth classes map drawn on the basis of field measures and Fig 6.10.

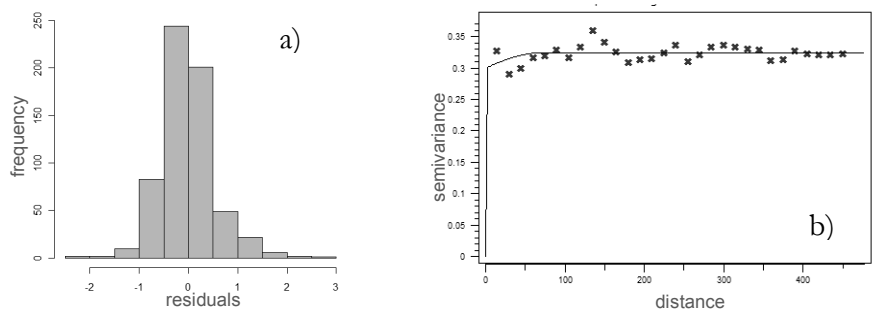

Figure 8.10: a) frequency histograms of the residuals of linear regression with soil depth classes as predictors and b) their variogram and variogram model.

When nugget effect is so high, only a stochastic simulations technique could lead to adequate results. In fact, Gaussian stochastic simulations were carried out with the intent to respect the variability of the values which are originally in the same class. Ten simulations were performed, and among them it was chosen for every cell the value that minimizes the variance of estimation, applying the automatic E-type procedure implemented in the software SGeMS and suggested in its *User's Guide* (Remy et al., 2009). The result was a little better than the kriging one, it was possible to observe variations between values within the same class, except for the higher ones that were still too much leveled, but the limits between the different classes still remain too evident.

The results of linear regression, regression kriging and Gaussian simulations with soil depth classes as predictors are summarized in Tab 8.4-8.5 and Fig 8.11. The high values of RMSE and NRMSE for the linear regression could be due to this flattening of the values of each class, also because the R^2 values are, on the contrary, higher than those of all the other methods previously analyzed. The values of R^2 in all the three methods indicate that the fit between the predicted values and measured ones is quite good. It means that, even if the final result is a little rigged, the use of a soil depth classes map as predictor permits to better reproduce the measured soil depth values than the use of environmental predictors. Regression kriging shows also very low RMSE and NRMSE values and this is a bit surprising considering the low variance shown by the variogram and so the small difference with respect to the linear regression map. Moreover, comparing the results of kriging to that of stochastic simulations, it is possible to see that the randomness introduced with the latter method causes the lowering of both the fit quality and estimate accuracy, but it was expected.

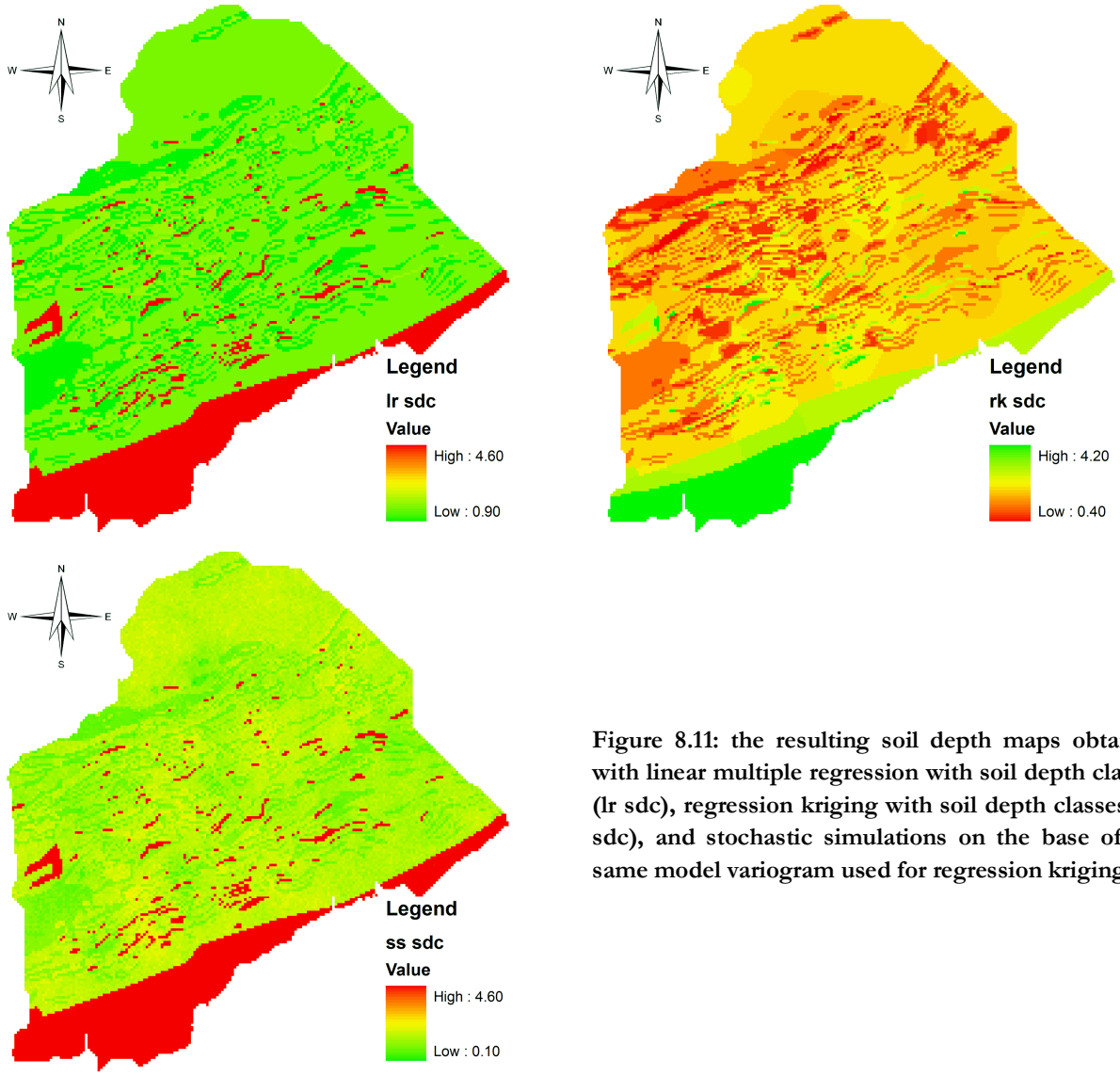

Figure 8.11: the resulting soil depth maps obtained with linear multiple regression with soil depth classes (lr sdc), regression kriging with soil depth classes (rk sdc), and stochastic simulations on the base of the same model variogram used for regression kriging.

Table 8.4: summary of the result of the linear regression performed with normalized data and soil depth classes as predictors. (VN) Validation respect to normalized test data; (VB) validation between back transformed results and original test data. For the significance: 0 < * < 0.001; 0.001 < ** < 0.01; 0.01 < * < 0.05; 0.05 < # < 0.1; 0.1 < $ < 1.**

	Linear Multiple Regression with soil depth classes	
Predictors	**Intercept**	**Coefficients**
Soil Depth Class 1	0.06034$	NA
Soil Depth Class 2		-1.21462***
Soil Depth Class 3		-0.16960 $
Soil Depth Class 4		0.91544***
Soil Depth Class 5		1.92747***
R^2 (VN)	0.5580	
RMSE (VN)	1.5490	
NRMSE (VN)	0.3236	
R^2 (VB)	0.5673	
RMSE (VB)	0.9744	
NRMSE (VB)	0.2830	

Table 8.5: summary of the results of regression kriging and Gaussian stochastic simulations performed with normalized data, normalized residuals and soil depth classes as predictors. (VN) Validation with respect to normalized test data; (VB) validation between back transformed results and original test data.

	Regression Kriging soil depth classes	**Gaussian simulation soil depth classes**
Variogram Model	Spherical	
Nugget	0.30	
Partial Sill	0.024	
Range	152	
R^2 (VN)	0.5659	0.5929
RMSE (VN)	0.6406	1.6210
NRMSE (VN)	0.1338	0.3386
R^2 (VB)	0.6833	0.6009
RMSE (VB)	0.4396	0.9699
NRMSE (VB)	0.1075	0.2372

Summarizing all the methods used and the results obtained, it is possible to notice that the lower NRMSE has been obtained with block ordinary kriging and regression kriging with soil depth classes, while the higher R^2 has been obtained using the soil depth classes map as predictor. Hence, it is possible to say that, at least for the specific problem analyzed, kriging is able to reduce the mean error of the estimate, therefore providing a better accuracy, while the use of the soil depth classes map can improve the quality of fit between the measured and predicted values.

Nevertheless, regression kriging with soil depth classes did not return the expected results. Besides the good correlation coefficient and mean error values, it is evident that the influence of the soil depth classes map is too strong (Fig 8.11); the limits between the classes are still very sharp. Probably the impossibility to well model the behaviour of residuals, resulting after linear regression, made the training points less important than the soil depth class map. In order to re-establish the correct function to the training points and use the soil depth classes map as reinforcement of field measures only, it was decided to try a co-kriging estimation rather than a regression kriging.

Co-kriging requires the definitions of a spatial structure both for the target variable and for the auxiliary one. In this case the primary variable was made up of the training set of measured points while the secondary variable was the soil depth map, derived from the field measures and the hypothesis of slope geometry shown in Fig 6.10. Considering the hypothesis at the base of the construction of the map the same spatial structure was applied to the training points, to the map, and to their reciprocal correlation. In addition, for this co-kriging estimation, a result with a resolution of 1 m x 1 m was directly calculated.

With respect to the block ordinary kriging with resolution 5 m x 5 m, the variogram model was constructed with greater accuracy, accounting also for the presence of a possible anisotropy in the spatial structure of the measures. In fact, looking at the map in Fig 8.9 it is possible to see how the terraces are aligned along a WSW – ENE direction. In fact, a direction of maximum correlation of 67.5° (azimuth) was recognized. In order to further verify the presence of an anisotropy, the variograms in this direction and in the direction perpendicular to it are presented in Fig 8.12. In the perpendicular direction an almost total absence of spatial structure is expected. The co-kriging was performed with the variogram model presented, both conditioning and not conditioning the results in the points of measures to the value of the field measured primary points, whose distribution was normalized before the estimate. The results are summarized in Tab 8.6 and Fig 8.13. The result obtained fixing the measured values in their points appears improved in terms of maximum fit,

while the result for 'not fix' values is able to minimize the error, even if the discrepancy of the two results is very low, especially in terms of NRMSE. In addition, looking at equations of the two regression lines of the two models in Fig 8.13, it is possible to see how the 'fix' intercept and slope coefficient are respectively very close to 0 and 1, thus remaining very similar to the ideal model. Also for this reason, in the end it was decided to use, for the following part of the work, the map obtained with the conditioning method (Fig 8.14).

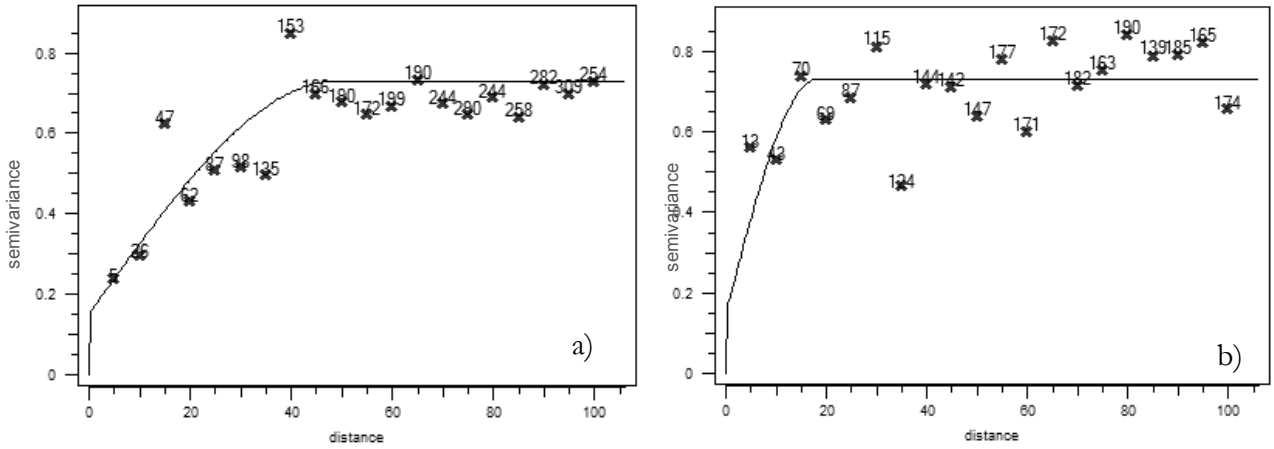

Figure 8.12: Variogram in 67.5° azimuth direction (a) and 157.5° azimuth direction (b). The variogram model can fit well the data in (a) but almost no spatial structure can be recognized in (b), underlining the occurrence of an anisotropy present in the data.

Table 8.6: summary of the results of co-kriging. In this case the validation was performed only with respect to the original measured values of test points.

	Co-Kriging fix	**Co-Kriging not fix**
Variogram Model	Spherical	
Nugget	0.15	
Partial Sill	0.58	
Range	49	
R^2 (VB)	0.6298	0.5793
RMSE (VB)	0.4677	0.4495
NRMSE (VB)	0.1375	0.1322

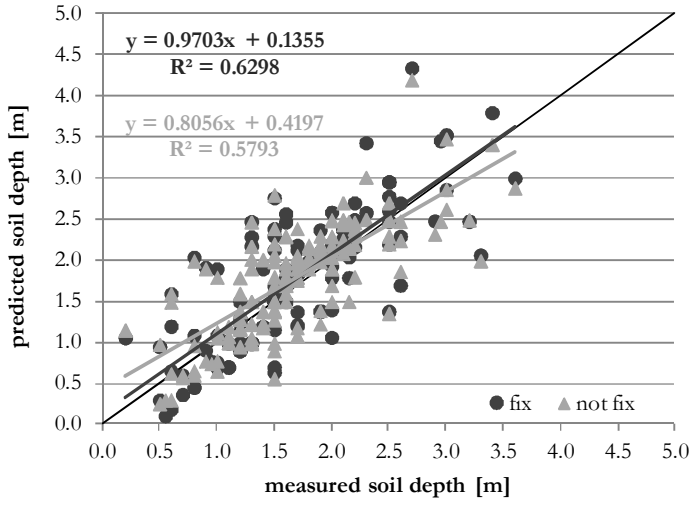

Figure 8.13: validation of the two co-kriging models. The "fix" model shows a better fit between measured and predicted values and also a greater similarity of its regression line with the bisector, image of the ideal model.

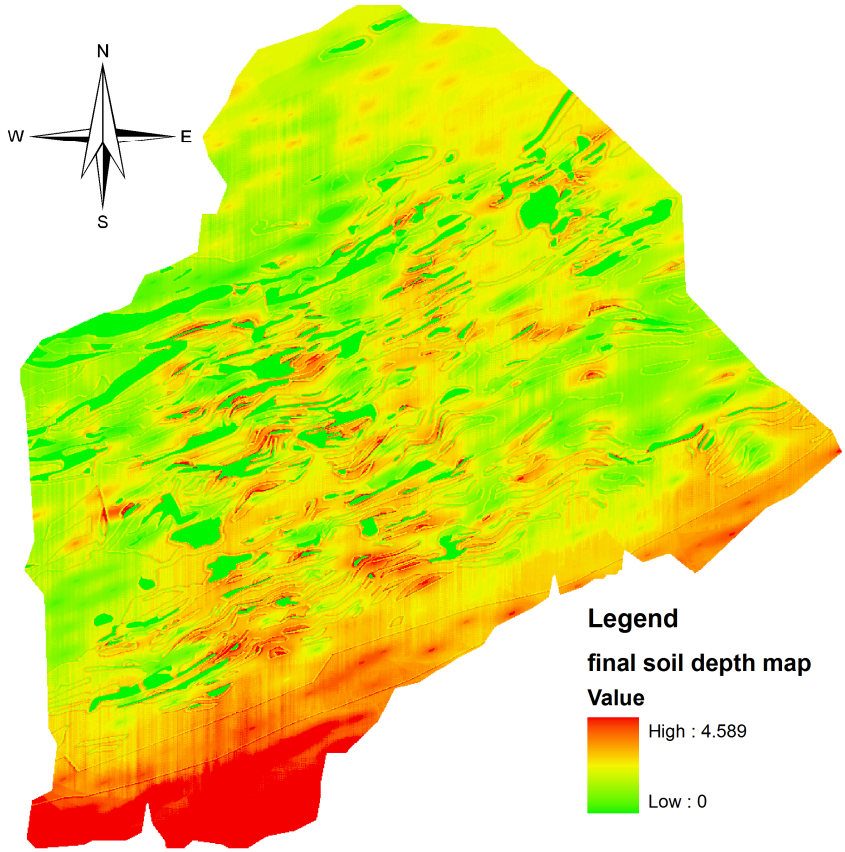

Figure 8.14: the final soil depth map obtained with co-kriging conditioned to the training values in the points of measure and with the rock outcrops imposed on the geostatistical result.

8.3 *Geophysical surveys: geo-electrical and radar methods*

In order to investigate the soil depth not only in correspondence to the dry stone walls, between May and July 2011 some 2D geo-electrical surveys (Earth Resistivity Imaging, ERI; Loke, 2001) were carried out on a selected small area of the Tresenda slope. These surveys were later integrated with Ground Penetrating Radar (GPR) surveys executed in the middle of November 2011, but unfortunately their elaboration is not finished yet and so these data are not presented in this work.

Geo-electrical methods are able to provide an estimate of the distribution of the electrical resistivity in the soil, executing indirect measures from the topographical surface. Soils can have different resistivity on the basis of their composition, grain size distribution, porosity, and water content. In particular, in the contest of Tresenda, it is expected to observe sharp increasing in resistivity at the contact surface between the porous soil, where water with conductive ions can be present, and hard bedrock. For a complete overview on the theoretical basis of the method, that is beyond the aim of the present work, it is possible to refer to the PhD Thesis of M. Mele (2008), and to Telford (1990), Pellerin (2002), Robinson (2008) and Reynolds (2011), where a wide literature review is given. Mauro Mele, a post-doc researcher at the University of Milan, has also helped in the organization, execution and interpretation of both geo-electrical and GPR surveys.

The equipment needed to perform this kind of analysis is made up of a current and a potentiometric dipole. The electric current is entered into the soil through two metallic electrodes (A and B – Fig 8.15) connected to an oscillator (current generator). This electricity generates, in other two electrodes (M and N), an electric potential that depends on: the current intensity, the distance between the four electrodes, the resistivity of the soil and the presence of possible anisotropies in it. Measuring the current and the electric potential and knowing the distances it is possible to calculate the apparent resistivity of the soil.

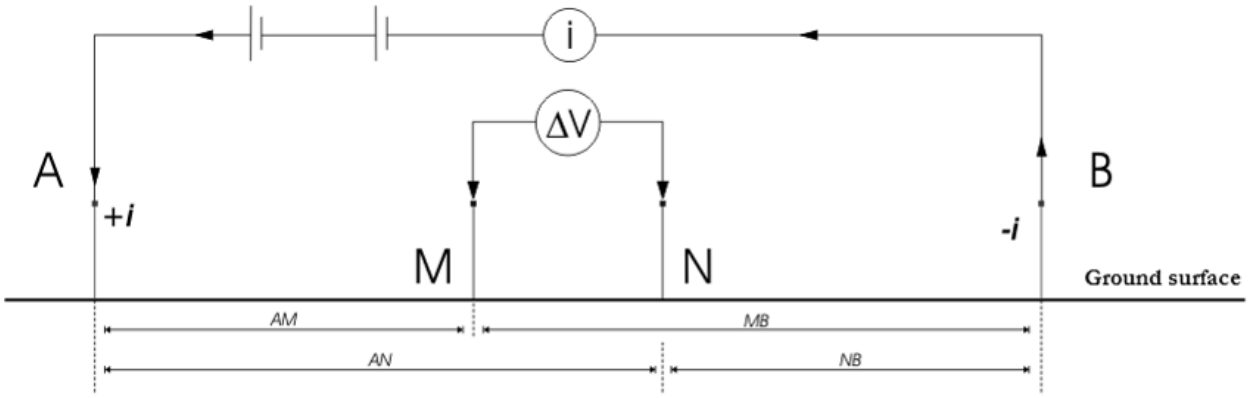

Figure 8.15: a simple scheme of the measuring setting (from Mele, 2008).

The resistivity is apparent, because in a situation that differs from that of an infinite, homogeneous and isotropic volume of investigation, it is the result of all the components of resistivity of each different soil crossed by the current. It loses its physical significance, as it can change from point to point depending on the relative distribution and geometry of the different soil layers. For this reason it is important to understand the numbers of geo-electrical soil layers interested in the survey and the depth of investigation reached during the acquisition.

It is possible to demonstrate, using the vectorial Ohm Law and considering a fixed distribution of electric resistivity in a volume of soil, that the investigation depth (z) increases with an increasing spacing (L) of the current electrodes. In particular, normalizing the result with respect to the superficial current, it results that the horizontal component of the current density becomes 0 for a z/L ratio equal to 10 (Telford, 1990).

Usually, the resistivity surveys along an acquisition line are performed increasing the spacing between the current electrodes with respect to the potentiometric electrodes, thus increasing the investigated volume from measure to measure (Fig 8.16).

The number of the electrical layers involved in the measure with the increasing spacing of the electrodes can be stated plotting, in a logarithmic graph, the value of the apparent resistivity with respect to the semi-distance between the electrode A and electrode B (AB/2). To every maximum, minimum and flex of the resulting curve should correspond a transition between different electric layers. Once the number of electrical layers are identified, it is possible to obtained their physical value of resistivity through the application of appropriate algorithms that solve an inverse problem. In fact, the estimations of the parameters that better justify the reaction of the investigated soils are searched, starting from a series of analytical measures. The depth of investigation of this type of measure, can be considered more or less ¼ of the semi-spacing of the current electrodes AB/2 (Telford, 1990; Reynolds, 2011).

Before planning the principal field campaign, a single day acquisition was performed in May 2011. During this survey, a total of two lines in two different areas were acquired(Fig 8.17). One line was longitudinal with respect to the terraces alignment while the other was transversal. The longitudinal line consisted of 32 electrodes, the transversal of 48; along every line the spacing between the poles was 1 m. These two test areas were chosen because one corresponds to the triggering zone of one of the 1983 events, while the second was indicated by Blahut et al. (2011) as a possible source area for debris flow/soil slip phenomena.

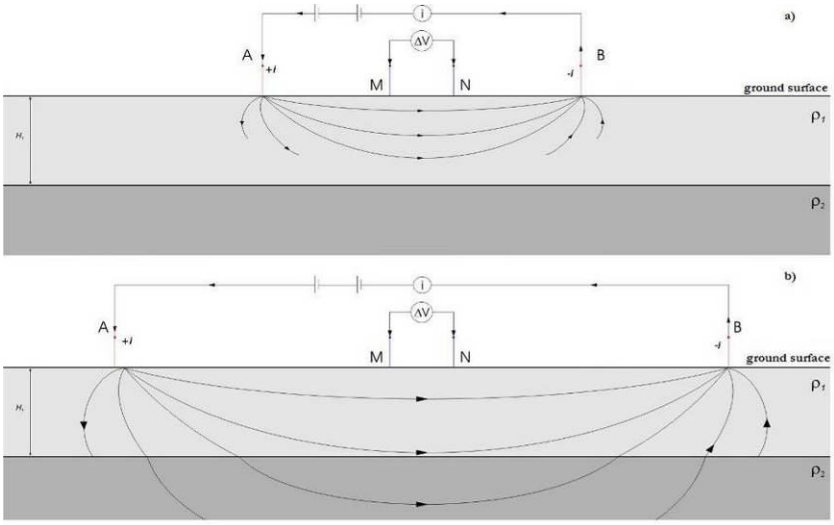

Figure 8.16: two successive measures along the same line with increasing distance of the current electrodes A and B and a correspondent higher volume of investigation, that leads to consider (b) two layers with a different electrical resistivity (ρ_1 and ρ_2) (from Mele, 2008).

Both the Wenner and the Schlumberger methods of acquisition were tested in the first longitudinal acquisition line, performed in the eastern area of Fig 8.17. With reference to Fig 8.15, in the Wenner method the current and the potentiometric dipoles are both symmetric with respect to the centre of the acquisition line, the current electrodes are external to the potentiometric ones, and the distance AM = MN = NB. The Schlumberger method is not very different; the dipoles, with the current ones external, are both symmetric with respect to the centre of the line too, but the distance between the electrodes can change. In fact it is a sort of extension of the Wenner method in which AM = NB ≥ MN. Therefore, with the Schlumberger method and the same number of electrodes more measures are possible than using the Wenner method, as more single combinations of four poles are possible. This method allows reaching higher depths with a greater resolution but clearly, it is also more time consuming.

The results obtained are very similar for the two methods, both in terms of apparent resistivity, which could be immediately analyzed on the field at the end of the acquisition, and inverse model (Fig 8.19). For this reason, in the successive measures it was decided to work only with the faster Wenner geometry. In general terms, the longitudinal line showed good results, revealing the effectiveness of the geo-electrical method to identify the contact area between a conductive soil and the resistive bedrock. In fact, in the first line acquired in the eastern test area, the bedrock cropped out on the right side of the section, where it is possible to see (Fig 8.19) a superficial, high resistive layer. Moving to the left, this layer becomes deeper and a clear contact with an overlaying conductive soil can be seen. More or less the same happens in the transversal section (Fig 8.20). In this case, a bedrock outcrop is present in the lower part of the section, where the method clearly identifies it. Moving uphill, the bedrock becomes progressively deeper and in the upper part of the section it cannot be detected. The method seems to work also in this case but, along this line, some problems arose in correspondence to the three dry walls present. All the three walls were higher than 1 m, therefore at least an electrode for each wall could not be inserted in the ground, causing some disturbances in the acquisition and in the measured apparent resistivity. In addition, the software used for the elaboration of the field data and the calculus of the inverse model does not permit the introduction of surfaces with angles higher than 60°.

Programming the second field campaign, these observation were taken into account, as well as the higher simplicity of access to the western area than to the eastern one. It was in fact decided to perform other six longitudinal sections with 48 electrodes and 48 meters long on the western area, that intersected the transversal one.

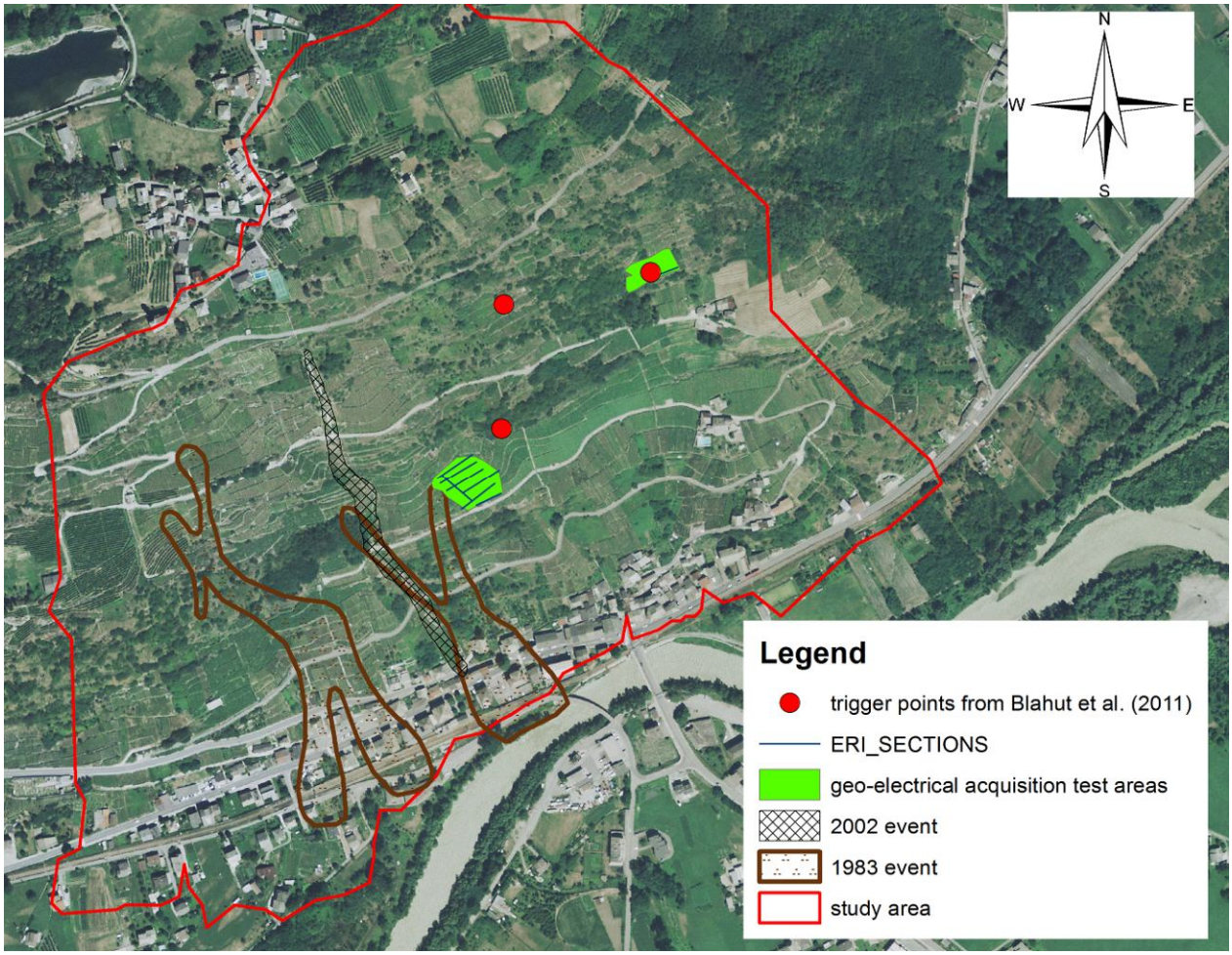

Figure 8.17: the acquisition test areas in function of the past events and the possible triggering points identified by Blahut et al. (2011).

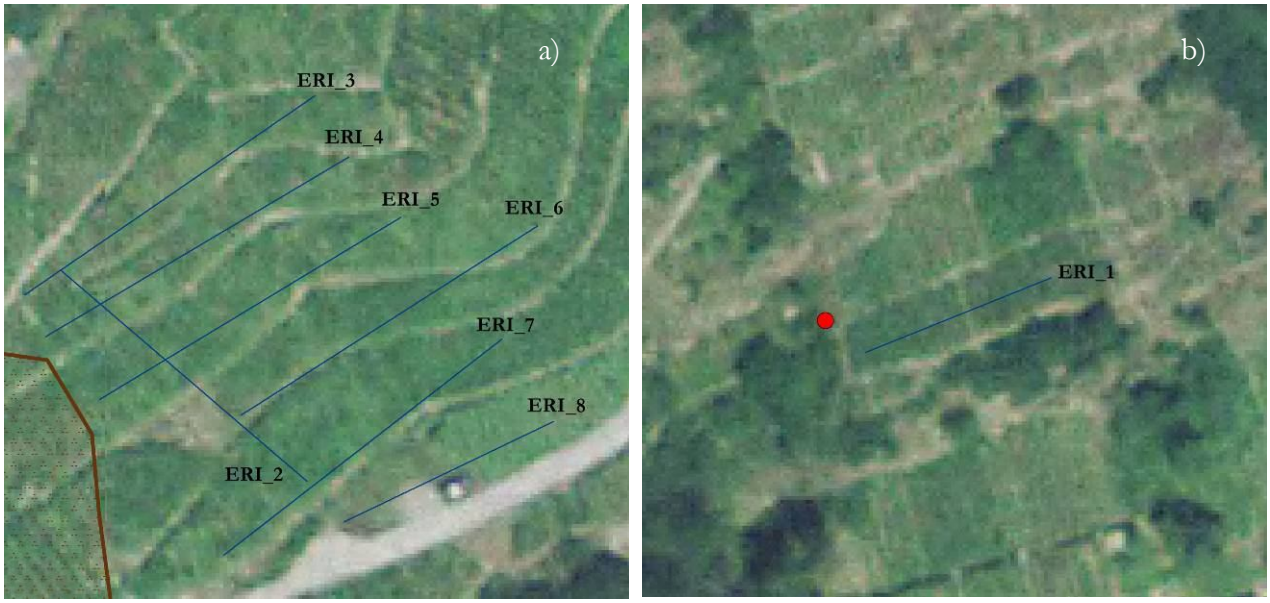

Figure 8.18: detail of the two test areas, shown in the previous image, with the reciprocal position of the sections acquired. a) Western test area; b) eastern test area.

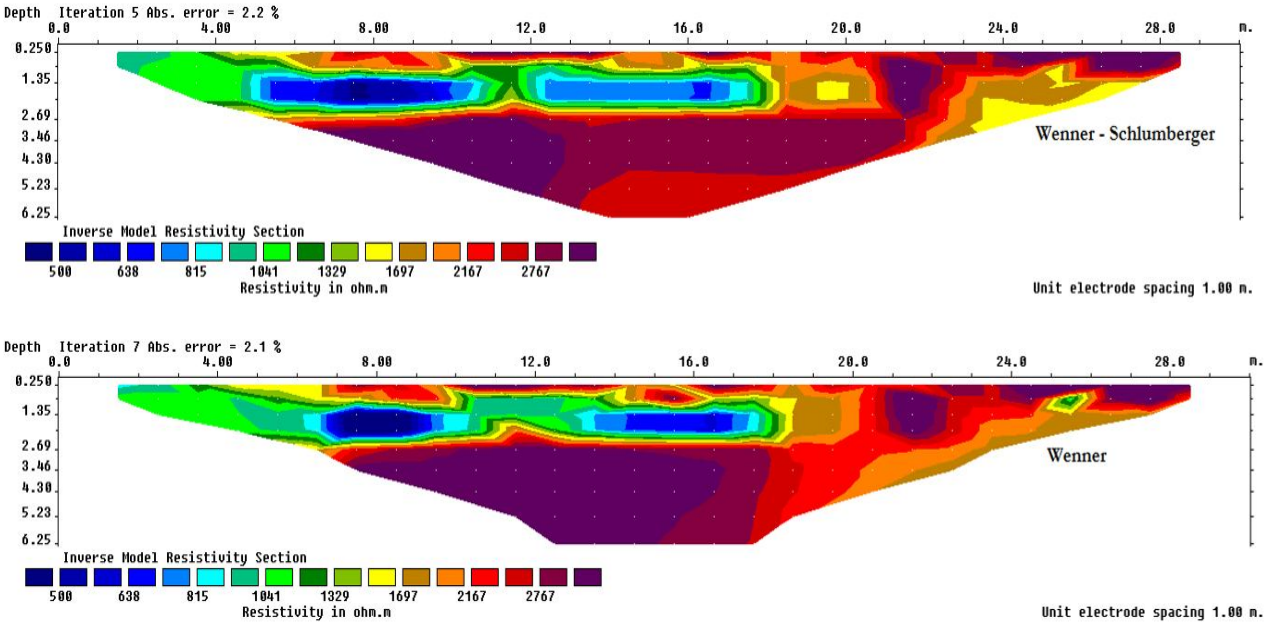

Figure 8.19: the results, in terms of inverse model resistivity sections, of the acquisition on the eastern area of the slope, performed with both the Wenner and Wenner–Schlumberger methods. In the two images it is possible to notice the sharp contact surface between a superficial conductive layer and a deeper resistive one, that on the right side becomes more and more superficial.

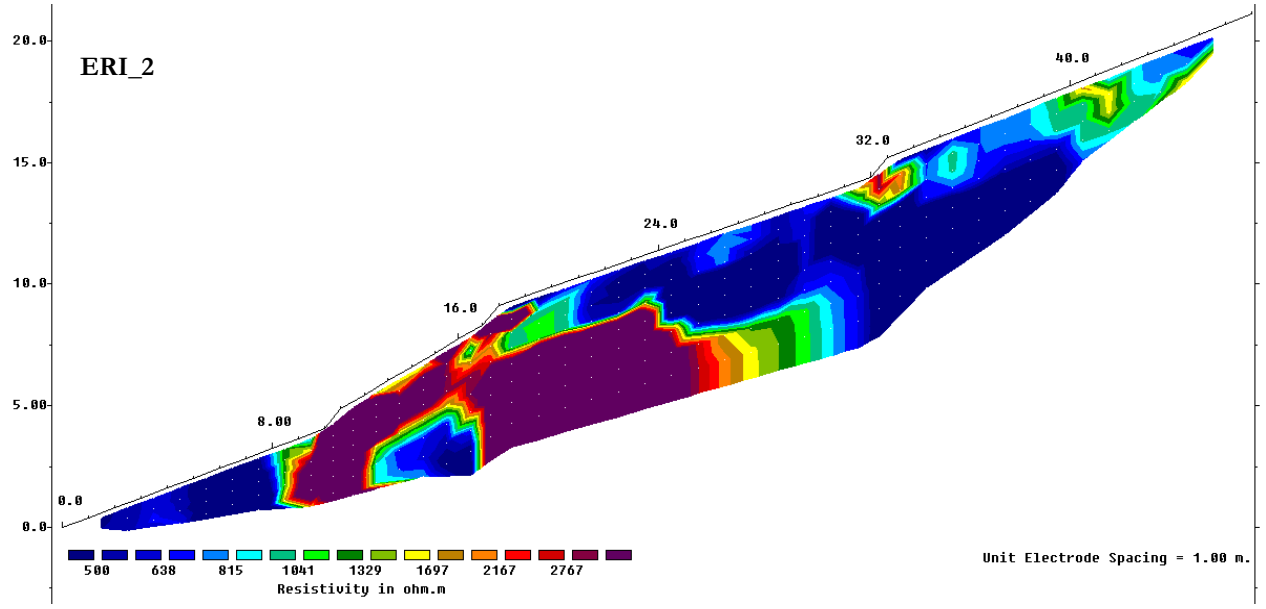

Figure 8.20: the resistivity inverse model of the transversal section with 48 electrodes acquired on the western test area.

These sections were acquired on six different terraces, more or less in the middle of their width, trying to retain a good compromise between a straight alignment and the maintenance of the line more or less always at the same height. The bedrock is visible in all the sections, numbered from uphill to downhill and shown in Fig 8.21, but it does not seem always continuous. During acquisition some problems were noticed in correspondence to the last 16 electrodes, probably due to a malfunctioning of a cable or of a link box between two cables, starting from the third acquisition line. For this reason, sections ERI_5, ERI_6, and ERI_7 appear truncated, while the section ERI_8 was directly acquired with only 32 electrodes.

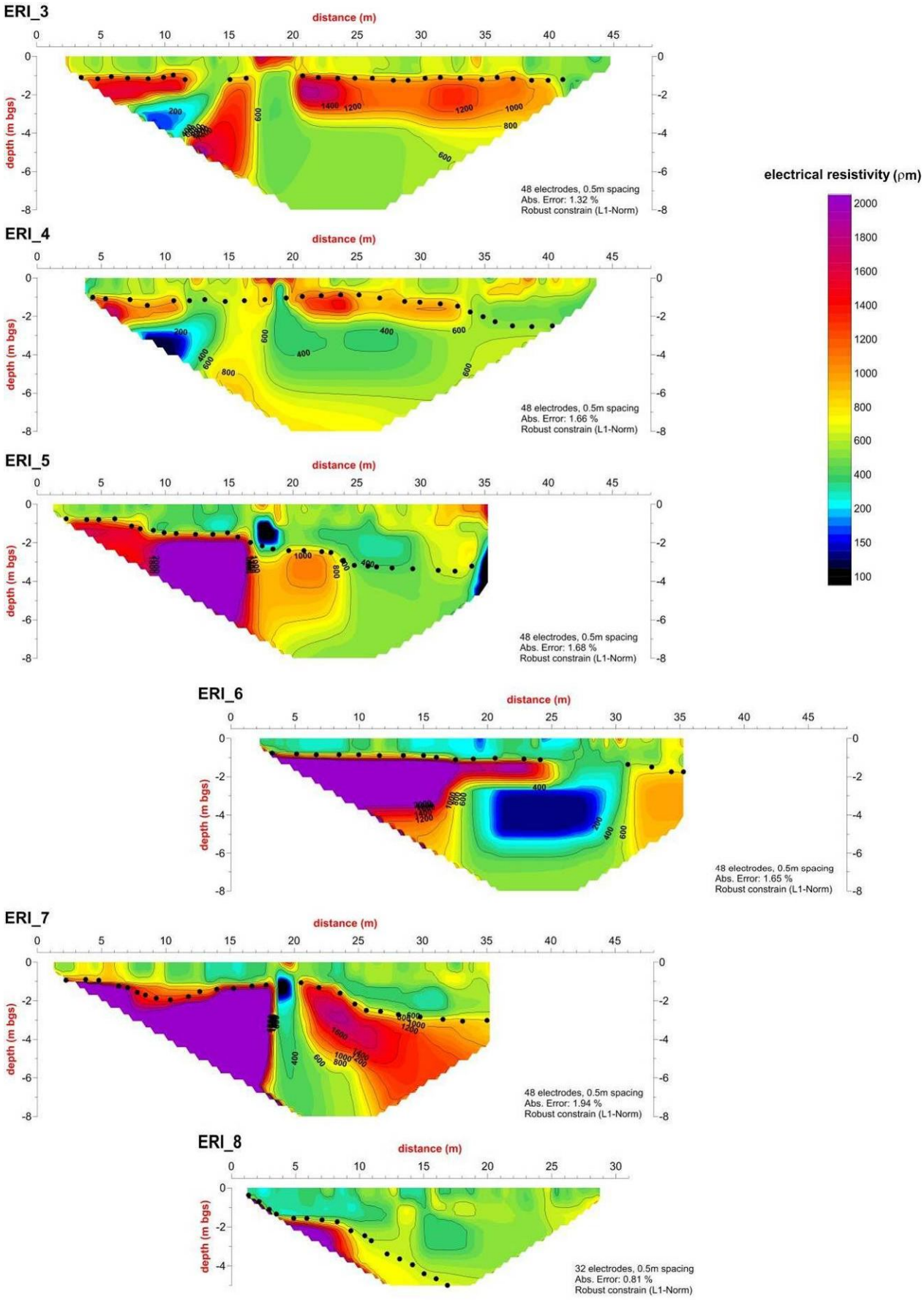

Figure: 8.21: the six sections acquired in the western test area during the campaign of July 2011. The black points represent the interpretation of the contact between soil and rock.

Analyzing the results it is possible to see how, in some circumstances, a conductive layer appears below a resistive one. It is the case of the section ERI_6, where the presence of a very low resistive layer is very evident, and of the central part of sections ERI_3 and ERI_4. These last two sections show also, on the left side, a column of conductive soil wedged into the resistive layer as a sort of column. A structure like this is also visible in the centre of the section ERI_7. Looking at the sections in their complexity, it is possible to say that the bedrock can be followed in a continuative way, from the uppermost section to the lower one, on the left side (West), where it can be found at a depth of approximately 2 m. On the contrary, in the central part a sort of transition zone is present and on the eastern side the bedrock is again visible in all the sections, except the ERI_8, but its depth is more variable. The central conductive lenses of soil can be aligned along the little valley visible in Fig 8.18a. On a concave area, the preferential accumulation of material can be easily explained. Moreover, considering the geological and geomorphological setting of the area, this morphological concavity could have a structural origin, thus adding also the possibility of a more fractured rock in that zone.

During the acquisition, the heights of the walls and the mean slope angle of each terrace were measured. In this way it was possible to reconstruct an approximate relative topography of the investigated area, with contour lines every 1 m (Fig 8.22). The zero level is set at the lowest altitude along the ERI_8 section. Then, after the positioning of the sections acquired on the map, it was possible, looking at the results of Fig 8.21, to attribute and reference some values of soil depth to each line. Once the soil depth values were put on the map, it was possible to calculate from interpolation the soil depth map, and then from the difference with the construct topography also the relative elevation of the bedrock.

Of great interest was the comparison between the soil depth map obtained with this method and the map estimated with the geostatistical analysis (Fig 8.14). Only for this little area it was in fact possible to calculate the difference between the two maps, the quality of their fit, and the accuracy of the statistical estimate with respect to the geo-electrical indirect measure. Anyhow, just looking quickly at the two maps, it is possible to see evident differences. For example, the geostatistical map hardly shows soil depth values around 4 m, with the exception of the area next to the valley floor, while the geo-electrical map shows two zones around these depths, in a relatively small area, on its right border. Looking at the map in Fig 8.23, where positive values indicate that the geo-electrical map has a soil depth higher than that of the geostatistical map, it is possible to notice how the already cited areas are those where the difference is bigger. This means that the geostatistical map, along the slope, tends to underestimate the deep soils, and this fact is also evident from the graph next to the map, where the fit line has a very low angle (around 10°) and the points, for geo-electrical soil depth higher than 2.0 m, are almost all under the 45° line, causing also a very low quality of fit between the two maps. On the other hand, for soil depth values between 1.0 and 2.0 m, the dispersion of the correspondent values estimated with the geostatistical methods appears very low, confirming a good quality of the estimate in this interval of values. This fact is coherent with the original measures with which the geostatistical analysis was performed. In fact, the walls were always considered funded on bedrock or in its proximity, but the geo-electrical surveys, with a particular reference to the section transverse with respect to the walls alignment (Fig 8.20), show that in some cases this is not true, at least in this area, and it is possible to find even 2 m or more of a conductive layer under the base of the wall.

Anyway, the calculated RMSE and NRMSE of the geostatistical map with respect to the geo-electrical one are not an optimum but also not too bad. The RMSE is in fact equal to 0.84 m, while the NRMSE is 0.20. The error exists, but considering the very high variability of the soil property investigated, it can be considered acceptable.

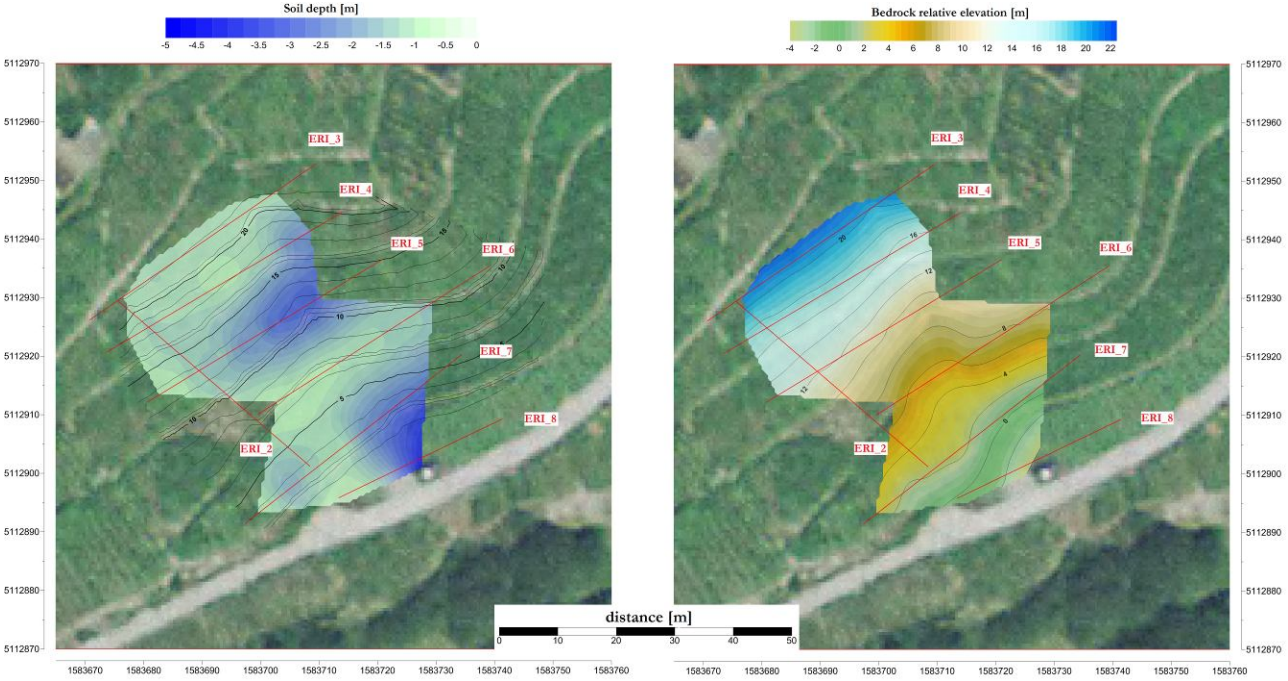

Figure 8.22: the interpretation of the performed geo-electric measures in terms of oil depth and bedrock surface height, with respect to a relative referencing system that has its zero in correspondence of the lowest point along the ERI_8 section (image produced by Mauro Mele).

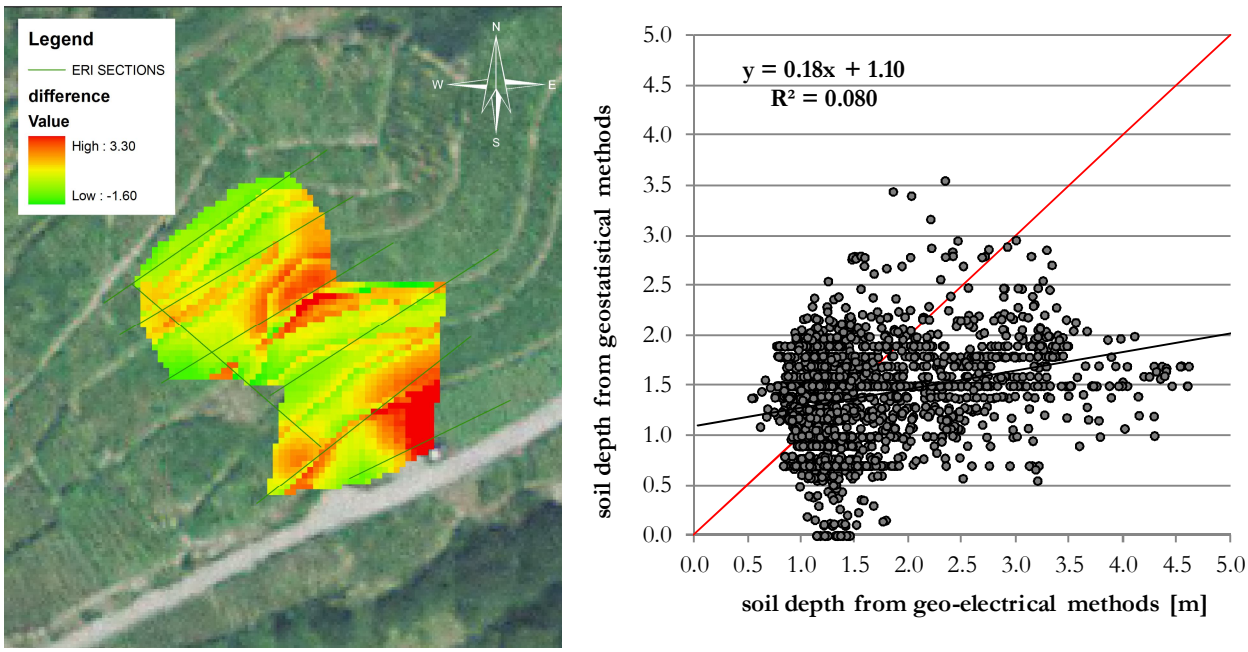

Figure 8.23: the map calculated for difference between the soil depth map obtained with the geo-electrical surveys and that estimated from geostatistical method. The graph next to it show the correlation between the two soil depth maps.

9 Chapter 9

HYDROLOGICAL-HYDROGEOLOGICAL MODELLING

The model used to perform a hydrological-hydrological analysis on the entire study area was STARWARS (van Beek, 2002), as already mentioned in the introduction to this third part of the work. STARWARS considers the hydrological processes of rainfall interception, canopy storage and evapotranspiration that act on the quantity of water that can reach the ground and can be available for infiltration. The quantity of water that can enter the ground in a certain time depends on the infiltration capacity, that usually is defined as a multiple of the saturated hydraulic conductivity and its value decreases as the infiltration process continues. Once in the ground, water is redistributed through the unsaturated horizon considering only its vertical, gravity driven, component of movement, calculated on the basis of Richards' equation (Richards, 1931). The horizontal component, which depends on gradients generated by the matric potential, is neglected because considered negligible with respect to the vertical one. The unsaturated soil is described through the Soil Water Retention Curve (SWRC), defined with the Farrel and Larson (1972) method, and the unsaturated hydraulic conductivity, that is calculated with the Millington and Quirk equation(1959, 1961). Laying the soil upon a semi impervious bedrock, when water arrives at the contact between the two different materials, it may form a perched groundwater table (PGT). If the PGT forms, also a saturated component of movement is considered in the model and it depends on the gradient of the water table itself. Water can also move into the bedrock layer, which is considered as a sort of infinite reservoir. The model compute the quantity of water that each timestep enters into the bedrock layer, but does not analyzed how it moves inside it. The model considers this water only as bedrock storage. When the available volume of water in a certain cell exceeds the infiltration capacity, it remains on the surface and it is involved in superficial runoff. The superficial runoff is based on the linear drain direction map derived from the DEM but it does not considered the physics of the process. At the end of each timestep calculated by the model, the runoff is in fact moved outside the study area, passing through the superficial outlet points recognized, where a discharge value is calculated. It is clear that in case of timesteps lasting a day, considering also the small dimensions of study area (0.6 km^2), the error introduced is low, while for hourly timesteps the procedure could introduce a significant error. An example could be an intense rainfall of few hours during which part of the water cannot infiltrate, followed by some hours of absence of precipitations during which, the previously rejected water, could enter into the soil after the partially redistribution of the water infiltrated before.

9.1 Parameterization of the model

Once understood how the model works and defined the base maps such as DEM, soil depth, land use, streams, and a map with the position of the sampling locations, that in this case corresponds to the area where the two mentioned continuous piezometer dataloggers were installed, it is necessary to define all the parameters requested by the model. An important variable is the land use, in fact a high number of parameters vary with it.

In this case a land use map with seven different classes was used. The classes are: 1) grasslands, woods, and shrubs; 2) vineyards and orchards; 3) urban; 4) prevalent rock; 5) valgelli; 6) rock outcrops; and 7) dry-stone walls. The parameters needed by the model that depend on the land use are: the saturated hydraulic conductivity (k_s), the porosity (n), the coefficient to define the infiltration

capacity respect to the hydraulic saturated conductivity (InCap), the crop coefficient (K_c) to reduce the reference evapotranspiration, the maximum canopy storage (C_{max}), and the partitioning factor (p) that divides the intercepted rainfall from throughfall.

On the other side, among the parameters that are constant for all the study area, there are: the coefficients of the SWRC model of the Farrel and Larson method (1972), and the input map of the meteorological parameters that are rainfalls and reference evapotranspiration (ET_0). Considering a unique SWRC for all the land uses is an approximation, but not so significant. In fact, for class 1 and 2 the soil is more or less the same, as it is possible to notice looking at the grain size curves reported in Annex III. Regarding classes 3 and 5, it is expected to find a soil similar to that of class 1 and 2 below the "urban" covering. Class 4 is made up of scattered rock outcrops and shallow soil. Where present, the soil is the same of the other classes, while in case of outcropping rock the soil depth is zero. In this case only the hydraulic conductivity of the bedrock surface (defined with a constant value) is of interest, because the bedrock is an infinite layer that only stores water. The same argument is clearly valid also for class 6. At the end, the only class for which an approximation is done is the dry-stone walls one.

Some initial conditions must be also defined: the initial water content conditions, the interception storage, the surface detention, and the initial bedrock storage. Depending on time and on different combination of rainfalls and evapotranspiration, these properties are evaluated and insert time after time.

The method of definition of these parameters is explained in the following part of this section, and at its end it is possible to find a short summary of the properties that vary with land use in Tab 9.1

The definition of certain parameters, such saturated hydraulic conductivity (k_s), porosity (n) and rainfalls, was easy. In fact, the values registered by instruments (rainfalls), derived from the laboratory analysis (n), or after the calibration of the models at the scale of the single terrace (k_s) were used. Regarding k_s, also in this case the two different values for a well-maintained and a bad-maintained wall were used and compared. Moreover, in this phase of the work, also urban areas were considered. Therefore, it was decided to put the k_s of these areas equal to that of soil, but considering a very low infiltration capacity, supposing that under the impermeable covering given by asphalt and cement the soil is the same. The same reasoning was done for the prevalent rock areas, therefore if some soil is present it has the same characteristics of that of other areas. Regarding walls, their infiltration capacity was lowered respect to that of soil, but less than that of urban areas.

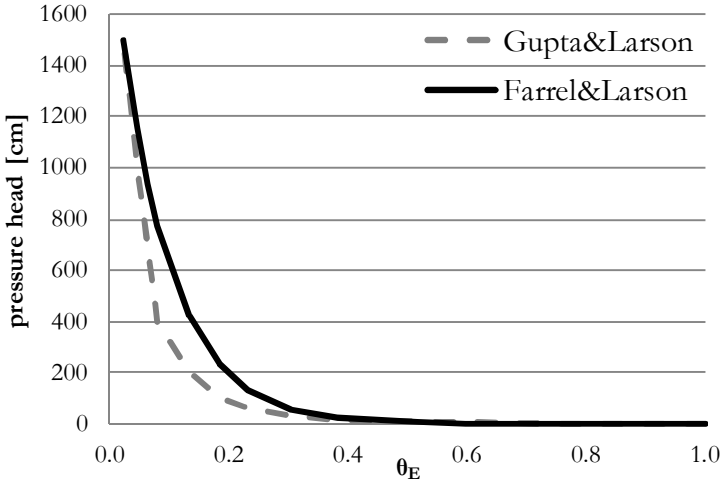

Figure 9.1: the comparison of the two SWRCs obtained with the method of Gupta & Larson and Farrel & Larson. The first was used in the modelling at the single terraced scale, while the second at the study area scale. θ_E is the relative degree of saturation

For other parameters their definition was relatively simple. For example, the SWRC had been already calculated with the Gupta and Larson method (1979) using the results of the grains size analysis, so the coefficients of the Farrel and Larson model were derived for comparison between the two curves (Fig 9.1), trying to obtain the best fit.

At last, parameters and variables such as evapotranspiration, the crop coefficient for the different land uses present on the study area, the maximum canopy storage, and the partitioning factor were particularly difficult to determine.

Probably, evapotranspiration is the most used of the above mentioned parameters and variables. Evapotranspiration must be distinguished in potential, reference evapotranspiration (ET_0), and crop evapotranspiration under standard conditions (ET_c). The latter depends on ET_0, that can be calculated from meteorological and climatic data relative to a precise measure station, and on the crop coefficient (K_c) typical for each crop and growth stage. Clearly, a limit to ET_c is represented by the available water storage.

The guide lines for the calculation of both reference and crop evapotranspiration can be found on the FAO Irrigation and Drainage Paper No. 56 (Allen et al., 1996), that not only reports the suggested methods but also furnishes some tables with the values of K_c that could be adopted for defined crops and growth stages. In particular, the Penman-Monteith method is the recommended one to calculate ET_0.

$$ET_0 = \frac{0.408 \cdot \Delta \cdot (R_n - G) + \gamma \frac{900}{T + 273} \cdot u_2 \cdot (e_s - e_a)}{\Delta + \gamma \cdot (1 + 0.34 \cdot u_2)} \text{ [mm/day]} \qquad \text{(eq. 9.1)}$$

Equation 9.1 is written for the reference crop, that is a hypothetical grass with specific height, surface resistance, and albedo. In the equation Δ represents the slope vapour pressure deficit in kPa/°C; R_n is the net radiation at the crop surface in MJ/(m^2 day); G is the soil heat flux in MJ/(m^2 day); γ is the psychometric constant in kPa/°C; T is the mean daily temperature at 2 m height in °C; u_2 is the wind speed at 2 m height in m/s; e_s is the saturation vapour pressure in kPa; and e_a is the actual vapour pressure in kPa.

Some of this parameters can be directly measured, while other can be calculated with suggested equations from others data. In particular, altitude above sea level and latitude must be known to adjust some parameters and to calculate some variables such as the value of the atmospheric pressure, the numbers of daylight hours, and the extraterrestrial radiation at the location of interest. Besides these geographical data, meteorological parameters as air temperature, humidity, radiation and wind speed are required to arrive at the definition of ET_0 through the equation 9.1.

In correspondence of weather stations where data about relative humidity, wind speed and solar radiation are not present, it is possible to use the Hargreaves equation (Eq 9.2), which is simpler than the Penman-Monteith, depending only on air temperature and extraterrestrial radiation (R_a – [MJ/(m^{2}day)]), that can be computed from latitude and altitude data. Temperature needed are the daily maximum (T_{max}), minimum (T_{min}), and mean (T_{mean}) expressed in °C.

$$ET_0 = 0.0023 \cdot (T_{mean} + 17.8) \cdot (T_{\max} - T_{\min})^{0.5} \cdot R_a \text{ [mm/day]} \qquad \text{(eq. 9.2)}$$

In order to use this method it is only requested a verification of the equation 9.2 at a weather station relative close to the location of interest, where the data needed for the application of the Penman-Monteith equation are present. The verification of the Hargreaves equation can be done comparing

the two results in graphical way and if there is a difference between the two, it is possible to adjust the Hargreaves equation using coefficients.

At the Teglio-Somasassa weather station (Fig 3.2), besides the hourly rainfall amount, the only available data are minimum, maximum, and mean temperature on an hourly base. Therefore, it was decided to use the Hargreaves equation to calculate ET_0. Clearly, the equation had been previously verified performing the estimate of the reference evapotranspiration with both the method at the weather station of ARPA Lombardia (Regional Agency for Environmental Protection) located in Sondrio, about 15 km far from study area. The comparison is showed in Fig 9.2. The result of the Hargreaves formula ($ET_{0\,Har}$) was later adjusted according to the relation:

$$ET_0 = ET_{0Har}/3.2 \text{ [mm/day]} \qquad \text{(eq. 9.3)}$$

Once calculated the ET_0, it need to be scaled to the crops present on study area in order to determine ET_C, that is the real rate of evapotranspiration that can occur from soil depending on the plants that characterized it. It is in fact intuitive that the capacity of a plant to suck and transpire water can be different depending on the dimensions of its roots, as well as on its height and leaves area. All the differences that distinguish each crop from the reference one are therefore taken into account with the crop coefficient (K_C). As already cited, K_C depends not only on each specific crop but also on its growth stage. In particular 4 different stages and three typical values are recognized (Fig 9.3).

$$ET_C = K_C \cdot ET_0 \text{ [mm/day]} \qquad \text{(eq. 9.4)}$$

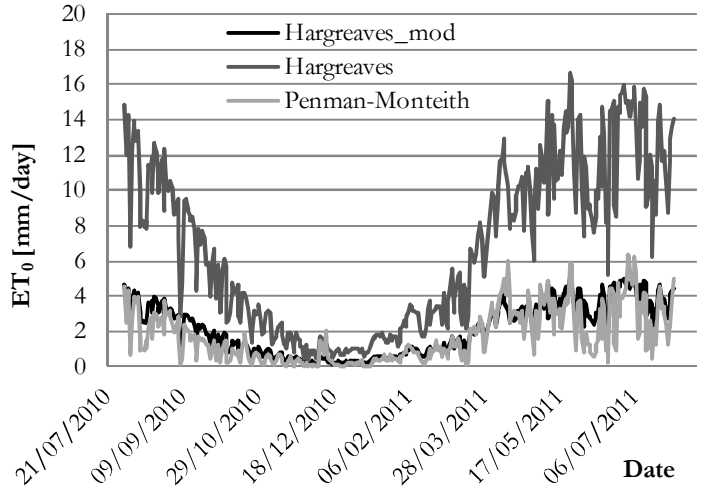

Figure 9.2: verification of the Hargreaves formula at the Sondrio weather station respect to the Penman-Monteith method. Input data consists of daily values for an entire year from August 1st, 2010 to July 31st, 2011.

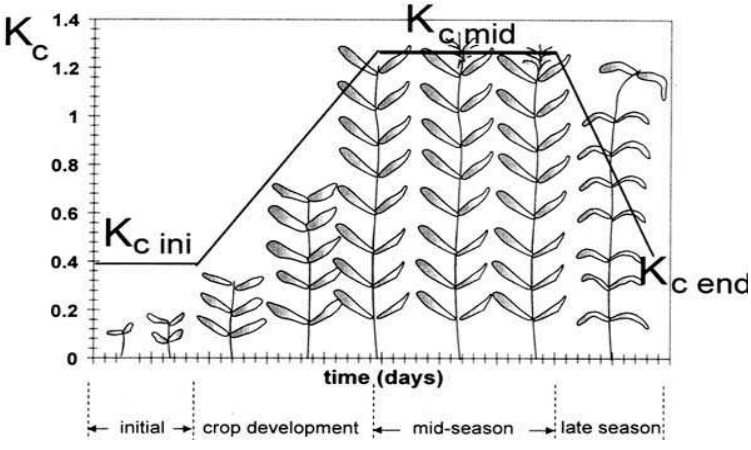

Figure 9.3: the four stages of growth considered in the definition of the crop coefficient and the corresponding three typical values that describes its variation in the course of one year. The values of K_C represented in this graph refer to a hypothetical crop (from Allen et al., 1996)

Natural vegetation is not present on four of these seven classes (classes 3 - 5 - 6 - 7), so a null K_C was assigned to them. The absence of vegetation means that transpiration is absent but that simple evaporation could occur. Nevertheless, not knowing how to scale the calculated reference evapotranspiration to such a case, it was decided to not compute it. Although this decision leads to a not complete and precise reproduction of the hydrological processes that interested the area, it can be defended considering that the rate of evapotranspiration in the area is very low. Moreover, the final aim is to identify areas prone to the initiation of superficial landslides and in this sense the omission of evapotranspiration is safety oriented. The values of $K_{C\ ini}$, $K_{C\ mid}$ and $K_{C\ end}$ for the other three classes are reported in Tab 9.1. The definition of these values was relatively easy only for vineyards and orchards. Besides wine grapes, the only other fruits cultivated on study area are apples. Some apple orchards are present in the area around the village of Somasassa, but their extension is negligible respect to the vineyards and they are also too small to justify the creation of a specific, stand-alone land use class. For this reason, it was decided to assign the K_C values suggested by Allen et al. (1996) for wine grapes to the land use class 2. The same authors suggested also a mean duration of 30, 60, 40 and 80 days for the initial, development, mid and late stages of growth respectively, with the plant date set in April. Considering that Valtellina is an alpine valley that differs from typical areas of vineyards cultivation, the plant date can be shift to middle-end April and probably the late stage shortened of more or less ten days.

The prevalent rock land use class is characterized by the presence of frequent, small outcrops that was impossible to map. Around these outcrops it is possible to find above all grass of various types and heights. It was therefore decided to attribute to this class a constant K_C value representing the mean grass covering, preferring an underestimation of it rather than a too high value.

The class for which it was more difficult to define the three different values of K_C for the different growth stages was the grasslands, wood, and shrubs class. The FAO Paper no 56 (Allen et al., 1996) considers only crops for agricultural purposes, so plants such chestnuts and false acacias that are widespread in this land use class are not taken into account, as well as any kind of shrub. The only plants considered are conifer trees for which a constant K_C of 1 is indicated, underlining that this value is valid for large forests and well watered conditions and so it can be easily reduced. Starting from this value and from the consideration that for crops with large leaf area values greater than one can be reached in their mid stage, it can be assumed that for chestnuts and false acacias such values are possible too. Nevertheless, considering that different species are present in the land use class 1, it was decided to adopt a conservative maximum $K_{C\ mid}$ of 1. This value represents a sort of minimum among the maximum, corresponding to the $K_{C\ mid}$ of grass, considering those of wood and shrubs higher than it. The other two values were assumed on the same base, thus assigning in this case to $K_{C\ ini}$ and $K_{C\ end}$ the values relative to wood and shrubs and therefore lower than one. In particular, looking at $K_{C\ ini\text{-}end}$ of tall deciduous fruit trees and bushes reported in Allen et al. (1996), it was possible to define a sort of mid $K_{C\ ini}$ value of 0.40 and a $K_{C\ end}$ equal to 0.60.

Another question was related to the definition of the duration of the different stages of growth. As the K_C of the class 1 varies considering the growth along a year of wood and bushes more than grass, the duration of the different phases must have to be referred to them. A little help was furnished by the scheme in Fig 9.4. Even if it is very general, it suggested relatively short initial, development, and end stages of growth for perennial deciduous trees and shrubs if compared to those of annual crops.

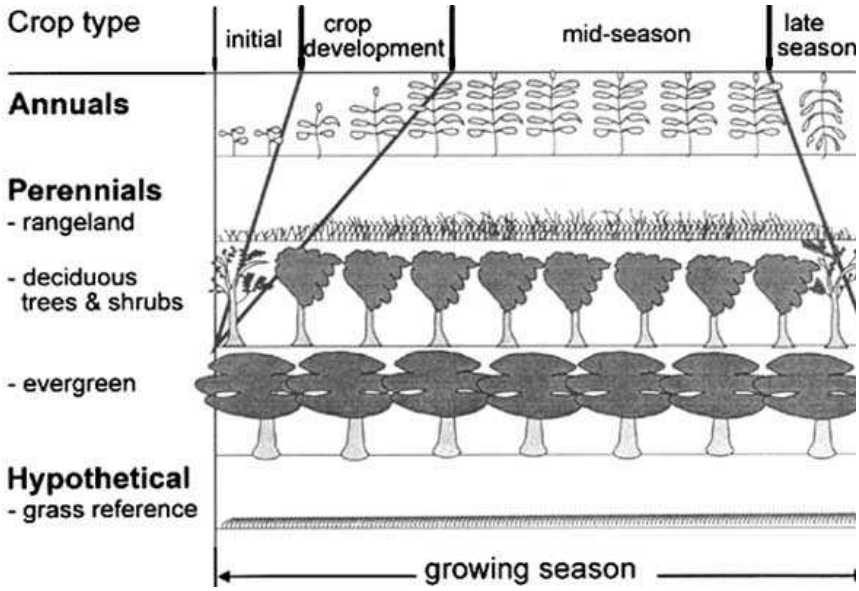

Figure 9.4: relative temporal length of the different growth stages for different types of crop.

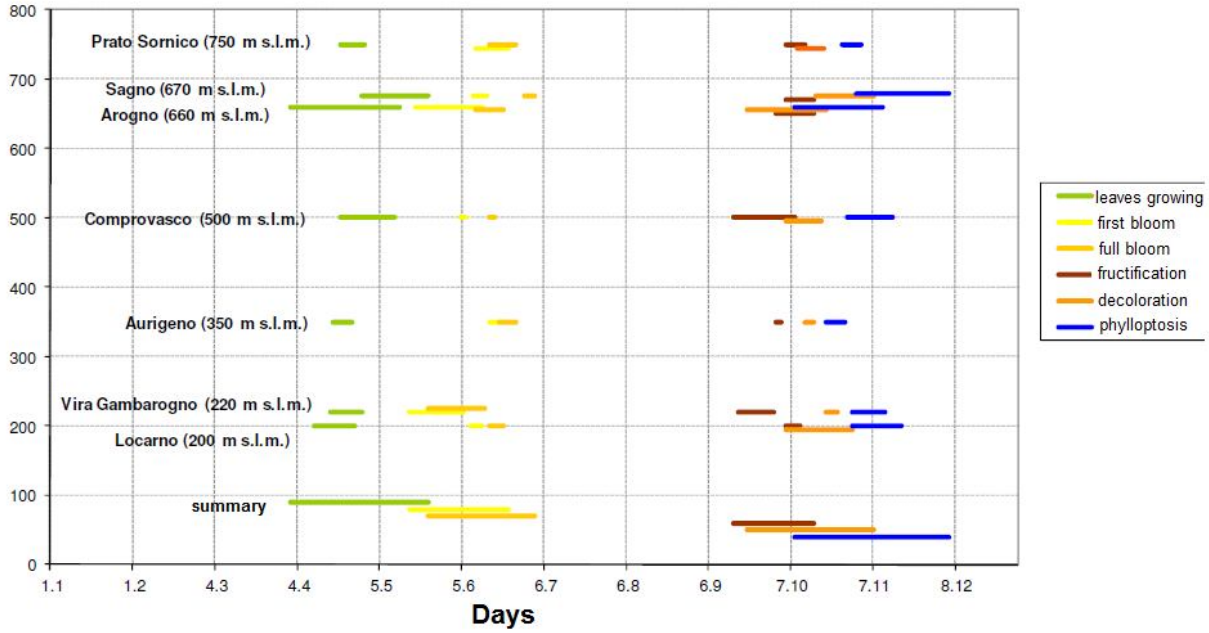

Figure 9.5: growth stages for chestnut in Ticino (Switzerland). Observations concerning the period 1996-1998 (image by Marco Conedera, Rete Fenologica Svizzera, personal communication).

A more specific help, at least regarding chestnuts, arrives from the graph of Fig 9.5, furnished by Dr. Marco Conedera of the Swiss Federal Institute for Forest, Snow and Landscape Research (WSL). The graph concerns the chestnut growth stages in Ticino (Switzerland) that is a Region relatively close to study area and comparable with it. From the graph it is possible to see how the initial stage starts at the beginning of April and last more or less two weeks, comparing it to the leaves growing stage. These two weeks are also in agreement with Fig. 9.4, where a short initiation phase is expected for perennial deciduous trees. Also the development stage, that can be compared to the period between the leaves growing and the initiation of the flowering time, is relatively short as expected and it arrives more or less to the middle of May. The mid-season lasts till the middle-end of September when fructification is almost finished, while the end stage arrives till the end of November. In the successive phase, during which the model is used, the value of K_C reported in Tab 9.1 are assigned respect the graph of Fig 9.4 and 9.5 depending on the period of the year modelled.

Once defined the parameters related to evapotranspiration, interception is the other hydrological process taken into account by STARWARS that need to be defined. At the end, after also an informal talk with Dr. Arianna Facchi, researcher of the Agricultural Hydrology Department of the University of Milan, it was decided to not consider interception in the modelling phase, as the effort to determine it would be disproportionately high respect to real effect that it has on the quantity of water that can or cannot arrive at the ground surface in an area such as that in study. In addition, not considering it is a conservative, safety oriented choice.

Table 9.1: the values of all the parameters needed by STARWARS that do not change with time.

	$K_{C\ ini}$	$K_{C\ mid}$	$K_{C\ end}$	k_s	n	InCap	C_{max}	p
Grassland, wood and shrubs	0.40	1.00	0.60	10^{-5} m/s	0.50	4	0	1
Vineyards and orchards	0.30	0.70	0.45	10^{-5} m/s	0.50	4	0	1
Urban	0	0	0	10^{-5} m/s	0.25	0.1	0	1
Prevalent rock	0.40	0.40	0.40	10^{-5} m/s	0.45	4	0	1
Valgelli	0	0	0	10^{-5} m/s	0.25	0.1	0	1
Rock outcrops	0	0	0	10^{-8}m/s	0.07	4	0	1
Dry-stone walls	0	0	0	5×10^{-4} 10^{-6} m/s	0.25	0.1	0	1

9.2 Modelling application

The model was used with different temporal scales, analyzing the results for both daily and hourly input meteorological data. At first the attention was turned to the reproduction of the hydrological-hydrogeological processes using daily timesteps. In particular, it was decided to model the entire month of September 2010. This choice was done for two different reasons, on one side during the last 15 days of August 2010 only 0.6 mm of rain fall on study area and so it made possible to consider a dry initial condition. On the other hand, rainfalls along the month were widespread and various both in terms of duration and intensity and they were able to form three different water table events on 13th, 18th and 25th September (Fig 9.6).

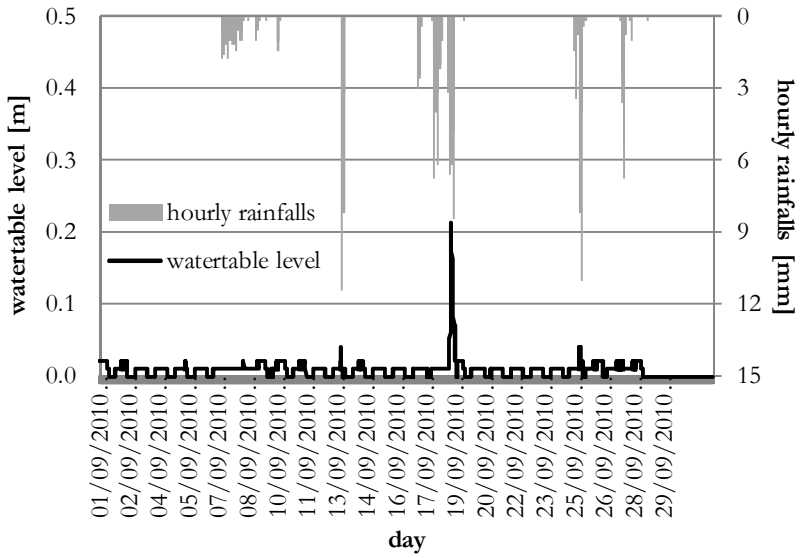

Figure 9.6: rainfalls and correspondent water table levels during September 2010. Water table levels refers to the piezometer installed on site A.

The first simulation was performed considering a three layers model. The three layers are made up of the same material and their function is only numerical. They are calculated as fraction of the entire soil depth: 0.3 the first layer, 0.4 the second, and 0.3 the third. In case of high soil depths, they permit to modify the hydrogeological characteristics of the investigated soil with depth, but this is not the case of this study, where soil properties are maintained constant along the whole vertical

profile. More in general, they allow to observe the progress of the infiltration and the vertical percolation of water into the ground, looking in particular at the evolution of the volumetric water content of the different layers. Although it is quite interesting, let the three layers active implies a further complexity into the model that results in an additional computational time and in a more complicated interpretation of the results. However, the use of the three layers model allowed to verify the importance of a parameter not yet cited in the previous description of the model, that is the minimum value of the vertical percolation ($Perc_{min}$).

Vertical percolation is the velocity with which the water can cross the unsaturated zone and reach an impermeable layer or a saturated horizon. In theory, it depends on the hydraulic conductivity but also on the gradient. With the three layers model, every horizon has its unsaturated depth with a specific Volumetric Water Content (VWC) and its percolation value. The percolation is calculated on the base of the VWC of the layer, that is related to the hydraulic conductivity through the SWRC, and the possible arrive of some water contributions from the overlying horizons, that can modify the VWC itself. Within the single timestep and the single layer, the percolation value used for defining and calculate the quantity of water that can cross the unsaturated zone is:

$$Perc = \sqrt{Perc_{ini} \cdot Perc_{end}} \qquad \text{(eq.9.5)}$$

where $Perc_{ini}$ is the percolation at the beginning of the timestep, calculated respect to the initial condition of the VWC of the examined layer, while $Perc_{end}$ is the value of percolation calculated after the arrive of a new water contribution. If Perc results equal to zero because the initial condition is completely dry, the model assigns to percolation a previous define value: $Perc_{min}$. Low values of $Perc_{min}$ cause a very slow redistribution of water. This is particularly evident using the three layers model, with a pretty high infiltration rate. Water can infiltrate but only few of it can cross all the first layer, so few water reaches the contact with the second layer, and still less water moves from the second to the third layer. Therefore, the evolution of the VWC of the first layer reflects on the second and that of the second layer on the third. From the top to the bottom of the soil horizon, a decreasing profile of the percolation value can be observed. This situation can degenerate taking to the formation of unreal saturated horizon at the layer interfaces within the same material (Fig 9.7). At the end, to avoid such problems, it was decided to reduce the model to a single layer. In addition, besides the problems that can cause, $Perc_{min}$ showed an important influence on the sensitivity of the model, therefore it was decided to adjust it for calibration. As already written, on a daily timestep scale the calibration of the model was done respect to the field data of September 2010, while the hourly analysis was performed using the rainfall data of the same two events used for the calibration and validation of the single terrace scale model.

Performing the analysis with only one layer, greater attention was given to the observation of different behaviours due to the different maintenance conditions of walls, as done for the single terrace scale analysis. Besides the observation points in correspondence of the two piezometers of site A and site C (cfr. Fig 3.2), other 6 and 7 points were chosen along two terraces, to monitor the evolution of the water table levels along the development of single terraces. These two chosen terraces differ one to the other for the fact that one of them is characterized by the presence of a bedrock outcrop immediately uphill of it (sampling terrace 2), while the other have another terrace uphill (sampling terrace 1). Sampling terrace 1 is the same where the site A piezometer is located. Other characteristics of terraces are similar, such as length, mean soil depth, and wall height. The position of the chosen terraces on the slope is presented in Fig 9.8.

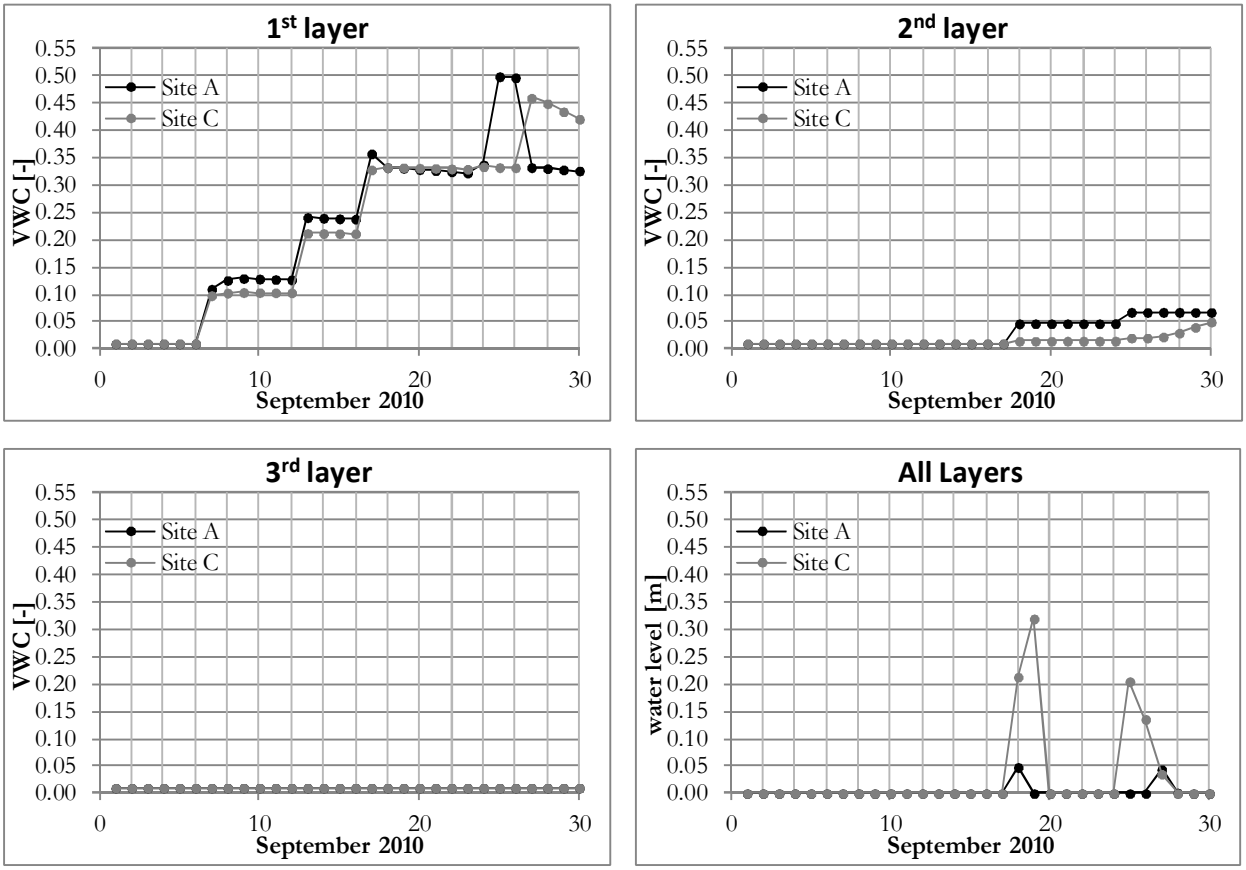

Figure 9.7: the VWC of the three layers and the corresponding water table levels of the entire soil profile for the extreme case of null $Perc_{min}$. In this case the third layer is always completely dry but a saturated horizon appears two times along the month in both the sites. See Fig 3.2 for the position of site A and site C piezometers.

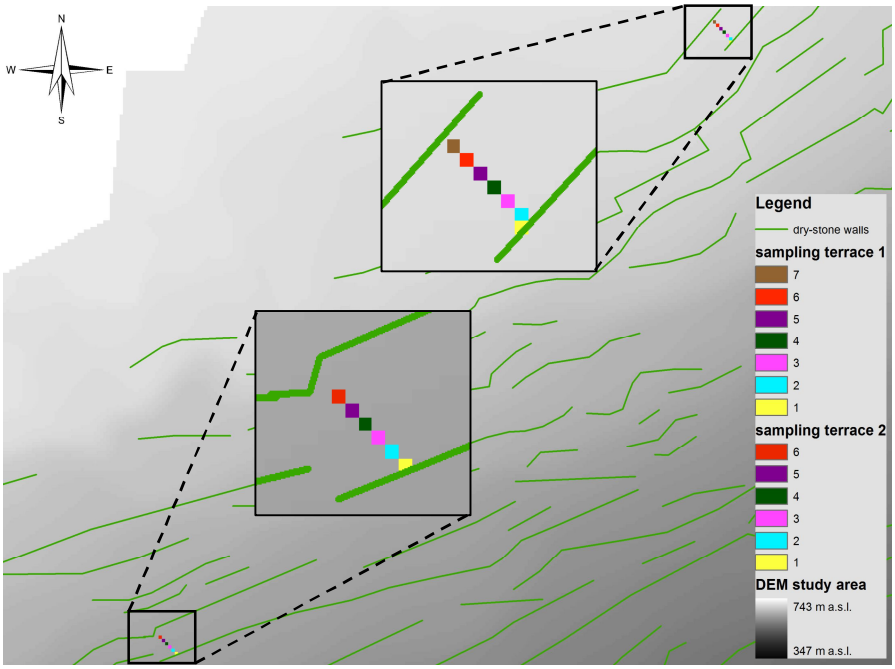

Figure 9.8: The position on the slope of the sampling terraces. Sampling terrace 1 is on the upper right corner, while sampling terrace 2 on the lower left corner. Both of them lies in the middle-high part of study area. The two yellow cells (1) correspond to walls and the cells from to 2 to 7 are the ones located in succession in the uphill direction. Cell 6 of sampling terrace 1 correspond to the position of site A piezometer.

9.2.1 Daily timestep modelling results

For the daily timestep, a good agreement between the registered field data and the model outputs was found with the $Perc_{min}$ parameter value equal to k_s. This is a reasonable value representing a vertical gradient equal to unity for the most unfavourable condition for infiltration. Besides the measured and calculated water levels calculated the simulated VWC is also shown. Except for the case in which the cell is completely saturated, VWC refers only to the unsaturated depth of each cell. VWC immediately responds to the rainfall input, while the water table level reaches its peak in the successive timesteps (Fig 9.9). This shift is due to the resolution of the time scale used for the simulation. In addition, the water table registered at site A always vanishes in a single step, while the water table of site C is often evident for several steps. This is due to the different soil depth of the two cells, in fact the cell corresponding to the piezometer of site A has a soil depth of 0.6 m, while in correspondence of site C piezometer the soil depth map is equal to 2 m. The k_s value of soil is around 0.8 m/day, and so all the infiltrated water is not able to reach the bedrock contact in a single time step. Regarding the water table levels of site A, comparing the calculated and the registered values it is possible to notice that the model is able to well reproduce the peaks in terms of time. The small peaks of 8th, 13th and 25th September are reproduced quite well also in terms of height, but a different level is calculated for the highest peak of September 18th. The difference is not very high and it is about 0.08 - 0.10 m. It could be due to a not precise value of soil depth or to a local k_s a little different from the one used, however the error is acceptable and the model works quite well at this time scale. On the contrary, on site C, water table values very different from the registered ones are calculated. A maximum level of about 0.5 m is calculated for the piezometer of site C, where no water response is registered on site during the whole month. This fact can be simply explained looking at Fig 9.10, where the water levels corresponding to the 19th September are put in relation with the land use map. In particular, it is possible to see evidences of perched water tables along the roads and near rock outcrops. Roads are within the urban land use class and therefore infiltration is almost impeded, and the same happens for outcrops whose k_s is much lower than that of soil. Therefore, on roads and bedrock outcrops, water cannot infiltrate and so it moves and infiltrates in the first not impermeable cell downhill. The cell corresponding to the position of the site C piezometer is one of these cells, in fact it is immediately downhill of a road. Actually, there is not this further water supply, because the site of the piezometer is divided from the road by a riddle that favours the flux of the water along the road itself, and this is probably the cause of the difference between the observed water level and the calculated one. Looking at Fig 9.10 also the principal drainage lines in correspondence of the little valleys present on the study area appear evident.

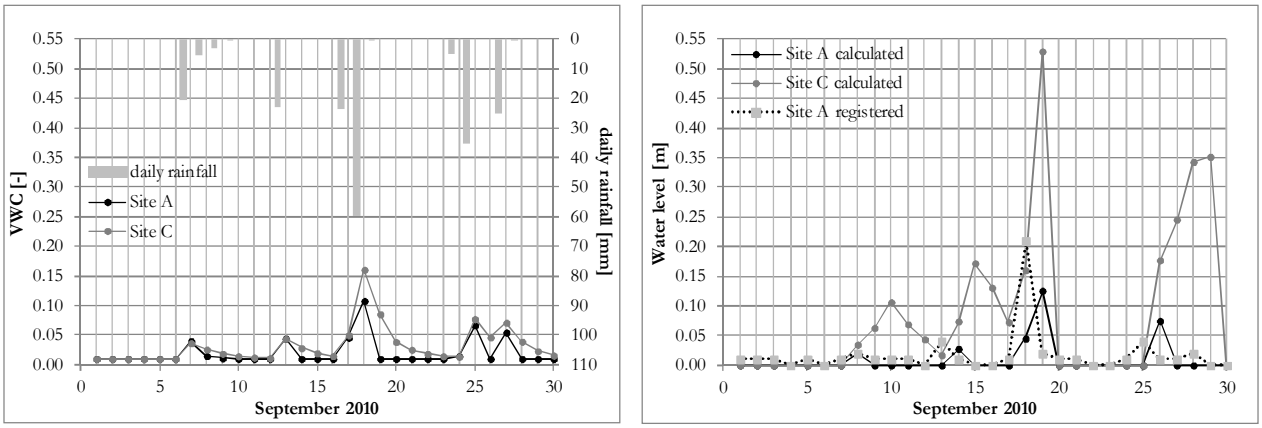

Figure 9.9: VWC and water table levels calculated at site A and site C during September 2010 using daily timesteps.

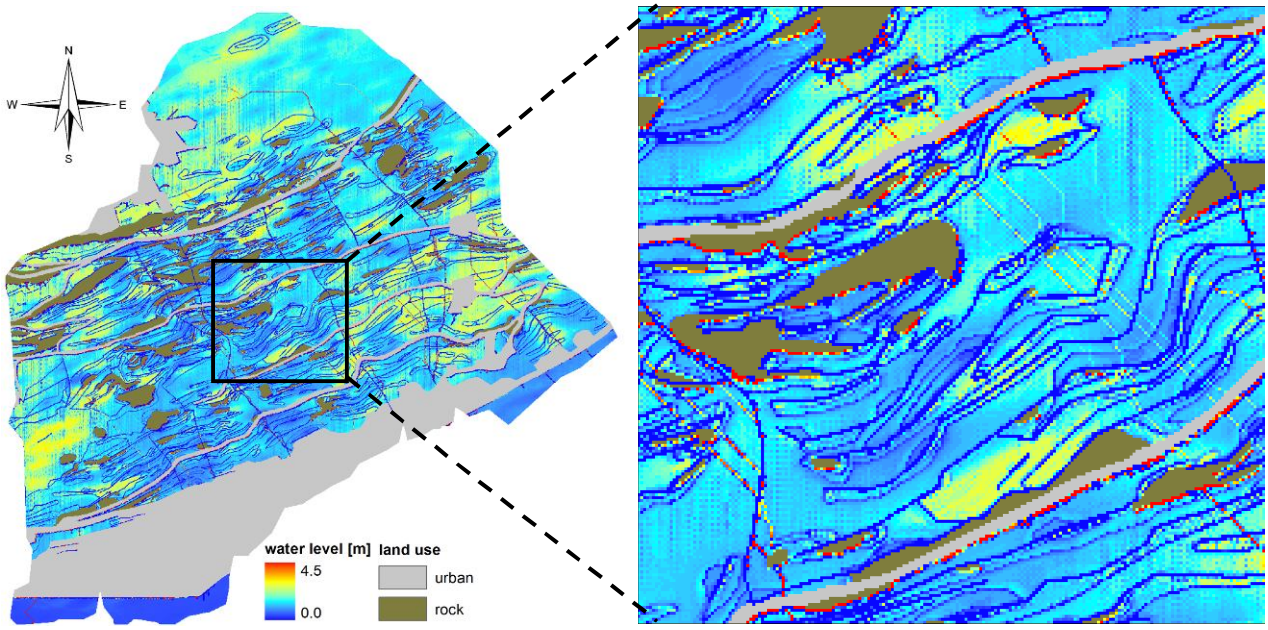

Figure 9.10: water levels calculated by the model for September 19th in relation with specific land use classes. On the left the entire study area is represented, while on the right there is a zoom of the area in the square.

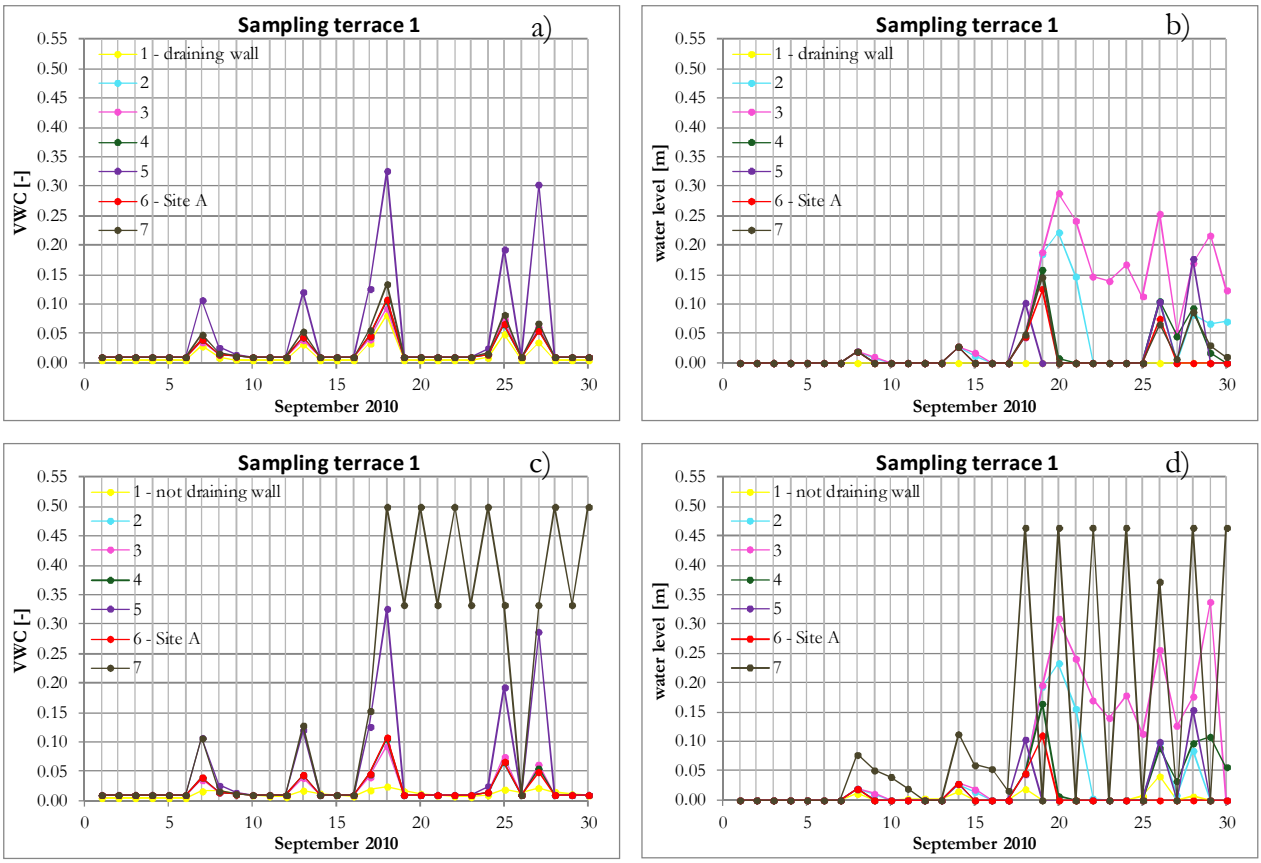

Figure 9.11: results related to sampling terrace 1. The legend is the same of Fig 9.8. On the left VWC, on the right water levels. The results obtained with a well maintained wall are on the upper line (a – b), while those with a bad maintained wall are on the lower line (c – d).

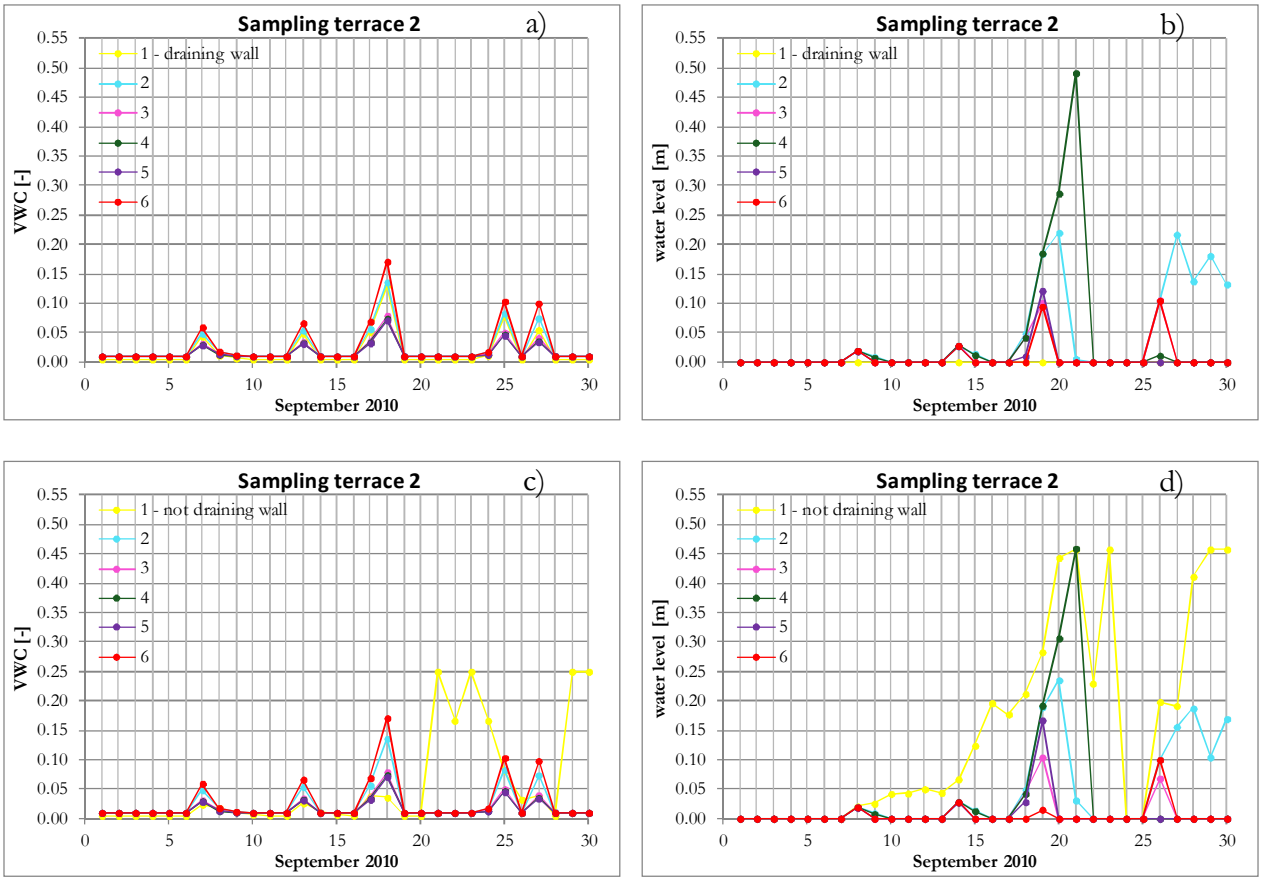

Figure 9.12: results related to sampling terrace 2. The legend is the same of Fig 9.8. On the left VWC, on the right water levels. The results obtained with a well maintained wall are on the upper line(a – b), while those with a bad maintained wall are on the lower line (c – d).

The differences in the infiltration and groundwater movement processes, due to the different state of maintenance of walls, can be better analyzed looking at the values of water level and VWC computed by the model along the two sampling terraces already shown in Fig 9.8. VWC and water levels of sampling terrace 1 are reported in Fig 9.11, those relative to sampling terrace 2 are in Fig 9.12.

With a good maintenance condition of walls, both the terraces show a similar trend for the VWC (Fig 9.11a – 9.12a). As already seen for the sample points in correspondence of the two piezometers of site A and site C, VWC reacts immediately to rainfall, as expected, and its variations are mainly due to the soil depth of each cell. In general, a high VWC corresponds to a low soil depth. In fact, on sampling terrace 1 the higher VWC is registered at cell 5, where the soil depth is only 0.3 m, while on sampling terrace 2 at cell 6, that has a soil depth of 0.4 m. Water levels (Fig 9.11b – 9.12b) are also coherent with those showed previously at site A and site C piezometers. Where the soil depth is higher, water takes more time to arrive at the contact between soil and bedrock and the groundwater table peak can be reached after more steps. In addition, it is possible to see how the wall is able to drain water and it never shows a saturated level in its cell. The only apparently anomalous behaviour is that of cell 3 on sampling terrace 1. On this cell a saturated horizon remains also between the 20th and the 25th September, when no rainfalls were registered, and so no recharge could arrive from the surface. The persistence of the groundwater table at this cell is probably due in part to a delay in the arriving of vertical percolation, since the cell has the higher soil depth of the entire terrace, and in part it is the result of a saturated lateral flux from another cell.

Changing the conditions of wall to bad maintained, all the cells, except those of walls and cell 7 on terrace 1, maintained the same evolution of VWC (Fig 9.11c – 9.12c). The VWC calculated on the wall cells with their bad maintained condition is always lower than that calculated with a well maintained condition, and a less rough general trend of this parameter can be observed. A lower infiltration capacity can in fact cause a lower effective infiltration in the cell, and a lower k_s can reduce the velocity of water redistribution both in vertical and lateral directions. The effect is that in the cell there is less water moving slower that can remain there for a longer time. This behaviour reflects not only on VWC but also on the evolution of the water table levels.

The trend of the VWC of cell 7 on sampling terrace 1 is related to the shallow soil thickness of the cell (0.45 m) and to the water filtration from the uphill cell that is a wall. The wall has a low hydraulic conductivity and so it slowly releases water in form of saturated flux to cell 7. Even if cell 7 has no water in its unsaturated level, its water table level lasts for several timesteps (two cases between the 5th and 15th September – Fig 9.11d) fed by the uphill cell. The following, up and down, trend of cell 7 for both VWC and water table levels depends on the reaching of saturation of the cell. In fact, if saturated, the cell cannot receive input of water, but can only lose it for saturated flux, loss to the underlying infinite layer, and evapotranspiration. The model does not allow internal loops and a recharge during the timestep, so in order to avoid a complete drying of the cell in the step following the saturation, the model imposes to the cell a VWC that corresponds to that at field capacity. The excess of water respect this VWC remains available for drainage. Therefore, water table can go to zero the step following saturation, but the VWC cannot be lower than the fixed limit. A similar situation can be observed not only for cell 7 on sampling terrace 1 but also for the wall cell 1 of sampling terrace 2 (Fig 9.12d). This wall shows also water levels higher than the wall of sampling terrace 1, that are probably related to higher contributions from surroundings cells.

Another data to be control regards the water budget check. At the end of the month, the total water input on the area is equal to 103'647 m^3, while total output is 65'629 m^3, with a total storage of 37'752 m^3. The difference between inputs and the sum of outputs and total storage is equal to +226 m^3 that considering the number of the single parameters permits to state that the mass balance is fairly respected.

9.2.2 Hourly timestep modelling results

Two different rainfall events were analyzed with hourly timestep. In particular it was chosen to reproduce the same events used for the calibration and the validation of the 2D model, that are those of 21-24 October 2009 and 17-24 February 2010. As for the daily timestep model, $Perc_{min}$ was set equal to k_s. In order to obtain the initial conditions for the hourly simulations, the previous days were modeled with daily timesteps. In particular, for the first event the days between the 1st September and the 20th October were reproduced, while for the second event it was decided to cycle the period from the 30th January to the 18th February. The 17th and the 18th February were included in the daily analysis because they registered only 1.8 and 5.2 mm of rain respectively, against the 34.2 mm of the 19th February, that it is the more interesting day and the only one during which water levels were also registered on site.

In the hourly modelling analysis, evapotranspiration is neglected. The scaling of the daily data is not precise, and considering the autumn-winter period, the usual low ET_0 values calculated in the study area as well as the fact that during a precipitation event evapotranspiration is almost null, it was considered that the error introduced was not relevant.

Also in this case, at the two sampling points that corresponds to site A and site C piezometers, there are no differences in the VWC and water level outputs calculated by the model for both a well maintained and a bad maintained wall. VWC responds immediately to the rainfall input, but the peak can be reached also in the timesteps after rainfall peak. In this case the peak of precipitation is enlightened by the highest increasing rate of the VWC curve (Fig 9.13a,c). Comparing the water levels registered at site A with those calculated at the same location, the model seems to underestimate the peaks registered on site. Regarding the event of October 2009 (Fig 9.13b), the model is able to reproduce neither the height nor the time of water table peak. Maybe the calculated peak could be assimilated to the second relative peak registered on site, but also in relation with this it has a delay of 3-4 hours, in addition to a height difference of about 0.2 m. The event of February 2010 is a little better reproduced by the model (Fig 9.13d). The time of the peak is well reproduced at 23.00 of 19th February and also the slope of the descendant limb of the hydrograph is comparable with that registered on site. The limit is clearly represented by the maximum level reached by the perched groundwater table that also in this case is about 0.2 m less than the site value.

At site C, no saturated water levels were registered for both the analyzed rainfall events. As for the daily timestep simulation, the Site C results are influenced by the position of the correspondent cell immediately downstream of an impermeable road. Therefore, the accumulation of water at the surface is higher than the effective quantity available on site for infiltration and this has clearly an influence on the water levels calculated. On the contrary, the fact that the peak arrives later, respect to both the registered and calculated levels at Site A (Fig 9.13b,d), is related to the high soil depth of the cell in the model, that it is around 2 m, while the piezometer on site A has a depth of 0.95 m and the site A cell in the model has a soil thickness of 0.6 m.

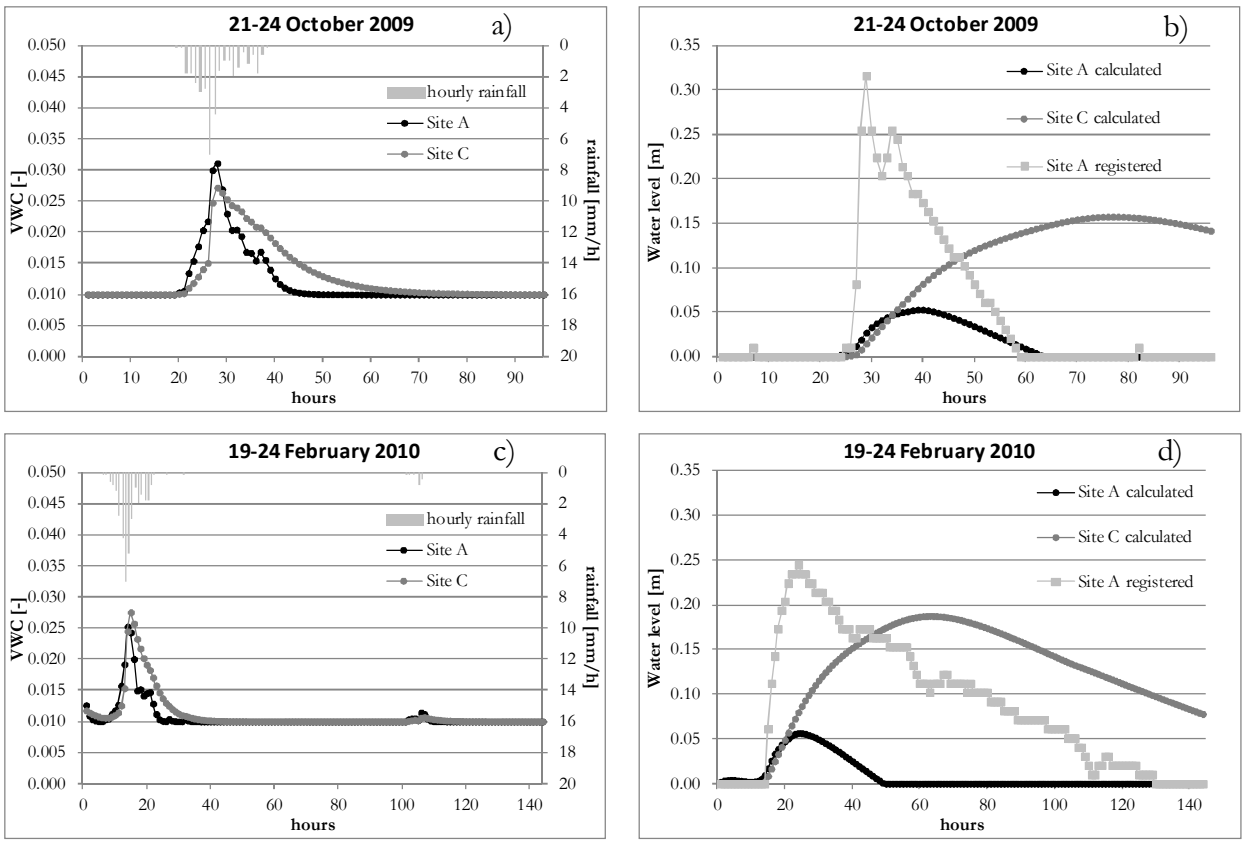

Figure 9.13: VWC and water levels calculated by the model at site A and site C piezometers compared with field registered data. At these sites there are no differences between the value calculated with a well maintained wall and a bad maintained one. Start time corresponds with 0.00 of 21st October and 19th February.

The analysis of the results along the two sampling terrace profiles do not add many information, but some data are interesting. Regarding terrace 1 (Fig 9.14 – 9.16) the only hydrograph that changes is that of cell 7, the cell immediately uphill of the cell that corresponds to the piezometer of site A and downstream of a dry-stone wall. On this cell, changing the condition of the walls from well maintained to bad maintained, the results of both the simulated events confirm the same behaviour and response of VWC and water table levels. In particular, during the bad maintained wall simulations, the water levels reached at this cell are very similar to those registered on site by the site A piezometer. The time of peak is well reproduced for the event of February 2010, while for the event of October 2009 the calculated maximum level corresponds, in terms of time, to the second relative peak. Moreover, for both the rainfall events simulated, also the heights are very similar to the measured ones. Excluding the first absolute peak of the October 2009 event, that the model is not able to reproduce, the values of the second relative peak of October 2009 and of the only peak of February 2010 are almost perfectly reproduced, with differences between the measured and the calculated in the order of only 2 cm. Probably, respect to the simulation done with the well maintained wall parameters, the additional quantity of water that arrives to cell 7 is due to the lowered infiltration capacity of the upstream wall and to a slower saturated flux that is able to add some water each step.

On sampling terrace 2 (Fig 9.15 – 9.17) the results obtained with the draining wall are instead almost equal to those obtained with a bad maintained wall and there is nothing particular to underline.

9.2.3 Summary of the results

At the hourly time scale, the model is able to reproduce the dynamics of the processes investigated with a sufficient detail and it is able to enlighten some criticisms related to local properties such as land use and soil depth. The different behaviour of a well maintained wall in respect to a bad maintained one is limited to the wall cell and sometimes to the immediate uphill or downhill cell. However, there are not evidences related to increasing VWC or water table levels along all the investigated terraces transversal profiles, as those shown in the 2D analysis performed at the single terrace scale. In addition, the model calculates very small, almost negligible water levels in correspondence of scarce rainfall events. This could be due to its numerical approximations, but if verified in further uses, the model could help in recognizing the formation of thin saturated horizon, sometimes hidden or semi hidden by the drift and the resolution of the instrument used on site. For example, the 7th September water level was disregarded in the previous rainfall events – groundwater table analysis (Chapter 4), because too close to the instrument resolution, but also the model enlightens it and so it could have been considered as a real saturated horizon and not as an error of the instrument..

At the hourly time scale, on all the analyzed cells, the first water level appears at the same time, even if with different values. Therefore, it seems that in a cell with a high percolation value the formation of the first saturated horizon is related mainly to the water that can infiltrate into the ground, and move from the top to the bottom of the cell itself. Lateral flux and soil depth seems to be secondary elements in this phase. On the contrary, the maintenance and the increasing of the water table level seem more related to the availability of a recharge during time, that can be the result of lateral or vertical fluxes, or a combination of the two. Also the drainage networks, both the superficial and the one at the soil-bedrock contact, have a great importance during this phase. The described condition of cell 7 on sampling terrace 1 is therefore ideal to develop an important water level, at least when its uphill wall is not able to rapidly infiltrate and drain water.

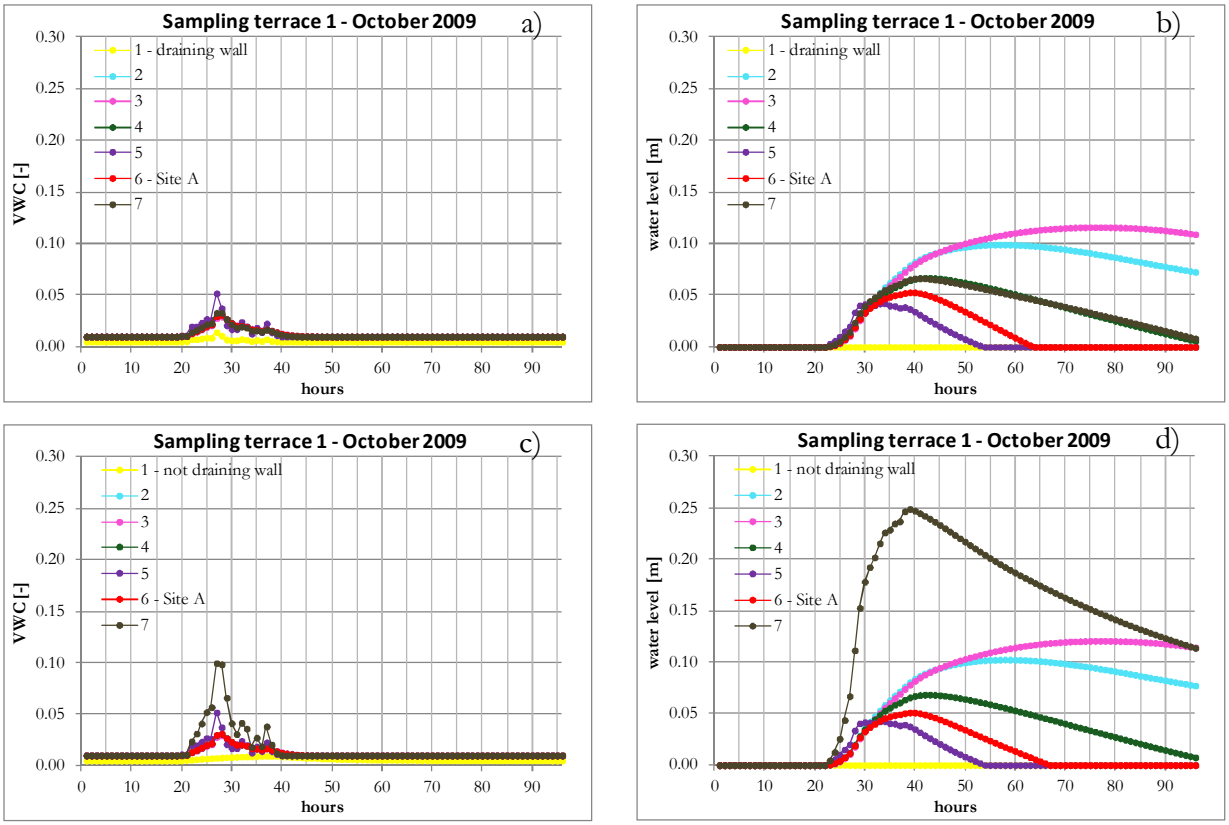

Figure 9.14: sampling terrace 1. Hourly simulation starting the 21st October 2009 at midnight. VWC on the left, water levels on the right. Draining wall on the upper line, bad maintained wall on the lower line.

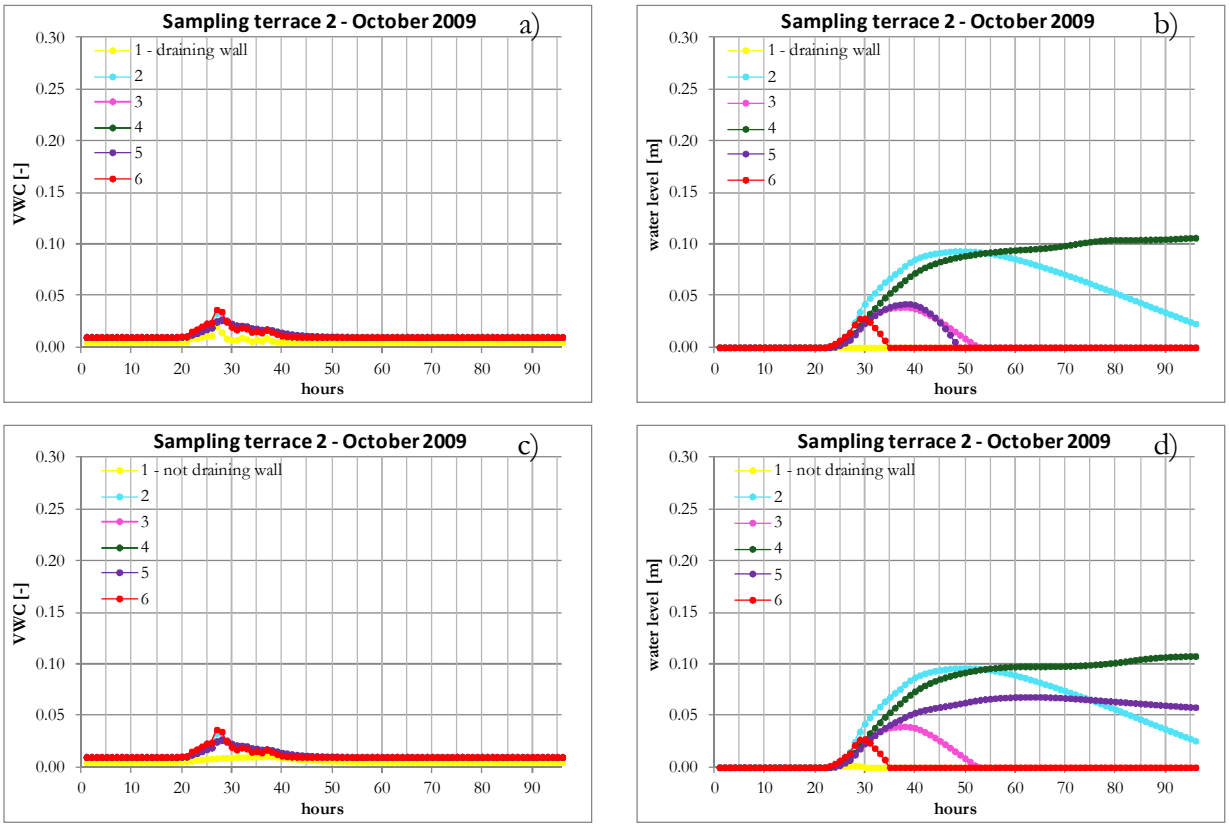

Figure 9.15: sampling terrace 2. Hourly simulation starting the 21st October 2009 at midnight. VWC on the left, water levels on the right. Draining wall on the upper line, bad maintained wall on the lower line.

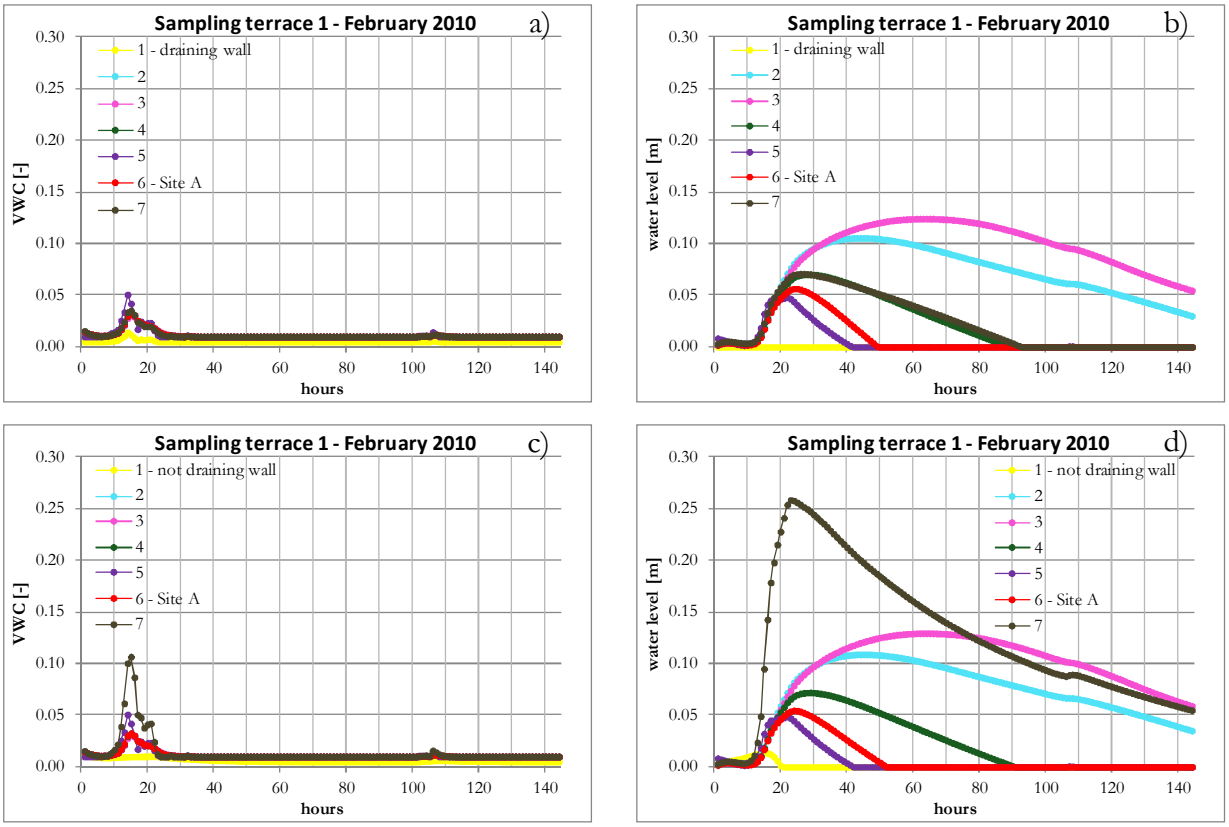

Figure 9.16: sampling terrace 2. Hourly simulation starting the 19th February 2010 at midnight. VWC on the left, water levels on the right. Draining wall on the upper line, bad maintained wall on the lower line.

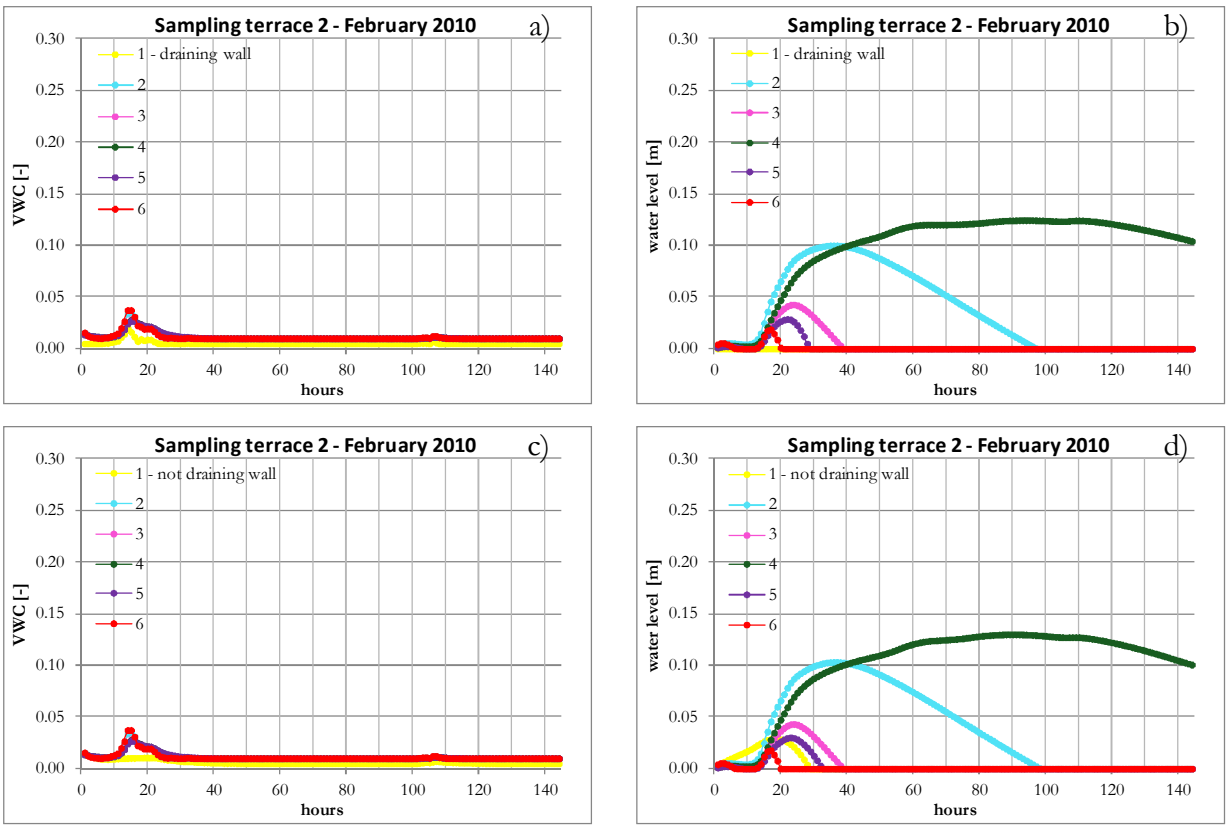

Figure 9.17: sampling terrace 2. Hourly simulation starting the 19th February 2010 at midnight. VWC on the left, water levels on the right. Draining wall on the upper line, bad maintained wall on the lower line.

Regarding walls, also with the hourly resolution time scale the model is able to well differentiate the behaviour of a well maintained wall and a bad maintained one only at the wall cell. At least with the two events analyzed, the model is not able to reproduce relevant changes in the VWC and water levels evolution of the cells behind the wall that lie on the same terrace. On the other hand, the lower infiltration capacity of the walls seems to have an effect on their downstream cell, that receives a greater amount of water and can developed higher water tables.

With the hourly timestep, STARWARS shows also a different behaviour from the 2D hydrogeological model. In fact, in that case, water levels form where the soil depth is low and then water redistributes along the contact between soil and bedrock for saturated flux, while with STARWARS, as just seen, saturation is independent from soil depth and it is driven by vertical unsaturated fluxes. The mechanism of formation of a water table seems therefore quite different, even if its maintenance has some common factors. In fact, also in the 2D analysis, the possibility to maintain a saturated horizon lies on the combination of vertical unsaturated and lateral saturated fluxes. Maybe, using the three layers model, also the difference in the water table formation could be reduced or better explained, but it goes beyond the aim of the use of this model, that is oriented to the definition of reliable water levels on all the study area for the following stability analysis. In this sense, even if with differences at the specific sampling sites between the calculated water levels and the registered ones, the model seems to work adequately.

These differences could in fact be due to multiple combinations of factors, from soil depth to the drainage lines and the assigned values of the different variables. Maybe, lowering the k_s and increasing the velocity of percolation it could be possible to get better results, in terms of water level, at the specific sampling points. Nevertheless, considering that with the defined setting the model works well at the daily time scale and that the time of the water level peaks are well reproduced also at the hourly time scale, changing the setting of only the hourly model could result in a loss of robustness of the model itself. At the known points the results might be better but there is not the guarantee that they would be as the same on all the study area.

Moreover, if the instrument will be used for civil protection or general urban planning purposes, it is important that it will be able to reproduce the most critical conditions and not the details of the interested process hour by hour. In this sense, a daily or half day resolution would be sufficient, and the model demonstrated to work well with this time scale.

10 Chapter 10

STABILITY ANALYSIS

The model developed by van Beek (2002) for the coupling with STARWARS is PROBSTAB. As already concisely mentioned in the introduction to this third part of the work, PROBSTAB is a stability model based on the infinite slope analysis. It incorporates a probabilistic approach to overcome the problem of a deterministic calculation of the factory of safety, considering also possible variations of acting and resistance forces, due to the uncertainty related to involved natural parameters.

However, PROBSTAB cannot be used on Tresenda study area. The presence of the terraces and the use of an high resolution DEM (1 m x 1 m) as topographical base cause the fall of the assumption of the infinite slope model, that requires a length of the slope much greater than the depth of soil potentially interested by the mass movement.

Various hypotheses were analyzed. A 3D analysis would have probably been the best solution but considering its complexity it was retained premature. In order to experience a not conventional methodological approach and to obtain preliminary results on the whole studied slope as well as a first overview on the possible causes and on the processes that could lead to instability it was decided to implement in PcRaster a simpler limit equilibrium analysis using the equations of a standard 2D problem for identified circular or not circular failure surfaces solved with the method of slices. In this contest, each cell was assimilated to a single slice. N-S lines representing the 2D sections to analyze were recognized. To better clarify the idea of line of section it is possible to look at Fig 10.1. At first, walls had been identified and then, from a cell characterized from the presence of a wall, a line of section was drawn till the reaching of the base of another wall. In this way, in the Y direction, 17635 lines of section were recognized. The stability of every one of these 17635 sections was later investigated through the application of a limit equilibrium analysis.

The choice of N-S sections is bonded to the structure of the software and to the available data. Maybe, it would have been more convenient to analyze sections parallel to the mean direction of maximum slope, perpendicular to the walls alignment. Anyway, to do this in a Raster environment it would have been necessary to rotate the grid of calculus. In a GIS environment, the rotation of the grid implies the re-calculation of the values of each cell for every map, even elevation and soil depth map, through particular interpolation techniques. In this case, the initial data would have become interpolated data, thus containing further possible errors. Moreover, also the hydrological-hydrogeological model should have been solved respect to that grid, since it furnishes some input to the stability model. In conclusion, this solution would have been better than the adopted one, if maps with a rotated grid had been used just from the first phases of the current areal study.

The classical geometry and the variables involved in a general limit equilibrium analysis, solved with the methods of slices, are summarized in Fig 10.2 Applying such a method, considering **n** slices the number of unknown quantities in the solving equation is 6**n**-2 (Tab 10.1), that can simply become 5**n**-2 assuming that the normal force at the base of each slice is applied at its center. On the contrary, the number of equation available to solve the problem is 4 (Tab 10.2), therefore the problem is undetermined.

In order to overcome the problem of the undetermined solution, many authors (Fellenius, 1936; Janbu, 1954; Bishop, 1955; Janbu, 1957; Morgestern and Price, 1965; Spencer, 1967; Sarma, 1973)

have proposed different methods, that differ one from the others for the assumptions made regarding the directions, magnitude, and point of application of some of the forces and for the use of forces or moments in the definition of the static equilibrium. Besides the point of application of the normal force at the base of the slice in its centerline, other common assumptions regards the magnitude, direction and point of application of the interslice forces. Another general assumption that needs to be underlined, because it could have some influence on the current analysis results, is that in all these methods the slices are considered infinitely wide in the direction transversal to the failure surface, without lateral boundaries and so without lateral forces.

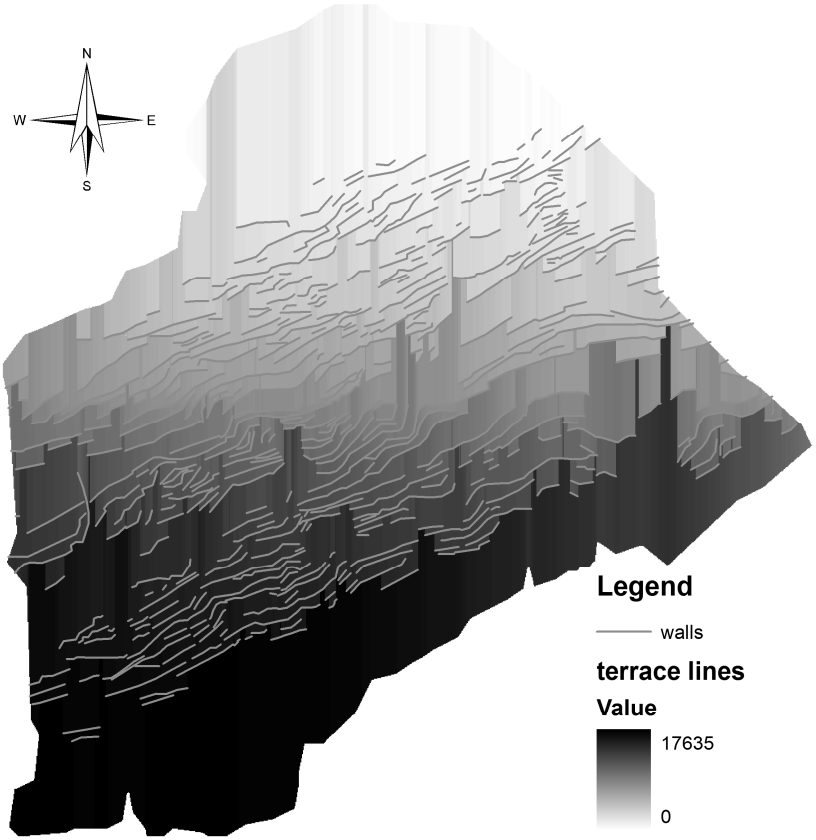

Figure 10.1: a map representing the 17635 lines of section recognized on study area.

Table 10.1: the unknown quantities in a general limit equilibrium analysis solved with the methods of slices.

n	Normal forces at the base of the slice N
n	Shear forces on the base of the slice T
n-1	Inter-slice normal forces E
n	Distance between the point of application of the forces N and the center of mass
n-1	Distance between the point of application of the forces E and the center of mass
n-1	Shear forces at the interface between slices X
1	Factor of Safety value
6n-2	Total number of unknown quantities

Table 10.2: the equations available for the solution of the stability problem in a general limit equilibrium analysis with the methods of slices.

n	Summation of horizontal forces
n	Summation of vertical forces
n	Summation of moments
n	Failure criterion
4n	Total number of available equations

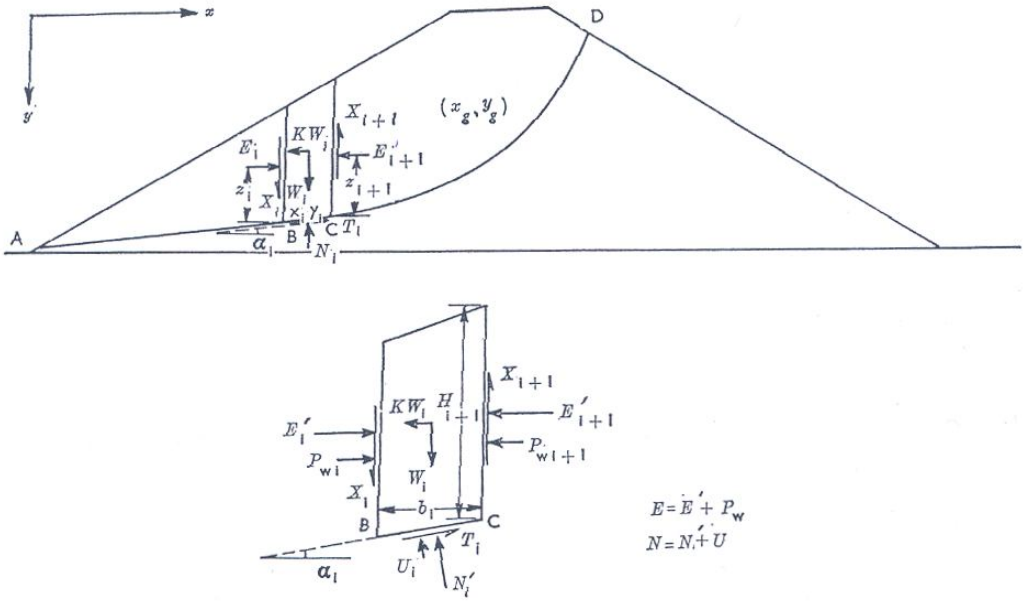

E'_i and E'_{i+1} = lateral thrust on vertical side of sections i and $i+1$ respectively in terms of effective stresses

X_i and X_{i+1} = shear forces on vertical side of sections i and $i+1$ respectively

P_{wi} and P_{wi+1} = resultant water pressure acting on vertical side of sections i and $i+1$ respectively

W_i = weight of ith slice

KW_i = horizontal force on ith slice acting at centre of gravity of slice

N'_i = normal force at base of slice in terms of effective stresses

U_i = force due to pore pressure at base of slice

T_i = shear force at base of slice

z_i = height of point of application of E_i above slip line

c'_i and ϕ'_i = effective shear strength parameters of material at base of slice.

$N_i = N'_i + U_i$

$E_i = E'_i + P_{wi}$

H_i = height of sliding mass at section i

K_c = critical horizontal accelerations, as fraction of gravity, required to bring mass of soil above slip line to state of limiting equilibrium

b_i = breadth of slice

α_i = angle made by slip line BC with the horizontal

x_i and y_i = co-ordinate of mid point of base of slice with respect to the axes

x_g and y_g = co-ordinate of centre of gravity of sliding mass with respect to the axes

$DE_i = E_{i+1} - E_i$

$DX_i = X_{i+1} - X_i$

Figure 10.2: geometry and forces involved in a limit equilibrium analysis with the methods of slices (from Sarma, 1973).

The method proposed by Fellenius (1936) does not considered interslice forces and assumes a circular failure surface. It calculates the equilibrium of the normal forces at the base of the slice and the global equilibrium of the moments. Bishop (1955) considers a circular failure surface along which, in the formulation of the stability problem, he takes into account both forces and moments equilibrium. Solving it, he simplifies the equations assuming that the interslice forces are horizontal. In this way the equilibrium in respect of moments is satisfied but not in respect of forces. Janbu (1954, 1957) assumes horizontal interslice forces as Bishop, but then introduces a correction factor to calculate also their shear and he calculates the equilibrium in respect of vertical and horizontal forces neglecting that of moments. Moreover, his failure surface is not circular. Morgestern and Price (1965) consider also non-circular failure surfaces and satisfy all the conditions of equilibrium, even considering the interslice forces, whose resultant is calculated through an arbitrary function. The limit of this model is that the solution can only be determined through an iterative procedure. Spencer (1967) assumes interslice forces constant throughout the sliding mass, that has a circular surface, and calculates equilibrium in respect of both forces and moments. The last analyzed method is that proposed by Sarma (1973). This method, as well as that of Morgestern and Price (1965), considers not only circular slip surfaces and it is able to take into account all the interslice forces. The equilibrium is satisfied in respect to both forces and moments and its advantage is that it can arrive to a solution without needing iterations. The assumptions made, besides the points of application of N forces, regard the relative magnitude of X forces and the introduction of an extra unknown.

In particular, Sarma (1973) calculates the critical horizontal acceleration that can lead the mass over the slip surface to the limit equilibrium state. This critical acceleration is another way of expressing the factor of safety, in fact a critical acceleration of 0 corresponds to a traditional factor of safety of 1. The usual factor of safety (FS) can be obtained from the critical acceleration (K_{acc}) with a short iterative calculation, or through an empirical formula proposed by Sarma and Bhave (1974). This formula is obtained considering several circular and non-circular slip surfaces and calculating the respective factor of safety and critical acceleration. Circular surfaces were analyzed with the Bishop's method (1955), while the non-circular surfaces with the Sarma's method (1973). The result is:

$$FS = 1.0 + 3.33 \cdot K_{acc} \quad \text{(eq. 10.1)}$$

Sarma (1979) modified his method including the possibility to consider also not vertical and not parallel boundaries for the different slices involved in the analysis.

Considering the advantages and the disadvantages of the exposed methods and that a raster analysis constrains the different properties expressed through maps within squared cells, it was decided to implement in PcRaster the first Sarma's method (1973), using the equation 10.1 to convert the K_{acc} values to FS values.

Starting from the vertical and horizontal equilibrium of the slice, with respect to Fig 10.2, Sarma derives the equilibrium of the whole mass as follow:

$$\sum DX_i \cdot \tan(\phi'_i - \alpha_i) + \sum K \cdot W_i = \sum D_i \quad \text{(eq. 10.2)}$$

where considering the pore pressure ratio (R_{ui})

$$D_i = W_i \cdot \tan(\phi'_i - \alpha_i) + (c'_i \cdot b_i \cdot \cos\phi'_i - R_{ui} \cdot W_i \cdot \sin\phi'_i) \cdot \sec\alpha_i / \cos(\phi'_i - \alpha_i) \quad \text{(eq. 10.3).}$$

Defining the equilibrium in respect to moments as

$$\sum DX_i \cdot [(y_i - y_g) \cdot \tan(\phi'_i - \alpha_i) + (x_i - x_g)] = \sum W_i \cdot (x_i - x_g) + \sum D_i \cdot (y_i - y_g) \quad \text{(eq. 10.4)}$$

and writing

$$DX_i = \lambda \cdot F_i \quad \text{(eq. 10.5)}$$

assuming

$$\sum F_i = 0 \quad \text{(eq. 10.6)}$$

after some substitution and passages it is possible to determine

$$\lambda = S_2 / S_3 \quad \text{(eq. 10.7)}$$

$$K_{acc} = (S_1 - \lambda \cdot S_4) / \sum Wi \quad \text{(eq. 10.8)}$$

where

$$S_1 = \sum D_i \quad \text{(eq. 10.9)}$$

$$S_2 = \sum W_i \cdot (x_i - x_g) + \sum D_i \cdot (y_i - y_g) \quad \text{(eq. 10.10)}$$

$$S_3 = \sum F_i \cdot [(y_i - y_g) \cdot \tan(\phi'_i - \alpha_i) + (x_i - x_g)] \quad \text{(eq. 10.11)}$$

$$S_4 = \sum F_i \cdot \tan(\phi'_i - \alpha_i) \quad \text{(eq. 10.12).}$$

F_i has infinite possible variations and so the problem has infinite possible solutions. To arrive to a single, determinate result, the author suggests to use the equation 10.13 to derive X_i, where γ is the natural bulk weight of the soil:

$$X_i = \lambda \cdot f_i \cdot \left[\left(K'_i - R_{ui} \right) \cdot \gamma \cdot H_i^{\,2} \cdot \tan \phi'_i / 2 + c'_i \cdot H_i \right] \qquad \text{(eq. 10.13)}$$

where f_i is the reciprocal of the local factor of safety and its value can be considered 1, and K'_i can be calculated as showed in eq 10.14; f_i is the extra unknown that the author needs to arrive to a determinate solution:

$$K'_i = \frac{1 - \sin \beta_i \cdot \left(\left(1 - 2 \cdot R_{ui} \right) \cdot \sin \phi'_i + 4 \cdot c'_i \cdot \cos \phi'_i / \gamma \cdot H_i \right)}{1 + \sin \phi'_i \cdot \sin \beta_i} \qquad \text{(eq. 10.14)}$$

$$\beta i = 2 \cdot \alpha_i - \phi'_i \qquad \text{(eq. 10.15).}$$

The system of equation is solved in PcRaster for every line of terrace, considering them one by one as single, independent, 2D sections. To do this it was necessary to implement an internal loop in the model, that needs to be solved 17635 times for every timestep. Clearly, the model is particularly expensive in terms of calculation time.

10.1 Parameterization of the model

The parameters that must be defined as input data to cycle the model are:

1. Dem map,
2. Soil depth map,
3. Bedrock surface map,
4. Slope of bedrock map,
5. The lines of section map,
6. Cohesion map,
7. Angle of internal friction map,
8. Dry bulk weight map,
9. Porosity map;
10. Water level map,
11. Volumetric water content map.

The topographical maps were defined as seen in the previous chapters 7 and 8, or calculated with simple GIS command. The physical and mechanical parameters of walls and soil were defined using the values obtained during the laboratory tests or from the results of the detailed scale stability model. Water level and volumetric water content are the results of STARWARS.

The bedrock slope map, obtained with the specific GIS command, is made up of values that refer to the maximum slope in the aspect direction. In order to use it in the model constructed, it was necessary to calculate its correspondent apparent value for the direction of the lines of section, applying simple trigonometric formulas.

Another parameter that needs to be adjusted before entering the principal loop of calculus is the bulk density. In fact, except for completely dry conditions, the bulk densities needed are the natural

or the saturated ones for the definition of the weight of each slice, and the buoyant one for the calculus of the shear forces.

10.2 Modelling results

The results presented in this section are still preliminary. They reveal some difficulties related to the use of this model, that can be due to both numerical and parameterization causes. As the model is very time consuming (it takes about a week for 30 timesteps), only results concerning the month of September 2010 are presented, and in particular only those calculated with a well maintained condition of walls and a daily timestep. On site, during September 2010 no failure events were observed.

During the simulation of the first days of the month, when the soil is completely dry, the model returns 3992 unstable lines of section of the 17635 total ones (Fig 10.3). Most of them are concentrated in the upper and lower part of the slope, where flat areas are present. In this situation, instability is not expected. The results of model are probably due to counterslopes that form on the bedrock surface. This surface is in fact calculated as a difference between the DEM and the soil depth map, therefore there is not a direct control on it. Counterslopes are enlightened by negative bedrock slope angles(Fig 10.4), that can influence the results, causing a sort of traction force in the soil that the method applied in the model is not able to manage. Michalowski (1995) underlines that the issue of kinematical admissibility of the failure was not even raised in the years in which the methods of slices were produced. In fact slice methods do not consider any stress-strain rate relation. The same Sarma (1973) enlightened that the physical acceptability of the solution must be checked, considering that only the solutions that do not violate the failure criterion above the slip surface and that do not cause tension in the material are acceptable. The violation is therefore related to E and X forces (Fig 10.2) that could depend on the geometry of the slip surface. The same Sarma (1973) suggests a smoothing of the slip surface in case the failure criterion was violated at one or two particular vertical sections. The problem is that in a distributed analysis the redrawn of the failure surface, assumed at the contact between soil and bedrock is not immediate. In addition, the model is still in a development phase and the mathematics for the explicit solution of the E and X forces at each cell still needs to be inserted. Therefore, till now, the indication of slip surface geometry and bedrock slope angle as the factors that lead to anomalous instability is only a probable, reasonable, hypothesis.

In the other calculated unstable areas there is the same possibility, and in addition it is possible that the derived DEM and the estimated soil depth map are not sufficiently precise and correct, so that unreal slopes could have formed at the bedrock surface and failure is consequently calculated. Anyway, the total number of unstable lines of section is 3992, that on a total of 17635 represents about the 20 %. Therefore, the error cannot be disregarded.

During the month, when rainfalls arrive and perched water tables form, further terraces become unstable. For example during the 19th September 2010, the day after the highest daily rainfall modeled, the total unstable sections are 4005, 12 more than in dry conditions. However, it is possible to see also sections that on the 1st September were unstable becoming stable(Fig 10.5). Maybe, this fact could be due to a combination of a null or almost null apparent bedrock slope angle and an increasing weight resulting in a higher resistance component. Considering a total of 4005 unstable sections, 12 of them are more or less the 0.3%. The percentage is extremely low, therefore it is possible to state that the model is able to recognize that the quantity of water fallen during September 2010 had had a limited influence on the stability of the area, even if not null as expected.

In addition, the 3992 initial unstable lines of section lead to think that also the successive failures could be driven not only by water but also from topographical and environmental factors that were not estimated in the correct way. These results are far from those expected and at the moment seem to partially limit the use of this model as a predictive instrument.

Considering that the model takes into account the apparent bedrock slope angle of the hypothetical sliding surface in the south direction, it was decided to modify this map, in order to obtain a null apparent bedrock slope angle for each cell with any original north-facing component of the sliding surface. It is a manipulation of the original data, but a null slope instead of a counterslope is safety oriented, considering the direction of the analysis, and should permit to erase a cause of malfunctioning of the model.

Using this base map, when completely dry, the model calculates 1331 unstable sections. Some problems still persist but in this case the percentage of the interested lines of section are much lower (7%). On 19th September the number of unstable sections becomes 1335, so increasing of only 4. Also in this case, some lines unstable during the 1st September become stable on the 19th. In general, the simulation with the modified maps confirm that the model seems to be particularly sensitive to bedrock slope angle rather than to water table formation.

Comparing the sections initially stable and later unstable obtained with both the original and modified bedrock aspect map, it is possible to see that only three of them are present in both the simulations (Fig 10.6). It was decided to investigate the characteristics of the cells making up these three unstable sections, in order to understand if it is possible to recognize some common features. Besides water level and volumetric water content, a focus was particularly done on soil depth and bedrock slope angle.

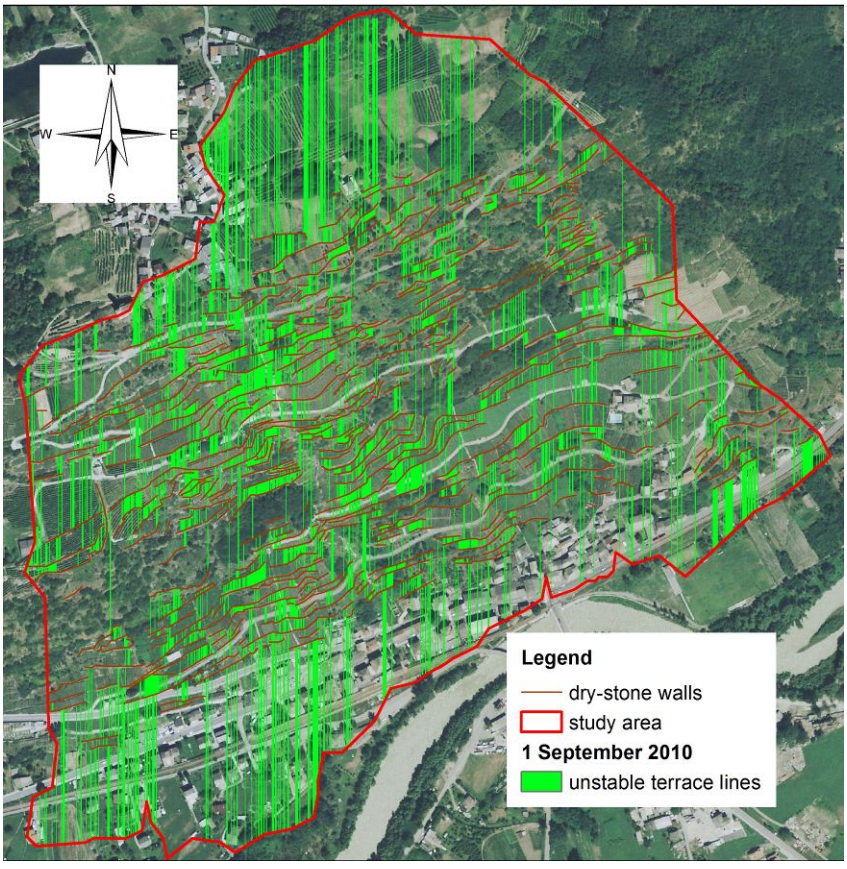

Figure 10.3: unstable terrace lines during the first timestep (1st September 2010), when the soil is completely dry.

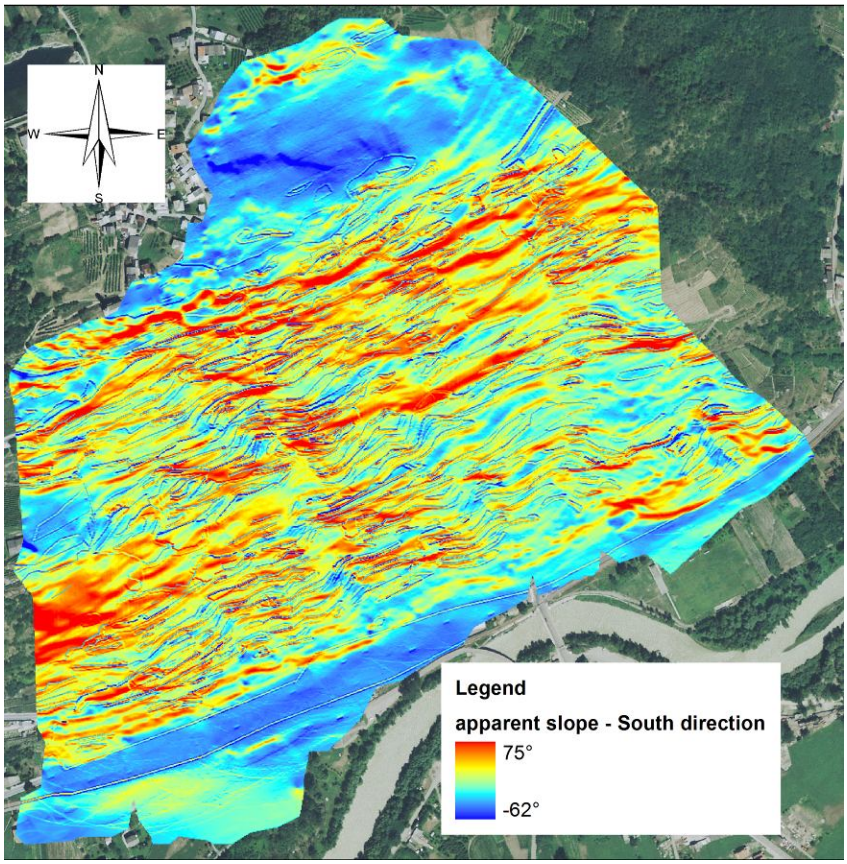

Figure 10.4: apparent slope in south direction, calculated for the terrace lines stability analysis.

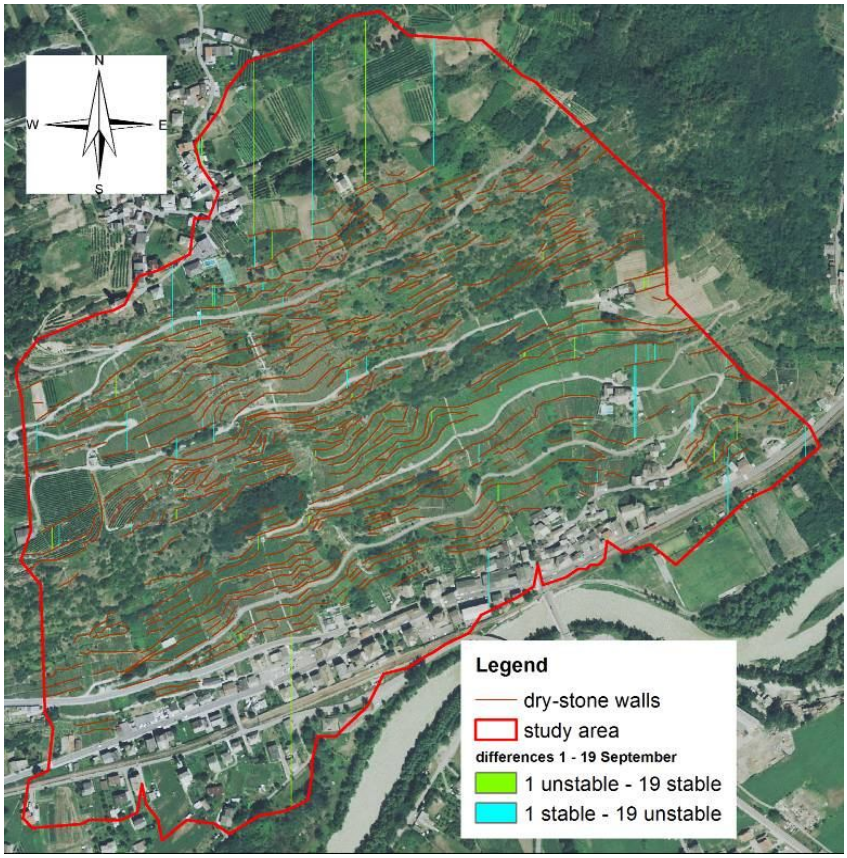

Figure 10.5: comparison between the stable and unstable terraces on the 1st September and the 19th September.

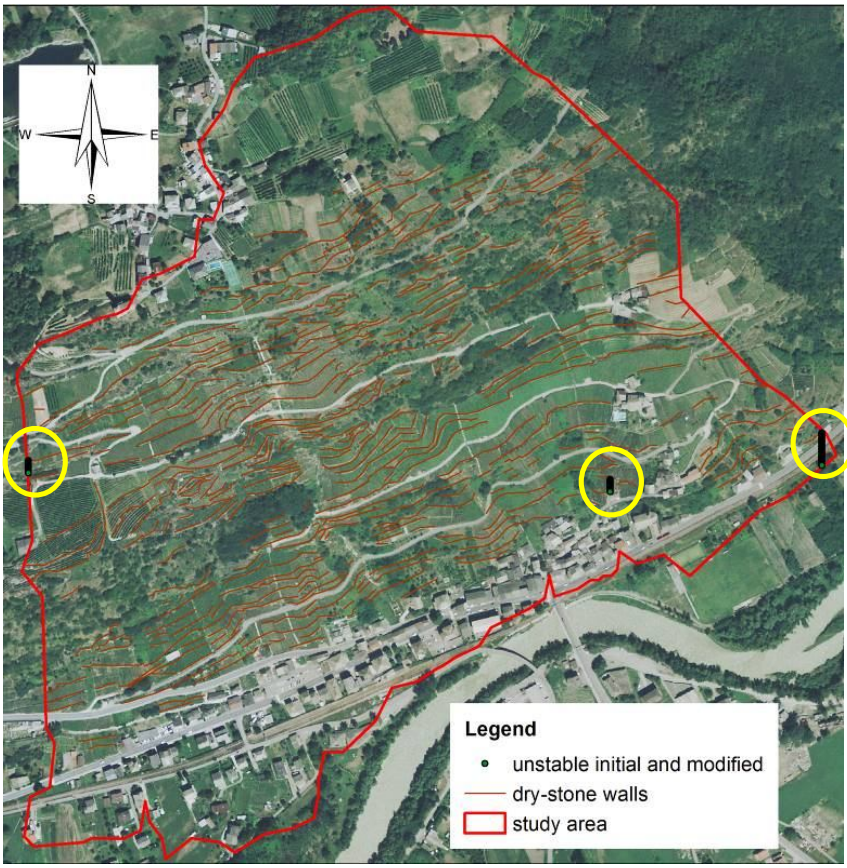

Figure 10.6: the sections stable on the 1st September and unstable on the 19th September for the simulations done with both the original and the modified aspect map.

In the following text, section1 denotes the line on the west of the study area, section 2 indicates the one in the center, and section 3 the one on the east (Fig 10.6). Sections 1 and 2 are made up of 16 cells, while section 3 is made up of 41 cell. Sections 1 and 3 are along the boundaries of the study area and in fact their lower cells are on a model boundary and not in correspondence of a wall.

No cells present a negative apparent slope also using the original bedrock aspect map in order to calculate it. Section 1 is characterized by the presence of 7 rock cells in its upper part with zero soil depth that contribute to the mean values showed in Tab 10.3. All these 7 cells have a slope lower than then medium one, but only one cell along the entire section have a slope lower to 30°, the friction angle of soil. The situation of the first cell downhill the bedrock outcrop appears particularly critic, in fact it is characterized by the highest water table level and by an almost maximum bedrock slope (54.3°). The combination between a high mean bedrock slope, the absence of the retaining structure along this section, and the presence of quite high water levels in cells with very high slopes could be the cause of failure of this section. In particular, slope seems to play a primary role in this context.

The role of slope seems to become less important on section 2. The cells with a slope greater than 30° (the friction angle of soil) are only 6 and only one above 40°. At the same time, it seems difficult that only water could be the cause of the calculated instability, in fact the maximum water level reached is 0.167 m. Maybe, failure could be trigger by water, considering the stability of these section in dry conditions, but a predisposing factor can be represented by the convex irregular form of the failure surface in its middle part. Bedrock slope is in fact almost constant in the upper part of the section around 25° - 30°, then it rapidly decrease from 26° to 1° in only a cell, and then it re-increases till 47° in 8 cells. Along these length the form of the failure surface is convex, and it could cause traction forces and therefore a not admissible Sarma's solution.

A similar explanation seems also to be the only one admissible for the failure of section 3. In this case, slope is lower than 30° in all the cells and the maximum water level is about 0.15 m. This section is particularly long and along its length it is possible to notice various inflection points in the bedrock slope trend.

The last shown results further enlighten what already hypothesized. The model seems to calculate instability for two main causes that are only partially related to the presence of water tables. In the analyzed cases in fact water levels are always quite low, as well as the water content of the unsaturated zone. Therefore water seems to play only a secondary role in the onset of instability. The main causes are factors related to probable, local unrealistic definition of the bedrock geometry, above all in terms of too high local bedrock slope angles as for section 1, and convex forms of the failure surface that cause distributions of the inter-slices forces that the model is not able to manage, thus causing a collapse whose kinematic is not admissible, as for sections 2 and 3.

Table 10.3: summary of the characteristics of the cells of the three terraces, unstable both with the original and the modified aspect map, during the simulation of the 19th September 2010. Slope is the apparent slope of the bedrock in south direction; sdepth is the soil depth; VWC the volumetric water content in the unsaturated zone; watlev the water level.

	Terrace line 1				Terrace line 2				Terrace line 3			
	slope [°]	**sdepth [m]**	**VWC [-]**	**watlev [m]**	**slope [°]**	**sdepth [m]**	**VWC [-]**	**watlev [m]**	**slope [°]**	**sdepth [m]**	**VWC [-]**	**watlev [m]**
Mean	38.9	0.64	0.013	0.072	23.9	0.77	0.012	0.120	7.4	2.33	0.026	0.082
Max	55.4	1.78	0.066	0.453	47.6	1.59	0.027	0.167	22.5	2.76	0.028	0.140

11 Chapter 11

DISCUSSION, CONCLUSIONS AND *FUTURE PLANS*

The aim of the work was to enhance the knowledge on the processes that could lead a slope, terraced by means of dry-stone walls, to the triggering of a superficial landslide. All the analysis were carried out on the slope uphill the small village of Tresenda, in Valtellina, that experienced several soil slip/debris flow event between 1983 and 2002.

A principal field work was carried out during summer 2009 and later integrated by other brief campaigns. Surveys, field tests, and the installation of instruments for the monitoring of water table levels permitted to construct a solid database, on which preliminary analysis on the hillslope hydrology and a following numerical modelling activity were developed.

The modelling analysis was divided in two distinct parts. At first a study at the single terrace scale was carried out. The objective was to understand in detail the hydrogeological processes, characteristics of terraced areas, and the stress-strain fields that they can induce. During this first phase a classical 2D finite elements – finite differences approach was used.

The second part moved the problem from a very detailed scale to an entire terraced slope, conscious of the importance of developing a tool for the prediction of critical condition of instability and for previsional instability mapping to guide civil protection actions. A coupled hydrogeological-stability analysis was carried out also in this phase, but using a raster GIS software with an embedded language for the modelling of environmental processes. The work on the extended study area, besides providing a general overview on the processes at a larger scale, gave the possibility to analyze also the influence of environmental variables, rather difficult to consider at a detailed scale, such as land use and soil depth.

The specific characteristics of the study area is the presence of the dry-stone walls. To Consider them in the performed analysis has represented the real challenge of the work. During the first phase, it was possible to define the hydrogeological and resistance properties of backfill soils and bedrock through field and laboratory data, but regarding walls it was necessary to do some assumptions and verify them during the calibration and validation phases of the modelling activity. The 2D detailed model demonstrated to be a good instrument for this purpose.

In addition, once calibrated and validated, the hydrogeological 2D model was able to show the effects of the variation of geometrical parameters, such as height of the wall and slope of the bedrock, of isotropic and anisotropic k_s, and of draining conditions of wall. In all this circumstances the model helped to explain the infiltration process in the context of the study, exploiting one of the main characteristics of a demonstrably reliable model, which is the ability to show something that is almost impossible to demonstrate in the field.

The 2D stability model has the same advantages of the hydrological one. First of all, it demonstrated to be an important instrument for helping in the calibration and final definition of the dry-stone wall resistance parameters, at first estimated with theoretical techniques. Secondly, but not less important, the model contributes in the understanding of the most important factors that act in favour or against stability, underlining for example the importance of the event antecedent rainfalls and conditions of wall. On the other hand, the stability model shows also some limits. The study was conducted both with the finite elements (FEM) and finite differences (FDM) methods, because

the mechanism of failure reproduced by the finite element code (same technique used for the 2D hydrogeological analysis) is not comparable with that described by people who had observed the soil slip/debris flow events of 1983. The FDM is able to well reproduce the mechanism of failure of a dry-stone wall, but at calibration it shows a lower value of cohesion than the FEM model. The models are different; the FEM model initially considers the soil unsaturated, followed by a successive, progressive saturation of it that causes a well-defined evolution of matric suction. On the contrary, the FDM model always considers a completely saturated soil, where the evidence of a water table is given by an overpressure. A rough preliminary reasoning could lead to think that the models are not in agreement, showing the FEM a larger cohesion than the FDM at calibration, although the first takes into account an apparent cohesion, given by matric suction, that increases the resistance capacity of the soil. Anyway, during the calibration phase of the FEM model, for cohesion values lower than the final one, failure often was observed when a water table was not present immediately behind the wall, but when it was still doing its uphill-downhill travel along the contact between soil and bedrock. Analyzing these failures and also the one that is obtained for a rainfall event with return time of 100 years and a bad maintained condition of wall, it is possible to hypothesize that the frontal surface, where the saturated soil is in contact with the unsaturated one, can act as a weakness surface along which a failure is more prone to happen. Maybe, even if it still needs to be demonstrated, also the slope of this surface could have an influence on the onset of an instability.

In the next future, some work still need to be done on these 2D models. The first idea is to compare the results obtained with the simplified geometry presented, that have a constant slope of bedrock, with results from a single terrace model whose soil depth and bedrock slope is known exactly from the geo-radar survey. Moreover, as it was demonstrated that the triggering of superficial landslides event on the study area is related to the combination of an extended antecedent rainfall with an extreme event of about 72 hours, it has been already planned a work with dr. Daniele Bocchiola, an hydrologist of Politecnico di Milano, to define the probability of occurrence of an extreme event combined with a certain amount of antecedent rainfall in the 5, 10 and 15 previous days, in order to statistically define the real return time of possible failures. Regarding the demonstration of the formation of the cited weakness surface at the contact between the saturated and the unsaturated zone, at first it was proposed to analyze the problem hand-drawing some different water table geometries and look at the reaction of the system. At the end it was decided to not perform such an analysis, because also the evolution of the matric suction has probably an influence on the process. Therefore, drawing the water table and performing a steady state analysis could have taken to misleading results. Also this analysis is expected to be done when the combined statistical rainfalls will be available.

Passing to the watershed scale analysis, the aim was to reproduce the dynamics of water table formation on the extended study area, in order to recognize the area more prone to water accumulation and so more critic from a stability point of view. In particular, the hydrological-hydrological model is requested to be able to reproduce the maximum water levels registered on site, because they corresponds to the most critical situations. STARWARS was therefore tested, and its results compared, at different temporal scales. In particular, daily and hourly timesteps were used. With the daily resolution, the model is able to well reproduce the water table peaks, even if with a single timestep delay due to the model structure. With the hourly timestep the time of peak is accurately reproduced but the model tends to underestimate the maximum height reached by the water table. With both the time resolutions, the model is not able to well reproduce the entire infiltration and water redistribution process as the very detailed 2D model. Also the difference in the behaviour between a well maintained and a bad maintained wall is often limited to the cell that correspond to dry-stone wall itself. Anyway, it is possible to affirm that the model can adequately

perform the expected task, in fact it is able to produce reliable series of water levels and water contents maps to use as input in the following stability model.

More problems arose during the stability analysis. The particular morphology of the study area and the will to include dry-stone walls in the analysis led to the necessity of use high resolution base maps for raster analysis. The use of these maps led to exclude the possibility of using a simple infinite slope model. The calculation is performed cell by cell and the soil depth of a cell 1m x 1m is never negligible respect to its length. It was therefore decide to try to implement a model based on the slices equilibrium method for circular and non circular failure surfaces of Sarma (1973). The method does not consider the equilibrium of the single cell (slice) but of a group of cells (slices) along the same failure surface. In this analysis, many failure surfaces were considered, one for every terrace line recognized, that is a single alignment of cells from the top of a dry-stone wall uphill to the base of another one. The failure surfaces are considered known at the contact between soil and bedrock. Considering these few, rough information, it is just possible to understand how the model results depend on soil depth and bedrock geometry. Great efforts were in fact made during this research work in order to obtain a good soil depth map and a reliable digital elevation model at the resolution requested, from which it was later possible to calculate the geometry of the bedrock for difference. Despite these efforts the first preliminary results of the model are not extremely satisfactory. Even modifying the slope map in order to avoid negative slope angle of the bedrock, a limited but meaningful number of lines of terrace is in fact unstable, also with completely dry conditions of soil. The first causes can be recognized in the general characteristics of the problem analyzed and in the intrinsic assumption of the model used to solve it. Maybe, above all when the sliding (bedrock) surface is irregular with alternations of convex and concave forms, it is possible that the lateral forces, acting on the cells boundaries parallel to the direction of analysis, could have some importance, but in a 2D analysis they are neglected. Another point is related to the N-S direction of analysis. With such an analysis the numerical model considers the interactions between cells along the designed line of section, but in reality these interactions are related to the orientation of the sliding surface. Therefore, the error is as much large as much complex the failure surface geometry is. A possible simple solution to reduce this problem is to develop an analysis where the sections are parallel to the mean topographical slope, assuming that this is the most probable direction of eventual sliding surfaces. Nevertheless also this assumption raises some doubts, due to the fact that the geometry of the bedrock is expected to be much more complex.

Other causes need to be searched in two different directions. On one side, it is possible that along certain slip surfaces the failure is not admissible from a kinematical point of view. On the other side, the Digital Elevation Model (DEM) and the soil depth map could have been estimated not in the correct way, thus causing unrealistic bedrock slope angles that can lead to instability. Both these facts are in part confirmed by the analysis of the three terrace lines unstable in wet conditions both using the original and the modified apparent slope map. In one case, all the cells of the terrace line have a slope greater than the soil friction angle and so few water can trigger instability, suggesting a problem in the determination of topography and soil depth map. In the other two cases, cells have low slopes and registered low water table levels, thus suggesting that the cause of the calculated failure probably lies somewhere else. A hypothesis is related to convex form of the failure surface in some points, that is very different from the classical concave surface represented in the explanation of the method. The convexity could cause tension in the material, that the model is not able to manage, with unrealistic distribution of the inter slices forces.

According to the shown results, the analysis at the study area scale clearly needs to be improved, in particular the stability model. Among the first things to do there is in fact the implementation of the equations to calculate the local factor of safety and of the inter slices forces for every cell, in order to have an instrument that can help to understand the kinematic admissibility of the eventual failures.

Another important problem is represented by the time needed by the stability model for the calculus of the outputs on the entire area. In this case, the only solution is represented by a division of the area in more sub areas, maybe neglecting the almost flat zone that have caused some problems, and where no failures are expected. Anyway, considering that the area is a sort of watershed, the hydrological-hydrogeological analysis should always be performed on the entire area, in order to consider all the possible water contributions in any cell.

When a good, definitive setting will be found also for the stability model (if it will be found), it could be used in combination with the hydrological-hydrogeological one with monthly, and/or annual rainfall timeseries, both real and statistical generated, in order to derive real return periods for the triggering of superficial landslide events in such a contest.

The work done till now contributes to a better and complete understanding of landslide events on terraced slopes and to their reasonable and physically based prediction. The present work represents an attempt, whose developments are still in progress and whose final success is not assumed. Very interesting results have been achieved, above all regarding the knowledge of the processes. Both the hydrogeological and the stability 2D, detailed models were able to illuminate particular aspects related to the analyzed terraced slopes, and well reproducing the processes they were also able to fix a base for the development and the use of the successive raster, more general models. In this moment, the real limit is represented by the stability analysis at the larger scale. Taking into account the walls primary, observed and proved, role in the failure dynamic, it was necessary to consider these structures in the performed analysis, and it led to ask for a resolution level that is very difficult to manage with the available instruments, at least at the proposed scale. The mathematical formulation of the problem needs also to be improved, and looking at all the problems risen with the proposed method, a 3D analysis might be the best attempt for a future successful development of the work.

Acknowledgements

Vorrei innanzitutto ringraziare Tiziana Apuani e Marco Masetti, i miei tutori, per avermi supportato e consigliato durante tutti e tre gli anni di lavoro e per avermi dato la possibilità, anche attraverso un rapporto basato sull'onestà e il rispetto reciproco, di un confronto pressoché continuo che mi ha permesso una costante crescita dal punto di vista critico e professionale, aiutata anche dall'ottimo ambiente creatosi dal punto di vista umano.

In secondo luogo devo ringraziare tutte le persone che mi hanno aiutato nel corso del lavoro concedendomi una parte più o meno grande del loro tempo per lavori di terreno, consulenze e confronti. Tra queste ci sono i miei compagni di ufficio, Federica e Alessandro, che talvolta mi hanno accompagnato sul terreno e consigliato nel corso del lavoro in quegli che sono gli aspetti più vicini alle tematiche di loro competenza; Sekhar Kuriakose, che mi ha aiutato nell'impostare il lavoro per la definizione della carta dello spessore del terreno durante il mio soggiorno all'ITC a Enschede, in Olanda; il dr. Ens van Beek che mi ha dato l'opportunità di utilizzare gli script dei suoi modelli; Fabio Villa, che mi ha supportato nella realizzazione del DEM; Mauro Mele, Mimmo e Davide, che mi hanno aiutato con le indagini geofisiche; Davide e Cristian che mi hanno accompagnato durante tutta la campagna di terreno dell'estate 2009; Marco Perfido, sempre disponibile ad aiutarmi in laboratorio; Serena Orsatti, che ha contribuito alle prove di laboratorio; Giovanni Di Trapani e Alessandro Gervasini, preziosi riferimenti in Comunità Montana a Tirano; il dr. Maurizio Azzola, che in qualità di osservatore diretto degli eventi del 1983 ha risposto cortesemente a tutte le domande che gli ho posto a riguardo; la dr.ssa Arianna Facchi, il dr. Marco Conedera e il prof. Luigi Mariani per avermi aiutato da un punto di vista "agrario" in una migliore comprensione dei processi idrologici; la dr.ssa Chiara Vassena e il prof. Mauro Giudici, che mi hanno aiutato a guardare dentro alle equazioni del metodo di Sarma; Ivan, Luisa, Erika, Serena, Matteo, Fulvio, Jan e Rainer, spero di non aver scordato nessuno, per aver scavato buchi, tirato cavi e trasportato boccioni d'acqua o qualsiasi altro tipo di peso nel corso di diverse prove di terreno.

Un ultimo ringraziamento, non meno importante degli altri, va ad Ilaria e alla mia famiglia. Loro ci sono sempre.

References

Aleotti, P., 2004. A warning system for rainfall-induced shallow failures. Eng Geo 73, 247–265.

Allen, R.G., Pereira, L.S., Raes, D., Smith, M., 1996. Irrigation and Drainage Paper No. 56. FAO, Rome, 326 pp.

Akaike, H., 1974. A new look at the statistical model identification. *IEEE Transactions on Automatic Control* 19 (6), 716–723.

Angeli, M.G., Buma, J., Gasparetto, P., Pasuto, A., 1998. A combined hillslope hydrology/stability model for low-gradient clay scope in the Italian Dolomites. *Eng Geol* 49, 1-13.

ASTM, 2010. Standard Practice for Classification of Soils for Engineering Purposes (Unified Soil Classification System) – American Society for Testing Materials D2487 – 10.

ASTM, 2007. Standard Test Method for Density and Unit Weight of Soil in Place by the Sand-Cone Method - American Society for Testing and Materials D1556 – 07.

ASTM, 2006. Standard Test Method for Permeability of Granular Soils (Constant Head) D2434 – 68.

ASTM, 2004. Standard Test Method for Direct Shear Test of Soils Under Consolidated Drained Conditions D3080 – 04.

Azzola, M., Tuia, T., 1983. Osservazione sui fenomeni franosi che hanno interessato i vigneti terrazzati a monte di Tresenda nel maggio 1983. *Geologia Tecnica* 4, 23-35.

Bacchini, M., Zannoni, A., 2003. Relations between rainfall and triggering of debris-flow: case study of Cancia (Dolomites, Northeastern Italy). *Nat Hazards Earth Syst Sci* 3, 71–79.

Baum R.L., Savage, W.Z., Godt, J.W., 2002. TRIGRS – A Fortran Program for Transient Rainfall Infiltration and Grid Based Regional Slope Stability Analysis, Open file report 02-424. US Department of the Interior and US Geological Survey: Denver, CO.

Biavati, G., Godt, J.W., McKenna, J.P., 2006. Drainage effects on the transient, near-surface hydrologic response of a steep hillslope to rainfall: implications for slope stability, Edmonds, Washington, USA. *Nat Hazards Earth Syst Sci* 6, 343-355.

Bishop, A.W., 1955. The use of the slip circle in the stability analysis of slopes. *Geotechnique* 5, 7-17.

Blahut, J., Poretti, I., De Amicis, M., Sterlacchini, S., 2011. Database of geo-hydrological disasters for civil protection purposes. Natural Hazards, available online, doi: 10.1007/s11069-011- 9893-6

Caine, N., 1980. The rainfall intensity-duration control of shallow landslides and debris flows. *Geografiska Annaler* 62A, 23–27.

Camera, C., Masetti, M., Apuani, T., 2011. Rainfall, infiltration, and groundwater flow in a terraced slope of Valtellina (Northern Italy): Field data and modelling. *Environ Earth Sci*, DOI 10.1007/s12665-011-1367-3, 12 pp.

Campbell, R.H., 1975. Soil slips, debris flows, and rainstorms in the Santa Monica Mountains and vicinity, Southern California. *US Geological Survey Professional Paper* 851, 1–20.

Cancelli, A., Nova, R., 1985. Landslides in soil debris cover triggered by rainstorms in Valtellina (Central Alps – Italy). *Proc. IV International Conference and Field Workshop on Landslides*, Tokio, 267-272.

Ceriani, M., Lauzi, S., Padovan, N., 1992. Rainfalls and landslides in the Alpine area of Lombardia Region–Central Alps–Italy. *Internationales Symposion Interpraevent*. Band 2 Bern, pp 9–20.

Ceriani, M., Lauzi, S., Padovan, N., 1994. Rainfall tresholds triggering debris flows, in the alpine area of Lombardia Region, Central Alps, Italy. *Man and Mountain'94*. First international congress for the protection and development of mountain environment. Ponte di Legno (BS, Italy), June 1994, pp 123–139.

Cestari, F., 2005. Prove geotecniche in situ. Ed. Geo-graph Segrate,3rd edn.

Cho, S.E., 2009. Infiltration analysis to evaluate the surficial stability of two-layered slopes considering rainfall characteristic. *Eng Geol* 105, 32-43.

Crosta, G.B., 1990. A study of slope movements caused by heavy rainfall in Valtellina (July 1987). *Proc 6th ICFL*, Milan, 247–258.

Crosta, G.B., Dal Negro, P., Frattini, P., 2003. Soil slips and debris flow on terraced slope. *Nat Hazards Earth Syst Sci* 3, 31-42.

Crosta, G.B., Frattini, P., 2001. Rainfall tresholds for triggering soil slips and debris flow. In: *Proceedings of EGS 2nd Plinius Conference 2000*. Mediterranean Storms, Siena, pp 463–488.

Crosta, G.B., Frattini, P., 2003. Distributed modelling of shallow landslides triggered by intense rainfall. *Nat Hazards Earth Syst Sci* 3, 81-93.

Crozier, M.J., 1999. Prediction of rainfall-triggered landslides: a test of the antecedent water status model. *Earth Surf Process and Landforms* 24, 825–833.

Dahal, R.K., Hasegawa, S., 2008. Rainfall thresholds for landslides in the Nepal Himalaya. *Geomorphology* 100(3–4), 429–443.

Dahal, R.K., Hasegawa, S., Nonomura, A., Yamanaka, M., Masuda, T., Nishino, K., 2009a. Failure characteristics of rainfall-induced shallow landslides in granitic terrains of Shikoku Island of Japan. *Environ Geol* 56, 1295–1310.

Dahal, R.K., Hasegawa, S., Yamanaka, M., Dhakal, S., Bhandary, N.P., Yatabe, R., 2009b. Comparative analysis of contributing parameters for rainfall-triggered landslides in the Lesser Himalaya of Nepal. *Environ Geol* 58, 567–586.

DB2000, 2003. Database of the CM Valtellina di Tirano mapped at 1:2,000 scale. CM Valtellina di Tirano. CD-ROM. Available at: http://www.cmtirano.so.it/sistemainformativo.php

Delmonaco, G., Leoni, G., Margottini, C., Puglisi, C., Spizzichino, D., 2003. Large scale debris-flow hazard assessment: a geotechnical approach and GIS modelling. *Nat Hazards Earth Syst Sci* 3, 443-455.

Dietrich, W.E., Montgomery, D.R., 1998. SHALSTAB: A Digital Terrain Model for Mapping Shallow Landslide Potential. University of California and University of Washington: Berkeley, CA.

Draper, N., Smith, H., 1998. Applied Regression Analysis, 3rd ed. Wiley, New York.

Ewen, J., Parkin, G., O'Connell, P.E., 2000. SHETRAN: distributed river basin flow and transport modeling system. *J Hydr Eng* 5(3), 250–258.

Farrel, D., Larson, W., 1972. Modelling the pore structure of porous media. *Wat Res Res* 8, 699-705.

Fellenius, W., 1936. Calculation of stability of earth dams. *Trans. 2nd Int. Congr. Large Dams* 4, 445.

Fleming, R.W., Ellen, S.D., Algus, M.A., 1989. Transformation of dilative and contractive landslide debris into debris flows—an example from Marin County, California. *Eng Geol* 27, 201–223.

Fredlund, D.G., Rahardjo, H., 1993. Soil Mechanics for Unsaturated Soils. Wiley, New York.

GEO-SLOPE International Ltd. (2002) SEEP/W – for finite element seepage analysis. User's Guide, Version 5, Calgary.

GEO-SLOPE International Ltd. (2002) SIGMA/W – for finite element seepage analysis. User's Guide, Version 5, Calgary.

Gessler, P., Moore, I., McKenzie, N., Ryan, P., 1995. Soil-landscape modelling and spatial prediction of soil attributes. *International Journal of Geographical Information Systems* 9 (4), 421– 432.

Goovaerts, P., 1999a. Using elevation to aid the geostatistical mapping of rainfall erosivity. *Catena* 34 (3–4), 227– 242.

Goovaerts, P., 1999b. Geostatistics in soil science: state-of-the-art and perspectives. *Geoderma* 89 (1– 2), 1 – 45.

Govi, M., Mortara, G., Sorzana, P.F., 1985. Eventi idrologici e frane. *Geol Appl e Idrog* 20(2), 359–375.

Graham, J., 1984. Methods of stability analysis. In: Slope Instability, Brundsen D. & Prior D.B. John Wiley & Sons, New York, 171-215.

Green, R.E., Corey, J.C., 1971. Calculation of hydraulic conductivity: a further evolution of some predictive methods. *Soil Sci Soc Am Proceed* 35, 3–8.

Gumbel, E.J., 2004. Statistics of extremes. Reprint of the 1958 edition, Dover Publications, Mineola, 375 p

Gupta, S.C., Larson, W.E., 1979. Estimating soil water retention characteristics from particle size distribution, organic matter percent, and bulk density. *Water Res Res* 15, 1633–1635.

Guzzetti, F., Peruccacci, S., Rossi, M., Stark, C.P., 2007. Rainfall thresholds for the initiation of landslides in central and southern Europe. *Meteorol Atmos Phys* 98, 239–267.

Guzzetti, F., Peruccacci, S., Rossi, M., Stark, C.P., 2008 The rainfall intensity-duration control of shallow landslides and debris flows: an update. Landslides 5(1), 3–17.

Harkness, R.M., Powrie, W., Zhang, X., Brady, K.C., O'Reilly, M.P., 2000. Numerical modeling of full-scale tests on drystone masonry retaining walls. *Geotechnique* 50, no. 2, 165-179.

Hengl, T., Heuvelink, G.B.M., Stein, A., 2004. A generic framework for spatial prediction of soil variables based on regression-kriging. *Geoderma* 120, 75 – 93.

Hoek, E., Marinos, P., 2000. Predicting Tunnel Squeezing. Tunnels and Tunnelling International. Part I – November 200, Part 2 – December 2000.

Hoek, E., Marinos, P., Benissi, M., 1998. Applicability of the geological streangth index (GSI) classification for very weak and sheared rock masses. The case of the Athens Schist Formation. *Bull Eng Geol Environ* 57, 151-160.

Hoek, E., Carranza-Torres, C.T., Corkum, B., 2002. Hoek-Brown failure criterion-2002 edition. *Proc. 5th North American Rock Mech Symp* 1, 267–273.

Huat, B.B.K., Ali, F.H., Low, T.H., 2006. Water infiltration characteristicsof unsaturated soil slope and its effect on suction and stability. *Geotech Geol Eng* 24, 1293–1306

Itasca Consulting Group Inc (2008) FLAC Version 6.00. User's Guide, Fourth Edition, Minneapolis.

Iverson, R.M., Reid, M.E., LaHusen, R., 1997. Debris-flow mobilization from landslides. *Annu Rev Earth Planet Sci* 25, 85-138.

Janbu, N., 1954. Stability analysis of slopes with dimensionless parameters. Harvard University, *Harv Soil Mech Ser* 46, 1–81.

Janbu, N., 1957. Earth pressures and bearing capacity calculations by generalized procedures of slices. *Proc 4th Int Conf Soil Mech* 2, 207-212.

Johnson, A.M., Rahn, P.H., 1970. Mobilization of debris flows. In: Macar, P. (Ed.), New Contributions to Slope Evolution Zeitschrift für Geomorphologie Neue Folge Supplementband, vol. 9, pp. 168–186.

Krige, D.G., 1951. A statistical approach to some mine valuations and allied problems at the Witwatersrand. *Master's thesis of the University of Witwatersrand.*

Kuriakose, S.L., van Beek, L.P.H., van Westen, C.J., 2009a. Parameterizing a physically based shallow landslide model in a data poor region. *Earth Surf Process Landforms* 34, 867-881.

Kuriakose, S.L., Devkota, S., Rossiter, D.G., Jetten, V.G., 2009b. Prediction of soil depth using environmental variables in an anthropogenic landscape, a case study in the Western Ghats of Kerala, India. *Catena* 79, 27-38.

Larsen, M.C., Simon, A., 1993. A rainfall intensity-duration threshold for landslides in a humid-tropical environment. *Puerto Rico Geogr Ann* A 75(1–12), 13–23.

Li, A.G., Yue, Z.Q., Tham, L.G., Lee, C.F., Law, K.T., 2005. Field monitored variations of soil moisture and matric suction in sarolite slope. *Can Geotech J* 42, 13–26.

Loke, M.H., 2001. 2D and 3D electrical Imaging Surveys. www.geoelectrical.com

Lourenço, P.B., Oliveira, D.V., Roca, P., Orduña, A., 2005. Dry joint stone masonry walls subjected to In_Plane combined loading. *J Struct Eng*, vol. 131, no. 11, 1665-1673.

Malet, J.P., van Asch T.W.J., van Beek L.P.H., Maquaire , O., 2005. Forecasting the behaviour of complex landslides with a spatially distributed hydrological model. *Nat Hazards Earth Syst Sci* 5, 71–85.

Marinos, V., Marinos, P., Hoek, E., 2005. The geological strength index applications and limitations. *Bull Eng Geol Environ* 64, 55-65.

Matheron, G., 1963. Principles of geostatistics. *Economic Geology* 58, 1246–1266.

McBratney, A., Odeh, I., Bishop, T., Dunbar, M., Shatar, T., 2000. An overview of pedometric techniques of use in soil survey. *Geoderma* 97 (3– 4), 293–327.

McKenzie, N., Ryan, P., 1999. Spatial prediction of soil properties using environmental correlation. *Geoderma* 89 (1– 2), 67–94.

Meisina, C., Scarabelli, S., 2007. A comparative analysis of terrain stability models for predicting shallow landslides in colluvial soils. *Geomorphology* 87, 207-223.

Mele, M., 2008. L'architettura degli acquiferi alluvionali: una metodologia integrate geologico-geofisica per la caratterizzazione a diverse scale. *PhD Thesis, University of Milan.*

Michalowski, R.L., 1995. Slope stability analysis: a kinematical approach. *Geotechnique* 45, 283-293.

Millington, R.J., Quirk, J.P., 1959. Permeability of porous media. *Nature* 183, 387–388.

Millington R.J., Quirk, J.P., 1961. Permeability of porous media. *Transactions of the Faraday Society* 57, 1200-1207.

Moore, I., Gessler, P., Nielsen, G., Peterson, G., 1993. Soil attribute prediction using terrain analysis. *Soil Science Society of America Journal* 57 (2), 443– 452.

Morgestern N.R., Price V.E., 1965. The analysis of the stability of generalised slip surfaces. *Geotechnique* 15, 79-93.

Nash, D., 1987. A comparative review of limit equilibrium methods of stability analysis. In: Anderson & Richards (Eds.), 11-75.

Odeh, I., McBratney, A., Chittleborough, D., 1994. Spatial prediction of soil properties from landform attributes derived from a digital elevation model. *Geoderma* 63 (3– 4), 197– 214.

Odeh, I., McBratney, A., Chittleborough, D., 1995. Further results on prediction of soil properties from terrain attributes: heterotopic cokriging and regression-kriging. *Geoderma* 67 (3 – 4), 215– 226.

Pack, R.T., Tarboton, D.G., Goodwin, C.N., 1998. The SINMAP Approach to Terrain stability Mapping. *Proc 8th Congress of the International Association of Engineering Geology*, Vancouver, British Columbia, Canada. International Association of engineering, Paris.

Pellerin, L., 2002. Applications of electrical and electromagnetic methods for environmental and geotechnical investigations. *Surveys in Geophysics* 23 (2-3), 101-132.

Powrie, W., Harkness, R,M., Zhang, X., Bush, D.I., 2002. Deformation and failure modes of drystone retaining walls. *Geotechnique* 52, no. 6, 435-446

Quan Luna, B., van Westen, C.J., Blahut, J., Camera, C., Apuani, T., Sterlacchini, S., 2010. From deterministic hazard modelling to risk and loss estimation. In: Mountain Risks: Bringing Science to Society. Proceedings of the International Conference, 24-26 November 2010, Florence, Italy. CERG Editions, Strasbourg, France, 572pp.

Quan Luna, B., Blahut, J., Camera, C., van Westen, C.J., Apuani, T., Jetten, V., Sterlacchini, S., under review. Quantitative risk assessment for debris flows based on physically-based dynamic run-out modelling. A case study in Tresenda, Northern Italy. Landslides, 33 pp.

Rahardjo, H., Ong, T.H., Rezaur, R.B., Leong, E.C., Fredlund, D.G., 2010. Response parameters for characterization of infiltration. *Environ Earth Sci* 60, 1369–1380.

Remy, N., Boucher, A., Wu, J., 2009. Applied geostatistics with SGeMS. A User's Guide. Cambridge University Press,Cambridge, 264pp.

Reynolds, J.M., 2011. An Introduction to applied and environmental Geophysics. Second Edition. Wiley, New York.

Richards, L.A., 1931. Capillary conduction of liquids through porous mediums. *Physics* 1 (5), 318–333.

Robinson, D.A., Binley, A., Crook, N., Day-Lewis, F.D., Ferrè, T.P.A., Grauch, V.J.S., Knight, R., Knoll, M., Lakshmi, V., Miller, R., Nyquist, J., Pellerin, L., Singha, K., Slater, L., 2008. Advancing process-based watershed hydrological research using near-surface geophysics a vision for, and review of, electrical and magnetic geophysical methods. *Hydrol Process* 22, 3604-3635.

Sarma, S.K., 1973. Stability analysis of embankments and slopes. *Geotechnique* 23, 423-433.

Sarma, S.K., 1979. Stability analysis of embankments and slopes. *J Geotech Eng Division*, GT 12, 1511-1524.

Sarma, S.K., Bhave, M.V., 1974. Critical acceleration versus static factor of safety in stability analysis of earth dams and embankments. *Geotechnique* 24, 661-665.

Servizio Geologico Italiano, 1969. Carta Geologica d'Italia 1:100000 – Foglio19 "Tirano".

Simoni, S., Zanotti, F., Bertoldi, G., Rigon, R., 2008. Modelling the probability of occurance of shallow landslides and channelized debris flows using GEOtop-SF. *Hydrol Process* 22, 532-545.

Spencer E., 1967. A method of analysis of the stability of embankments assuming parallel interslice forces. *Geotechnique* 17, 11-26.

Sturges, H.A., 1926. The choice of a class interval. . *American Statistical Association*, Vol 21, No 153, 65–66.

Talebi, A., Troch, P.A., Uijlenhoet, R., 2008. A steady-state analytical slope stability model for complex hillslopes. *Hydrol Process* 22, 546-553.

Telford, W.M., 1990. Applied Geophysics. Second edition. Cambridge University Press, Cambridge.

Tofani, V., Dapporto, S., Vannocci, P., Casagli, N., 2006. Infiltration, seepage and slope instability mechanisms during the 20-21 November 2000 rainstorm in Tuscany, central Italy. *Nat Hazards Earth Syst Sci* 6, 1025-1033.

Trandafir, A.C., Sidle, R.C., Gomi, T., Kamai, T., 2008. Monitored and simulated variations in matric suction during rainfall in a residual soil slope. *Environ Geol* 55, 951–961.

Tsai, T.L., Chen, H.E., Yang, J.C., 2008. Numerical modeling of rainstorm-induced shallow landslides in saturated and unsaturated soils. *Environ Geol* 55, 1269–1277.

van Beek, R., 2002. Assessment of the influence of changes in land use and climate on landslide activity in a Mediterranean environment. PhD Thesis, University of Utrecht, Utrecht, The Netherlands, 363 pp.

van Beek, L.P.H., van Asch, Th.W.J., 2004. Regional Assessment of the effects of land-use change on landslide hazard by means of physically based modelling. *Nat Hazards* 31, 289-304.

Venables, W.N., Ripley, B.D., 2002. Modern Applied Statistics with S. Springer-Verlag, New York. 518 pp.

Villemus, B., Morel, J.C., Boutin, C., 2007. Experimental assessment of dry retaining wall stability on a rigid foundation. *Eng Struct* 29, 2124-2132.

Walker, P., McCombie, P., Claxton, M., 2007. Plane strain numerical model for drystone retaining walls. *Geotech Eng* 160, Issue GE2, 97-103.

Wieczorek, G.F., 1987. Effect of rainfall intensity and duration on debris flows in central Santa Cruz Mountains, California. *Geol Soc Am Rev Eng Geol* 7, 93–104.

Xu, L., Dai, F.C., Gong, Q.M., Tham, L.G., Min, H., 2011. Irrigation-induced loess flow failure in Heifangtai Platform, North-West China. *Environ Earth Sci*. doi:10.1007/s12665-011-0950-y.

Zezere, J.L., Trigo, R.M., Trigo, I.F., 2005. Shallow and deep landslides induced by rainfall in the Lisbon region (Portugal): assessment of relationships with the North Atlantic Oscillation. *Nat Hazard Earth Syst Sci* 5, 331–344.

Zhang, M., Liu, J., 2010. Controlling factors of loess landslides in western China. *Environ Earth Sci* 59, 1671–1680.

Zhang, X., Koutsabeloulis, N.C., Hope, S., Pearce, A., 2004. A finite element analysis for the stability of drystone masonry retaining walls. *Geotechnique* 54, no. 1, 57-60.

ANNEX I - DOUBLE RING INFILTROMETER TESTS

$$k = \frac{QL}{AH}$$

k = saturated Hydraulic conductivity;

Q = discharge;

L = inner ring depth in the ground;

A = basal surface of the inner ring;

H = hydrostatic head created in the inner ring before the beginning of the test.

L and H can change and can be measured at the beginning of every test. A depends only on the ring used, and in this case is equal to 0.068 m^2.

Q = v * A, where the infiltration velocity (v) is extrapolated from the graph Time vs. Total Cumulated Infiltrated Water and considered equal to the angular coefficient of the trend line of the last five measures, in which the velocity is considered stable for the reaching of the saturated condition.

Site A – Test 1

Time (t) min	Δt min	Tank level (h_{tank}) mm	Δh_{tank} mm	Infiltrometer coeff. mm	Infiltrated Water mm	Cumulated mm	Mean velocity mm/min
0.0	/	37	0	0.43	0.0	0.0	0.0
10.6	10.6	45	8.0	0.43	3.5	3.5	0.3
17.2	6.5	52	7.0	0.43	3.0	6.5	0.4
24.5	7.3	59	7.0	0.43	3.0	9.5	0.4
32.2	7.7	67	8.0	0.43	3.5	13.0	0.4
40.3	8.1	70	3.0	0.43	1.3	14.3	0.4
41.8	1.6	73	3.0	0.43	1.3	15.6	0.4
44.9	3.1	76	3.0	0.43	1.3	16.9	0.4
51.3	6.4	81	5.0	0.43	2.2	19.0	0.4
53.0	1.7	85	4.0	0.43	1.7	20.8	0.4
64.4	11.4	90	5.0	0.43	2.2	22.9	0.4
78.4	14.0	95	5.0	0.43	2.2	25.1	0.3
79.5	1.1	100	5.0	0.43	2.2	27.2	0.3
94.1	14.7	104	4.0	0.43	1.7	29.0	0.3
105.0	10.9	110	6.0	0.43	2.6	31.6	0.3
106.7	1.7	114	4.0	0.43	1.7	33.3	0.3

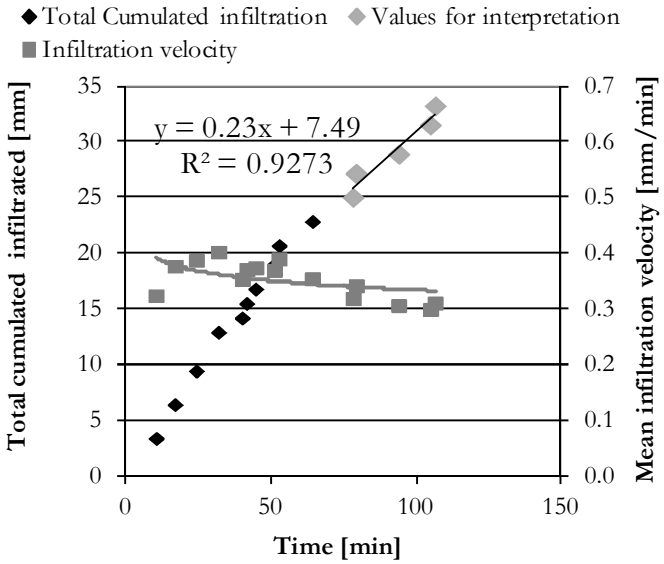

$k_s = 2.05 \times 10^{-6}$ m/s

Figure A1.1: data and interpretation of the double ring infiltrometer test performed on site A. The infiltrometer coefficient is the ratio between the basal area of the inner ring and the basal area of the tank, and it permits the re-scaling of the measures of the infiltrated water (in mm). The reading of this measures is in fact done on the tank scale but for the interpretation of the test they need to be referred to the ring.

Site C – Test 1

Time (t) min	Δt min	Tank level (h_{tank}) mm	Δh_{tank} mm	Infiltrometer coeff. mm	Infiltrated Water mm	Cumulated mm	Mean velocity mm/min
0.00	/	67	0	0.43	0.0	0.0	0.0
0.58	0.58	180	113.0	0.43	48.9	48.9	83.8
1.50	0.92	203	23.0	0.43	9.9	58.8	39.2
2.40	0.90	220	17.0	0.43	7.4	66.2	27.6
3.42	1.02	245	25.0	0.43	10.8	77.0	22.5
4.50	1.08	270	25.0	0.43	10.8	87.8	19.5
5.92	1.42	310	40.0	0.43	17.3	105.1	17.8
7.55	1.63	350	40.0	0.43	17.3	122.4	16.2
10.45	2.90	428	78.0	0.43	33.7	156.1	14.9
11.78	1.33	465	37.0	0.43	16.0	172.1	14.6
14.12	2.33	527	62.0	0.43	26.8	198.9	14.1

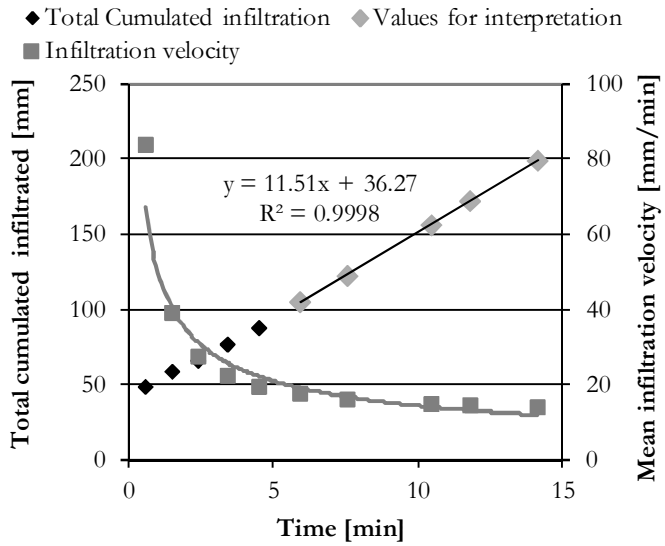

$k_s = 5.48 \times 10^{-5}$ m/s

Figure A1.2: data and interpretation of the first double ring infiltrometer test performed on site C. The infiltrometer coefficient is the ratio between the basal area of the inner ring and the basal area of the tank, and it permits the re-scaling of the measures of the infiltrated water (in mm). The reading of this measures is in fact done on the tank scale but for the interpretation of the test they need to be referred to the ring.

Site C – Test 2

Time (t) min	Δt min	Tank level (h_{tank}) mm	Δh_{tank} mm	Infiltrometer coeff. mm	Infiltrated Water mm	Cumulated mm	Mean velocity mm/min
0.00	/	39	0	0.43	0.0	0.0	0.0
1.70	1.70	54	15.0	0.43	6.5	6.5	3.8
4.13	2.43	82	28.0	0.43	12.1	18.6	4.5
12.27	8.13	205	123.0	0.43	53.2	71.8	5.9
13.80	1.53	232	27.0	0.43	11.7	83.5	6.0
15.73	1.93	264	32.0	0.43	13.8	97.3	6.2
17.37	1.63	276	12.0	0.43	5.2	102.5	5.9
18.83	1.47	290	14.0	0.43	6.1	108.6	5.8
20.27	1.43	305	15.0	0.43	6.5	115.0	5.7
21.87	1.60	322	17.0	0.43	7.4	122.4	5.6
23.42	1.55	340	18.0	0.43	7.8	130.2	5.6
25.00	1.58	356	16.0	0.43	6.9	137.1	5.5
26.85	1.85	374	18.0	0.43	7.8	144.9	5.4
28.42	1.57	389	15.0	0.43	6.5	151.4	5.3
30.15	1.73	410	21.0	0.43	9.1	160.4	5.3
32.28	2.13	431	21.0	0.43	9.1	169.5	5.3
33.77	1.48	450	19.0	0.43	8.2	177.7	5.3
35.68	1.92	469	19.0	0.43	8.2	186.0	5.2
38.88	3.20	508	39.0	0.43	16.9	202.8	5.2

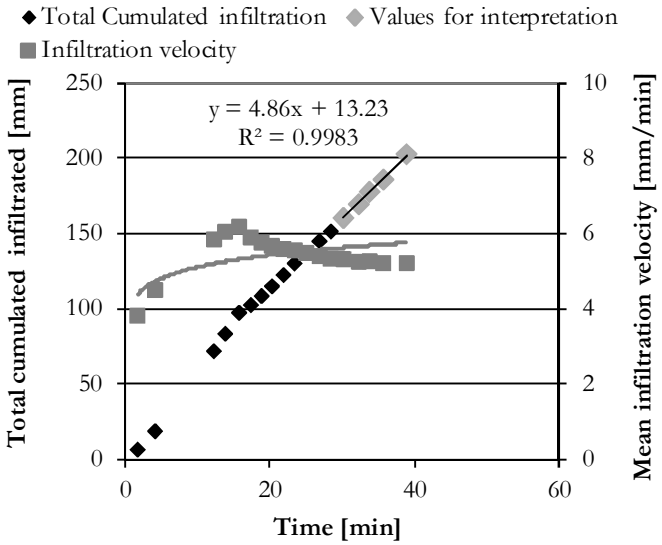

$k_s = 2.16 \times 10^{-5}$ m/s

Figure A1.3: data and interpretation of the second double ring infiltrometer test performed on site C. The infiltrometer coefficient is the ratio between the basal area of the inner ring and the basal area of the tank, and it permits the re-scaling of the measures of the infiltrated water (in mm). The reading of this measures is in fact done on the tank scale but for the interpretation of the test they need to be referred to the ring.

Site D – Test 1

Time (t) min	Δt min	Tank level (h_{tank}) mm	Δh_{tank} mm	Infiltrometer coeff. mm	Infiltrated Water mm	Cumulated mm	Mean velocity mm/min
0.00	/	70	0	0.43	0.0	0.0	0.0
0.85	0.85	78	8.0	0.43	3.5	3.5	4.1
1.77	0.92	85	7.0	0.43	3.0	6.5	3.7
2.60	0.83	93	8.0	0.43	3.5	9.9	3.8
3.50	0.90	101	8.0	0.43	3.5	13.4	3.8
4.37	0.87	109	8.0	0.43	3.5	16.9	3.9
5.58	1.22	120	11.0	0.43	4.8	21.6	3.9
6.95	1.37	135	15.0	0.43	6.5	28.1	4.0
8.45	1.50	147	12.0	0.43	5.2	33.3	3.9
10.15	1.70	163	16.0	0.43	6.9	40.2	4.0
12.47	2.32	181	18.0	0.43	7.8	48.0	3.9
14.45	1.98	198	17.0	0.43	7.4	55.4	3.8
15.48	1.03	204	6.0	0.43	2.6	58.0	3.7
16.60	1.12	218	14.0	0.43	6.1	64.0	3.9
17.98	1.38	231	13.0	0.43	5.6	69.6	3.9
19.28	1.30	243	12.0	0.43	5.2	74.8	3.9
20.73	1.45	254	11.0	0.43	4.8	79.6	3.8
22.03	1.30	266	12.0	0.43	5.2	84.8	3.8
23.70	1.67	279	13.0	0.43	5.6	90.4	3.8
24.63	0.93	284	5.0	0.43	2.2	92.5	3.8
26.10	1.47	304	20.0	0.43	8.6	101.2	3.9
27.60	1.50	315	11.0	0.43	4.8	106.0	3.8
28.97	1.37	323	8.0	0.43	3.5	109.4	3.8
30.10	1.13	334	11.0	0.43	4.8	114.2	3.8
31.10	1.00	345	11.0	0.43	4.8	118.9	3.8
32.40	1.30	360	15.0	0.43	6.5	125.4	3.9
33.63	1.23	373	13.0	0.43	5.6	131.0	3.9
34.78	1.15	389	16.0	0.43	6.9	138.0	4.0
36.08	1.30	402	13.0	0.43	5.6	143.6	4.0
37.67	1.58	414	12.0	0.43	5.2	148.8	3.9
38.95	1.28	427	13.0	0.43	5.6	154.4	4.0
40.42	1.47	433	6.0	0.43	2.6	157.0	3.9
41.82	1.40	450	17.0	0.43	7.4	164.3	3.9
43.63	1.82	464	14.0	0.43	6.1	170.4	3.9
45.83	2.20	478	14.0	0.43	6.1	176.4	3.8
46.27	0.43	491	13.0	0.43	5.6	182.1	3.9
47.60	1.33	504	13.0	0.43	5.6	187.7	3.9
49.12	1.52	515	11.0	0.43	4.8	192.5	3.9
50.65	1.53	530	15.0	0.43	6.5	198.9	3.9
52.05	1.40	541	11.0	0.43	4.8	203.7	3.9
53.57	1.52	553	12.0	0.43	5.2	208.9	3.9
55.02	1.45	566	13.0	0.43	5.6	214.5	3.9

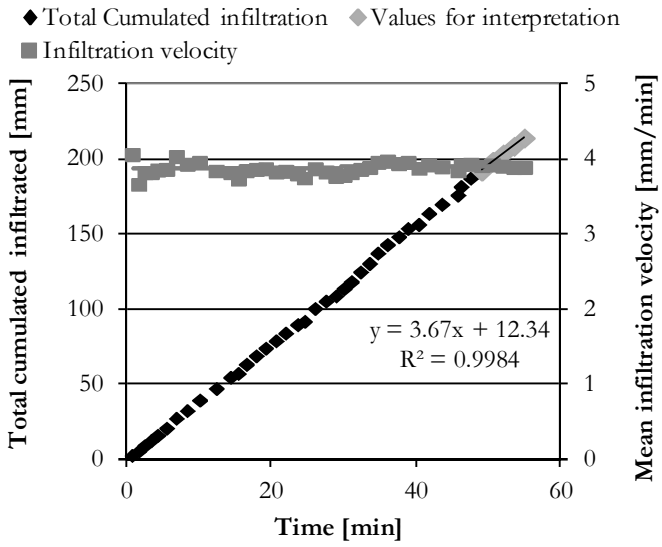

$k_s = 2.82 \times 10^{-5}$ m/s

Figure A1.4: data and interpretation of the first double ring infiltrometer test performed on site D. The infiltrometer coefficient is the ratio between the basal area of the inner ring and the basal area of the tank, and it permits the re-scaling of the measures of the infiltrated water (in mm). The reading of this measures is in fact done on the tank scale but for the interpretation of the test they need to be referred to the ring.

Site D – Test 2

Time (t) min	Δt min	Tank level (h_{tank}) mm	Δh_{tank} mm	Infiltrometer coeff. mm	Infiltrated Water mm	Cumulated mm	Mean velocity mm/min
0.00	/	50	0	0.43	0.0	0.0	0.0
0.45	0.45	52	2.0	0.43	0.9	0.9	1.9
1.13	0.68	59	7.0	0.43	3.0	3.9	3.4
1.90	0.77	67	8.0	0.43	3.5	7.4	3.9
2.80	0.90	75	8.0	0.43	3.5	10.8	3.9
3.63	0.83	83	8.0	0.43	3.5	14.3	3.9
4.10	0.47	87	4.0	0.43	1.7	16.0	3.9
4.68	0.58	91	4.0	0.43	1.7	17.7	3.8
5.65	0.97	103	12.0	0.43	5.2	22.9	4.1
7.03	1.38	118	15.0	0.43	6.5	29.4	4.2
8.20	1.17	130	12.0	0.43	5.2	34.6	4.2
9.20	1.00	138	8.0	0.43	3.5	38.1	4.1
10.60	1.40	159	21.0	0.43	9.1	47.1	4.4
11.83	1.23	168	9.0	0.43	3.9	51.0	4.3
19.45	7.62	249	81.0	0.43	35.0	86.1	4.4
20.88	1.43	267	18.0	0.43	7.8	93.8	4.5
22.53	1.65	283	16.0	0.43	6.9	100.8	4.5
23.63	1.10	299	16.0	0.43	6.9	107.7	4.6
25.08	1.45	315	16.0	0.43	6.9	114.6	4.6
27.65	2.57	346	31.0	0.43	13.4	128.0	4.6
29.23	1.58	363	17.0	0.43	7.4	135.4	4.6
30.53	1.30	379	16.0	0.43	6.9	142.3	4.7
32.03	1.50	395	16.0	0.43	6.9	149.2	4.7
33.43	1.40	411	16.0	0.43	6.9	156.1	4.7
35.12	1.68	422	11.0	0.43	4.8	160.9	4.6
36.45	1.33	444	22.0	0.43	9.5	170.4	4.7
38.03	1.58	462	18.0	0.43	7.8	178.2	4.7
39.80	1.77	479	17.0	0.43	7.4	185.5	4.7

41.28	1.48	496	17.0	0.43	7.4	192.9	4.7
42.80	1.52	511	15.0	0.43	6.5	199.4	4.7
44.37	1.57	535	24.0	0.43	10.4	209.7	4.7
46.20	1.83	556	21.0	0.43	9.1	218.8	4.7

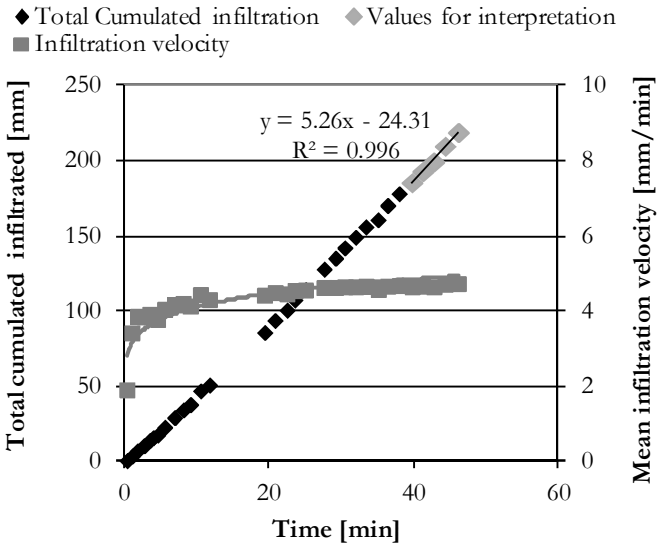

$k_s = 3.88 \times 10^{-5}$ m/s

Figure A1.5: data and interpretation of the second double ring infiltrometer test performed on site d. The infiltrometer coefficient is the ratio between the basal area of the inner ring and the basal area of the tank, and it permits the re-scaling of the measures of the infiltrated water (in mm). The reading of this measures is in fact done on the tank scale but for the interpretation of the test they need to be referred to the ring.

Site E – Test 1

Time (t) min	Δt min	Tank level (h_{tank}) mm	Δh_{tank} mm	Infiltrometer coeff. mm	Infiltrated Water mm	Cumulated mm	Mean velocity mm/min
0.00	/	60	0	0.43	0.0	0.0	0.0
2.57	1.7	63	3.0	0.43	1.3	1.3	0.5
3.65	1.08	81	18.0	0.43	7.8	9.1	2.5
5.00	1.35	92	11.0	0.43	4.8	13.8	2.8
6.12	1.12	100	8.0	0.43	3.5	17.3	2.8
7.52	1.40	113	13.0	0.43	5.6	22.9	3.0
9.07	1.55	124	11.0	0.43	4.8	27.7	3.1
10.43	1.36	136	12.0	0.43	5.2	32.9	3.2
12.02	1.59	149	13.0	0.43	5.6	38.5	3.2
13.48	1.46	161	12.0	0.43	5.2	43.7	3.2
14.92	1.44	173	12.0	0.43	5.2	48.9	3.3
16.43	1.51	187	14.0	0.43	6.1	54.9	3.3
17.93	1.50	200	13.0	0.43	5.6	60.5	3.4
19.37	1.44	213	13.0	0.43	5.6	66.2	3.4
21.13	1.76	226	13.0	0.43	5.6	71.8	3.4
22.50	1.37	241	15.0	0.43	6.5	78.3	3.5
24.05	1.55	255	14.0	0.43	6.1	84.3	3.5
25.45	1.40	269	14.0	0.43	6.1	90.4	3.6
27.33	1.88	286	17.0	0.43	7.4	97.7	3.6
29.25	1.92	300	14.0	0.43	6.1	103.8	3.5
30.92	1.67	315	15.0	0.43	6.5	110.3	3.6
32.45	1.53	330	15.0	0.43	6.5	116.8	3.6

34.25	1.80	345	15.0	0.43	6.5	123.3	3.6
35.83	1.58	360	15.0	0.43	6.5	129.7	3.6
37.48	1.65	374	14.0	0.43	6.1	135.8	3.6
39.03	1.55	390	16.0	0.43	6.9	142.7	3.7
40.67	1.64	405	15.0	0.43	6.5	149.2	3.7
43.25	2.58	422	17.0	0.43	7.4	156.6	3.6
44.47	1.22	438	16.0	0.43	6.9	163.5	3.7
46.28	1.81	454	16.0	0.43	6.9	170.4	3.7
47.87	1.59	470	16.0	0.43	6.9	177.3	3.7
49.73	1.86	486	16.0	0.43	6.9	184.2	3.7
50.83	1.10	500	14.0	0.43	6.1	190.3	3.7
52.5	1.67	513	13.0	0.43	5.6	195.9	3.7
53.73	1.23	526	13.0	0.43	5.6	201.5	3.8
55.12	1.39	540	14.0	0.43	6.1	207.6	3.8

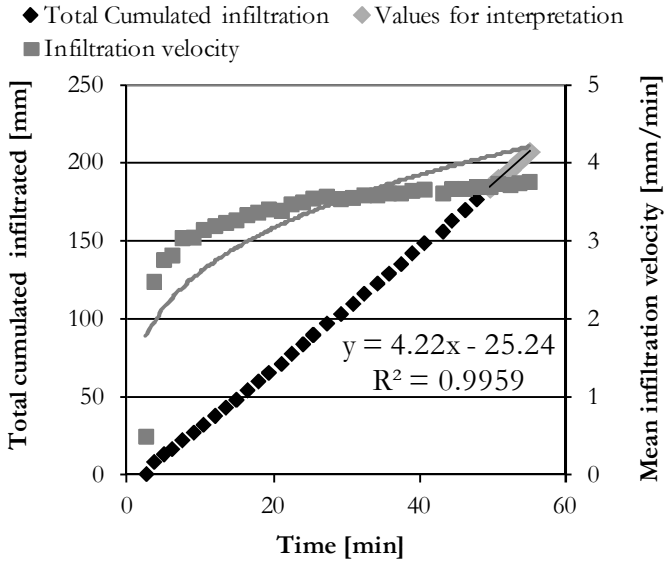

$k_s = 3.48 \times 10^{-5}$ m/s

Figure A1.6: data and interpretation of the first double ring infiltrometer test performed on site E. The infiltrometer coefficient is the ratio between the basal area of the inner ring and the basal area of the tank, and it permits the re-scaling of the measures of the infiltrated water (in mm). The reading of this measures is in fact done on the tank scale but for the interpretation of the test they need to be referred to the ring.

Site E – Test 2

Time (t) min	Δt min	Tank level (h_{tank}) mm	Δh_{tank} mm	Infiltrometer coeff. mm	Infiltrated Water mm	Cumulated mm	Mean velocity mm/min
0.00	/	37	0	0.43	0.0	0.0	0.0
0.60	0.36	45	8.0	0.43	3.5	3.5	5.8
1.87	1.27	62	17.0	0.43	7.4	10.8	5.8
2.65	0.78	70	8.0	0.43	3.5	14.3	5.4
3.38	0.73	80	10.0	0.43	4.3	18.6	5.5
4.25	0.87	93	13.0	0.43	5.6	24.2	5.7
5.45	1.20	104	11.0	0.43	4.8	29.0	5.3
6.53	1.08	116	12.0	0.43	5.2	34.2	5.2
8.90	2.37	140	24.0	0.43	10.4	44.5	5.0
10.13	1.23	155	15.0	0.43	6.5	51.0	5.0
11.73	1.60	171	16.0	0.43	6.9	58.0	4.9
13.05	1.32	185	14.0	0.43	6.1	64.0	4.9

14.42	1.37	198	13.0	0.43	5.6	69.6	4.8
15.77	1.35	213	15.0	0.43	6.5	76.1	4.8
17.00	1.23	226	13.0	0.43	5.6	81.7	4.8
18.55	1.55	241	15.0	0.43	6.5	88.2	4.8
19.83	1.28	255	14.0	0.43	6.1	94.3	4.8
21.20	1.37	267	12.0	0.43	5.2	99.5	4.7
22.52	1.32	281	14.0	0.43	6.1	105.5	4.7
23.90	1.38	300	19.0	0.43	8.2	113.7	4.8
25.20	1.30	312	12.0	0.43	5.2	118.9	4.7
26.67	1.47	326	14.0	0.43	6.1	125.0	4.7
28.27	1.60	345	19.0	0.43	8.2	133.2	4.7
30.02	1.75	364	19.0	0.43	8.2	141.4	4.7
31.07	1.05	371	7.0	0.43	3.0	144.4	4.6
32.17	1.10	393	22.0	0.43	9.5	154.0	4.8
33.55	1.38	409	16.0	0.43	6.9	160.9	4.8
35.22	1.67	424	15.0	0.43	6.5	167.4	4.8
36.43	1.21	441	17.0	0.43	7.4	174.7	4.8
37.83	1.40	454	13.0	0.43	5.6	180.3	4.8
38.40	0.57	458	4.0	0.43	1.7	182.1	4.7
39.42	1.02	470	12.0	0.43	5.2	187.3	4.8
40.77	1.35	484	14.0	0.43	6.1	193.3	4.7
42.52	1.75	500	16.0	0.43	6.9	200.2	4.7
43.90	1.38	516	16.0	0.43	6.9	207.2	4.7
45.47	1.57	532	16.0	0.43	6.9	214.1	4.7
46.83	1.36	550	18.0	0.43	7.8	221.9	4.7
48.28	1.45	566	16.0	0.43	6.9	228.8	4.7

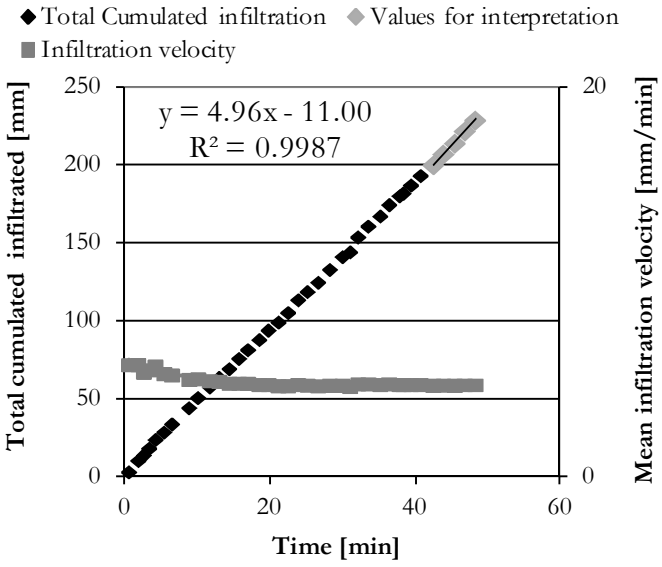

$k_s = 4.08 \times 10^{-5}$ m/s

Figure A1.7: data and interpretation of the second double ring infiltrometer test performed on site E. The infiltrometer coefficient is the ratio between the basal area of the inner ring and the basal area of the tank, and it permits the re-scaling of the measures of the infiltrated water (in mm). The reading of this measures is in fact done on the tank scale but for the interpretation of the test they need to be referred to the ring.

ANNEX II - HOLE INFILTROMETER TESTS

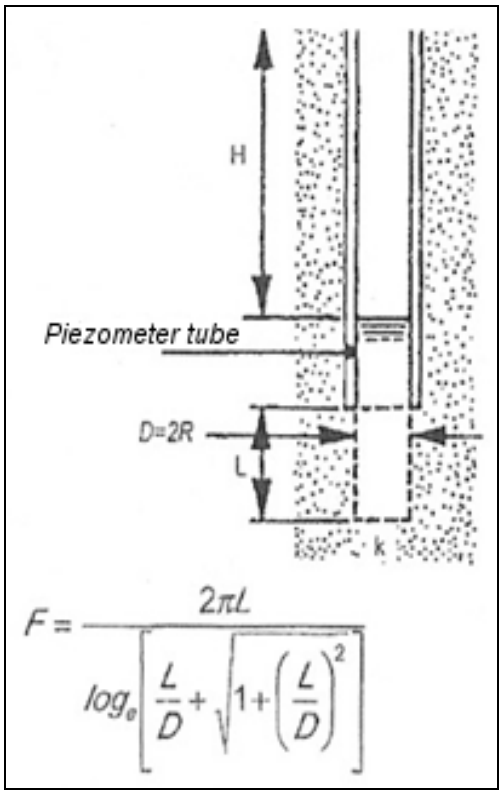

Figure A2.1: scheme of the geometry of the test. D is the inner diameter of the piezometric tube; H is the height of the hole where filtering is impeded; L is the height of the filtering part of the piezometer.

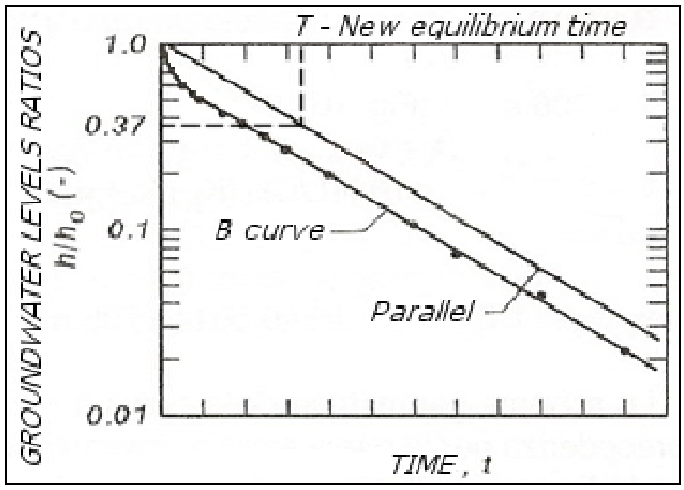

Figure A2.2: interpretation scheme of the hole infiltrometric tests. Modified from Cestari (2005). h is the groundwater level measured in the piezometer in different times during the test, while h_0 is the static supposed groundwater level.

$$k = \frac{A}{FT}$$

k = saturated Hydraulic conductivity;

A = filtering area of the piezometer tube;

F = form coefficient dependent on the characteristics of the piezometer, calculated as shown in Fig. 1;

T = time for the reaching of a new equilibrium.

The test consists in the input of water into the piezometer tube and in measuring the decreasing levels. The measures were done using a continuous piezometric datalogger that acquired data every 2 seconds. The test is performed in an unsaturated soil and so it was decided to interpret it as a Lefranc test in unsaturated soils with an unknown static level of groundwater table.

For the interpretation, the scheme used is that proposed in Fig. 2. At first a static groundwater level must be defined. It can be done, considering that curve B has to assume a straight trend. If the curve assumes a concave trend it means that the supposed static groundwater level is too deep, while a convex trend indicate that the level is too shallow. Once recognized the straight trend, a line parallel to it and passing for (0, 1) need to be drawn. The time value of this line that corresponds to h/h0 = 0.37 is the new equilibrium time (T) that permits to calculate the saturated hydraulic conductivity from the formula shown above.

Site A – Test 1 – August 2009

h_0, Supposed groundwater level	**1.40**	**m**
Total lenght of the piezometric tube:	0.95	m
H, not filtering lenght:	0.10	m
L, filtering lenght:	0.85	m
D, inner diameter of the piezometric tube:	0.036	m
F, Form coefficient:	**1.385**	**(-)**
A, Mean filtering area	**0.096**	**m^2**
T, New equilibrium time	**1691**	**s**
Hydraulic conductivity (m/s) k=A/FT	**4.10E-05**	**m/s^2**

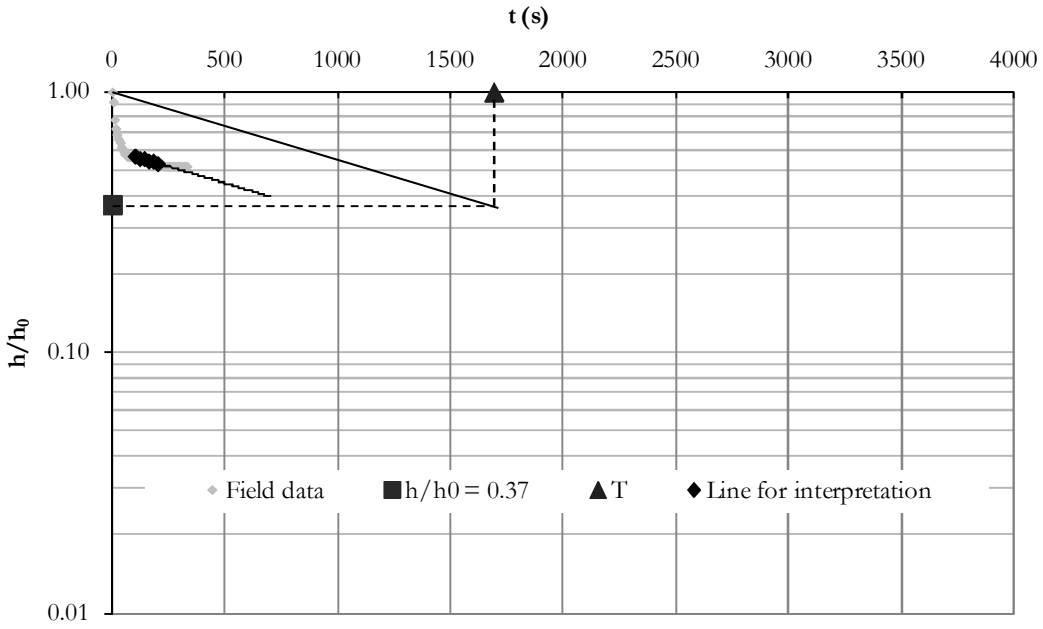

Site A – Test 2 – September 2009

h_0, Supposed groundwater level	**1.40**	**m**
Total lenght of the piezometric tube:	0.95	m
H, not filtering lenght:	0.10	m
L, filtering lenght:	0.85	m
D, inner diameter of the piezometric tube:	0.036	m
F, Form coefficient:	**1.385**	**(-)**
A, Mean filtering area	**0.096**	**m^2**
T, New equilibrium time	**52100**	**s**
Hydraulic conductivity (m/s) k=A/FT	**1.33E-06**	**m/s^2**

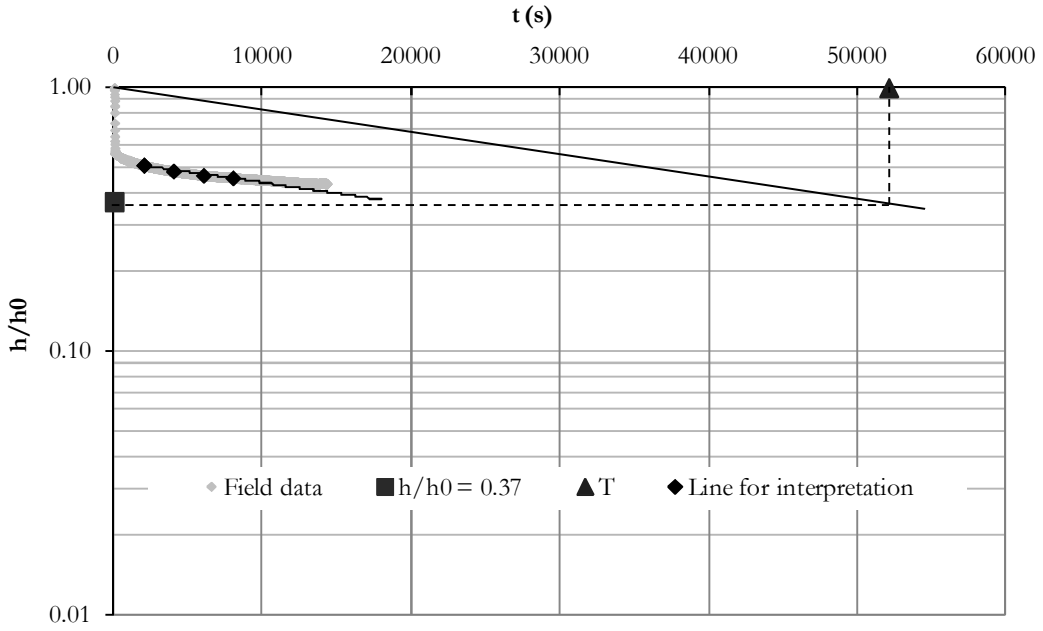

Site A – Test 3 – October 2009

h_0, Supposed groundwater level	**1.40**	**m**
Total lenght of the piezometric tube:	0.95	m
H, not filtering lenght:	0.10	m
L, filtering lenght:	0.85	m
D, inner diameter of the piezometric tube:	0.036	m
F, Form coefficient:	**1.385**	**(-)**
A, Mean filtering area	**0.096**	**m^2**
T, New equilibrium time	**1840**	**s**
Hydraulic conductivity (m/s) k=A/FT	**3.77E-05**	**m/s**

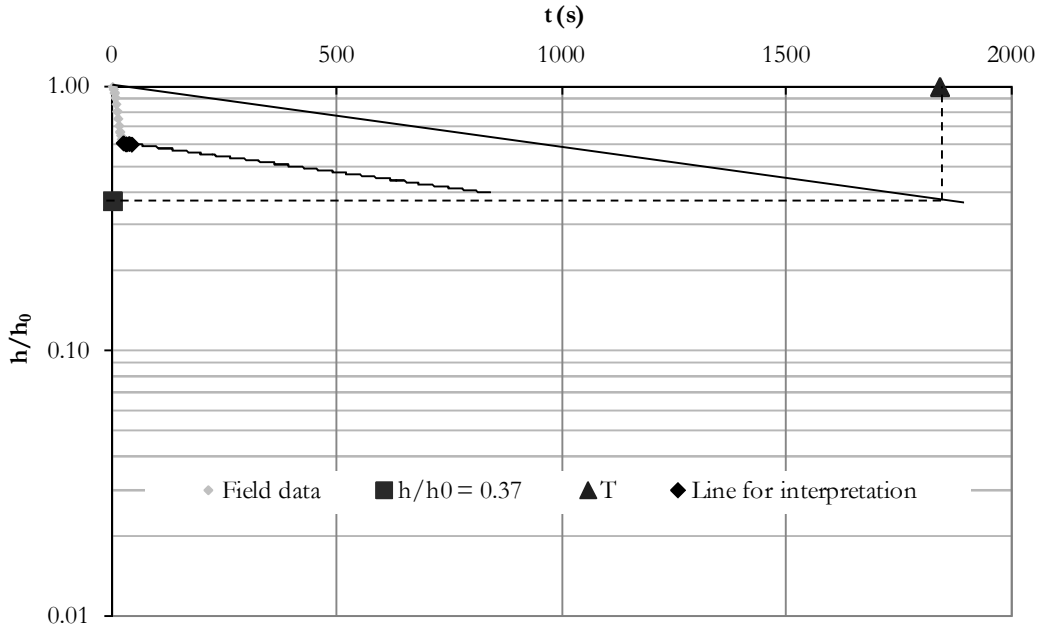

Site B – Test 1 – October 2009

h_0, Supposed groundwater level	**1.80**	**m**
Total lenght of the piezometric tube:	0.90	m
H, not filtering lenght:	0.10	m
L, filtering lenght:	0.80	m
D, inner diameter of the piezometric tube:	0.036	m
F, Form coefficient:	**1.325**	**(-)**
A, Mean filtering area	**0.090**	**m^2**
T, New equilibrium time	**1042**	**s**
Hydraulic conductivity (m/s) k=A/FT	**6.56E-05**	**m/s**

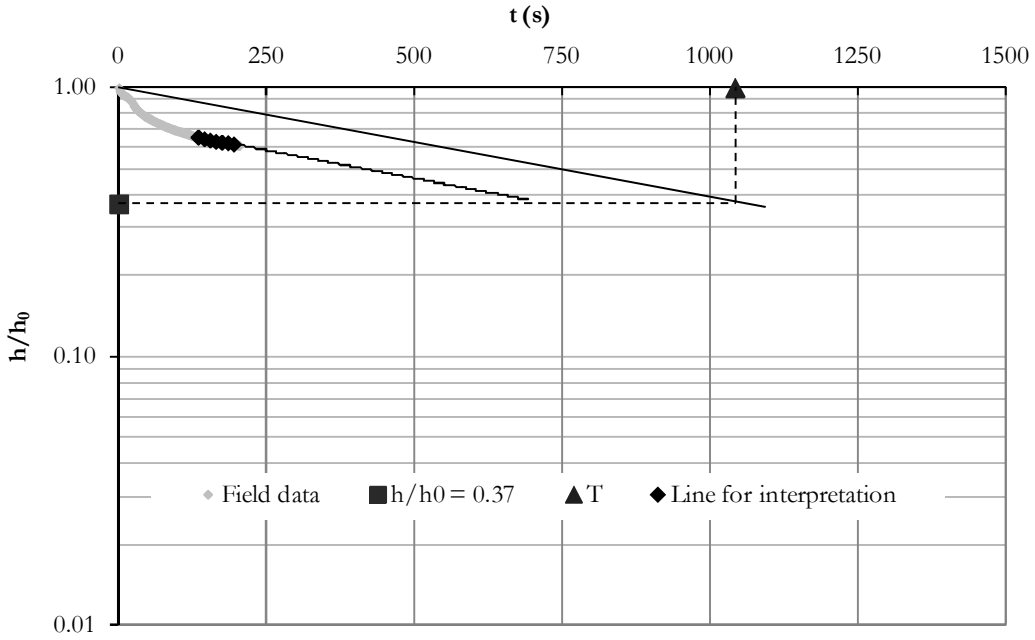

Site C – Test 1 – October 2009

h_0, Supposed groundwater level	**1.80**	**m**
Total lenght of the piezometric tube:	0.90	m
H, not filtering lenght:	0.10	m
L, filtering lenght:	0.80	m
D, inner diameter of the piezometric tube:	0.036	m
F, Form coefficient:	**1.325**	**(-)**
A, Mean filtering area	**0.090**	**m^2**
T, New equilibrium time	**12720**	**s**
Hydraulic conductivity (m/s) k=A/FT	**5.37E-06**	**m/s**

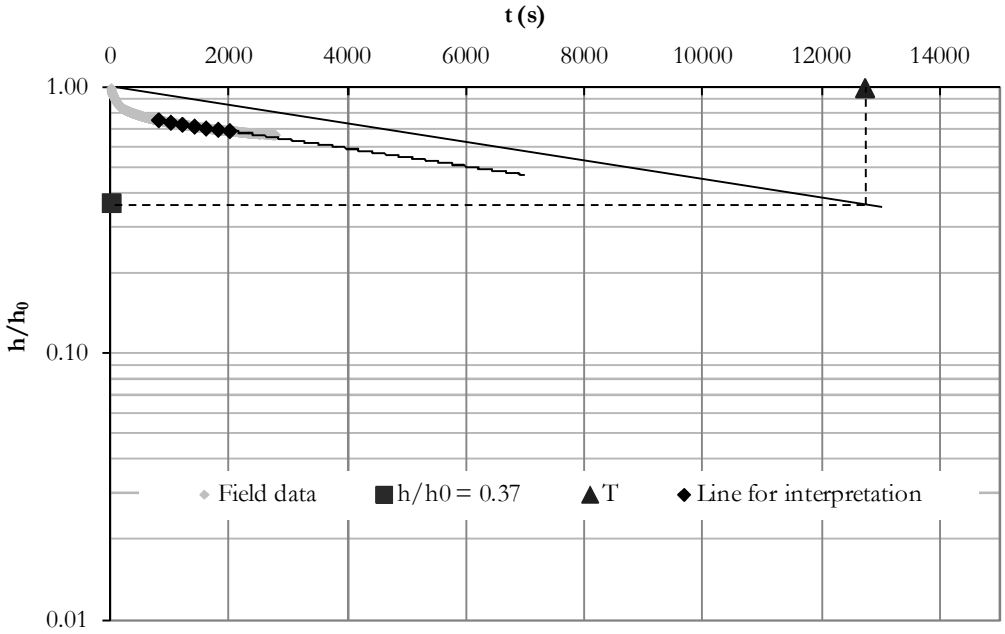

Site D – Test 1 – October 2009

h_0, Supposed groundwater level	**1.70**	**m**
Total lenght of the piezometric tube:	0.90	m
H, not filtering lenght:	0.10	m
L, filtering lenght:	0.80	m
D, inner diameter of the piezometric tube:	0.036	m
F, Form coefficient:	**1.325**	**(-)**
A, Mean filtering area	**0.090**	**m^2**
T, New equilibrium time	**3755**	**s**
Hydraulic conductivity (m/s) k=A/FT	**1.82E-05**	**m/s**

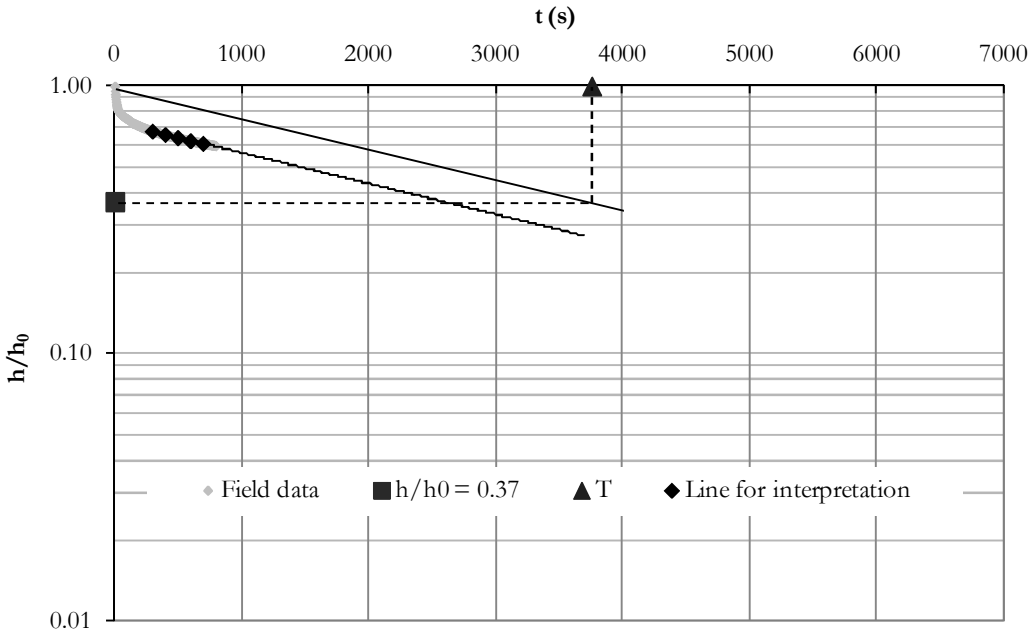

Site E – Test 1 – September 2009

h_0, Supposed groundwater level	**1.50**	**m**
Total lenght of the piezometric tube:	0.90	m
H, not filtering lenght:	0.05	m
L, filtering lenght:	0.85	m
D, inner diameter of the piezometric tube:	0.036	m
F, Form coefficient:	**1.385**	**(-)**
A, Mean filtering area	**0.096**	**m^2**
T, New equilibrium time	**4490**	**s**
Hydraulic conductivity (m/s) k=A/FT	**1.55E-05**	**m/s**

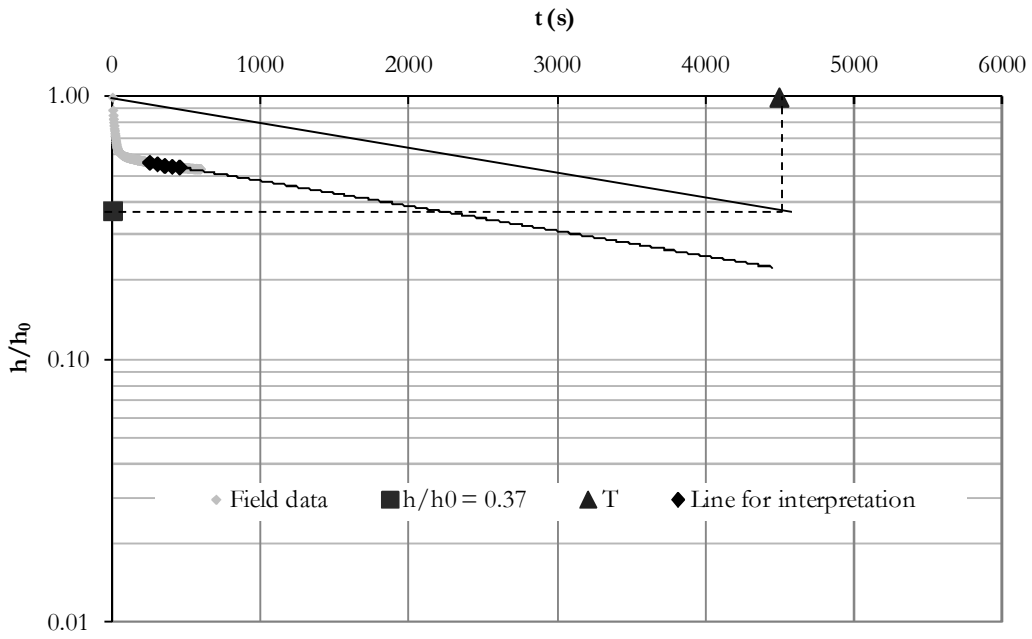

Site E – Test 2 – October 2009

h_0, Supposed groundwater level	**1.50**	**m**
Total lenght of the piezometric tube:	0.90	m
H, not filtering lenght:	0.05	m
L, filtering lenght:	0.85	m
D, inner diameter of the piezometric tube:	0.036	m
F, Form coefficient:	**1.385**	**(-)**
A, Mean filtering area	**0.096**	**m^2**
T, New equilibrium time	**6075**	**s**
Hydraulic conductivity (m/s) k=A/FT	**1.14E-05**	**m/s**

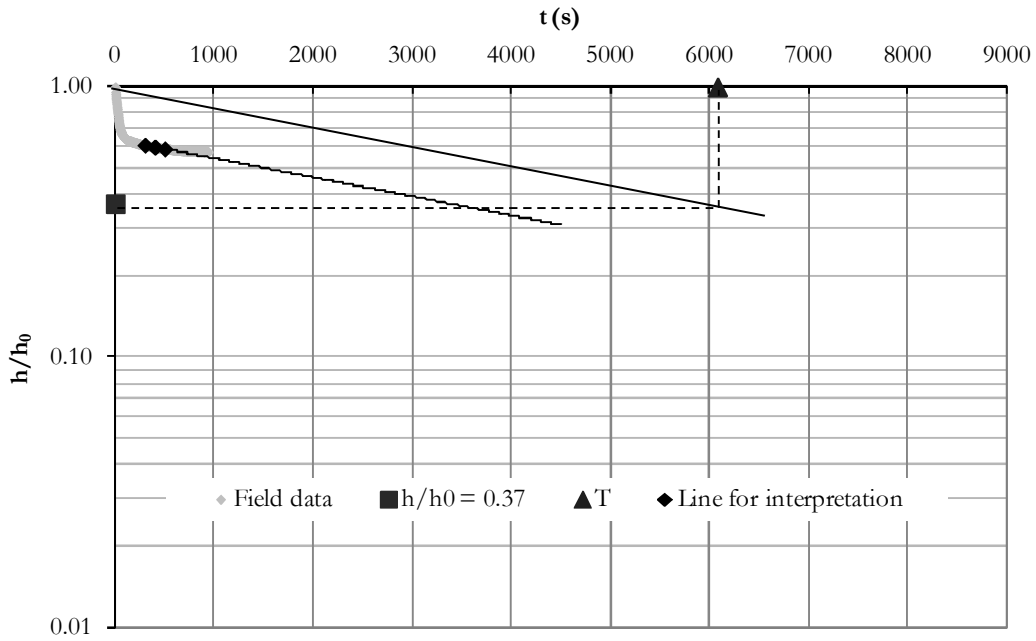

Site F – Test 1 – October 2009

h_0, Supposed groundwater level	**1.30**	**m**
Total lenght of the piezometric tube:	0.90	m
H, not filtering lenght:	0.05	m
L, filtering lenght:	0.85	m
D, inner diameter of the piezometric tube:	0.036	m
F, Form coefficient:	**1.385**	**(-)**
A, Mean filtering area	**0.096**	**m^2**
T, New equilibrium time	**6735**	**s**
Hydraulic conductivity (m/s) k=A/FT	**1.03E-05**	**m/s**

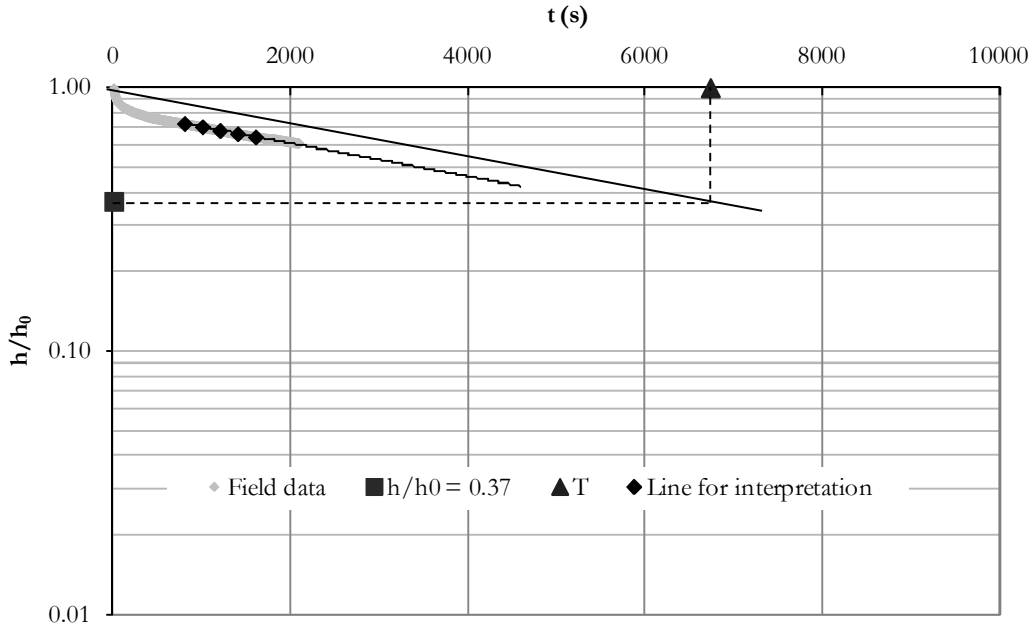

Site G – Test 1 – August 2009

h_0, Supposed groundwater level	**2.00**	**m**
Total lenght of the piezometric tube:	1.40	m
H, not filtering lenght:	0.40	m
L, filtering lenght:	1.00	m
D, inner diameter of the piezometric tube:	0.036	m
F, Form coefficient:	**1.564**	**(-)**
A, Mean filtering area	**0.113**	**m^2**
T, New equilibrium time	**630**	**s**
Hydraulic conductivity (m/s) k=A/FT	**1.15E-04**	**m/s**

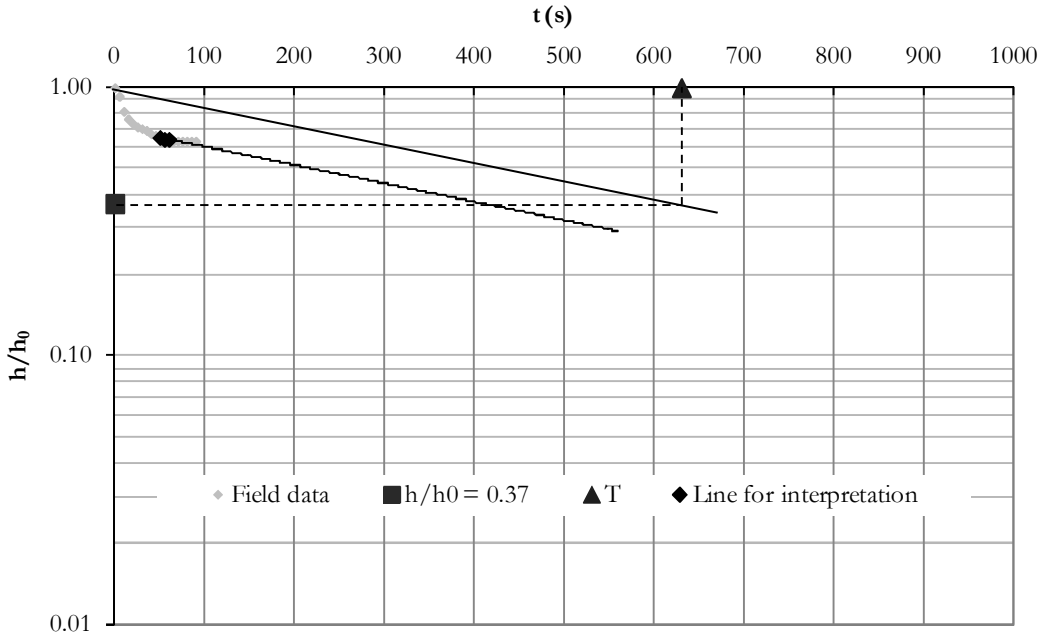

Site G – Test 2 – September 2009

h_0, Supposed groundwater level	**2.00**	**m**
Total lenght of the piezometric tube:	1.40	m
H, not filtering lenght:	0.40	m
L, filtering lenght:	1.00	m
D, inner diameter of the piezometric tube:	0.036	m
F, Form coefficient:	**1.564**	**(-)**
A, Mean filtering area	**0.113**	**m^2**
T, New equilibrium time	**717**	**s**
Hydraulic conductivity (m/s) k=A/FT	**1.01E-04**	**m/s**

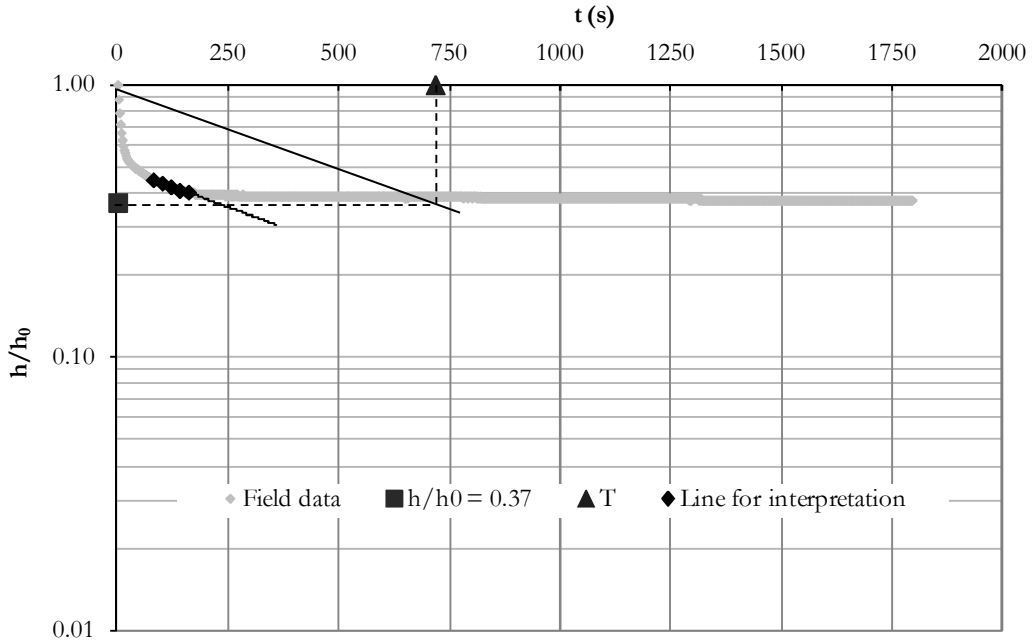

ANNEX III – GRAIN SIZE ANALYSIS

Site A

Table A3.1: laboratory data for the drawing of the grain size curves of different samples from Site A.

A_a (SM)		A_o (GM)		A_d (SM)		A_f (SM)	
D [mm]	**%**	**D [mm]**	**%**	**D [mm]**	**%**	**D [mm]**	**%**
19.10000	100.0	72.00000	100.0	24.20000	100.0	36.40000	100.0
9.50000	90.0	19.50000	79.3	9.50000	88.0	9.50000	76.6
4.76000	80.2	9.50000	64.5	4.76000	77.5	4.76000	70.6
2.40000	72.0	4.76000	57.3	2.40000	67.5	2.40000	63.2
1.20000	62.4	2.40000	51.1	1.20000	56.9	1.20000	53.9
0.60000	57.2	1.20000	43.5	0.60000	52.1	0.60000	49.3
0.30000	40.3	0.60000	40.2	0.30000	38.1	0.30000	35.1
0.15000	28.5	0.30000	29.9	0.15000	28.2	0.15000	24.8
0.07400	21.0	0.15000	22.9	0.07400	21.0	0.07400	17.7
0.06244	12.1	0.07400	18.9	0.06380	10.4	0.06205	10.7
0.04553	9.7	0.06271	10.6	0.04624	8.4	0.04734	5.4
0.03339	6.6	0.04586	8.2	0.03342	6.5	0.03352	5.3
0.02429	4.0	0.03321	6.4	0.02403	5.1	0.02399	4.4
0.01736	3.0	0.02397	4.7	0.01718	4.0	0.01723	3.2
0.01280	2.2	0.01715	3.8	0.01267	3.1	0.01267	2.6
0.00909	1.7	0.01265	2.9	0.00903	2.4	0.00902	2.1
0.00646	1.2	0.00902	2.2	0.00642	1.9	0.00638	2.1
0.00459	0.7	0.00637	1.2	0.00456	1.5	0.00452	1.9
0.00325	0.6	0.00457	1.0	0.00324	0.9	0.00323	0.9
0.00230	0.5	0.00324	0.7	0.00230	0.5	0.00246	0.6
0.00133	0.1	0.00230	0.4	0.00133	0.4	0.00133	0.5
		0.00133	0.3				

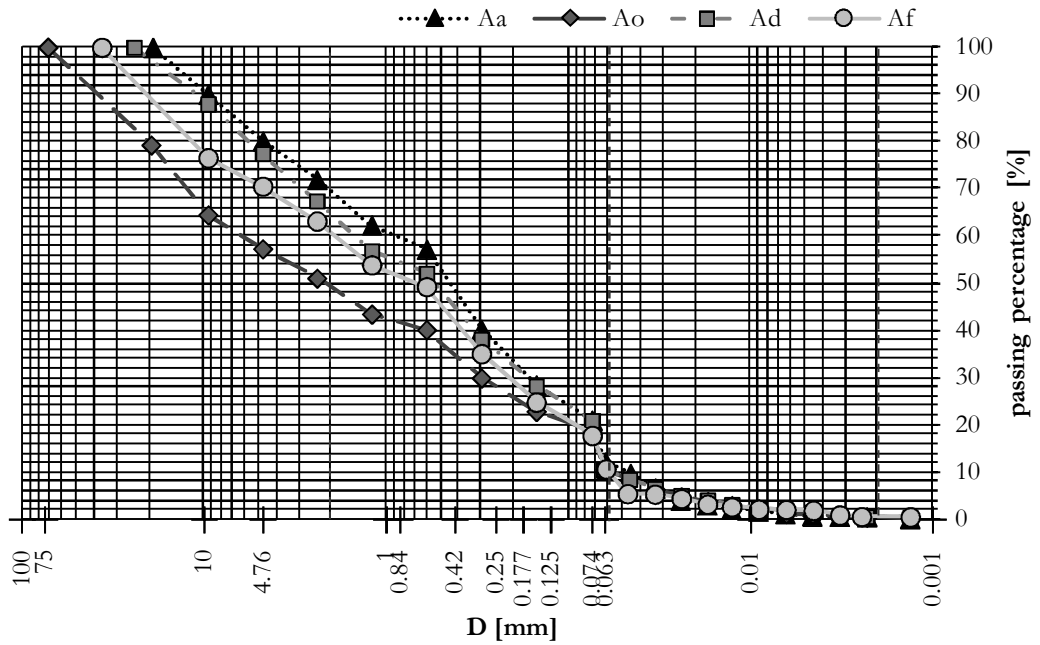

ID	Description ASTM	% pebbles	% gravel	% sand	% silt	% clay	D60	D10	Cu D60/D10
A_a	SM (silty sand with gravel)	0.0	19.8	59.2	20.5	0.5	0.9	0.044	20
A_o	GM (silty gravel with sand)	0.0	42.7	38.4	17.9	1.0	6.4	0.047	136
A_d	SM (silty sand with gravel)	0.0	22.5	61.2	14.8	1.5	1.4	0.07	20
A_f	SM (silty sand with gravel)	0.0	29.4	52.8	15.8	1.9	2	0.05	40

Figure A3.1: grain size curves from samples collected in Site A in August 2009 (A_a), October 2009 (A_o), December 2009 (A_d), and February 2010 (A_f).

Site B

Table A3.2: laboratory data for the drawing of the grain size curves of different samples from Site B.

B_o (GSM)		B_f (GM)	
D [mm]	**%**	**D [mm]**	**%**
36.00000	100.0	34.70000	100.0
19.50000	84.7	9.50000	55.3
9.50000	72.8	4.76000	46.1
4.76000	58.9	2.40000	36.8
2.40000	49.9	1.20000	28.3
1.20000	40.8	0.60000	24.6
0.60000	36.9	0.30000	15.1
0.30000	26.8	0.15000	9.8
0.15000	20.8	0.07400	7.5
0.07400	17.5	0.06150	4.8
0.06244	9.9	0.04538	3.6
0.04553	7.6	0.03334	2.4
0.03339	5.1	0.02426	1.5
0.02429	3.7	0.01734	1.1
0.01736	2.5	0.01275	0.9
0.01280	1.8	0.00906	0.8
0.00909	1.4	0.00642	0.7
0.00646	1.0	0.00458	0.3
0.00459	0.6	0.00325	0.2
0.00325	0.2	0.00246	0.2
0.00230	0.0	0.00133	0.1
0.00133	0.0		

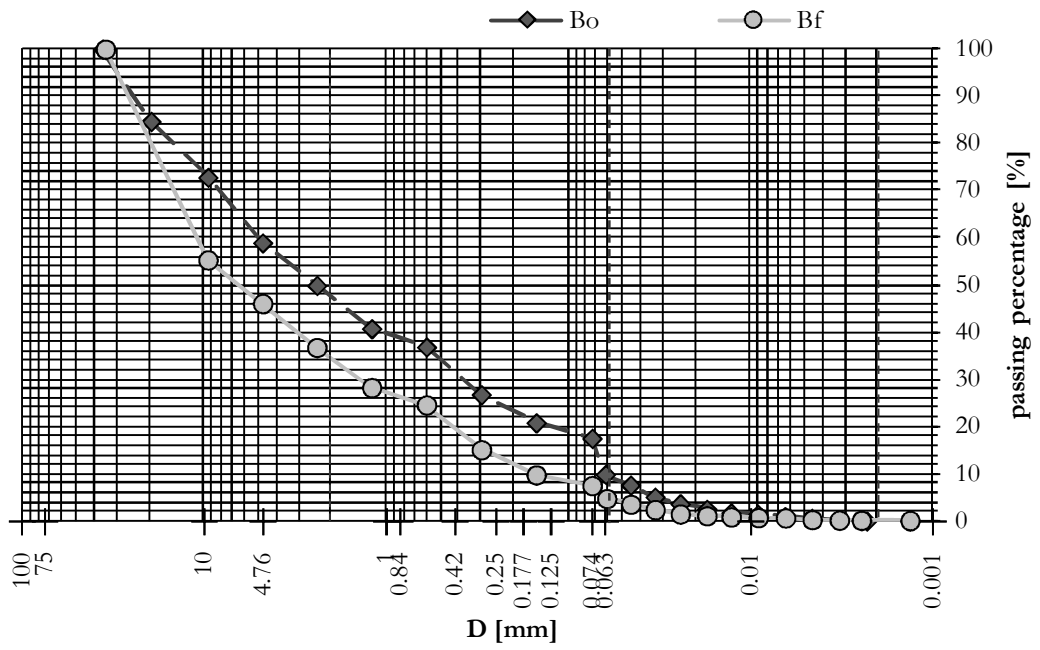

ID	Description ASTM	% pebbles	% gravel	% sand	% silt	% clay	D60	D10	Cu D60/D10
B_o	GSM (silty gravel and sand)	0.0	41.1	41.4	16.5	1.0	5.1	0.065	78
B_f	GM (silty gravel with sand)	0.0	53.9	38.6	7.0	0.5	11	0.15	73

Figure A3.2: grain size curves from samples collected in Site A in October 2009 (B_o), and February 2010 (B_f).

Site C

Table A3.3: laboratory data for the drawing of the grain size curves of different samples from Site C.

C_a (GM)		C_o (SM)		C_d (GM)		C_f (GM)	
D [mm]	%	D [mm]	%	D [mm]	%	D [mm]	%
37.70000	100.0	36.00000	100.0	46.00000	100.0	71.20000	100.0
9.50000	67.2	19.50000	83.8	9.50000	70.5	50.58000	61.9
4.76000	60.6	9.50000	78.4	4.76000	61.9	9.50000	31.1
2.40000	55.3	4.76000	68.1	2.40000	55.6	4.76000	26.8
1.20000	48.8	2.40000	60.3	1.20000	48.3	2.40000	22.3
0.60000	45.2	1.20000	51.7	0.60000	45.1	1.20000	17.7
0.30000	34.7	0.60000	48.0	0.30000	36.6	0.60000	15.8
0.15000	26.5	0.30000	38.4	0.15000	30.5	0.30000	10.3
0.07400	19.7	0.15000	31.5	0.07400	25.4	0.15000	7.0
0.06216	11.7	0.07400	25.7	0.06433	11.9	0.07400	5.9
0.04560	9.0	0.06161	16.1	0.04624	10.2	0.06155	3.1
0.03347	6.0	0.04511	12.8	0.03334	8.2	0.04507	2.4
0.02403	4.7	0.03282	9.9	0.02401	6.2	0.03295	1.8
0.01725	3.4	0.02385	7.0	0.01723	4.6	0.02383	1.3
0.01269	2.8	0.01701	6.0	0.01267	3.8	0.01699	1.2
0.00903	2.2	0.01254	5.0	0.00903	2.9	0.01257	0.9
0.00642	1.7	0.00897	3.7	0.00642	2.2	0.00895	0.8
0.00459	0.6	0.00639	2.9	0.00456	1.6	0.00638	0.6
0.00325	0.6	0.00455	2.1	0.00324	1.1	0.00454	0.4
0.00230	0.6	0.00323	1.3	0.00230	0.5	0.00323	0.3
0.00133	0.1	0.00230	0.7	0.00133	0.4	0.00246	0.2
		0.00133	0.1			0.00133	0.1

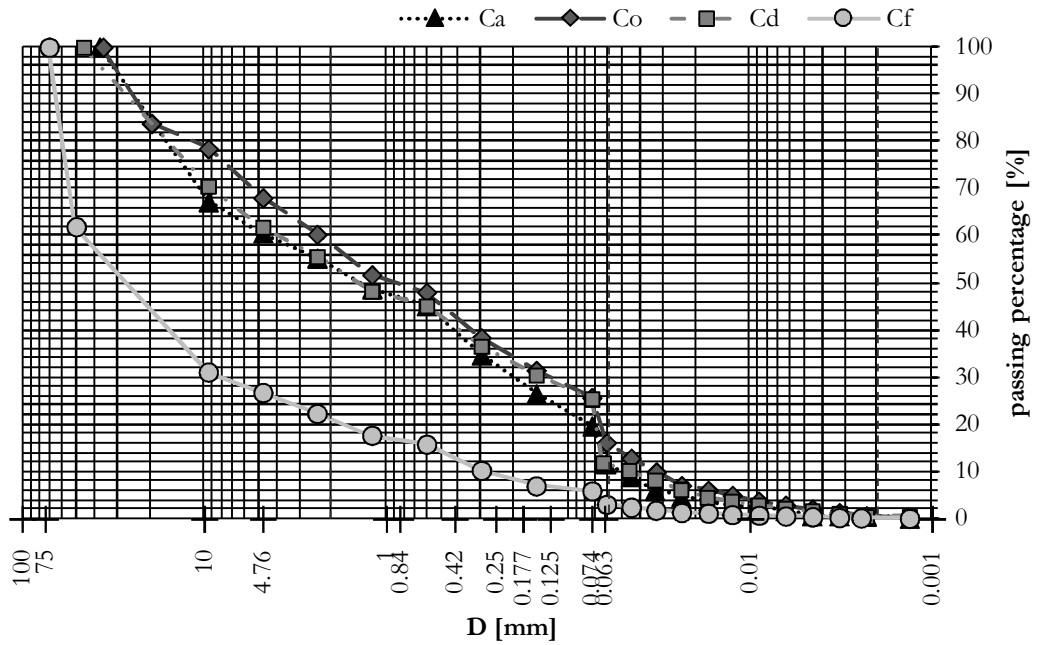

ID	Description ASTM	% pebbles	% gravel	% sand	% silt	% clay	D60	D10	Cu D60/D10
C_a	GM (silty gravel with sand)	0.0	39.4	35.7	24.0	1.0	4.5	0.05	90
C_o	SM (silty sand with gravel)	0.0	31.9	42.4	23.7	2.0	2.9	0.035	83
C_d	GM (silty gravel with sand)	0.0	38.1	36.4	24.0	1.5	4	0.045	89
C_f	GM (silty gravel with sand)	0.0	73.2	21.9	4.4	0.5	42	0.3	140

Figure A3.3: grain size curves from samples collected in Site A in August 2009 (C_a), October 2009 (C_o), December 2009 (C_d), and February 2010 (C_f).

Site D

Table A3.4: laboratory data for the drawing of the grain size curves of different samples from Site D.

D_a (SM)		D_o (SM)	
D [mm]	**%**	**D [mm]**	**%**
25.20000	100.0	39.00000	100.0
9.50000	80.6	19.50000	90.2
4.76000	70.7	9.50000	79.1
2.40000	61.8	4.76000	67.9
1.20000	52.1	2.40000	60.0
0.60000	47.3	1.20000	51.3
0.30000	33.0	0.60000	47.3
0.15000	22.4	0.30000	36.4
0.07400	16.2	0.15000	29.0
0.06244	9.2	0.07400	24.1
0.04553	7.0	0.06161	15.1
0.03339	4.8	0.04454	13.2
0.02429	3.9	0.03269	9.7
0.01736	2.8	0.02365	7.5
0.01280	2.2	0.01699	5.8
0.00909	1.6	0.01254	4.7
0.00646	1.1	0.00897	3.5
0.00459	0.9	0.00639	2.7
0.00325	0.6	0.00454	2.1
0.00230	0.4	0.00323	1.3
0.00133	0.2	0.00230	0.7
		0.00133	0.2

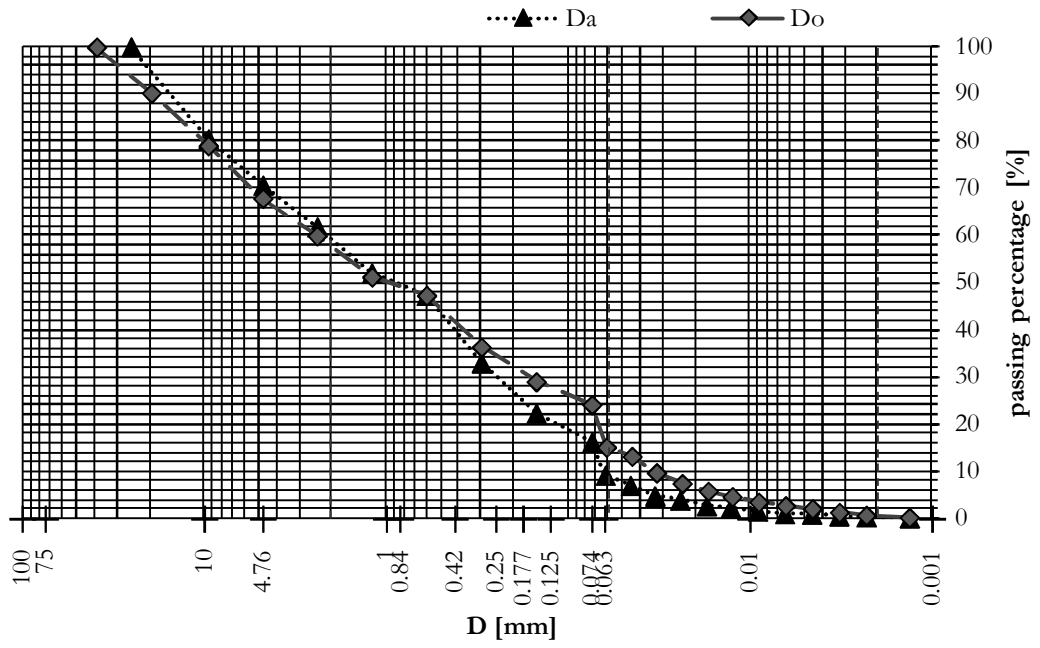

ID	Description ASTM	% pebbles	% gravel	% sand	% silt	% clay	D60	D10	Cu D60/D10
D_a	SM (silty sand with gravel)	0.0	29.3	54.4	14.2	2.0	2.2	0.065	34
D_o	SM (silty sand with gravel)	0.0	32.1	43.8	22.1	2.0	2.4	0.035	69

Figure A3.0.4: grain size curves from samples collected in Site A in August 2009 (D_a), and October 2009 (D_o).

Site E

Table A3.5: laboratory data for the drawing of the granulometric curves of different samples from Site E.

E_a (SM)		E_o (GM)		Ed (GM)	
D [mm]	%	D [mm]	%	D [mm]	%
23.90000	100.0	60.00000	100.0	38.00000	100.0
9.50000	88.4	19.50000	70.3	9.50000	64.8
4.76000	80.2	9.50000	64.7	4.76000	57.8
2.40000	70.5	4.76000	56.2	2.40000	52.1
1.20000	60.9	2.40000	48.1	1.20000	45.0
0.60000	56.3	1.20000	40.5	0.60000	41.7
0.30000	42.1	0.60000	37.3	0.30000	31.7
0.15000	31.5	0.30000	28.5	0.15000	25.3
0.07400	22.8	0.15000	22.8	0.07400	21.3
0.06244	15.4	0.07400	19.3	0.06216	12.7
0.04553	14.3	0.06161	12.1	0.04511	10.6
0.03339	9.5	0.04507	9.7	0.03321	7.2
0.02429	4.4	0.03319	6.6	0.02524	0.3
0.01736	1.0	0.02429	3.7	0.01797	0.0
0.01280	0.4	0.01761	1.6	0.01313	0.0
0.00909	0.3	0.01295	0.9	0.00929	0.0
0.00646	0.1	0.00919	0.6	0.00656	0.0
0.00459	0.0	0.00651	0.4	0.00464	0.0
0.00325	0.0	0.00461	0.2	0.00328	0.0
0.00230	0.0	0.00327	0.0	0.00232	0.0
0.00133	0.0	0.00232	0.0	0.00134	0.0
		0.00134	0.0		

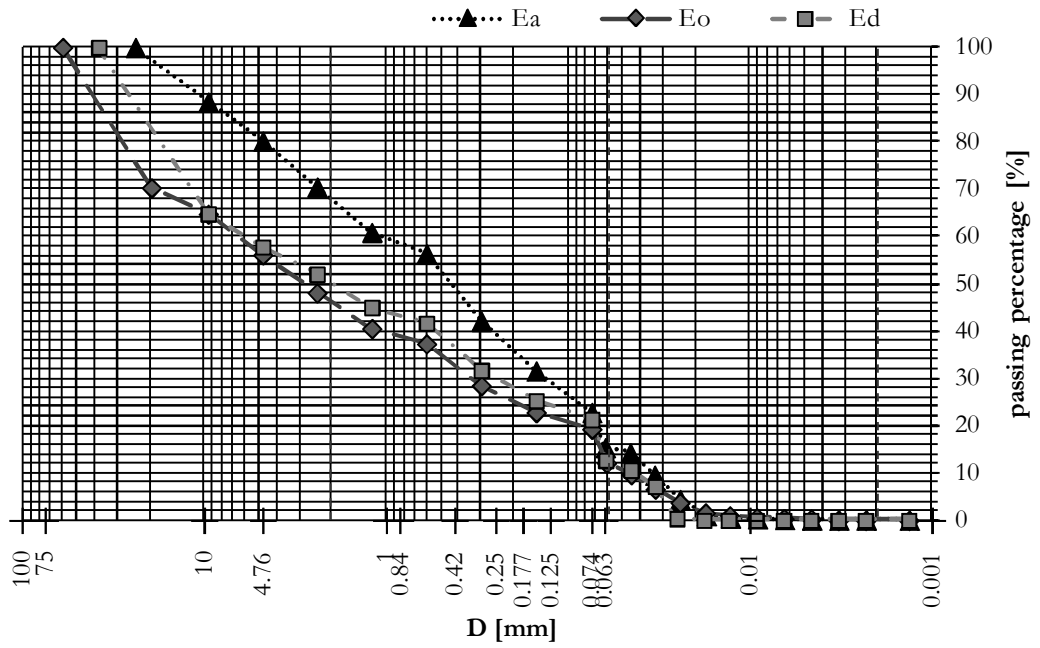

ID	Description ASTM	% pebbles	% gravel	% sand	% silt	% clay	D60	D10	Cu D60/D10
E_a	SM (silty sand with gravel)	0.0	19.8	57.4	22.6	0.2	1.2	0.034	35
E_o	GM (silty gravel with sand)	0.0	43.8	36.9	19.3	0.0	6.7	0.068	99
E_d	GM (silty gravel with sand)	0.0	42.2	36.5	21.3	0.0	4	0.045	89

Figure A3.5: grain size curves from samples collected in Site A in August 2009 (E_a), October 2009 (E_o), and December 2009 (E_d).

Site F

Table and Figure A3.6: laboratory data for the drawing of the grain size curve of the sample from Site F, collected in October 2009 (F_o).

F_o (GM)	
D [mm]	**%**
32.00000	100.0
19.50000	81.6
9.50000	69.2
4.76000	55.7
2.40000	46.5
1.20000	37.7
0.60000	34.3
0.30000	25.4
0.15000	20.3
0.07400	17.3
0.06161	10.8
0.04492	8.9
0.03262	7.1
0.02349	5.8
0.01693	4.4
0.01250	3.6
0.00890	3.1
0.00634	2.4
0.00453	1.7
0.00322	1.3
0.00228	1.2
0.00133	0.6

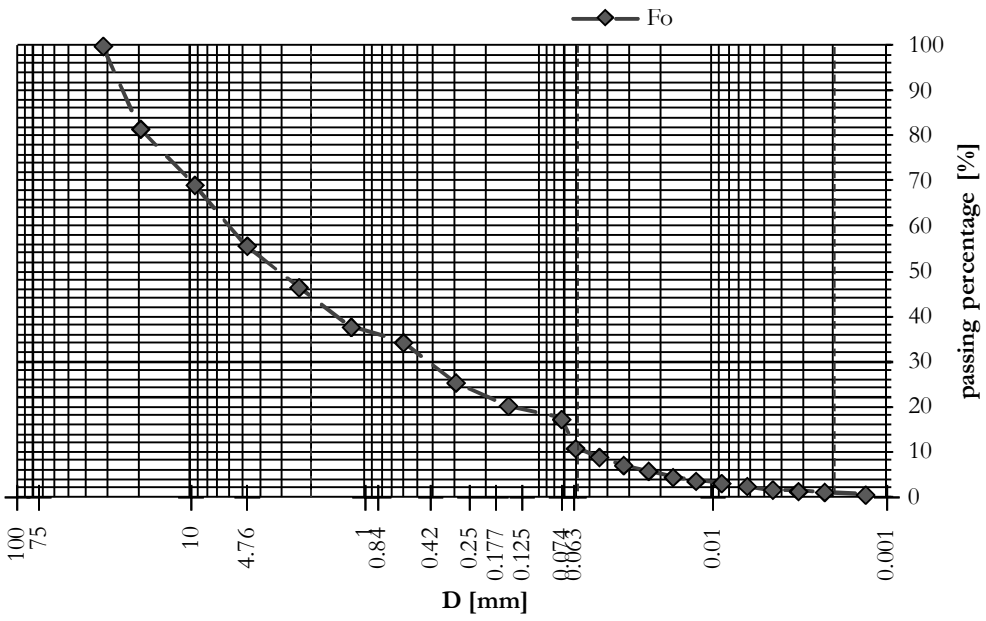

ID	Description ASTM	% pebbles	% gravel	% sand	% silt	% clay	D60	D10	Cu D60/D10
F_o	GM (silty gravel with sand)	0.0	44.3	38.4	15.3	2.0	6	0.056	107

Site G

Table and Figure A3.7: laboratory data for the drawing of the grain size curve of the sample from Site G, collected in October 2009 (G_o).

G_o (GW-GM)	
D [mm]	**%**
49.10000	100.0
9.50000	54.7
4.76000	47.2
2.40000	40.2
1.20000	32.1
0.60000	28.5
0.30000	18.8
0.15000	13.6
0.07400	11.7
0.06271	6.6
0.04605	4.9
0.03334	3.8
0.02403	2.8
0.01724	2.1
0.01268	1.7
0.00902	1.4
0.00641	1.1
0.00456	0.8
0.00325	0.4
0.00230	0.2
0.00133	0.2

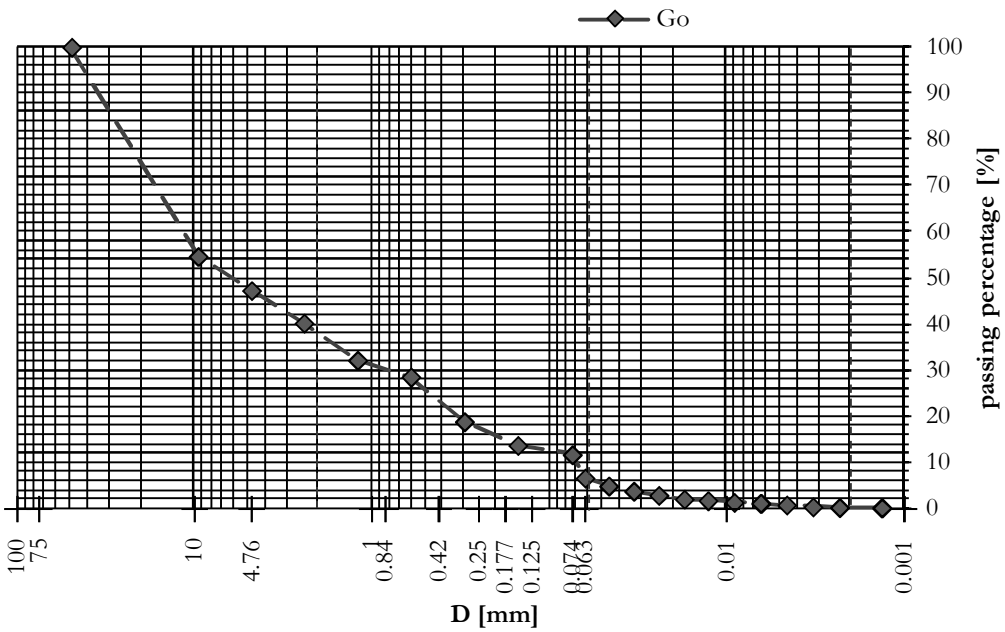

ID	Description ASTM	% pebbles	% gravel	% sand	% silt	% clay	D60	D10	Cu D60/D10
G_o	GW - GM (well graded gravel with silt and sand)	0.0	52.8	35.6	10.6	1.0	11	0.07	157

Other samples based on landuse

Table A3.8: laboratory data for the drawing of the grain size curves of samples dependent on the landuse of the collection sites.

Grass (SM)		Orchard (SM)		Wood (GM)	
D [mm]	**%**	**D [mm]**	**%**	**D [mm]**	**%**
25.40000	100.0	25.50000	100.0	29.40000	100.0
9.50000	69.6	9.50000	78.3	9.50000	62.7
4.76000	61.2	4.76000	65.9	4.76000	56.1
2.40000	54.0	2.40000	57.1	2.40000	48.6
1.20000	46.6	1.20000	47.7	1.20000	40.7
0.60000	42.9	0.60000	43.9	0.60000	37.1
0.30000	32.4	0.30000	33.6	0.30000	26.6
0.15000	24.9	0.15000	27.1	0.15000	19.6
0.07400	19.4	0.07400	22.9	0.07400	15.9
0.06271	10.9	0.05992	16.6	0.06105	10.5
0.04605	8.1	0.04511	11.4	0.04605	6.7
0.03321	6.6	0.03256	9.6	0.03334	5.1
0.02381	5.4	0.02349	7.7	0.02399	3.9
0.01708	4.3	0.01693	5.9	0.01712	3.3
0.01258	3.5	0.01245	5.2	0.01264	2.6
0.00902	2.3	0.00893	3.7	0.00900	2.0
0.00643	1.6	0.00636	2.9	0.00641	1.5
0.00455	1.4	0.00453	2.2	0.00455	1.3
0.00324	0.8	0.00324	1.1	0.00324	0.8
0.00230	0.4	0.00230	0.7	0.00229	0.6
0.00133	0.3	0.00133	0.5	0.00133	0.4

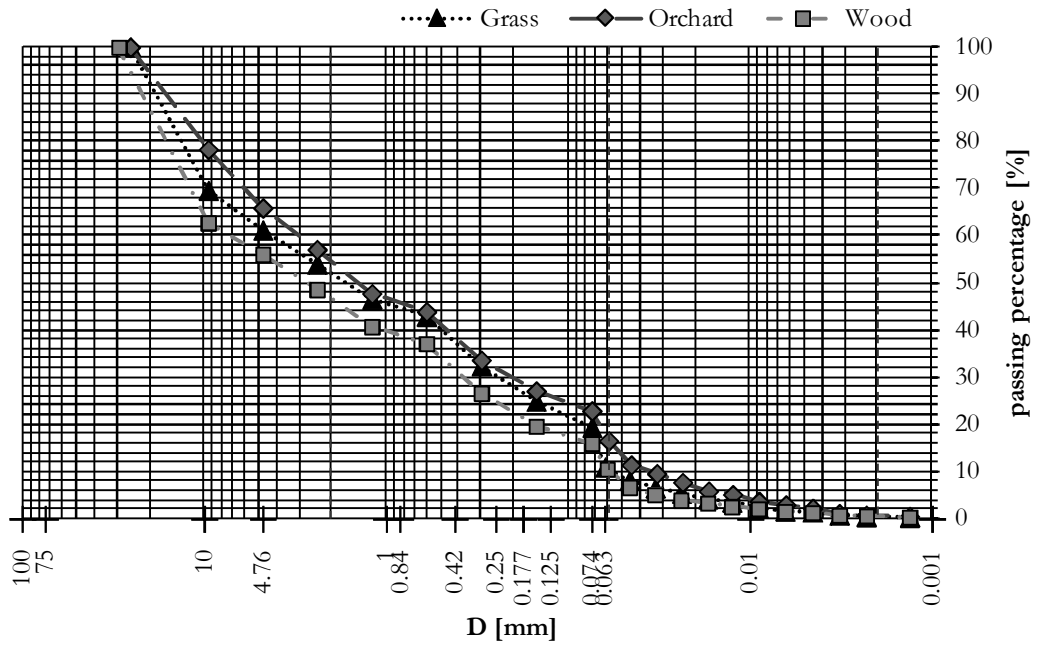

ID	Description ASTM	% pebbles	% gravel	% sand	% silt	% clay	D60	D10	Cu D60/D10
Grass	SM (silty sand with gravel)	0.0	38.8	41.8	17.7	1.7	4.5	0.06	75
Orchard	SM (silty sand with gravel)	0.0	34.1	43.0	20.6	2.3	3	0.035	86
Wood	GM (silty gravel with sand)	0.0	43.9	40.2	14.4	1.5	6	0.058	103

Figure A3.8: grain size curves from samples collected on sites characterized by different landuse.

ANNEX IV – PERMEAMETER TESTS

Falling Head Tests

Permeameter Characteristics [cm]			
L =	11.68	A =	81.233
r_A =	5.085	r_a =	2.1

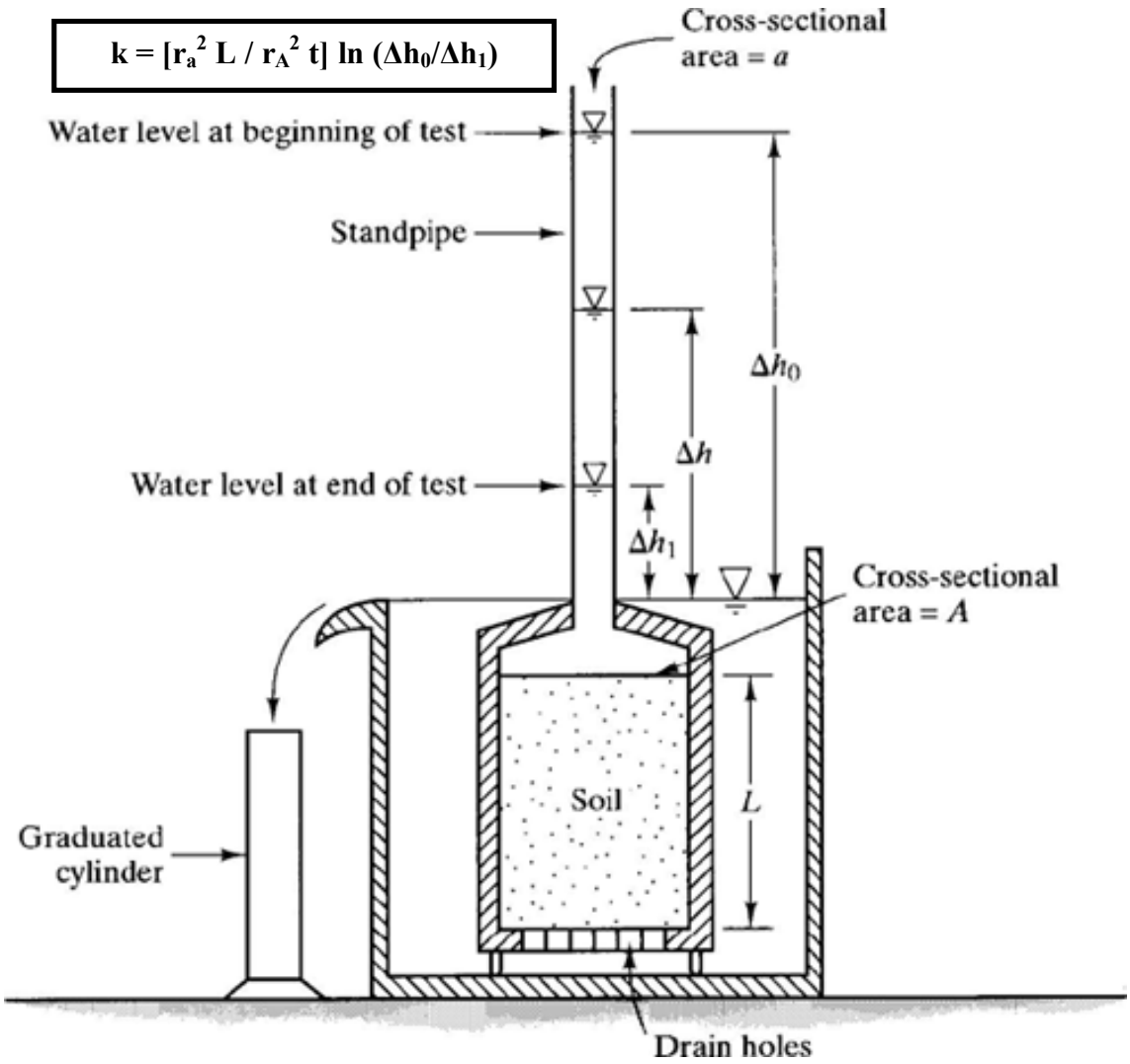

Figure A4.1: scheme of a falling head permeameter test, with the formula to calculate the saturated hydraulic conductivity (k). r_a is the radius of the standpipe, while r_A is that of specimen; t is time between Δh_0 and Δh_1.

Sample A_d

t	Δt	Tank level	Δlevel	Δh
min	min	mm	mm	cm
00.00		0.00		101.00
01.36	01.36	2.00	2.00	99.00
03.09	01.33	4.00	2.00	97.00
04.49	01.40	6.00	2.00	95.00
06.26	01.37	8.00	2.00	93.00
08.15	01.49	10.00	2.00	91.00
09.58	01.43	12.00	2.00	89.00
11.45	01.47	14.00	2.00	87.00
13.37	01.52	16.00	2.00	85.00
15.52	02.15	18.00	2.00	83.00
17.34	01.42	20.00	2.00	81.00
19.20	01.46	22.00	2.00	79.00
21.56	02.36	24.00	2.00	77.00
24.03	02.07	26.00	2.00	75.00
26.22	02.19	28.00	2.00	73.00
28.44	02.22	30.00	2.00	71.00
31.22	02.38	32.00	2.00	69.00
33.40	02.18	34.00	2.00	67.00
36.29	02.49	36.00	2.00	65.00
39.10	02.41	38.00	2.00	63.00

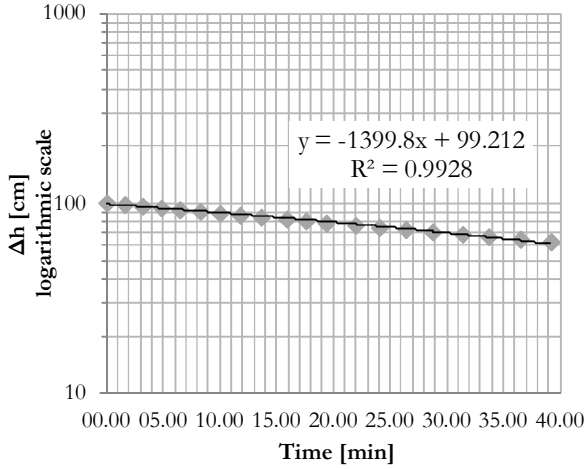

Figure A4.2: interpretation graph of the test and values used for the calculus of the hydraulic conductivity (k).

t [min]	Δh_0 [cm]	Δh_1 [cm]
39.10	101.00	63.00
k	2.40×10^{-2} **[cm/min]**	4.00×10^{-6} **[m/s]**

Sample C_d

t min	Δt min	Tank level mm	Δlevel mm	Δh cm
00.00		0.00		103.00
01.40	01.40	2.00	2.00	101.00
03.43	02.03	4.00	2.00	99.00
05.27	01.44	6.00	2.00	97.00
06.59	01.32	8.00	2.00	95.00
09.24	02.25	10.00	2.00	93.00
11.29	02.05	12.00	2.00	91.00
13.38	02.09	14.00	2.00	89.00
15.53	02.15	16.00	2.00	87.00
18.07	02.14	18.00	2.00	85.00
20.29	02.22	20.00	2.00	83.00
22.53	02.24	22.00	2.00	81.00
25.35	02.42	24.00	2.00	79.00
27.57	02.22	26.00	2.00	77.00
30.42	02.45	28.00	2.00	75.00
33.25	02.43	30.00	2.00	73.00
36.19	02.54	32.00	2.00	71.00
39.05	02.46	34.00	2.00	69.00
42.08	03.03	36.00	2.00	67.00
45.20	03.12	38.00	2.00	65.00
48.21	03.01	40.00	2.00	63.00

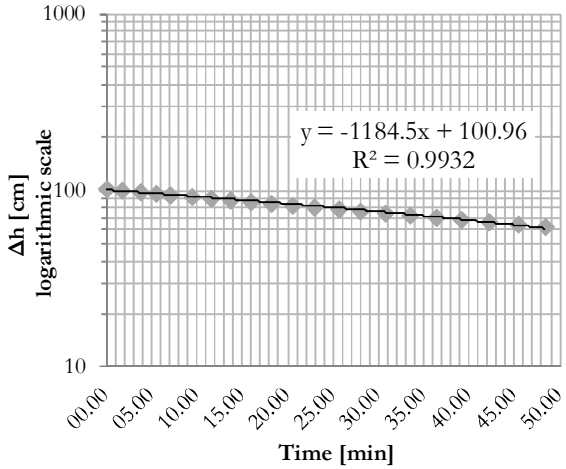

Figure A4.3: interpretation graph of the test and values used for the calculus of the hydraulic conductivity (k).

t [min]	Δh_0 [cm]	Δh_1 [cm]
23	103.00	63.00
k	1.90×10^{-2} **[cm/min]**	3.17×10^{-6} **[m/s]**

Sample E_d

t min	Δt min	Tank level mm	Δlevel mm	Δh cm
00.00		0.00		103.00
01.52	01.52	2.00	2.00	101.00
03.47	01.55	4.00	2.00	99.00
05.52	02.05	6.00	2.00	97.00
07.55	02.03	8.00	2.00	95.00
10.03	02.08	10.00	2.00	93.00
12.16	02.13	12.00	2.00	91.00
14.30	02.14	14.00	2.00	89.00
16.49	02.19	16.00	2.00	87.00
18.33	01.44	18.00	2.00	85.00
21.40	03.07	20.00	2.00	83.00
24.02	02.22	22.00	2.00	81.00
26.30	02.28	24.00	2.00	79.00
29.04	02.34	26.00	2.00	77.00
31.59	02.55	28.00	2.00	75.00
34.45	02.46	30.00	2.00	73.00
37.38	02.53	32.00	2.00	71.00
40.42	03.04	34.00	2.00	69.00
43.26	02.44	36.00	2.00	67.00
46.55	03.29	38.00	2.00	65.00

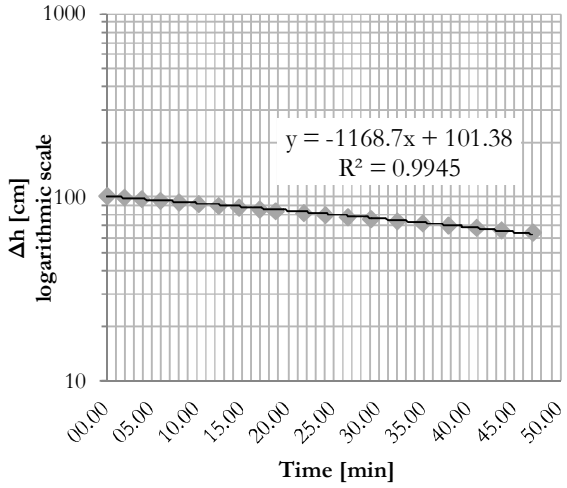

Figure A4.4: interpretation graph of the test and values used for the calculus of the hydraulic conductivity (k).

t [min]	Δh_0 [cm]	Δh_1 [cm]
46.55	103.00	65
k	1.96×10^{-2} **[cm/min]**	3.26×10^{-6} **[m/s]**

Sample A_f

t min	Δt min	Tank level mm	Δlevel mm	Δh cm
00.00		0.00		101.00
01.00	01.00	1.20	1.20	99.80
02.00	01.00	2.10	0.90	98.90
03.00	01.00	3.00	0.90	98.00
04.00	01.00	3.90	0.90	97.10
05.00	01.00	4.90	1.00	96.10
06.00	01.00	5.80	0.90	95.20
07.00	01.00	6.80	1.00	94.20
08.00	01.00	7.75	0.95	93.25
09.00	01.00	8.65	0.90	92.35
10.00	01.00	9.55	0.90	91.45
11.00	01.00	10.50	0.95	90.50
12.00	01.00	11.40	0.90	89.60
13.00	01.00	12.25	0.85	88.75
14.00	01.00	13.05	0.80	87.95
15.00	01.00	13.95	0.90	87.05
16.00	01.00	14.85	0.90	86.15
17.00	01.00	15.70	0.85	85.30
18.00	01.00	16.50	0.80	84.50
19.00	01.00	17.30	0.80	83.70
20.00	01.00	18.10	0.80	82.90
21.00	01.00	18.90	0.80	82.10
22.00	01.00	19.70	0.80	81.30
23.00	01.00	20.50	0.80	80.50

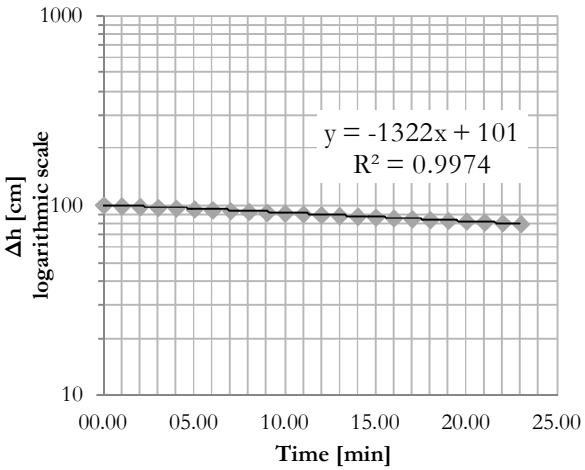

Figure A4.5: interpretation graph of the test and values used for the calculus of the hydraulic conductivity (k).

t [min]	Δh_0 [cm]	Δh_1 [cm]
23	101.00	80.50
k	1.96×10^{-2} **[cm/min]**	3.27×10^{-6} **[m/s]**

Sample B_f

t min	Δt min	Tank level mm	Δlevel mm	Δh cm
00.00		0.00		101.00
01.00	01.00	4.40	4.40	96.60
02.00	01.00	8.70	4.30	92.30
03.00	01.00	12.70	4.00	88.30
04.00	01.00			
05.00	01.00	20.10		
06.00	01.00	23.60	3.50	77.40
07.00	01.00	26.80	3.20	74.20
08.00	01.00	30.00	3.20	71.00
09.00	01.00	33.00	3.00	68.00
10.00	01.00	35.90	2.90	65.10
11.00	01.00	38.70	2.80	62.30
12.00	01.00	41.30	2.60	59.70
13.00	01.00	43.90	2.60	57.10
14.00	01.00	46.50	2.60	54.50
15.00	01.00	48.70	2.20	52.30
15.58	00.58	50.00	1.30	51.00

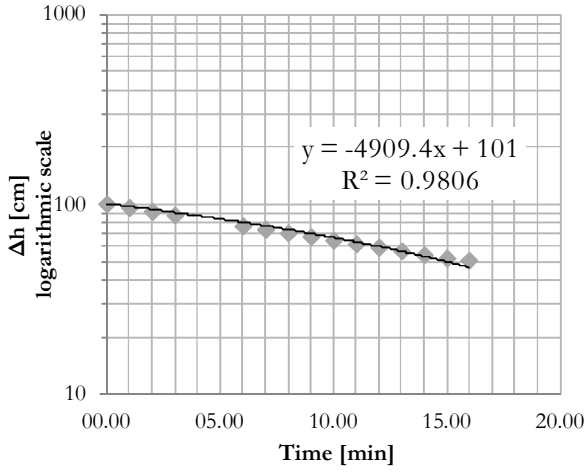

Figure A4.6: interpretation graph of the test and values used for the calculus of the hydraulic conductivity (k).

t [min]	Δh_0 [cm]	Δh_1 [cm]
15.58	101.00	51.00
k	8.52×10^{-2} **[cm/min]**	1.42×10^{-5} **[m/s]**

Sample G_f

t min	Δt min	Tank level mm	Δlevel mm	Δh cm
00.00		0.00		82.20
01.00	01.00	0.85	0.85	81.35
02.00	01.00	1.70	0.85	80.50
03.00	01.00	2.45	0.75	79.75
04.00	01.00	3.10	0.65	79.10
05.00	01.00	3.60	0.50	78.60
06.00	01.00	4.10	0.50	78.10
07.00	01.00	4.55	0.45	77.65
08.00	01.00	4.95	0.40	77.25
09.00	01.00	5.35	0.40	76.85
10.00	01.00	5.70	0.35	76.50
11.00	01.00	6.00	0.30	76.20
12.00	01.00	6.20	0.20	76.00
13.00	01.00	6.40	0.20	75.80
14.00	01.00	6.70	0.30	75.50
15.00	01.00	6.90	0.20	75.30
16.00	01.00	7.00	0.10	75.20
17.00	01.00	7.20	0.20	75.00
18.00	01.00	7.30	0.10	74.90
19.00	01.00	7.40	0.10	74.80
20.00	01.00	7.50	0.10	74.70

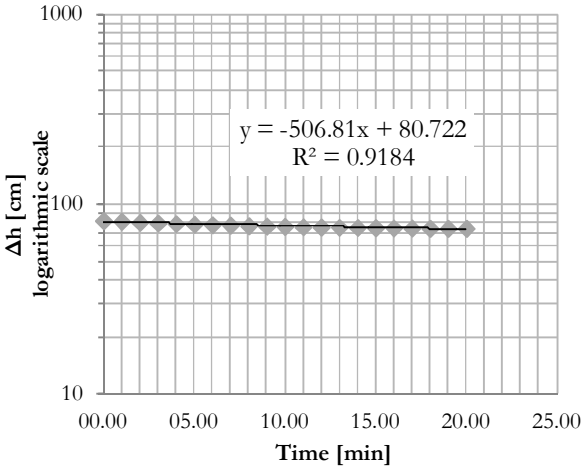

Figure A4.7: interpretation graph of the test and values used for the calculus of the hydraulic conductivity (k).

t [min]	Δh_0 [cm]	Δh_1 [cm]
20	82.20	74.70
k	1.27×10^{-2} **[cm/min]**	2.12×10^{-6} **[m/s]**

Constant Head Tests

Permeameter Characteristics [cm]			
L =	11.68	A =	81.233
r_A =	5.085	r_a =	2.1

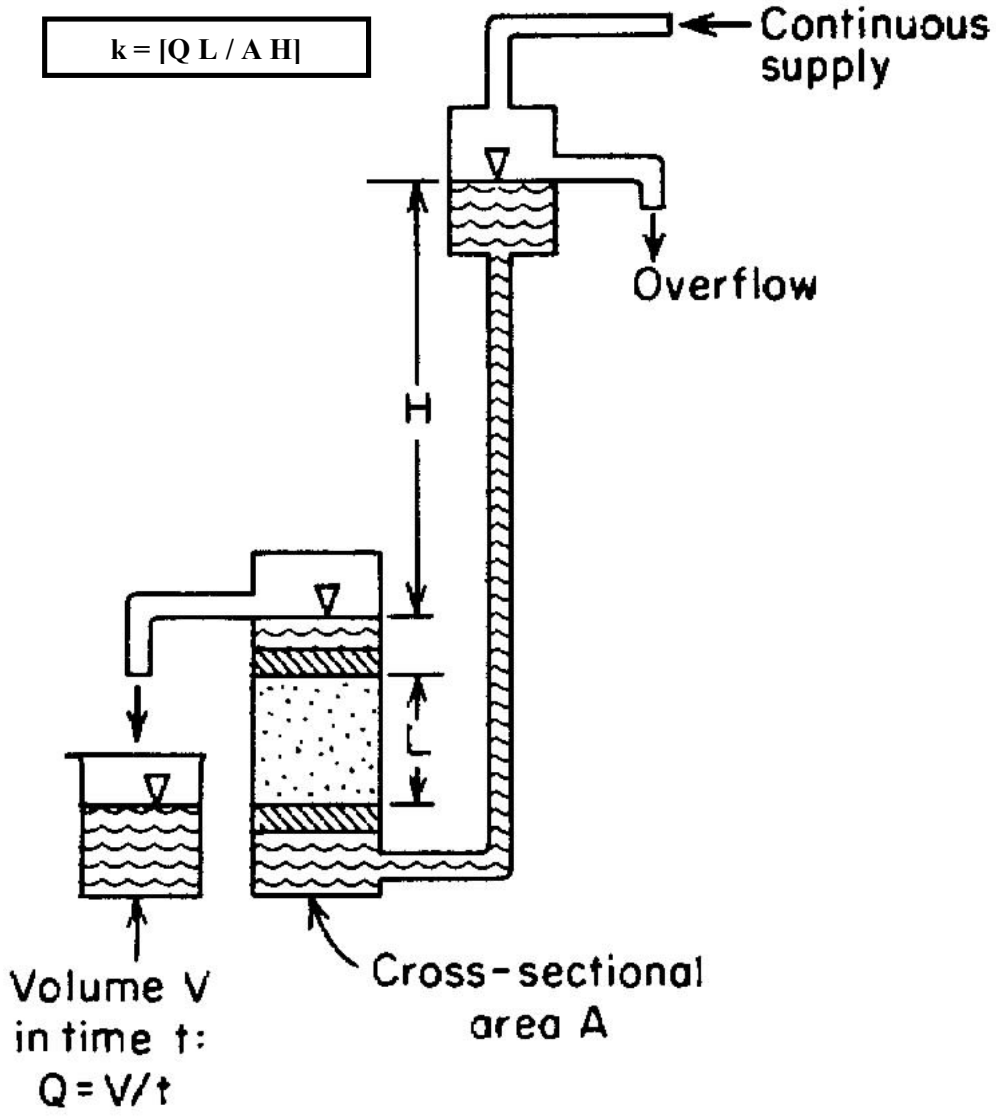

Figure A4.8: scheme of a constant head permeameter test, with the formula to calculate the saturated hydraulic conductivity (k). r_a is the radius of the standpipe, while r_A is that of specimen.

Sample A_d

t [min]	Δt [min]	V [ml]	ΔV [ml]
00.00		0	
00.59	00.59	15	15
01.20	00.21	25	10
02.38	01.18	35	10
03.34	00.56	45	10
04.27	00.53	55	10
05.18	00.51	65	10
06.16	00.58	75	10
07.09	00.53	85	10
07.57	00.48	95	10

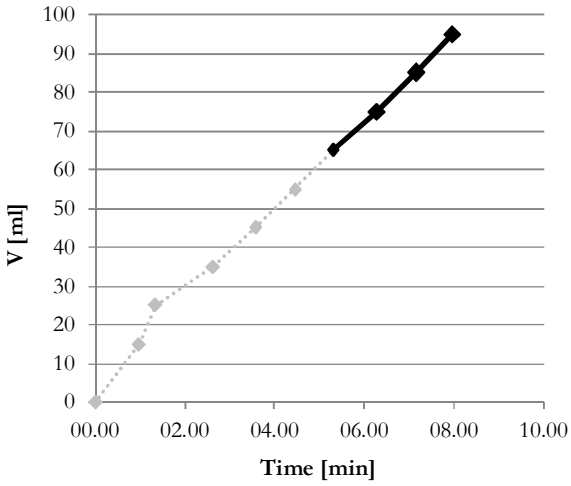

Figure A4.9: interpretation graph of the test and values used for the calculus of Q and k.

Q =	11.43 ml/min	0.19 cm^3/s
k =	2.35×10^{-4} cm/s	2.35×10^{-6} m/s

Sample C_d

t [min]	Δt [min]	V [ml]	ΔV [ml]
00.00		0	
00.55	00.55	15	15
01.32	00.37	25	10
02.38	01.06	35	10
03.32	00.54	45	10
04.23	0.51	55	10
05.17	00.54	65	10
06.12	00.55	75	10
07.08	00.56	85	10
07.50	00.42	95	10

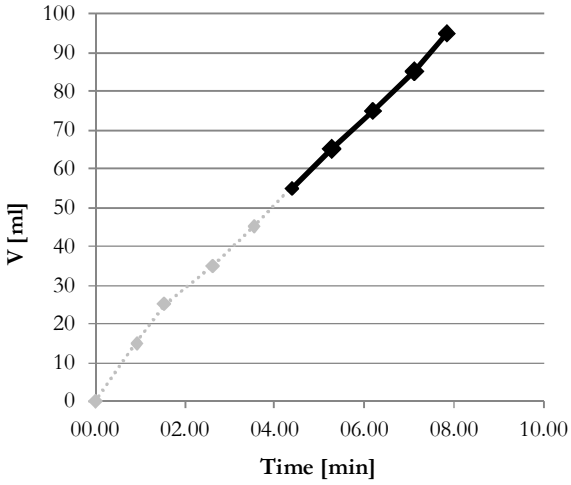

Figure A4.10: interpretation graph of the test and values used for the calculus of Q and k.

Q =	11.63 ml/min	0.19 cm^3/s
k =	2.39×10^{-4} cm/s	2.39×10^{-6} m/s

Sample E_d

t [min]	Δt [min]	V [ml]	ΔV [ml]
00.00		0	
00.52	00.52	15	15
01.42	00.50	25	10
02.36	00.54	35	10
03.31	00.55	45	10
04.18	00.47	55	10
05.17	00.59	65	10
06.09	00.52	75	10
07.07	00.58	85	10
07.49	00.42	95	10

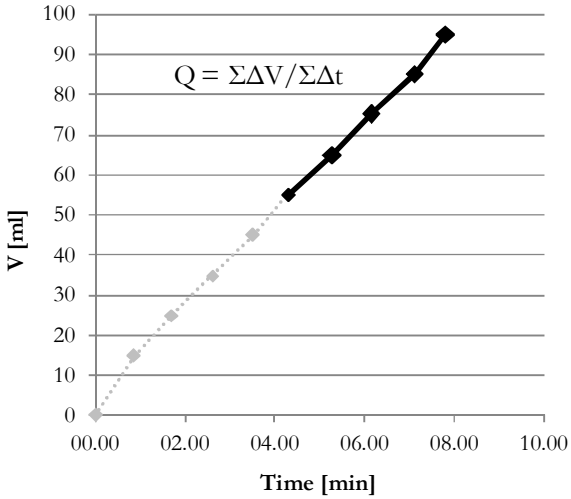

Figure A4.11: interpretation graph of the test and values used for the calculus of Q and k.

Q =	11.63 ml/min	0.19 cm^3/s
k =	2.40×10^{-4} cm/s	2.40×10^{-6} m/s

Sample A_f

t [min]	Δt [min]	V [ml]	ΔV [ml]
00.00		100	
02.30	02.30	130	30
04.25	01.55	150	20
05.34	01.09	160	10
06.33	00.59	170	10
07.39	01.06	180	10
08.36	00.57	190	10
09.35	00.59	200	10
10.39	01.04	210	10
11.46	01.07	220	10
12.43	00.57	230	10
13.39	00.56	240	10
14.33	00.54	250	10
15.40	01.07	260	10
16.43	01.03	270	10
17.43	01.00	280	10
18.41	00.58	290	10
19.39	00.58	300	10
20.39	01.00	310	10
21.38	00.59	320	10

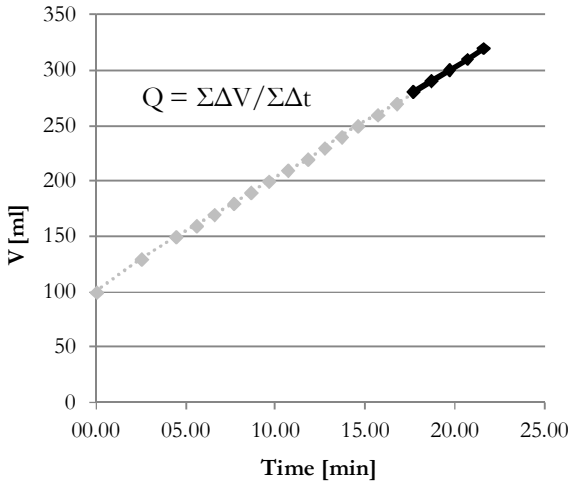

Figure A4.12: interpretation graph of the test and values used for the calculus of Q and k.

Q =	10.16 ml/min	0.17 cm^3/s
k =	2.08×10^{-4} cm/s	2.08×10^{-6} m/s

Sample B_f

t [min]	Δt [min]	V [ml]	ΔV [ml]
00.00		100	
00.49	00.49	150	50
01.56	01.07	200	50
02.19	00.23	220	20
02.46	00.27	240	20
03.26	00.40	270	30
04.03	00.37	300	30
04.40	00.37	330	30
05.17	00.37	360	30
06.02	00.45	390	30
06.41	00.39	420	30
07.21	00.40	450	30
08.02	00.41	480	30
08.43	00.41	510	30
09.23	00.40	540	30
10.03	00.40	570	30

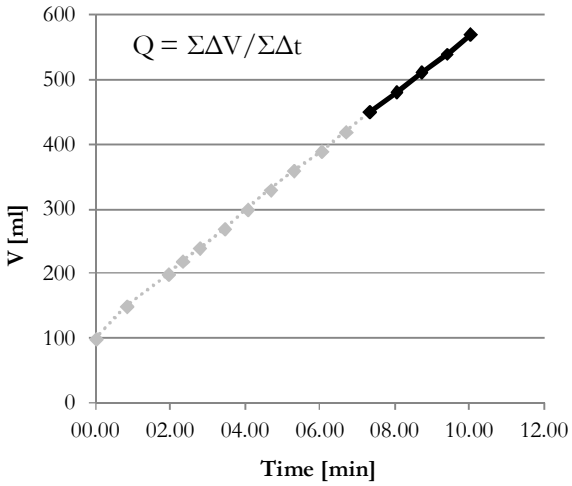

Figure A4.13: interpretation graph of the test and values used for the calculus of Q and k.

Q =	44.64 ml/min	0.74 cm^3/s
k =	9.15×10^{-4} cm/s	9.15×10^{-6} m/s

Sample G_f

t [min]	Δt [min]	V [ml]	ΔV [ml]
00.00		200	
00.34	00.34	230	30
01.08	00.34	260	30
01.45	00.37	290	30
02.22	00.37	320	30
02.57	00.35	350	30
03.33	00.36	380	30
04.09	00.36	410	30
04.44	00.35	440	30
05.19	00.35	470	30
05.57	00.38	500	30
06.34	00.37	530	30
07.11	00.37	560	30
07.48	00.37	590	30
08.25	00.37	620	30

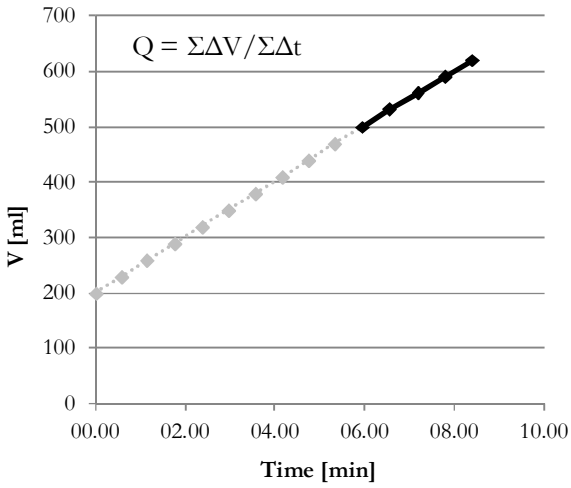

Figure A4.14: interpretation graph of the test and values used for the calculus of Q and k.

Q =	48.39 ml/min	0.81 cm^3/s
k =	9.92×10^{-4} cm/s	9.92×10^{-6} m/s

ANNEX V – DIRECT SHEAR TESTS

Sample Site-A_d with organic content

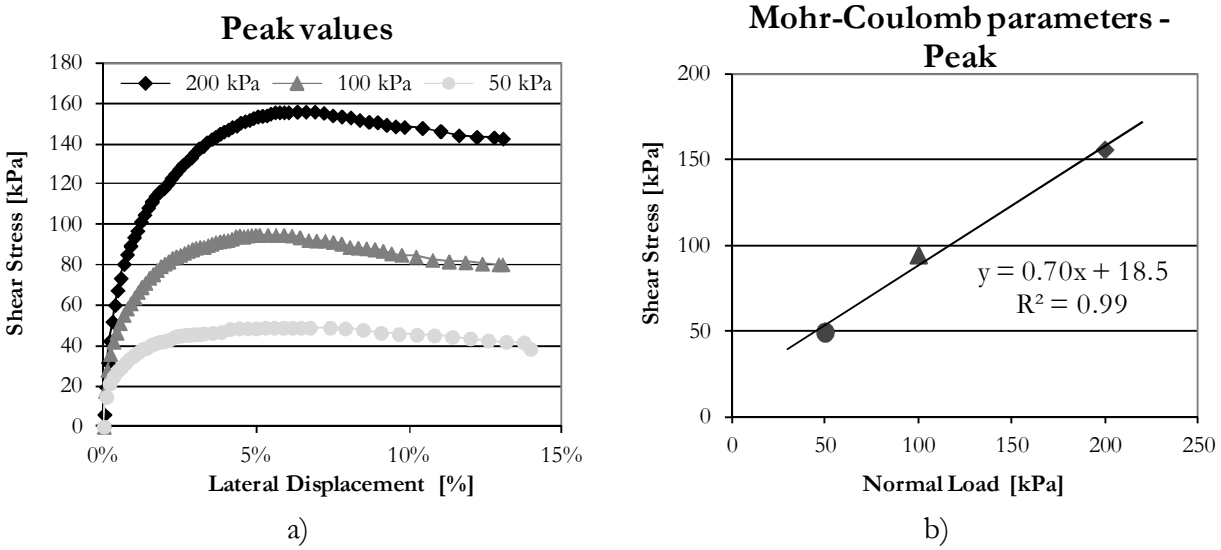

a) b)

Figure A5.1: peak values calculated for sample A_d with organic content. a) stress – strain curves under different normal load; b) maximum registered shear stress for every different normal load and determination of the Mohr-Coulomb cohesion (c) and friction angle (ϕ).

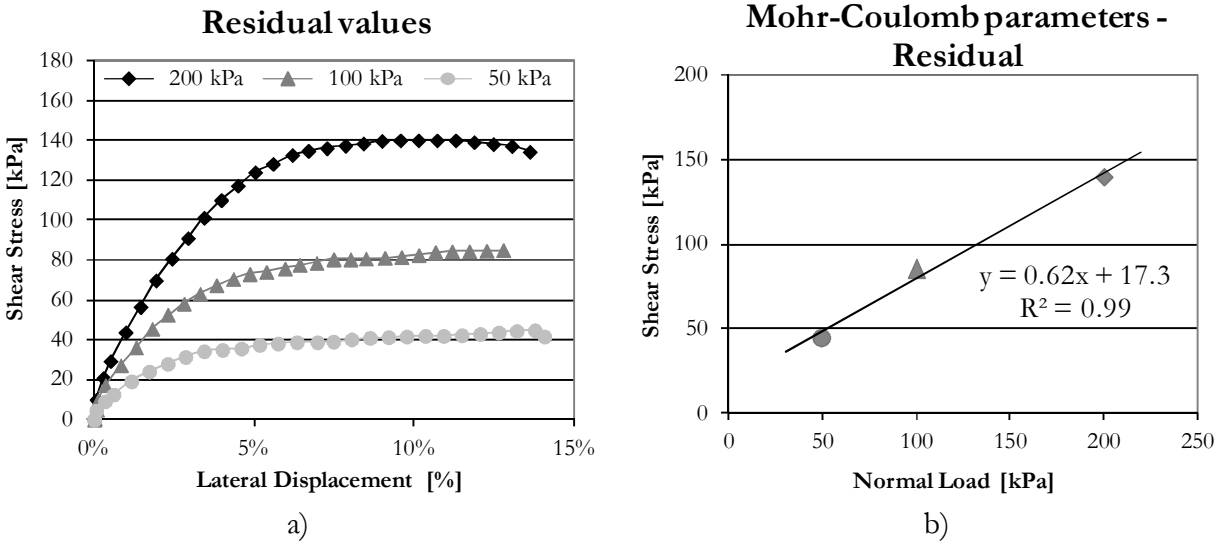

a) b)

Figure A5.2: residual values calculated for sample A_d with organic content. a) stress – strain curves under different normal load; b) maximum registered shear stress for every different normal load and determination of the Mohr-Coulomb cohesion (c) and friction angle (ϕ).

Sample Site-A_d without organic content

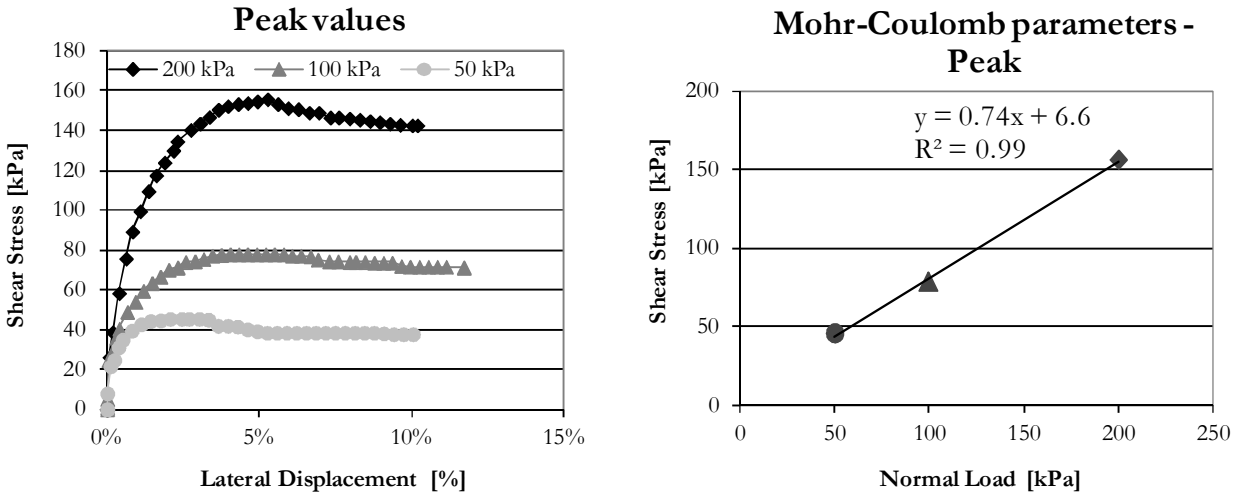

a) b)

Figure A5.3: peak values calculated for sample A_d without organic content. a) stress – strain curves under different normal load; b) maximum registered shear stress for every different normal load and determination of the Mohr-Coulomb cohesion (c) and friction angle (ϕ).

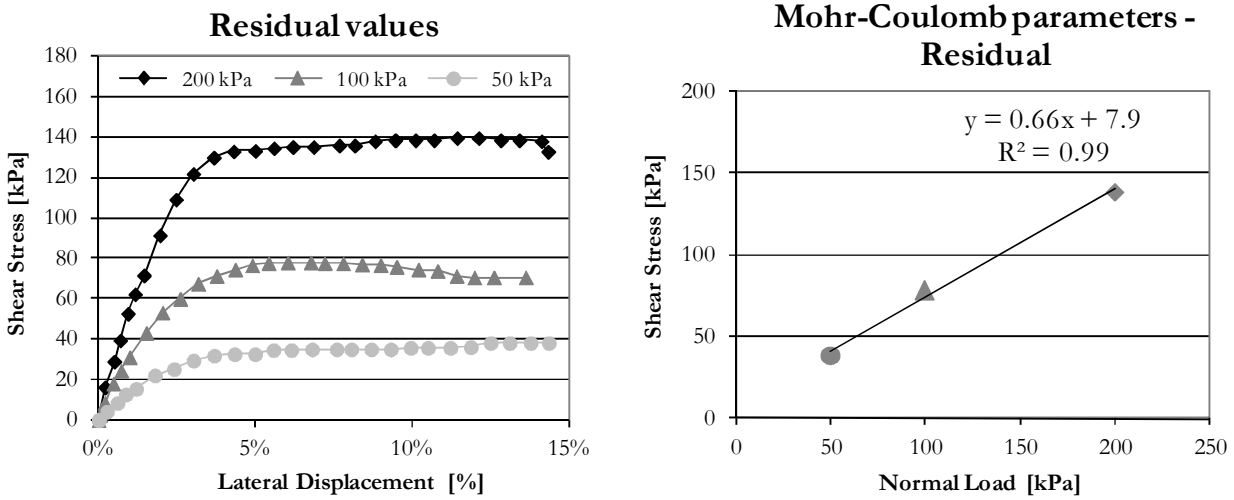

a) b)

Figure A5.4: residual values calculated for sample A_d without organic content. a) stress – strain curves under different normal load; b) maximum registered shear stress for every different normal load and determination of the Mohr-Coulomb cohesion (c) and friction angle (ϕ).

Sample Site-C_d with organic content

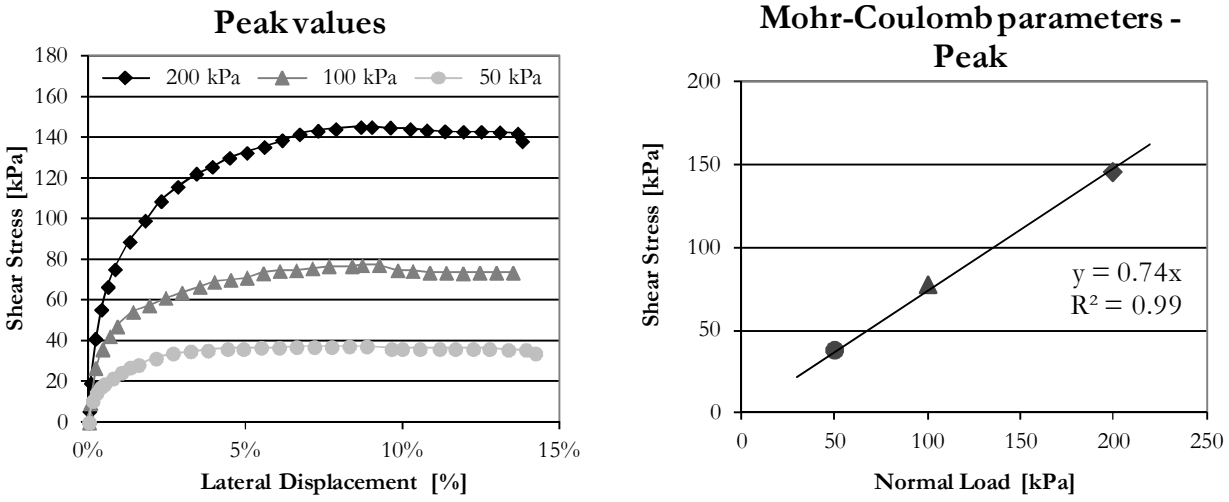

a) b)

Figure A5.5: peak values calculated for sample C_d with organic content. a) stress – strain curves under different normal load; b) maximum registered shear stress for every different normal load and determination of the Mohr-Coulomb cohesion (c) and friction angle (ϕ). Considering the GM granulometric composition of the sample, cohesion was set to 0 kPa.

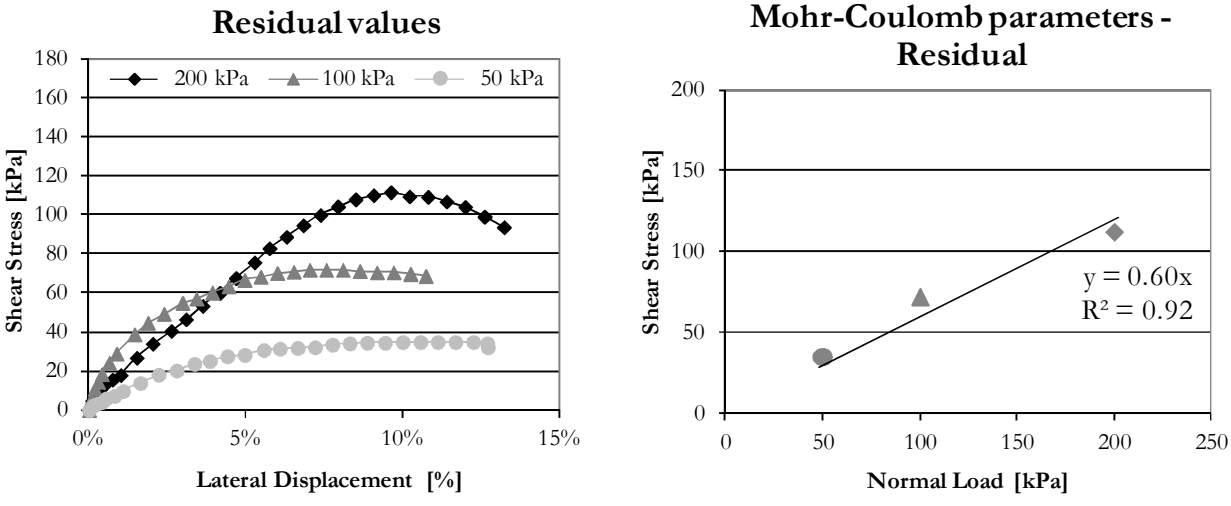

a) b)

Figure A5.6: residual values calculated for sample C_d with organic content. a) stress – strain curves under different normal load; b) maximum registered shear stress for every different normal load and determination of the Mohr-Coulomb cohesion (c) and friction angle (ϕ). Considering the GM granulometric composition of the sample, cohesion was set to 0 kPa.

Sample Site-C_d without organic content

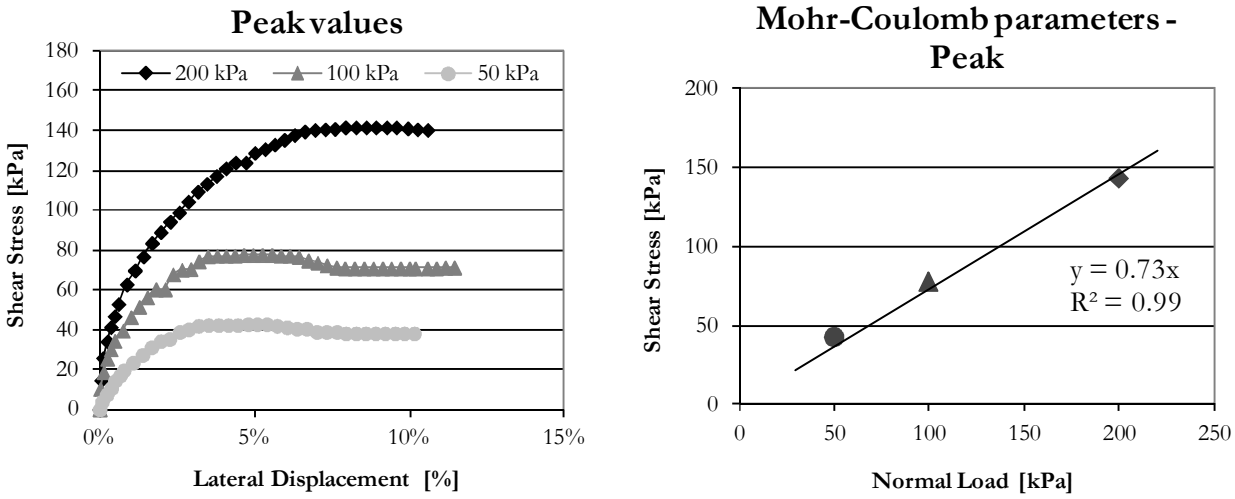

Figure A5.7: peak values calculated for sample C_d without organic content. a) stress – strain curves under different normal load; b) maximum registered shear stress for every different normal load and determination of the Mohr-Coulomb cohesion (c) and friction angle (ϕ). Considering the GM granulometric composition of the sample, cohesion was set to 0 kPa.

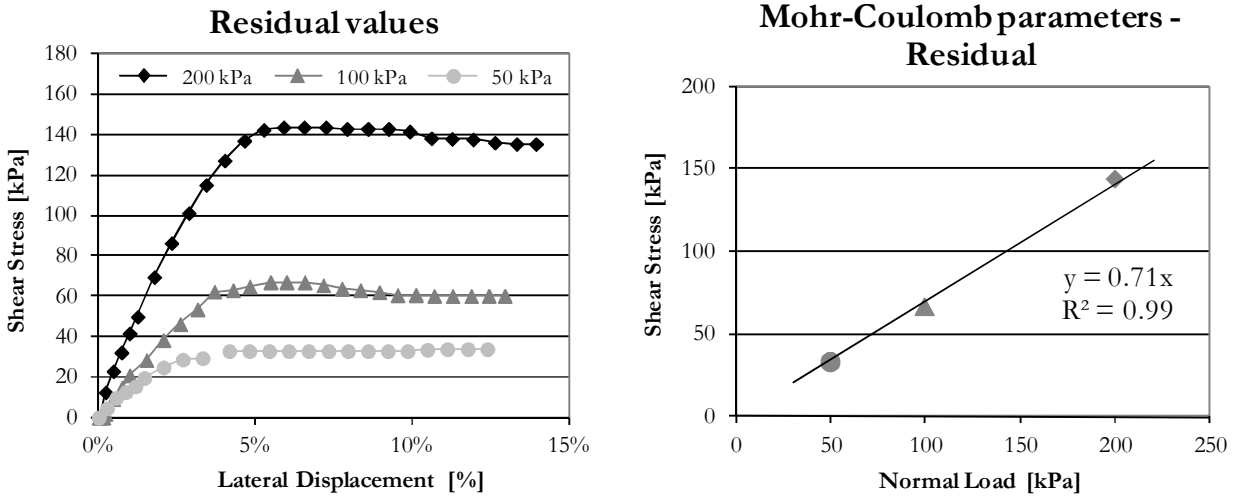

Figure A5.8: residual values calculated for sample C_d without organic content. a) stress – strain curves under different normal load; b) maximum registered shear stress for every different normal load and determination of the Mohr-Coulomb cohesion (c) and friction angle (ϕ). Considering the GM granulometric composition of the sample, cohesion was set to 0 kPa.

Sample Site-E_d with organic content

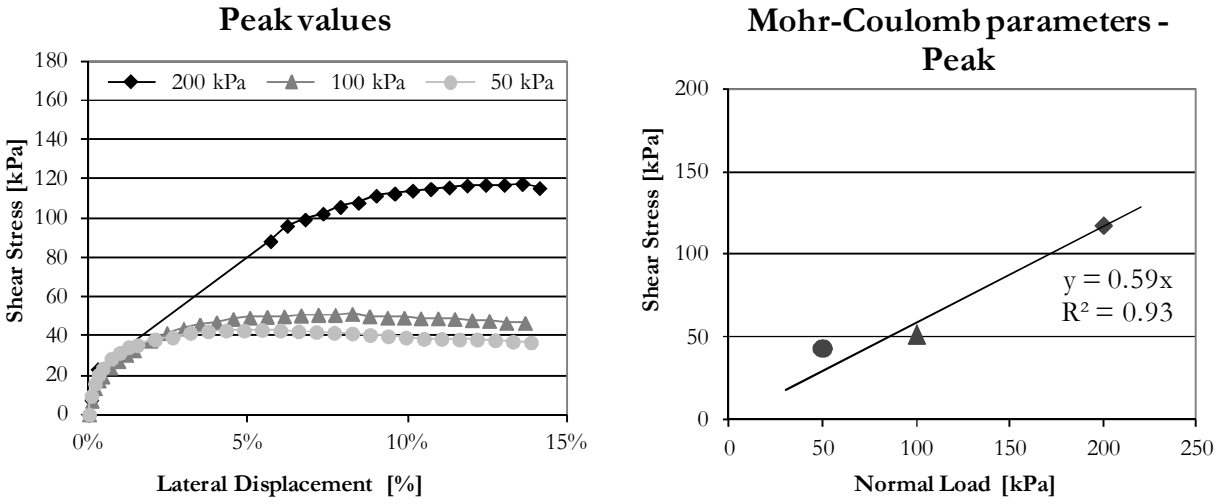

Figure A5.9: peak values calculated for sample E_d with organic content. a) stress – strain curves under different normal load; b) maximum registered shear stress for every different normal load and determination of the Mohr-Coulomb cohesion (c) and friction angle (ϕ). Considering the GM granulometric composition of the sample, cohesion was set to 0 kPa.

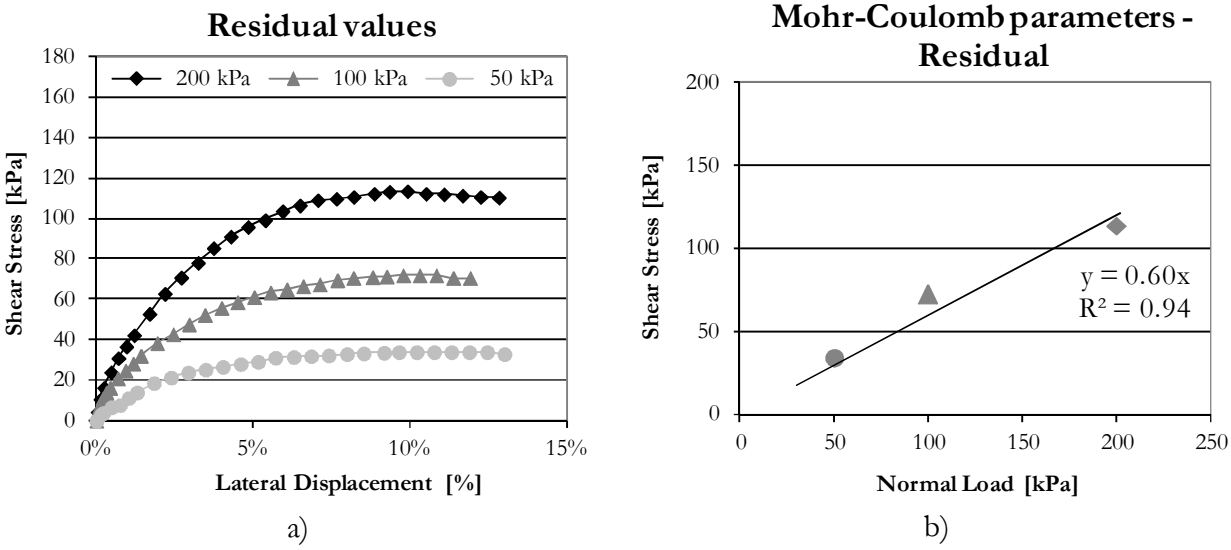

Figure A5.10: residual values calculated for sample E_d with organic content. a) stress – strain curves under different normal load; b) maximum registered shear stress for every different normal load and determination of the Mohr-Coulomb cohesion (c) and friction angle (ϕ). Considering the GM granulometric composition of the sample, cohesion was set to 0 kPa.

Sample Site-E_d without organic content

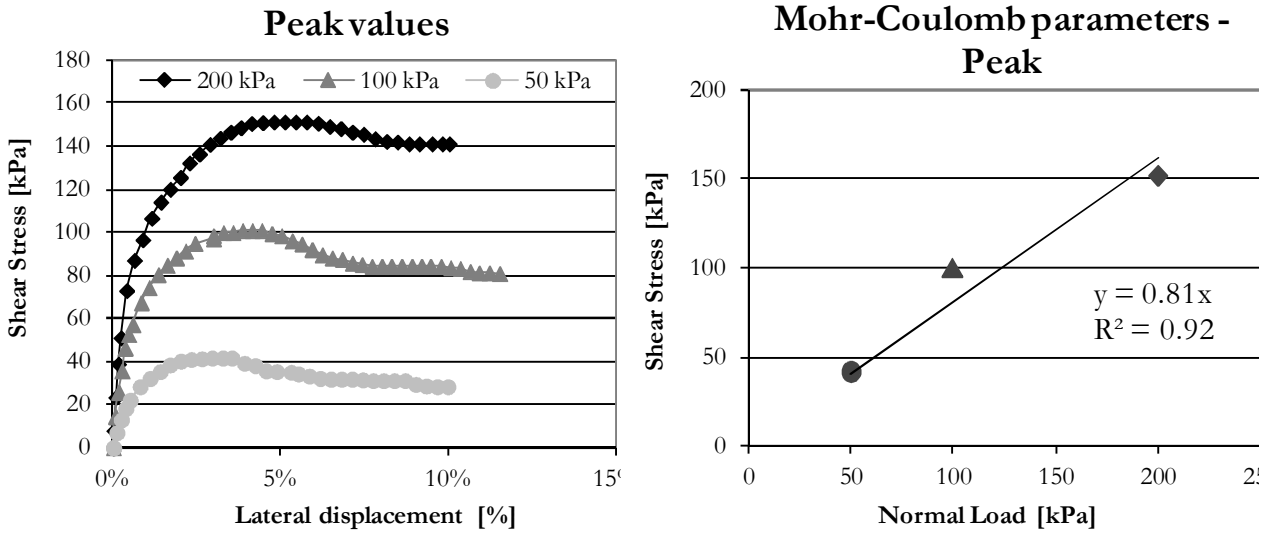

a) b)

Figure A5.11: peak values calculated for sample E_d without organic content. a) stress – strain curves under different normal load; b) maximum registered shear stress for every different normal load and determination of the Mohr-Coulomb cohesion (c) and friction angle (ϕ). Considering the GM granulometric composition of the sample, cohesion was set to 0 kPa.

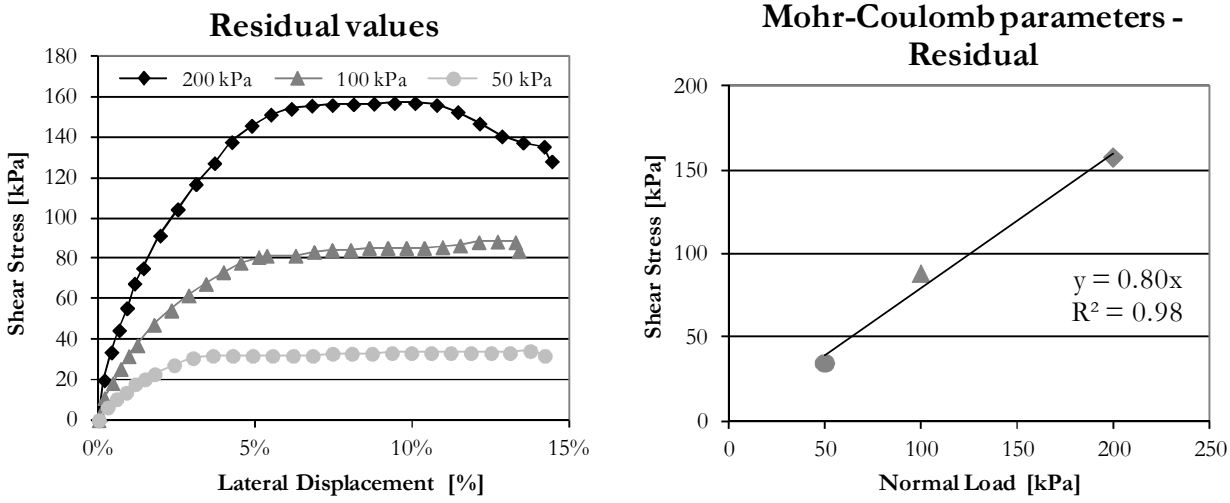

a) b)

Figure A5.12: residual values calculated for sample E_d without organic content. a) stress – strain curves under different normal load; b) maximum registered shear stress for every different normal load and determination of the Mohr-Coulomb cohesion (c) and friction angle (ϕ). Considering the GM granulometric composition of the sample, cohesion was set to 0 kPa.

ANNEX VI – DENSITY FIELD MEASURES

	A_a*	C_a	D_a	E_a	G_f	B_f	A_f
REFERENCE VALUES							
γ_{sc} - bulk density of the calibrated sand (g/cm^3)	1.310	1.310	1.310	1.310	1.310	1.310	1.310
Cone Volume (Vc) (cm^3)	1033.8	1033.8	1033.8	1033.8	1033.8	1033.8	1033.8
Tare weight (T) - weight of the box of the extracted soil (g)	664.4	676	667.7	669.2	849.7	562.3	570.6
FIELD CALCULATED QUANTITIES							
P1 - initial weight of the sand (g)	8500.0	8500.0	8500.0	8500.0	8500.0	8500.0	8500.0
P2 - weight of the remained sand(g)	5660.4	5517.4	5212.5	5388.3	4425.4	4019.8	3373.8
P3 = (P1-P2). Weight of the used sand (g)	2839.6	2982.6	3287.5	3111.7	4074.6	4480.2	5126.2
V = P3/γsc - Vc. In situ volume of the extracted soil (cm^3)	1133.8	1243.0	1475.7	1341.5	2076.6	2386.2	2879.3
P'4 = gross weight of the natural soil (g)	1830.6	2681.4	2708.2	2746.7	4096.3	4047.5	4633.0
P4 = P'4-T. Net weight of the soil in natural conditions (g)	1166.2	2005.4	2040.5	2077.5	3246.6	3485.2	4062.4
Wn - Water content respect to the dry weight (%)	7.2	2.6	3.8	12.1	11.5	9.1	10.2
P'5 - Gross weight of the dry soil (g)	1752.2	2630.6	2633.6	2522.7	3762.1	3756.0	4256.4
P5 = P4/(1+Wn). Net weight of the dry soil (g)	1087.8	1954.6	1965.9	1853.5	2912.4	3193.7	3685.8
γ_0 - Natural bulk density of soil (g/cm3)	1.029*	1.613	1.383	1.549	1.563	1.461	1.411
γ_d - dry bulk density of the soil (g/cm3)	0.959*	1.572	1.332	1.382	1.402	1.338	1.280

Figure A6.1: field data and following calculation for the determination of the natural and dry bulk densities of soils. * enlightens an error in the performing of the test on sample A_a that in fact gives too low values of bulk density.